Semiconductor Nanowires Grown by Molecular Beam Epitaxy for Electronics Applications

Ivan Isakov

Department of Electronic and Electrical Engineering

University College London

A thesis submitted in partial fulfillment of the requirements for the degree of

Doctor of Philosophy

2015

I, Ivan Isakov confirm that the work presented in this thesis is my own. Where information has been derived from other sources, I confirm that this has been indicated in the thesis.

Acknowledgements

The present work was not possible without the help and assistance of my colleagues and friends. First of all, I would like to acknowledge my supervisor Professor Paul Warburton for his invaluable help in my establishment as an independent researcher, experimentalist and scientist in general. His irony, ability to teach all the details of the work in scientific research environment, openness to all my initiatives and willingness to work through my un-Englishness cannot be underrated.

I would like to thank separately my colleagues Dr Marina Panfilova, who taught me everything she knew about molecular beam epitaxy and that I can "change only one parameter at once", and Dr Marion Sourribes whose state-of-the-art experience in the nanowire device fabrication gave me a huge base for my own research. Both Marina's and Marion's charisma and friendship helped me launch my work in the lab and they have been supporting it all the way.

I would like to thank my colleagues and friends, with whom I shared not only desks, lab and cleanroom space, but also houses, conferences, parties, trips and more: the "grande familia" of Nick Constantino, Dr Arnaud Blois, Nuno Braz, Chris Nash, Tim Wootton, Thuong Thuong Nguyen, Dr Ed Osley, Dr Huan Wang, Dr Jon Fenton, Dr Yuji Suzuki and Dr Marius Bauza. I would like to thank Dr Ed Romans, whose academic experience, intelligence and humour always helped me to "channel my creativity" in return for cookies.

I am greatful to the molecular beam epitaxy team: Dr James Aldous, Dr James Sagar and Maddison Coke. Thanks for their help with taking over MBE laboratory and proof-reading my thesis (especially James Aldous for the "plentitude" of his hilarious remarks).

I would like to thank my friends-compassionate PhD students from UCL and LCN Aizhan Bestembayeva, Dr Nuruzzaman Noor and Dr Atahl Nathanson.

I am thankful to all the people and collaborators that helped me with experiments: Steve Etienne, Mike Creswell and Suguo Huo from LCN clean-room, Dr Steve Firth from UCL, Professor Huiyun Liu from UCL, Dr Vasiliki Tileli from Imperial College London, Dr John Hutchison form University of Oxford, Dr Heather Greer and Professor Wuzong Zhou from University of St. Andrews, Dr Paul Carrington from Univeristy of Lancaster, Christian Mietze and Prof Donat Joseph As from Paderborn University, Dr Paul Edwards from University of Strathclyde.

I would like to express my special gratitude to my parents Tatyana and Alexander for all that they have done for me, for supporting and encouraging me all the time, and my fiancée Katya whose warm teas helped me go through the most depressing moments of thesis-writing.

Abstract

One-dimensional nanostructures such as semiconductor nanowires are very attractive for application in next generation electronics. This work presents an experimental study of InAs-based and ZnO-based nanowires grown by molecular beam epitaxy for electronics applications.

InAs, InAsP and InAsSb nanowires were grown self-catalytically on silicon. Phosphorus incorporation was studied by means of HRTEM, XRD, EDX and PL. The phosphorus incorporation rate was shown to be 10 times smaller than that of arsenic. InAs and InAsP nanowires exhibit the wurtzite structure with a high density of stacking faults and phase boundaries. Conversely, InAsSb nanowires exhibit the zincblende structure with the density of stacking faults decreasing as the antimony content increases. Antimony incorporation and reduction of the stacking fault density improves the nanowire mobility.

ZnO and ZnMgO nanowires and ZnO/ZnMgO core-shell nanowire heterostructures were grown by plasma-assisted molecular beam epitaxy on various substrates with gold particles as a growth catalyst. Nanowire growth was shown to occur only at temperatures between 700 and 850 °C and Zn pressures between 1 and 3×10^{-7} Torr. A two-step growth procedure on silicon was implemented to increase the yield of nanowire growth. Mg incorporation was shown to be 4 times smaller than that of Zn. At Mg content higher than 20 %, MgZnO rocksalt phase segregation is observed in the as-grown samples. Core-shell nanowires were fabricated by growing the shell at a lower temperature of 500 °C.

ZnO nanowire field effect transistors were fabricated and optimised. High- and low-temperature transport measurements allowed determination of the bulk nanowire and contact properties. Nanowires grown on sapphire and silicon were compared. Nanowires grown on sapphire exhibit an extra donor that determines their low temperature conductivity and give a wider photoluminescence band-edge emission peak. A novel technique to measure the spectrum of deep traps in nanowire field effect transistors was implemented to study ZnO nanowires.

Contents

List of Figures

LIST OF FIGURES

List of Tables

LIST OF TABLES

Chapter 1

Introduction

"640KB ought to be enough for anybody" Bill Gates[a], 1981

1.1 Background

1.1.1 Transistors

It is truly difficult to imagine that just in the past decade the memory density in our USB-flash drives has risen by more than 1024 times. No one will take the epigraph for this chapter seriously any more, even if you put Terabytes instead of kilobytes. Moore's law, which states the number of transistors on an integrated circuit doubles approximately every two years, has held true for the last 40 years as the dimensions of transistors and memory storage cells shrink inexorably. This thesis was written with the help of a microprocessor with a 32 nm process (32 nm being a half distance between identical features), and some of my colleagues are writing their theses on 22 nm processors. Most of this reduction of the component sizes was achieved through traditional scaling [1]. Unfortunately this scaling inevitably leads to a higher leakage current through the thinner gate oxide due to quantum tunneling, and to the inability to further reduce the transistor supply voltage. These, in turn, dramatically increase the power consumption. Several routes are proposed in order to overcome these problems. One of them, the re-

[a]To be fair, this quotation is only attributed to Bill Gates, as no real evidence exists and Bill Gates himself denies saying that.

fining of the transistor 3D-geometry (using finFET or Tri-FET) has already been used by Intel for their 22 nm process and below [2]. Some of the many extensively studied technologies that have a high potential for lower power devices include: high-mobility channels (Ge, GeSb, InAs, InSb), the exploitation of on-chip silicon photonics for core-to-core communications and the use of spin logic to remarkably reduce the supply voltage [3]. Another promising way is to exploit a novel bottom-up approach for fabricating novel two- and one-dimensional materials, such as graphene and transitional metal dichalcogenides (MoS_2 and WSe_2), carbon nanotubes and nanowires. 1D-materials can be electrostatically controlled on the very small scale as opposed to thin film transistors; they have higher crystal quality and thus potentially higher mobility than thin films.

1.1.2 Advantages of nanowires

One of the main advantages of nanowires over thin films is that nanowires can grow on almost arbitrary substrates without any structural defects such as dislocations. Nanowires are believed to release the misalignment strain on their sidewalls [4], as opposed to thin films, which release the strain by creating misfit dislocations, which may be detrimental to the device performance.

Nanowires made of polar materials, such as GaN and ZnO, usually grow in the polar directions (along the c-axis), with the non-polar surface exposed on the side facets. The radial growth on the non-polar side facets helps in eliminating effects of the built-in electric field of the polar surface, and therefore increases the electroluminescent activity of nanowire LEDs [5].

Photonic nanowires can act as both light emitters and waveguides [6]. Nanowire solar cells trap light more efficiently than thin films and thus can use up to 10 times less material with the same efficiency [7]. Nanowires which have both semiconductor and piezoelectric properties, such as ZnO, GaN and InN, can be fabricated into piezotronic devices [8], which will be much more sensitive than their thin films counterparts, and can be used as accurate pressure sensors, nanogenerators, piezoelectric transistors and piezoelectric diodes.

In addition to these benefits, the combination of materials inside the nanowire expands the palette of possible devices even further, allowing fabrication of p-n

diodes [9], memory storage devices, laser diodes [10], quantum cascade lasers, photodetectors [11], giant magnetoresistance cells, resonant tunnelling diodes [12] and single electron transistors [13].

As nanowires with diameters on the order of their Bohr radius are in fact one-dimensional materials, quantum laws govern their properties. These laws may facilitate creation of the devices with not just better sensitivity or better accuracy, but with completely new principles of operation. The exotic Majorana particle (a particle which is its own antiparticle) in nanowires, the search for which has started recently, is a perfect example of the completely new quantum behaviour that does not have any analogues in the macro world.

1.1.3 Disadvantages of nanowires

As with any new material, considerable research is still required for nanowires to find a niche in the electronics market. Several problems need to be faced, one of them being the integration of nanowire technology with the developed CMOS technology. Direct growth of nanowires on silicon offers a potential for this integration. However, the usual route for nanowire growth is the vapour-liquid-solid (VLS) method that requires a metal seed particle for the nanowire growth. The metals typically used as catalysts are gold and silver, which both diffuse into silicon and create deep defect states which are detrimental for the silicon device properties. One of the possibilities to overcome this problem is to use catalyst-free and self-catalysed growths. Recently some research groups have started investigating this approach [14].

The full control of nanowire properties is still lacking. Fabrication of an array of perfectly uniform nanowires is still a very difficult task. This lack of control will also hinder the fabrication of the nanowire functional devices, such as heterostructures and quantum wells. To overcome this problem, very accurate growth techniques should be used. Molecular beam epitaxy (MBE) allows very slow growth rates, high control over the growth substrate and growth parameters, very clean elemental sources, and growth of heterostructures with the most abrupt interfaces achieved [15; 16]. This makes MBE the most reliable growth technique that can be potentially used to improve nanowire uniformity.

Semiconductor nanowires, like all semiconductor structures, are significantly affected by impurities and defects. Moreover, due to the high surface-to-volume ratio, surface states are much more important for nanowires than for bulk semiconductors. There are many techniques to investigate the properties of nanoscale devices, but at present no technique exists which allows the measurement of quantum states in nanowire devices, that is reliable, highly sensitive, non-destructive, and requires neither ultra-low temperatures nor laborious sample preparation. Such techniques are urgently needed for modern nanoelectronics, as was highlighted in the International Technology Roadmap for Semiconductors 2013 [17]. Bulk materials, on the other hand, have been studied extensively by variety of techniques, one of the most accurate and versatile of those being deep level transient spectroscopy (DLTS) [18]. In its best conditions, it can detect impurities at a concentration of one part in 10^{12} of material host atoms. Usually it operates by monitoring capacitance transients produced by electrically pulsing the semiconductor junction at different temperatures. This generates a spectrum with peaks for each quantum state. However, it cannot be applied to single nanowires due to the nanowire's small contact area. Developing the DLTS technique for its application to nanowire research will expand the nanowire investigation technique toolkit, and may provide invaluable information on the electronic properties of nanowires.

1.2 Materials investigated in this work

This work has two different materials families as its research objects: InAs-based nanowires and ZnO-based nanowires.

InAs is used today in the infrared detectors and high electron mobility transistors due to its low energy band gap of 0.334 eV and high electron mobility of 40,000 $cm^2/(V{\cdot}s)$ which is 100 times higher than that of silicon. InAs-based nanowires have the potential to be used in future integrated nanowire-CMOS devices. Self-catalytical growth of the wires on silicon avoids gold diffusion from the gold catalyst into silicon. The combination of InAs with InP or InSb offers extension of nanowire functionalisation. As will be shown in this work and in other works [14], self-catalysed nanowires grow with a multitude of interphase

boundaries which limit the nanowire mobility. Doping InAs with other materials (such as Sb) may reduce the amount of these boundaries [19]. Moreover, InAs and InSb with their strong spin-orbit interaction were proposed to become a medium for a Majorana particle search. Therefore, the optimisation of the self-catalysed growth of InAs, InAsP and InAsSb nanowires using MBE, and the study of the effect of phosphorus and antimony incorporation into InAs is the first task of this thesis.

ZnO is one of the most prominent materials in the metal oxide family [20]. It is a transparent semiconductor with optoelectronic, piezoelectric and possible spintronic applications. It has a wide direct band gap (3.37 eV at room temperature) and a high exciton binding energy (67 meV), which is 3 times larger than that of GaN. Another benefit of ZnO is that both zinc and oxygen are earth abundant materials, as opposed to gallium or indium. Although the growth of high-quality ZnO thin films is hindered by the lack of suitable substrates, ZnO nanostructure growth is routinely achieved via a variety of methods [21; 22]. Improvement of the nanowire growth, and fabrication of the core-shell and axial heterostructures and functional electronic devices that would be able to compete with the usual materials, are the main directions in today's ZnO nanotechnology.

1.3 Structure of the thesis

The work presented in this thesis is broken down into three main topics: the self-catalysed growth of InAs nanowires and related alloys; gold-catalysed growth of ZnO and ZnO/ZnMgO core-shell nanowires; and the fabrication of ZnO nanowire field effect transistors.

Chapter 2 provides the scientific background and world perspective on the current nanowire research with the main focus on ZnO-based and InAs-based nanowires.

Chapter 3 gives an account of the methods used in this work: experimental techniques and theoretical models.

The experimental work is presented in chapters 4 to 6. Chapter 4 describes InAs nanowire growth by self-catalysed MBE, and presents the study of phosphorus and antimony incorporation in the InAs nanowires. Chapter 5 describes

gold-assisted oxide-MBE growth of the ZnO nanowires on various substrates, Mg incorporation into the ZnO nanowires and ZnO/ZnMgO core-shell heterostructure growth. Chapter 6 describes the electronics applications of the ZnO nanowires: fabrication and optimisation of the nanowire field effect transistor, correlation between optical and electrical properties of the nanowires grown on different substrates, and introduces a novel method of investigation of the deep level traps and surface states in ZnO nanowires.

Chapter 7 summarises the work, presents conclusions and outlines future work that is needed for the development of the structures studied in the present work.

Chapter 2

Semiconductor nanowires

2.1 Nanowire applications

A brief survey of nanowire applications is presented in this section. More information on nanowires can be found in the following reviews: [23–25] on nanowire electronics, [26] on InAs-nanowire devices, [11; 27] on ZnO nanowires, [28] on nanowire growth.

Low-dimensional systems have one or more dimensions in the range 1 to 100 nm. Two-dimensional nanostructures or quantum wells have been in a wide use for 40 years [29]. Semiconductor nanowires are 1-dimensional structures that are limited in 2 dimensions. Although the growth of the first nanowires was described 50 years ago [30], nanowire research has progressed relatively slowly until recently due to the difficulties of synthesis and fabrication of nanowires with well-controlled properties. Progress in the study of carbon nanotubes (another 1-dimensional material [31]) boosted semiconductor nanowire research. In the last 15 years, together with the development of growth techniques, nano-fabrication and manipulation equipment, a lot of effort has been directed into nanowire research. As a result, a large variety of nanowires of different semiconductor materials and nanowire devices have been fabricated.

Optical devices include ultraviolet optically [32] and electrically pumped ZnO nanowire-array lasers [10; 33], electrically pumped single nanowire laser [34] (on CdS nanowire), infrared lasers [35] and tunable, surface plasmon-polariton en-

hanced lasers [36]. Nanowire photodiodes [11; 37–39] (and those based on ZnO nanowires [40; 41]) and solar cells [42; 43] have been fabricated. Nanowire light emitting display (LED) technology has matured over the past 10 years [44–46], and is already able to compete with comparable thin film technologies. Many companies are at their final stage before releasing to market, including large industrial players such as Samsung, Panasonic and LG alongside small startups such as glō, Aledia and Ecospark [47] (figure 2.1.a,b).

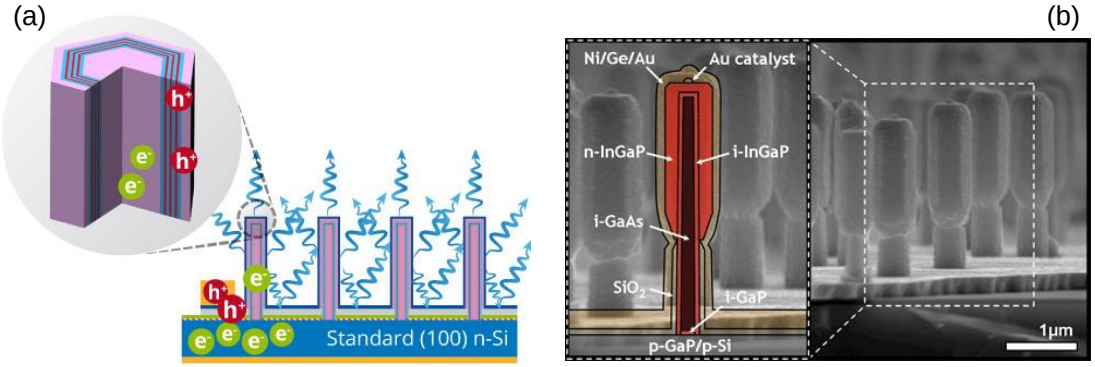

Figure 2.1: (a) Aledia nanowire core-shell GaN LED, from [48]; (b) glō nanowire core-shell InGaP LEDs, from [5].

Improved structural properties and one-dimensional transport can lead to electronic devices with better performance. Nanowire field effect transistors with different geometries have been fabricated [26; 49–52]. The best top-gate field effect transistor has enabled InAs nanowire room temperature mobilities higher than 6,000 $cm^2/(V{\cdot}s)$ [50]. Devices exploiting quantum effects in nanowires have been fabricated, such as single-electron transistors [13; 53] and resonant tunneling diodes [12; 54].

Due to the large surface-to-volume ratio, nanowires are very surface-sensitive. This surface sensitivity has been exploited in the fabrication of nanowire gas sensors [55; 56]. The large surface area of nanowires accommodates strain; this has been used in lithium ion battery performance improvement [57].

It has been shown that ZnO and InAs nanowires can be used as tips for scanning tunneling microscopy [58; 59].

Nanowires may contribute to thermoelectric materials research [60]. In order

to improve the efficiency of thermoelectric materials, it is desirable to increase the electrical conductivity and to decrease the thermal conductivity. Nanowires are believed to have high phonon scattering due to their dimensions, and thus reduced thermal conductivity. A giant thermoelectric voltage was demonstrated on InAs nanowires due to their very high charge carrier mobility [61].

It is believed that nanowires made of materials with high spin-orbit coupling, may hold the key to observing and manipulating the so far elusive Majorana particles [62; 63]. The Majorana particle (or Majorana fermion) is a quasiparticle that is its own antiparticle, and which is believed to reside on the tips of the nanowire and be extremely stable against thermal fluctuations.

A new scientific field combining nanoelectronics and piezoelectronics, "piezotronics", was created by the Zhong Lin Wang group [8; 64; 65]. It studies ZnO nanowire based piezoelectric field effect transistors.

This large array of potential nanowire applications requires a large amount of high quality research on optimising the conditions of the nanowire growth and nanowire device fabrication. The next sections address the issues of the nanowire growth and nanowire device fabrication.

2.2 Nanowire growth

2.2.1 Vapour-liquid-solid growth

The first account of nanowire growth was made by Wegner 50 years ago. He described the hypothesis of the vapour-liquid-solid (VLS) growth [30]. VLS growth is based on the presence of three phases: growth material vapours, a liquid catalyst (*e.g.* gold) and a solid surface (substrate or the nanowire stem). The growth principle can be explained with the help of the growth material/catalyst material phase diagram (figure 2.2.a). We will use the example of silicon and gold [66]:

A small particle of gold is placed on the surface of the silicon wafer. The substrate is subsequently heated to a temperature T_{sub}, shown in figure 2.2.a. Si vapour is introduced in the growth chamber. As soon as silicon arrives at the gold surface at temperature T_{sub}, a liquid alloy film of composition CL1 is formed on the surface of the gold particle. The liquid gold-silicon alloy, of

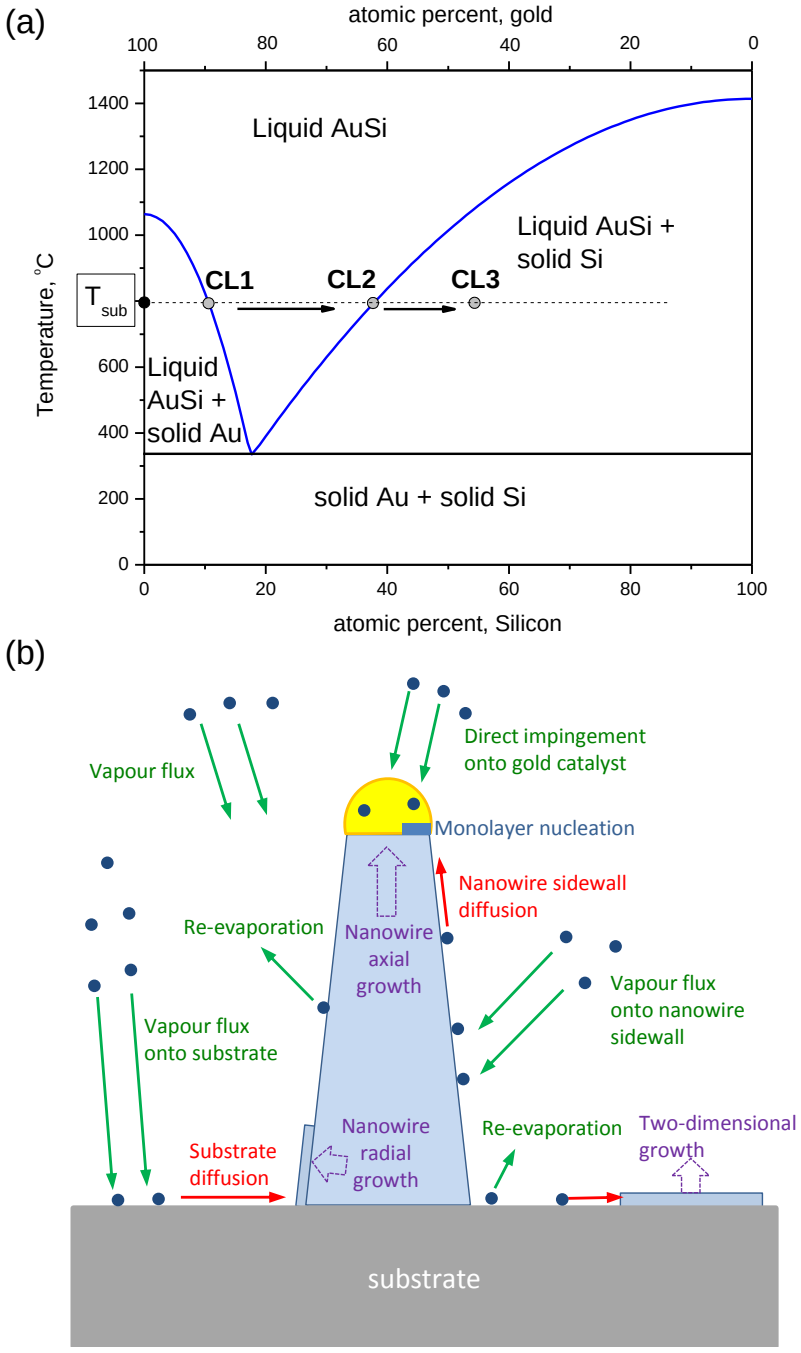

Figure 2.2: (a) VLS growth Au-Si phase diagram; (b) schematic of the processes taking part in the nanowire VLS growth.

composition CL1, is a preferential sink for silicon atoms arriving from the vapour. During subsequent deposition of silicon, the liquid layer spreads and thickens until all solid gold is dissolved. From this point on, the composition of the liquid droplet increases from CL1 to CL2, to a higher silicon concentration. Since the deposition is carried out at constant temperature, the liquid droplet saturates with silicon at CL2. The silicon content of the liquid increases further, resulting in supersaturation (CL3). When the supersaturation is large enough, a silicon crystal nucleates on the liquid-solid interface and the silicon monolayer grows relatively quickly. The liquid is now in contact with solid silicon, and the liquid composition will again be close to the equilibrium value CL2. The next monolayer growth step will happen after the liquid gold is supersaturated with silicon. The process of the droplet supersaturation with silicon takes a much longer time than the monolayer nucleation and growth [67].

Although nanowires are frequently grown with the use of gold catalyst, the mechanisms behind the VLS growth are still unclear. Several theories of VLS growth have been proposed [68–72].

The main parameters that govern the nanowire growth are the properties of the growth chamber and substrate (kinetic), and the properties of the ternary vapour-liquid-solid interfaces (chemical) – shown in figure 2.2.b. The kinetic parameters are: the material flux onto the substrate and directly onto the catalyst and the diffusion lengths of the atoms on the substrate surface and on the nanowire sidewalls (the diffusion length depends on the sticking coefficient and re-evaporation rate). The chemical parameters are: the chemical potential of the vapour atoms dissolved in gold, the liquid droplet surface and interface tension, and the wetting angle of the catalyst particle. In different conditions, kinetic or chemical processes may determine the growth, *e.g.* the Gibbs-Thomson effect of elevated chemical potential in the liquid droplet will affect the nanowire growth by decreasing the growth rates of the thinner wires or, in the extreme case, by prohibiting the growth of the wires with radii below a certain critical value [73]. In [69] it was shown that in the slow growth rate MBE technique the gold droplet is mainly fed by the substrate adatoms, reaching the top by migrating along the sidewalls without re-evaporation.

Gold catalyst growth has resulted in highly controllable nanowire morphology

and physical properties. Nanowires with diameters down to 4 nm have been fabricated [74]. Full control over polytypism (wurtzite and zincblende structures) of the InAs nanowires have been achieved by use of the VLS method [75; 76].

There is a wide variety of techniques for semiconductor nanowire growth: electrochemical deposition, aqueous chemical growth, pulsed laser deposition, metal organic vapour phase epitaxy (MOVPE) or chemical vapour deposition (CVD), plasma enhanced chemical vapour deposition (PECVD), pulsed laser deposition (PLD), carbo-thermal evaporation, vapour phase transport, aerotaxy, chemical beam epitaxy (CBE) and molecular beam epitaxy (MBE) [27; 32; 77–80]. Each has its own advantages and disadvantages, and by choosing one over another, researchers are able to reach a compromise between the cost of the growth instrument and the quality of the resultant structure.

Although metal catalyst MBE growth has been regularly used to grow InAs nanowires [81; 82], only one group has reported using MBE to grow ZnO nanowires [83]. Heo *et al.* observed growth of non-uniform array of single crystal ZnO nanowires with the use of silver catalyst at approximately 400 °C.

2.2.2 Metal catalyst for VLS growth

There are several methods to prepare gold particles, each offering its own advantages. One of the most used methods is the de-wetting of thin gold layer by the high-temperature annealing [84]. Depending on the annealing time and temperature, substrate material and roughness, it is possible to control the size distribution of gold particles. Notwithstanding its popularity, this method does not allow full control over the particle sizes and positions. Full control over these properties can be obtained by electron beam lithography [51] or nanoimprint lithography [85]. In order to grow nanowires on an arbitrary surface, it is possible to deposit a catalyst by focused ion beam deposition [86]. Other methods with controlled particle sizes but uncontrolled positions include colloidal gold deposition or gold aerosol deposition [87]. Some other less used methods are: nanosphere lithography, the chemical arrangement of Au nanocrystals from suspensions, gold deposition masks based on porous alumina *etc.* [28].

Several other materials have been investigated as possible catalysts for nanowire

growth: silver, nickel, gallium, aluminium [83; 88–90]. Nickel, gold and silver impurities diffuse during the growth from the catalyst to the silicon substrate, creating deep traps in silicon which affect electron transport [90], therefore, they cannot be used for direct integration of nanowires on silicon microchips. Aluminium catalyst was used instead of gold to eliminate the effect of deep levels [88], as it is used as a metal contact during the usual silicon microfabrication steps. Although the foreign metal catalyst provides highly controllable conditions for the nanowire growth, the nanowire appears to be contaminated with catalyst metal atoms on the order of 0.1 atomic per cent, as was shown by atom probe tomography [91]. In order to reduce the foreign atom contamination, gallium droplets may be used to grow GaAs and GaP nanowires [89].

The liquification of the catalyst-particle is not always necessary. In some conditions the diffusion of the growth material through the solid catalyst is enough to promote growth [92; 93]. The growth mechanism is thus called vapour-solid-solid (VSS) mechanism. Sometimes no specially prepared catalyst is used for nanowire growth. These methods are referred to as "non-catalysed" or "self-catalysed" growth.

2.2.3 Non-catalysed methods

In order to promote one-dimensional growth various methods are used [71; 94]: oxide-assisted growth, self-catalytic growth, vapour-solid *etc.* In some cases growth parameters may be used to make growth in one specific direction favorable. For compound semiconductors one possibility is to have a very large ratio between two vapours – *e.g.* As-rich conditions for InAs or O-rich conditions for ZnO [95].

ZnO nanowires can grow without any catalysts on a variety of substrates, such as sapphire [77], ZnO [96; 97], GaN [98], silicon [98], metals [99] and graphene [100]. Self-catalysed ZnO nanowire growth is typically observed at high vapour flow rates (500 sccm) and vapour pressures (3 Torr and higher). ZnO usually grows in a single crystalline wurtzite structure with minimal density of planar defects.

In recent years, InAs nanowires have been grown self-catalytically by MBE

and CBE [95; 101–103]. A thin oxide layer is found to be the necessary condition for the nanowire growth [89; 104]. Some researchers have achieved InAs nanowire growth on etched holes in silicon oxide [105]. Sometimes the strain between the nanowire and the substrate may lead to a critical diameter of the nanowire in self-catalysed growth [106].

In most cases, no droplet is visible on the InAs nanowire tip after the growth completion. There was a debate in the scientific community as to whether the growth is governed by the vapour-solid or vapour-liquid-solid growth [103; 107]. Recently, Grap *et al.* observed droplets on the tips of self-catalysed InAs nanowires by gradually lowering the As_4 beam flux during the substrate cooling [108]. As a conclusion to this debate, the VLS growth mechanism is recognised as a governing mechanism for the InAs nanowire growth. Figure 2.3 schematically shows the mechanism outlined in [107]. According to this work, nanowires grow in the following sequence: during the heating of the oxidised substrate, small openings in the oxide layer form (figure 2.3.b). Indium is deposited in the SiO_x openings and the In on the SiO_x surface diffuses to the immobile In droplets at the SiO_x openings (figure 2.3.c). At the interface between these In particles and the substrate underneath, nanowire growth is initiated by enhancing the growth rate in one direction in a VLS mechanism (figure 2.3.d). After deactivation of the In supply the In droplet and gaseous As form InAs (*i.e.* the indium droplet recrystallises, figure 2.3.e).

In contrast to gold-assisted growth, self-catalysed growth has one problem that is detrimental to the performance of the electronic devices: nanowires grow in two phases, hexagonal wurtzite (WZ) and cubic zincblende (ZB), and have a large density of stacking faults and ZB-WZ phase boundaries. The free energies of these two phases, WZ and ZB, are very similar and they appear randomly along the wire. According to another theoretical explanation of the WZ and ZB growth [109], the new atomic layer nucleation starts at the point of solid/liquid/vapour interface, where exists a major difference between ZB and WZ nuclei. At low level of catalyst droplet supersaturation, WZ phase nucleation is favoured over ZB phase. This explains the regular observation of ZB phase at the beginning of the nanowire growth. The difference in the WZ and ZB structures is outlined in the next paragraph.

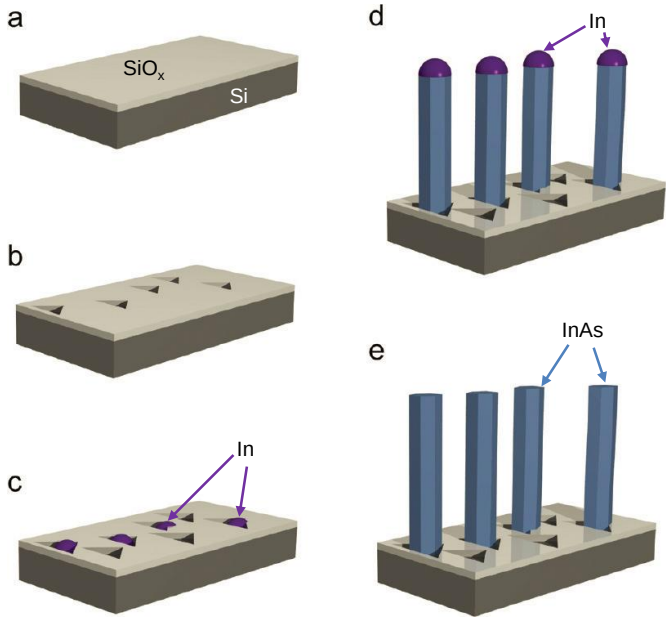

Figure 2.3: Schematic of the growth mechanism of the self-catalysed growth of nanowires, from [107].

III-V nanowires usually grow in the (111) or (0001) direction for ZB and WZ structures respectively. The difference in wurtzite, zincblende and 4H structures is presented in figure 2.4.a-c (from [110; 111]). In the direction of nanowire growth the structures can be presented as alternating layers. The order in which these layers alternate is different for wurtzite and zincblende structures. The zincblende structure, sometimes called "3C", is presented as ABCABC... Here, "C" denotes the cubic symmetry and "3" – that the layers repeat each other after 3 layers. Hexagonal wurtzite structure, or "2H" ("H" for hexagonal), is presented as ABABAB.., and the 4H structure as ABCBABCB... In principle, the zincblende and wurtzite structures' spacings can be simply geometrically recalculated. However, XRD measurements show that the geometrical recalculation is not valid in real structures. A small displacement from the cubic structure is presented in figures 2.4.b,c. The authors [110; 111] introduce a parameter called "hexagonality", which is the fraction of wurtzite phase in the structure, with hexagonality equal to 0% in cubic zincblende structures, and 100% in hexagonal wurtzite. They show that the the distance between layers is dependent on hexagonality (figure 2.4.d).

Density functional theory calculations confirm the measurements. For structures with randomly mixed zincblende and wurtzite crystal plane ordering observed in self-catalysed III-V nanowires, examination of HRTEM images allows measurement of hexagonality. This method is explained in much more detail in [49].

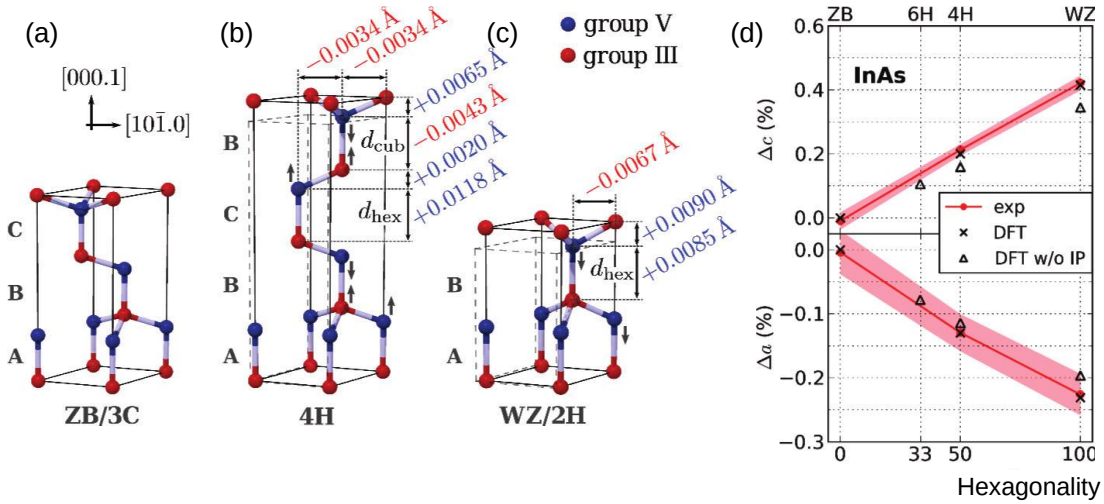

Figure 2.4: (a,b,c). Sketch of the unit cell structures of ZB/3C, 4H, and WZ/2H, respectively. The theoretically obtained deformation of the unit cell as a whole and the atomic basis within, exaggerated by a factor of 30, is shown in comparison to the ideal cell constructed from the cubic lattice constant (dashed lines). The numerical values of the unit cell distortions, especially of the bond lengths d_{hex} and d_{cub}, are given for InSb. Qualitatively the same changes were found for InAs. The direction of the displacement of the atoms due to the internal parameters is indicated by arrows. (d). Experimental and theoretical relative deviations Δa and Δc of the lattice parameters are given as function of hexagonality. The colored dots denote the average experimental values and the shaded areas indicate the experimental error of a single measurement. DFT results for internal parameters set to zero (triangles) as well as after optimisation (crosses) are shown, from [110].

Control over WZ-ZB phase intermixing is very important in device applications, as the stacking faults and phase boundaries act as scattering centres for charge carriers and increase the resistivity of nanowires [49; 82].

2.2.4 Ternary compound nanowires.

Nanowire ternary compounds can expand the potential functionality of the nanowires and enable band-gap engineering.

2.2.4.1 ZnO-based ternary compounds

ZnO based heterostructures are promising candidates for applications in blue and ultraviolet light-emitting devices. The band gap of ZnO can be adjusted from 3.3 to 1.8 eV by alloying with CdO [112; 113]. Blue electroluminescence in ZnCdO nanowires with Cd concentration of up to 45 % and peak luminescence of 2.02 eV has been achieved [114].

The band gap of MgO is 7.7 eV and by alloying with MgO, the band gap of ZnO can be extended [115; 116]. The comparison of room temperature photoluminescence spectra of ZnO and ZnMgO nanowires is shown in figure 2.5.a [117]. The challenge in ZnMgO growth arises due to the fact that MgO grows in cubic rock-salt structure whereas ZnO is hexagonal wurtzite. Thus, when doping ZnO with Mg, there is a risk of the MgO cubic phase precipitation [118; 119]. The growth of structures with maximum Mg content without phase separation are observed at nonequilibrium conditions with the choice of an appropriate substrate. The highest Mg level in $Zn_{1-x}Mg_xO$ samples has been achieved in thin films grown on a wurtzite BeO buffer layer with x reaching 55 % [116].

Heo *et. al* [117; 120–122] showed that the Mg content has an interesting effect on the growth of nanowire structures: at low Mg content, wurtzite $Zn_{1-x}Mg_xO$ with the same x over the nanowire is observed; with higher x, Mg tends to segregate on the outer side of the nanowire forming a Mg-rich wurtzite sheath surrounding the wurtzite Zn-rich core; after further increasing x (about 50 %) the Mg-rich sheath becomes cubic rock-salt, whereas the Zn-rich core stays wurtzite. At even higher x, cubic $Zn_{1-x}Mg_xO$ nanowires grow with no change of Mg content over the diameter of a nanowire. The change in composition of the nanowire can be observed by high resolution transmission electron microscopy (HRTEM), high-angle annular dark field (HAADF) TEM and energy dispersive X-ray spectroscopy (EDX).

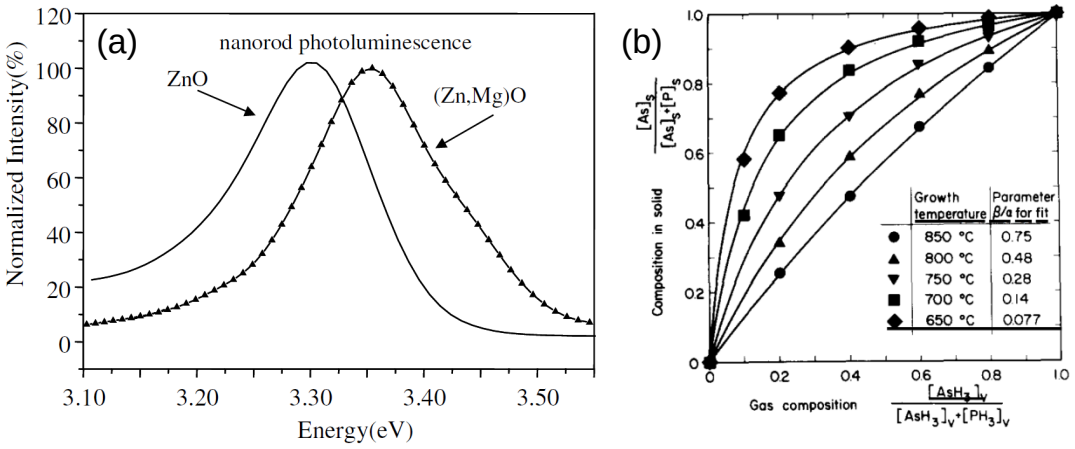

Figure 2.5: (a) Photoluminescence spectra of ZnMgO nanorods, from [117]. (b) $P_{\mathrm{As}}/(P_{\mathrm{As}} + P_{\mathrm{P}})$ gas composition dependence of the As composition, x, in solid $\mathrm{InAs}_{1-x}\mathrm{P}_x$ thin films at different temperatures, from [123].

2.2.4.2 InAs-based ternary compounds

InAs can be alloyed with other III-V materials such as GaAs, InP, InSb, AlN, GaN. The mechanisms of ternary compound growth were investigated for different growth conditions [124–127]. In some conditions, InAsP growth can be regarded as simultaneous growth of InAs and InP in a solid solution. Investigation of the molecular-beam epitaxy growth of $\mathrm{InAs}_{1-x}\mathrm{P}_x$ thin films with different phosphorus fluxes in the chamber shows that the P fraction in solid films x is not the same as the P fraction in the vapour during the growth at different temperatures (figure 2.5.b). This indicates that the phosphorus and arsenic are not incorporated in the film at the same rate, and the ratio between these rates depend on temperature. Alloying between InAs and InP in gold-catalysed nanowires has been studied [70; 128]. Self-catalysed InAsP nanowires, with In droplets as seeds, were realised by MOVPE [129]. The alloying was studied by photoluminescence [70], micro-photoluminescence mapping [14], TEM geometric phase analysis [102], EDX [128] and photocurrent spectroscopy [130]. Self-catalysed ternary InGaAs nanowires grown by MOVPE [131] and molecular beam epitaxy [14] were realised. No study on self-catalysed InAsP and InAsSb nanowires by MBE has been carried out so far.

2.2.5 Axial nanowire heterostructures

Axial heterostructures, which make use of the compositional variation along the wire, have been realised in semiconductor nanowires. Nanowire devices such as quantum dots and pn-junctions have been realised in Si/Ge, GaN/AlGaN, InAs/InP nanowires *etc.* [12; 132–135]

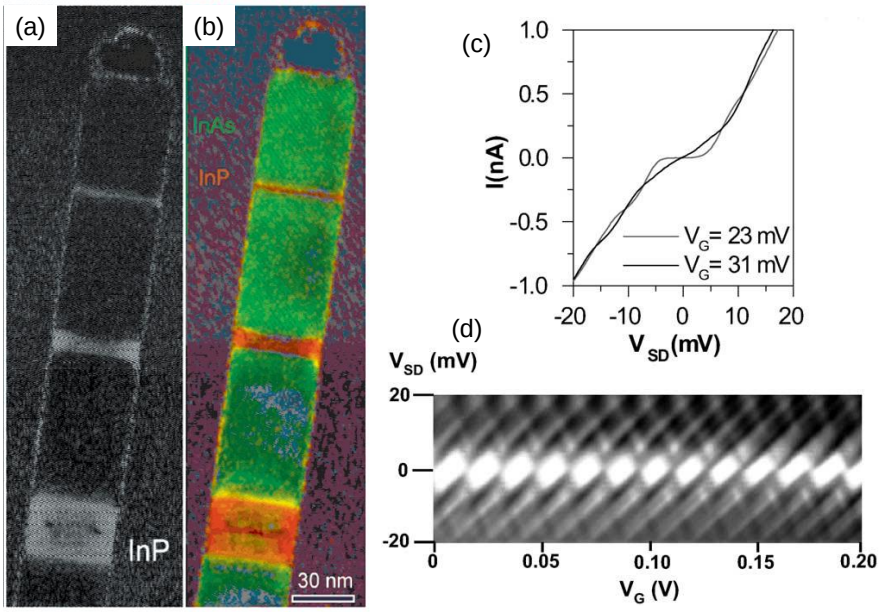

Figure 2.6: (a) An inverse Fourier transform image of the HRTEM image of the multiple quantum well InAs/InP nanowire structure using the information closest to the InP part of the split 200 reflection in the Fourier transform of the HRTEM image; InP (bright) is located in three bands with approximately 25, 8 and 1.5 nm width, respectively; (b) Superimposed HRTEM and inverse Fourier transform images, using an identical mask over the InP and InAs parts of the 200 reflection, respectively. InAs lattice spacings have been color-coded with green and InP spacings with red, from [53]; (c) I–V measurements at 4.2 K for a double-barrier wire with a 100 nm long InAs segment. One curve corresponds to Coulomb blockade, and the other when the blockade has been lifted by changing V_G; (d) A grayscale plot of the differential conductance as a function of source–drain and gate voltage of the same wire. Darker areas correspond to a high differential conductance, whereas the white, rectangular-shaped areas correspond to Coulomb blockade, from [54].

InAs nanowires have been grown with other group III or V material insertions.

Nanowire axial heterostructures, with combination of InAs/InP [53; 136; 137], InAs/InSb [102], InAs/GaAs [138] have been demonstrated. The material interface between the segments is shown to be abrupt (see figure 2.6.a,b), however the strain between segments is shown to stretch for 10–20 nm. Both single electron transistors based on the Coulomb blockade and resonant tunneling diodes were realised on the InAs/InP axial heterostructures (figure 2.6.c,d).

ZnO/ZnMgO axial heterostructures have been fabricated on the tip of nanowires [139; 140], however no electronic devices have been realised on these structures yet.

The heterostructures may be used not only as barriers for electrons (i.e. across the heterostructure), but as well as the localisation of the carriers along the heterostructure. High abruptness of the heterostructures, achieved by the MBE growth, has allowed fabrication of two dimensional electron gases (2DEGs) on the ZnO/ZnMgO heterointerface in thin film geometry. The highest possible mobility in oxide materials of 770,000 $cm^2/(V{\cdot}s)$ at a temperature of 0.5 K [141; 142] and fractional Hall effect [143] have been realised on these structures. In order to realise nanowire devices based on the heterostructures with localised charges along the heterostructure, the compositional variation should be created not axially along the wire, but radially. These nanowire heterostructures are called core-shell heterostructures.

2.2.6 Core-shell nanowires

As opposed to the usual semiconductor devices which were first created in a thin film geometry and then transferred to nanowire geometry, core shell structures are only possible in nanowires (figure 2.7). The geometry of nanowires allows fabrication of core-shell structures, which due to their axial symmetry may allow much better control of the carriers and optical properties and result in both photon and carrier confinement. Various materials have been made into core-shell nanowires, such as Si/Ge [144; 145], ZnO/ZnMgO [121; 146], InGaP/GaP [55], InAs/InP [147; 148] and GaN/AlGaN [48]. For certain materials, the shell was shown to passivate the surface of the wire, *i.e.* remove the surface levels of the core nanowire, and therefore improve the conductivity along the wire in

InAs/InP core-shell nanowires [147; 148] or improve the luminescent intensity of the core in GaAs/GaP core-shell nanowires [149]. In addition, in the case of ZnO/ZnMgO growth, ZnMgO growth on ZnO m- or a-planes results in less strain and less dislocation formation than growth on ZnO c-plane. It happens because the lattice mismatch between ZnO and ZnMgO a-lattice parameters is 3 times smaller than the mismatch between c-lattice parameters [150].

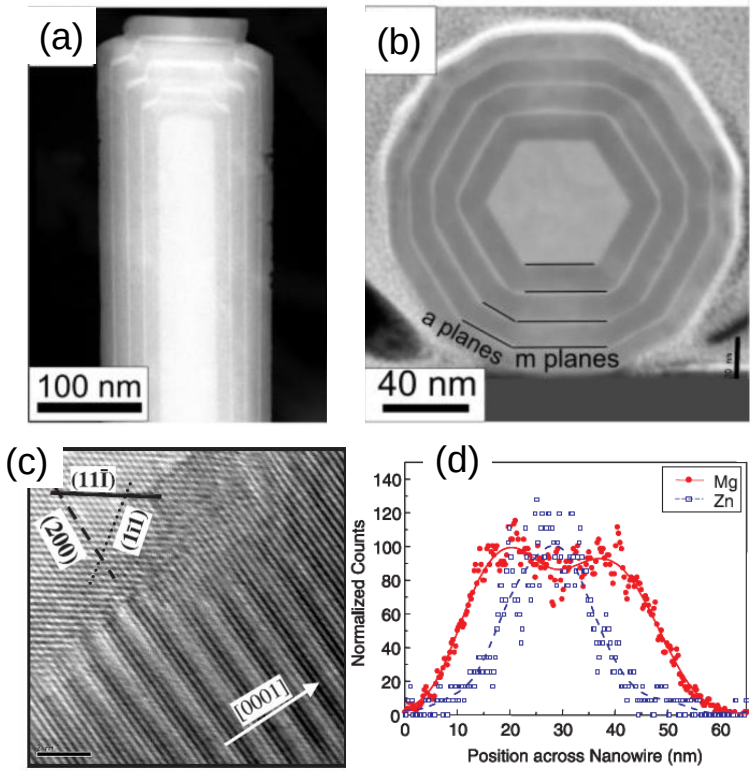

Figure 2.7: (a) Core-shell nanowire HAADF STEM image; (b) cross-section HAADF STEM image, from [146]; (c) HRTEM image of wurtzite ZnO/cubic MgZnO interface; (d) compositional line scan across the nanowire probed by STEM EDX spectroscopy, from [121].

In order to grow core-shell nanowires different growth mechanisms should be exploited for growing the core and shell, *e.g.* VLS growth for the axial core growth, and VS growth for the radial shell growth [147]. Carrying out the core and shell growths at different temperatures causes different growth mechanisms. The shell is grown at either lower or higher temperature, depending on the system

[147; 151].

ZnO/ZnMgO core-shell heterostructures were fabricated by MOVPE [146; 151–153], by lowering the shell growth temperature by approximately 300-400 °C, figure 2.7.a. Cao *et al.* [154] showed that during PLD growth, the growth temperatures for the shell and core were kept the same; only the laser repetition rate was reduced for the shell growth.

Additionally, core-shell heterostructure formation can be done via annealing or via radial diffusion of dopants. For example, preparation of the Si/SiO_2 core-shell nanowires can be done via a simple anneal in oxygen atmosphere. As shown in section 2.2.4, during ZnMgO nanowire MBE growth with Mg content higher than 20 %, Mg segregates on the surface, creating a cubic Mg-rich MgZnO shell around the wurtzite Zn-rich ZnMgO core [117; 122] (figure 2.7.c,d).

Due to high lattice mismatch between the core and shell, dislocations and dislocation loops may form at the heterointerface in the ZnO/ZnMgO nanowires with Mg content higher than 20 % [146; 155].

The change in the composition of the core-shell nanowire can be observed by HRTEM and by high-angle annular dark field (HAADF) TEM, by energy dispersive X-ray spectroscopy (EDX), or by atom probe tomography. The easiest way to measure compositional contrast is to direct the electron beam perpendicularly to the nanowire growth direction figure 2.7.a. This technique requires minimal sample preparation, although it does not give the highest accuracy possible. TEM and EDX done on the nanowire cross-section give much more accurate information, although this require laborious sample preparation (figure 2.7.b).

Core-shell nanowire optics

When growing core-shell nanowires with thin multiple shells of alternating materials, it is possible to fabricate multiple quantum wells (MQWs) with cylindrical geometry. The quantum confinement in these quantum wells will give rise to new quantum levels for electrons and holes, which in turn will lead to new luminescence lines due to electron-hole recombination.

The optical properties of the ZnO/ZnMgO MQW core-shell nanowires were studied by low temperature photoluminescence (PL) and room temperature cathodoluminescence (CL) [139; 146; 156] (figure 2.8.a,c). While PL usually studies

arrays of nanowires, CL may probe different parts of a single nanowire to see the spatially located luminescent centres, and discriminate between axial and radial multiple quantum levels (figure 2.8.c). The luminescent peaks corresponding to the quantum wells can be observed in the low temperature PL (figure 2.8.a). The energy of a peak position can be derived from the solution of the cylindrical Schrödinger equation for a given width and ZnMgO barrier height [139; 156] (Figure 2.8.b). Figure 2.8.d shows the emission energy below the ZnO band gap at the tip of the nanowire. This is attributed to the quantum confined Stark effect due to the high polarisation field in the c-axis direction in ZnO [146].

The nanowire shell can be used to improve the lasing properties of the nanowires. Choi *et al.* demonstrated that a GaN core with diameter comparable to the Bohr radius of the exciton for GaN (11 nm) and the higher band gap of the AlGaN shell lead to an effective carrier confinement [6]. In addition, the AlGaN sheet has a lower refractive index than the GaN core thus creating a waveguiding structure with a simultaneous exciton and photon confinement. When the core is optically pumped, it acts as a gain medium while the shell functions as a Fabry-Perot optical cavity. In 2008, the Lieber group reported an InGaN/GaN MQW core-shell nanowire laser with lower threshold power pump density due to the multiple quantum well structure [46]. The structure demonstrated lasing from 365 to 495 nm depending on the InGaN quantum-well indium composition.

Core-shell nanowire electronics

It was shown that ZnMgO shell of ZnO/ZnMgO core-shell nanowire increases the carrier mobility of the ZnO core by three times [157]. In Si/Ge and III-V core-shell nanowires with the core diameter on the order of Bohr radius, the improved charge confinement may lead to the formation of a high mobility one-dimensional electron or hole gas [144; 145; 147]. Li *et al.* have achieved an electron mobility of 21,000 $cm^2/(V{\cdot}s)$ at 5 K in GaN/AlN/AlGaN core-shell heterostructure nanowires [158], and Tilburg *et al.* have achieved comparable low temperature carrier mobilities in InAs/InP core-shell nanowires [148].

For nanowires with diameters larger than Bohr radius, the core-shell heterostructure may lead to the formation of a cylindrical two-dimensional electron

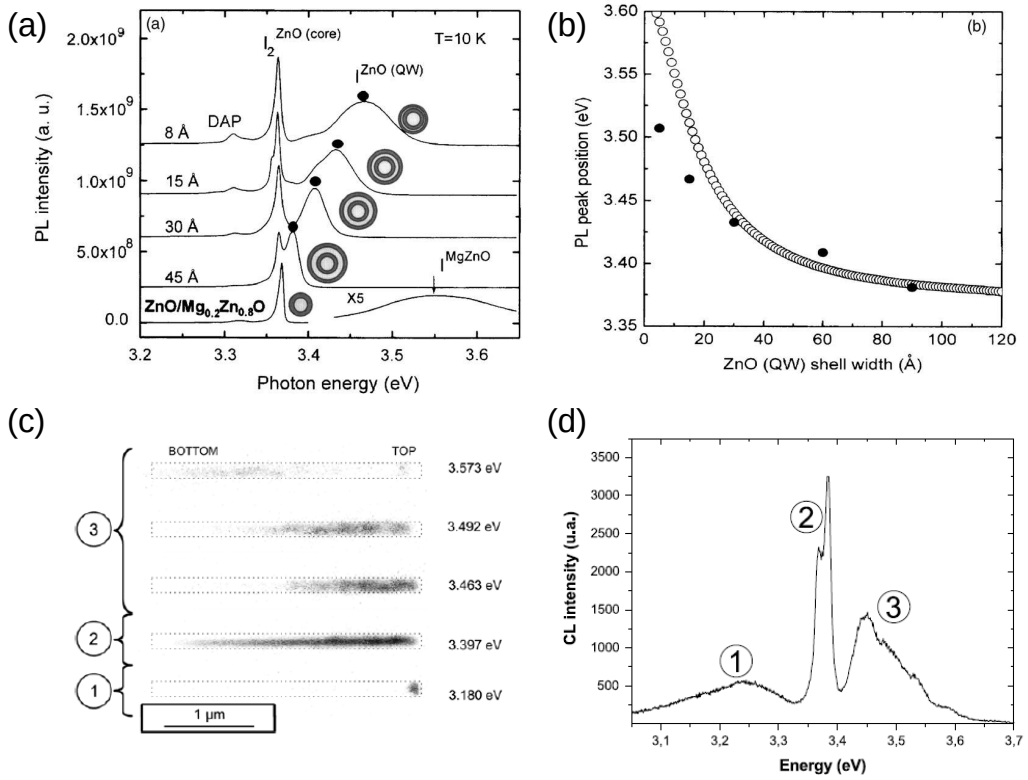

Figure 2.8: (a) PL spectra at 10 K of $ZnO/Mg_{0.2}Zn_{0.8}O$ core/shell nanorod heterostructures and $ZnO/Mg_{0.2}Zn_{0.8}O/ZnO/Mg_{0.2}Zn_{0.8}O$ multishell nanorod quantum structures with different ZnO QW shell widths of 45, 30, 15, 8 Å. (b) Well-width dependent PL peak positions in $ZnO/Mg_{0.2}Zn_{0.8}O$ coaxial quantum structures, solid circles, and theoretically calculated values, open circles, in one period of one-dimensional square potential wells. In this calculation, Jang *et al.* employed the following parameters: 0.28 m_o and 1.8 m_o for the effective masses of electrons and holes, respectively, a ratio of conduction and valence band offsets $\Delta E_c/\Delta E_v$ of 9, and a band gap offset ΔE_g of 250 meV, from [156]; (c-d) Spatially resolved CL spectroscopy on a single nanowire from the MQW sample: Emissions from ZnO near band edge (2), axial, which due to quantum confined Stark effect has energy lower than band gap (1), and radial (3) quantum wells are visible, from [146].

gas. A cylindrical 2DEG may be detected in a parallel magnetic field by conductivity oscillations: those with a period of magnetic flux $\Phi_0 = hc/e$ for ballistic transport and those with a period of half the magnetic flux for diffusive transport in disordered materials [159]. Recently cylindrical 2DEGs has been observed in GaAs/InAs [160] and in In_2O_3/InO_x [161] core-shell nanowires.

ZnO-based heterostructure nanowires by MBE.

The MBE growth offers many advantages over other techniques, such as CVD, MOVPE or PLD, by allowing highly controllable fabrication of heterostructures with abrupt interfaces, with a low density of defects and minimal disorder. Although MBE growth has already led to the fabrication of 2DEGs at the interface of ZnO/ZnMgO thin film heterostructures [16; 162], the MBE growth of ZnO/ZnMgO axial and core-shell nanowires have not been studied sufficiently so far. Highly abrupt interface and quantum confinement in the core-shell nanowires may potentially lead to the fabrication of cylindrical 2DEGs at the ZnO/ZnMgO heterointerface and to better photon confinement.

2.3 Nanowire field-effect transistors

One of the aims of nanowire research is to find a substitute for planar transistors on CMOS microchips. Nanowire field effect transistors (FETs) with back-gate or top-gate electrodes have been examined for this role [163]. Moreover, the nanowire transistor is a universal device to study many nanowire properties, such as charge carrier type, charge carrier concentration and mobility, the conductivity mechanism and contact properties.

Nanowire FETs have been fabricated in various gate geometries: back-gate [49], top-gate [50], self-aligned air-gap gate [164] and surround gate [51; 165; 166]. The surround gate offers the best electrostatic control over the charge carriers in the nanowire. Usually the surround gate requires laborious sample fabrication. Dhara *et al.* has however shown a "facile" technique for fabrication of surround gate transistors on InAs nanowires [52].

The optimisation of the gate dielectric, metal contacts and surface passivation of the nanowires resulted in room temperature mobilities of 11,500 $cm^2/(V{\cdot}s)$ in

InAs nanowires [147].

Although some materials have been realised into FETs with repeatable properties, full control is still lacking for a lot of nanowire devices. Blömers *et al.* have shown that different InAs nanowires may have completely different temperature dependences of the transport properties: semiconductor-type behaviour with nonlinear IV characteristics or metal type behaviour [167], and these behaviours can be tuned by the gate voltage. They showed that the reason for the different temperature behaviour of both groups is differing amounts of surface electron accumulation owing to trapped surface charges. Moreover, these surface charges may fluctuate along the wire and thus may induce variation of the carrier concentrations and local depletion regions. Due to the same reason, the barrier heights can vary from wire to wire.

In addition, surface states may cause hysteresis in the transfer characteristics (the gate voltage dependence of the drain source voltage) in the nanowire FETs. It was shown that adsorption of H_2O species on Ge nanowires causes hysteresis, which can be eliminated by HfO dielectric deposition onto the Ge nanowires [168]. Passivation of ZnO nanowires by a thin polyimide layer or Al_2O_3 increases the conductivity of the nanowire by reducing the density of surface states [169; 170].

ZnO nanowire FETs

In typical back-gate configurations in atmosphere, the field effect mobility of ZnO NW-FETs ranges from 3 to 40 $cm^2/(V{\cdot}s)$, with an on-off ratio of around 10^4 to 10^7 [166; 171–174]. ZnO nanowires have a large amount of surface defects, mainly oxygen vacancies, that will adsorb gas species and act as scattering and trapping centres and affect nanowire transport properties [11]. Hong *et al.* fabricated two kinds of ZnO nanowires on Au-coated substrates and catalyst-free substrates and showed that catalyst-free ZnO nanowires have reduced surface defect density and thus better performance [173]. Kim *et al.* have shown a novel method of growing horizontal ZnO nanowires catalyst-free directly on patterned graphene sheets, which act as both seed and source-drain electrode [100].

The best performance non-passivated ZnO nanowire-FETs have been demonstrated by Cha *et al.* with self-aligned planar gate electrodes and a well defined nanosize air gap dielectric [164] (figure 2.9). These ZnO nanowire-FETs exhibits

excellent performance with an on–off ratio of 10^6 and a field effect mobility of almost 1000 $cm^2/(V{\cdot}s)$ which is the highest value for ZnO NW-FETs without any specific treatment like passivation. Additionally, Chang *et al.* have achieved the carrier mobility exceeding 4000 $cm^2/(V{\cdot}s)$ by passivating ZnO nanowire surface with SiO_2/Si_3N_4 bilayer [175].

The quality of the Ohmic drain-source contacts is very important for any FET performance. Ohmic contacts to ZnO nanowires are obtained by electron-beam evaporation of Ti/Au [40; 176], thermal evaporation of Al/Au [171], or sputtering of Nb [164]. Chang *et al.* reported that dipping ZnO into HF before contact metallisation reduces the contact resistance [170]. Post processing of the devices by plasma treatment or annealing reduces the contact resistance as well [170; 177]. Detailed reviews on Ohmic contacts to ZnO can be found in [20; 178].

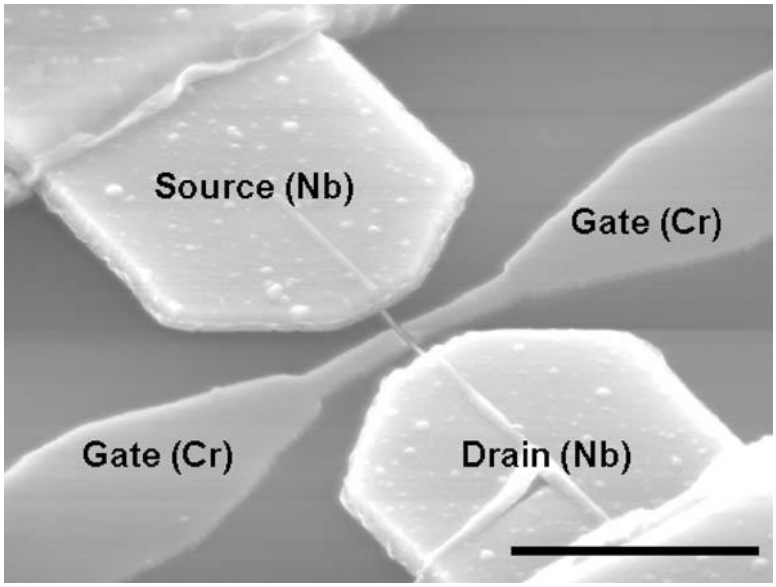

Figure 2.9: ZnO nanowire field effect transistor with self-aligned nanogap gate electrodes, scale bar is 2.5 μm, from [164]

.

2.4 Electrically active defects

2.4.1 Defects in semiconductors

One of the reasons why semiconductors have become the principal materials in the electronics market is the unique ability to drastically change their properties with just a small fraction of the foreign material impurities. Fabrication of n- and p-type conductivity materials, manipulation of the charge carrier concentration and mobility, control over light emission and absorption, – all this is possible with the help of foreign impurities. The properties of the semiconductor can be affected not only by foreign material atoms, but also by the intrinsic crystallographic defects, such as 0D defects (vacancies and interstitials), 1D defects (dislocations) and 2D defects (stacking faults and twin- and grain-boundaries). Although usually these crystal defects are undesirable since they become non-radiative recombination centres or charge trapping centres [179], some attempts have been made to use these defects, *e. g.* dislocations, as luminescent centres for silicon photonics [180] or high mobility channels [181].

Historically, electrically active defects in semiconductors are divided into shallow defects (having their energy level close to the conduction band minimum or valence band maximum, $E_c - E_{\mathrm{defect}}, E_{\mathrm{defect}} - E_v \lessapprox kT_{\mathrm{B}}$), and deep levels (situated deeply in the band gap, $E_c - E_{\mathrm{defect}}, E_{\mathrm{defect}} - E_v \gg kT_{\mathrm{B}}$). The shallow levels are usually directly responsible for the conductivity and carrier concentration, and their properties may be studied by the IV-characteristics, FET measurements, photoluminescence. Deep levels usually affect the transport properties indirectly by trapping and scattering the charge carriers, hence reducing the lifetime of the free carriers, reducing radiative band-to-band recombination and changing the energy levels of luminescence. In silicon, gold, silver and nickel act as deep levels, trapping charge carriers and reducing the overall mobility of the device. Thus it is undesirable to have gold in any of the fabrication steps of a silicon based device. Crystallographic defects and surface states may act as deep levels as well.

ZnO exhibits plenty of native and foreign defects, all of which affect the electronic properties of ZnO. First of all, ZnO acts as an n-type semiconductor without any intentional foreign material doping. The origin of the n-type conductivity

was studied for a long time, with many different assumptions suggested, such as oxygen vacancies or Zn interstitials. Although it was shown that oxygen vacancies are deep donors and cannot explain the observed n-type conductivity in ZnO, they can compensate the p-type doping [182]. Zn interstitials are shallow donors, although they have high formation energies and high diffusion probability.

Hydrogen is the main candidate for an "intrinsic" n-type doping of ZnO [183]. As opposed to all other semiconductors, where H is an amphoteric impurity, always counteracting the prevailing conductivity of the material, in ZnO H occurs exclusively in the positive charge state, i.e. it always acts as a donor [183].

Look *et al.* [184] have argued that not hydrogen, but complex consisting of zinc-interstitial and substitution of oxygen for nitrogen (Zn_i-N_O) may act as main n-type dopant in ZnO.

ZnO may be doped by many other materials, such as Al, Ga and In up to degenerate conditions [182]. Lithium is present in the zinc ore, and may dope ZnO with holes. The list of shallow donors and acceptors in ZnO are shown in table 2.1.

Table 2.1: Shallow defects in ZnO. Adapted from [182].

Impurity	Character	Ionization energy, meV	$n_{\max}$ or $p_{\max}$, cm$^-$3
Al	Donor	120	8×10^{16}
Ga	Donor	–	3.7×10^{20}
In	Donor	–	
F	Donor	80	5×10^{20}
H	Donor	35	–
Li	Acceptor	–	
Cu	Acceptor	–	
N	Acceptor	100	9×10^{16}

Recently deep levels in ZnO thin films have been studied by deep level transient spectroscopy, with a variety of deep level defects observed [185–188]. Many of these defects still have debatable origin, although correlation between annealing in different atmospheres (O, Zn, N, Ar), ion implantation and deep level concentrations has given strong evidence for the source of deep levels. The parameters of the main deep levels in ZnO and their tentative origins are given in

table 2.2.

Table 2.2: Deep level defects in ZnO.

Impurity	Energy	Origin
T1	30 meV	tentatively assigned to interstitial zinc [186]
E1	111 meV	related to the oxygen vacancy [186]
E2	190 meV	donor, promoted by O-rich conditions[185]
E3	300 meV	evidence for their native origin [186] oxygen vacancy [187] evidence of hydrogen involvement [188]
E5b	850-1000 meV	observed in oxygen-implanted and thermally annealed ZnO thin films [185]

2.4.2 Defects in nanowires

Nanowires, as for any semiconductor, have a variety of electrically active defects. However, due to their unique geometry and growth, they acquire a different range of defects and experience a variety of surface effects. For example, InAs and GaAs nanowires grow with mixed wurtzite-zincblende stacking, which is not possible in the bulk crystal configuration. These stacking faults, twin boundaries and phase boundaries have been shown to affect the electrical conductivity of InAs nanowires by becoming the scattering centres for carriers [82; 189]. Furthermore, the large surface area affects the luminescent and electrical properties by trapping free carriers [147; 149; 168]. For example, oxygen molecule adsorbed on the nanowire surface attracts an electron and forms negatively charge surface level O_2^-. This decreases the conductivity of the nanowire by reducing the number of conducting electrons [190].

The effects of deep levels on nanowire transport properties have not been studied in much detail yet, mainly due to the very small dimensions of the nanowires. The common electrical methods of investigating deep levels are usually based on the measurement of small changes in the current or capacitance of the semiconductor sample. These methods include thermostimulated capacitance, thermostimulated current, electron paramagnetic resonance, low frequency noise

spectroscopy and deep level transient spectroscopy [18] (DLTS) and its derivatives (e.g. photoinduced current spectroscopy – PICTS, current transient spectroscopy and others). The values of the nanowire capacitance are usually below 1 pF, and they cannot be measured by conventional capacitance methods nor by capacitance-DLTS. Therefore, only a few papers have been published on nanowire deep levels recently. DLTS in combination with PICTS was used to study catalyst-related electrical defects in an array of Si nanowires [90]. DLTS was also used to study single GaN nanowire pn-junction [9], and low frequency noise spectroscopy was applied by Motayed *et al.* to study the metal catalyst effect on individual Si nanowires [191; 192].

A different approach to study deep levels in miniature devices (such as modern field-effect transistors) has been realised by current-mode DLTS (I-DLTS) as opposed to capacitance-mode DLTS [193]. Here the relaxation of the current through the channel is measured in response to a gate voltage pulse. This method usually gives information not only about the majority carrier traps, but also surface carrier traps [193]. I-DLTS can be carried out directly on a device in the transistor geometry, and doesn't need separate fabrication steps. As nanowire field effect transistors are thought to become constituents of future electronic devices, I-DLTS is a promising technique to study them.

In conclusion, there are many challenges that the nanowire technology is facing nowadays. In this work, we are addressing only a small part of them.

Chapter 3

Experimental methods and theory

3.1 Substrate preparation

Degenerately p-type doped Si (111), Si(110) and Si(100) 2 and 3 inch wafers 500 μm thick and Al_2O_3(0001) 2 inch wafers and 10×10mm cut-out wafers 300 μm thick were used as growth substrates. Before processing wafers were cleaned in acetone, 2-propanol and DI water.

3.1.1 Gold-catalyst formation

The size and distribution of gold catalyst particles is important for nanowire growth. The size of the particles determines the diameter of the nanowires. The distribution may determine the number of atoms that diffuses on the surface from the point of impingement to the nanowire growth site and hence the growth rate.

3.1.1.1 Gold thin film deposition and annealing

One of the methods to introduce an array of gold particles on the substrate is to evaporate thin layer of gold and anneal it.

The evaporation of gold (99.999%) was carried out in the Edwards Auto 306 thermal evaporator. The deposition rate used was approximately 0.02 nm/sec. The thickness of the layer as measured by standard quartz crystal thickness monitor was 2.5 ± 0.2 nm. The substrate with a gold film is transferred into MBE ultra-high vacuum chamber and annealed using temperatures of 500 – 900 °C.

The gold particle distribution after annealing on different substrates is discussed in the experimental chapter 5.1.

3.1.1.2 Electron Beam Lithography

Another method of gold-particle formation is top-down patterning using electron beam lithography (EBL). This method provides regularly shaped and positioned gold dots. The EBL was performed using the Carl Zeiss SUPRA 40 VP field-emission gun scanning electron microscope with Raith 150^{two} EBL-system.

The procedure is as follows (figure 3.1): first, the 100 nm layer of polymethyl methacrylate (PMMA) resist was spin-coated on the substrate. Then the substrate with PMMA layer is exposed to the 10 kV electron beam in spot-mode according to a predesigned pattern in the EBL chamber (figure 3.1.a). Electron dose ranges from 0.01 to 0.05 pC for different spot sizes. The diameter of the exposed spots is dependent on the dose and it ranges from 30 to 100 nm. The exposure of the PMMA to high energy electrons breaks bonds in the polymer, which is then easily dissolved in the methyl isobutyl ketone : isopropanol (MIBK:IPA 3:1) solution (figure 3.1.b). The developed structure is then coated with a 20 nm gold film (figure 3.1.c) and put into acetone overnight to remove the remaining PMMA. This process removes the PMMA together with gold layer, leaving only the gold on Si intact (the so-called "Lift-off process", figure 3.1.d).

3.1.1.3 Colloidal gold

Colloidal gold particles of diameter 50 nm were deposited on the substrate at a temperature of 120 °C and cleaned in acetone, 2-propanol and DI water to remove residual impurities from the solution (0.01% $HAuCl_4$ and others).

3.2 Molecular Beam Epitaxy (MBE)

3.2.1 MBE principles

Molecular Beam Epitaxy is one of the most popular vacuum deposition techniques used to create single crystals. A schematic of a typical MBE system is shown in

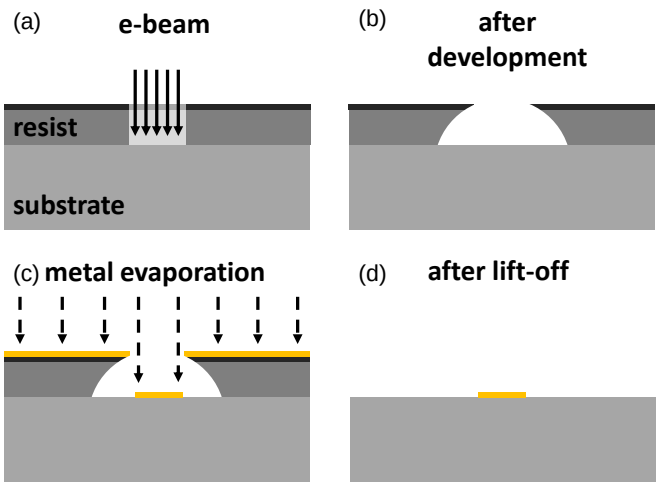

Figure 3.1: Schematic electron beam lithography process. (a) a layer of organic resist is spun on a substrate and a predesigned pattern is irradiated with a beam of electrons. (b) After development, an opening is left in the resist. (c) Metal is evaporated on the top of the substrate and the remaining resist. (d) The remaining resist is removed during the lift-off process and the metal is left at the predesigned positions

figure 3.2. MBE exploits ultra-high vacuum (UHV) and uses extremely pure materials (higher than 5N). The base pressure in the systems used in this work (10^{-11} Torr) is achieved by the use of turbo pump, ion pump and cryo-pump simultaneously, within a liquid nitrogen cooling shield. The formation of the thin film crystal occurs on the heated substrate by the interaction of one or several atomic or molecular beams. In UHV conditions the mean free path of the particles is greater than the dimensions of the chamber (for example, in a vacuum of 10^{-7} Torr, the mean free path of N_2 molecules is 1 km), so particles of different species don't interact unless they are on the substrate.

The plasma assisted MBE (PA-MBE) uses a radio frequency plasma generator to introduce free radicals (in the case of this work, oxygen) into the chamber. The plasma ignition and its stable operation are known to be difficult tasks at low pressures, so the pressures in PA-MBE are usually higher than in conventional solid source MBE. However, pressures over 10^{-4} Torr cannot be used in MBE growth because the mean free path is reduced to 1 meter or less, *i.e.* less than the chamber dimensions. The working pressures in the PA-MBE growth used in

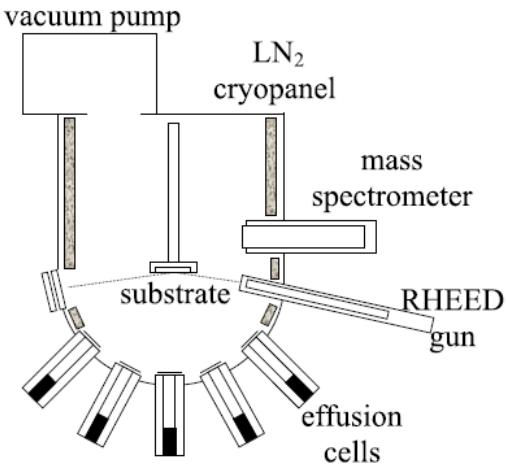

Figure 3.2: Typical MBE schematic.

this work ranged from 10^{-6} to 10^{-5} Torr.

3.2.2 II-VI oxide MBE

The oxide MBE used in this work is an SVT Associates machine (figure 3.3). It is a PA-MBE system with Zn (6N) and Mg (5.5N) effusion cells, and oxygen (5.5N) RF plasma source. The background pressure is approximately 5×10^{-11} Torr.

3.2.2.1 Plasma source

The oxygen plasma is formed using a standard capacitively coupled plasma source (SVT Associates) which operates at 13.56 MHz. RF energy of between 100 W and 600 W is supplied to the cell through a water cooled copper coil. Oxygen is introduced into the tube with a leak valve. The flow of oxygen may be varied from 0.1 to 10 sccm. The standard settings used in this work were 2 sccm flux and 300 W power.

A residual gas analyzer, quadrupole mass spectrometer (SRS200), was used to monitor the gases in the MBE chamber (see figure 3.4) After stabilising the plasma source for 15 minutes the pressure of H_2, N_2, CO_2, NO and Ar gases is reduced. The pressures of H atoms, water vapour, carbon dioxide are still quite high. However the pressure of all of them is more than 3 orders of magnitude less

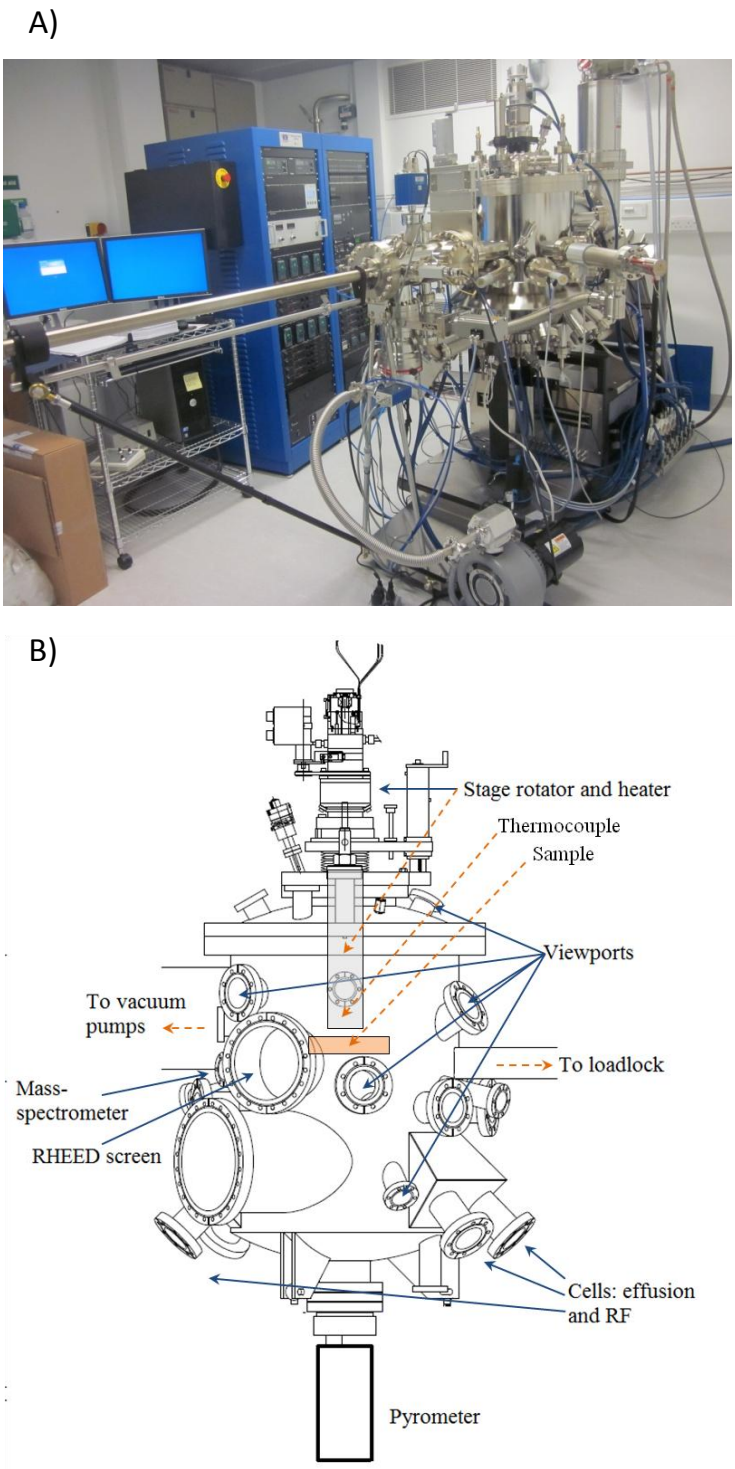

Figure 3.3: SVTa oxide MBE: (a) photo, (b) schematic, looking from the side (SVT Associates manual).

than that of oxygen molecules and oxygen atoms, which remain the main source for the oxide growth.

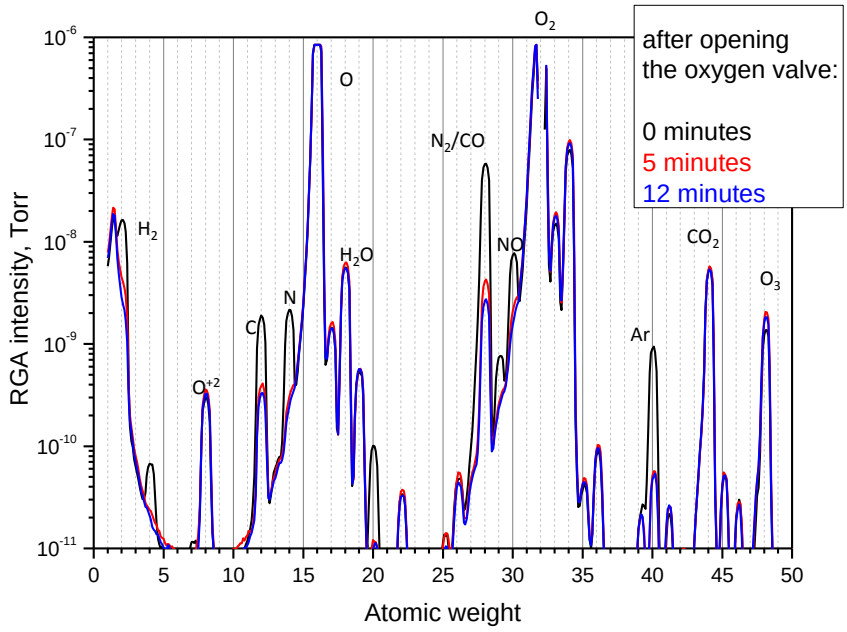

Figure 3.4: RGA spectrum of the gases in the chamber at different times after the switching on of the oxygen plasma source. The O and O_2 signals at 16 and 32 atomic weights are beyond the limits of the plot and are higher than 10^{-6} Torr.

3.2.2.2 Cells

The Zn and Mg fluxes in the chamber are controlled by the temperature of the Zn and Mg cells. The fluxes can be quantified by a vacuum gauge that is inserted in the chamber under the sample. The measured pressure is called the Beam Equivalent Pressure (BEP). The dependence of BEP on the temperature of the Zn cell is presented in figure 3.5. The rotation of the sample holder makes some vapour species accumulate close to the perimeter of the substrate making the BEP slightly different at these positions.

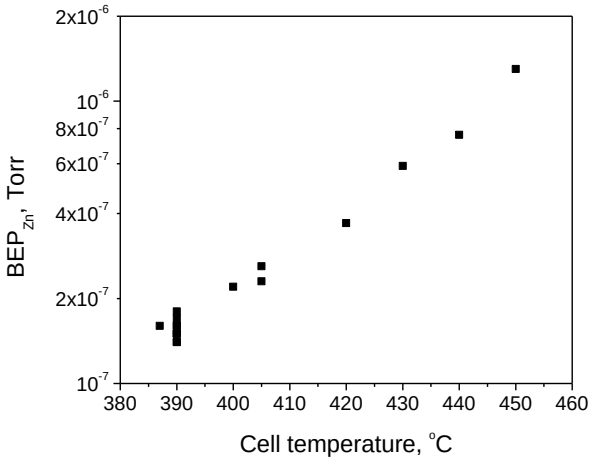

Figure 3.5: Dependence of Zn beam equivalent pressure (BEP) on the Zn cell temperature.

3.2.2.3 Substrate heating

The sample holder is heated by a radiative spiral heater. A thermocouple situated above the heater is used to measure the temperature of the substrate. The amplitude of the temperature fluctuations during the growth is about 5 degrees (measured by pyrometer). A circular semiconductor substrate is attached to a metallic substrate holder at its perimeter. At the points of contact the temperature is different from the middle of the substrate. The varying temperature and pressure at the perimeter of the substrate make the growth conditions different from those in the middle in the region within about 2 mm from the substrate holder.

3.2.2.4 Reflection high-energy electron diffraction

Reflection high-energy electron diffraction (RHEED) is an in-situ technique for monitoring film growth. A focused electron beam of energy 15 kV is incident on the sample at 3 degrees grazing incidence and diffracts from it onto a fluorescent screen.

The crystallographic orientation of the sample, the reconstruction of the surface and the crystal structure of the grown crystal may be obtained by looking

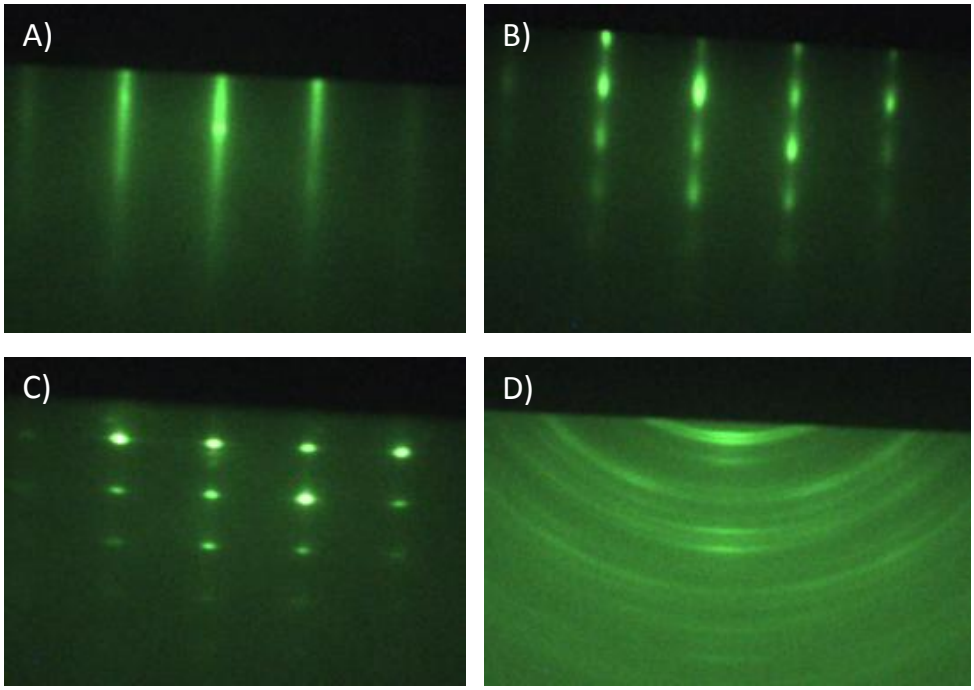

Figure 3.6: RHEED patterns observed during various ZnO growths in the oxide MBE: (a) 2-dimensional layer-by-layer growth; (b) transition to 3-dimensional island growth; (c) oriented nanowire/cluster growth; (d) disoriented or polycrystalline growth.

at the RHEED reflections (figure 3.6). Figure 3.6.a shows the RHEED pattern of 2-dimensional layer-by-layer growth. Figure 3.6.b shows the transition of the 2-dimensional growth into 3-dimensional island growth. Figure 3.6.c shows oriented cluster growth, which is also applicable to nanowires. Figure 3.6.d shows not oriented or polycrystalline crystal growth. When growing thin 2-dimensional films, RHEED oscillations may be used to monitor the layer-by-layer growth and obtain the growth rates.

3.2.3 III-V MBE

For growth of InAs-based materials, to avoid III-V and II-VI material cross-contamination, a different machine was used: VEECO instrument equipped with solid source for In and Cracker cells for As_4 and P_2 (figure 3.7). The III-V growth was carried out by Dr Marina Panfilova and Professor Huiyun Liu.

Figure 3.7: Veeco III-V MBE

3.3 Growth models

3.3.1 Thin film growth. Simplified model

Several surface phenomena are responsible for thin film growth: the incoming flux j, the adsorption on the surface (sticking) with rate r_a, the diffusion of the atoms on the surface and the desorption of atoms from the surface with rate r_d. The rate of growth, R_growth, is the number of atoms n_tf that have stuck on the surface per unit time:

$$R_\mathrm{growth} = \frac{\mathrm{d}n_\mathrm{tf}}{\mathrm{d}t} = r_\mathrm{a} n_\mathrm{free}, \tag{3.1}$$

where n_free is the number of particles diffusing on the surface. The rate of change of the number of free atoms will depend on the incoming flux and the adsorption and desorption of free atoms:

$$\frac{\mathrm{d}n_\mathrm{free}}{\mathrm{d}t} = -r_\mathrm{a} n_\mathrm{free} - r_\mathrm{d} n_\mathrm{free} + j. \tag{3.2}$$

If we consider dynamic equilibrium in the system, the number of free atoms on the surface should be constant:

$$\begin{aligned} \frac{\mathrm{d}n_\mathrm{free}}{\mathrm{d}t} &= 0 \\ j &= r_\mathrm{a} n_\mathrm{free} + r_\mathrm{d} n_\mathrm{free} \\ R_\mathrm{growth} &= \frac{r_\mathrm{a} j}{r_\mathrm{a} + r_\mathrm{d}} = \frac{j}{1 + r_\mathrm{d}/r_\mathrm{a}} \end{aligned} \tag{3.3}$$

The rate of adsorption and desorption are represented in the following form:

$$r_{d,a} = \nu_{d,a} \mathrm{exp}\left(-\frac{\Delta E_{d,a}}{k_\mathrm{B} T}\right), \tag{3.4}$$

where $\Delta E_\mathrm{d,a}$ are the activation energies of the processes and $\nu_{d,a}$ are the frequency factors [194]. Taking formulas 3.3 and 3.4 we get:

$$R_\mathrm{growth} = \frac{j}{1 + \frac{\nu_d}{\nu_a} \cdot \exp\left(-\frac{\Delta E_\mathrm{d} - \Delta E_\mathrm{a}}{k_\mathrm{B} T}\right)}. \tag{3.5}$$

This formula can be used to obtain the growth parameters such as the ratio of desorption and absorption factors, ν_d/ν_a , and the difference between desorption and adsorption activation energies $\Delta E_\mathrm{d} - \Delta E_\mathrm{a}$.

3.3.2 VLS nanowire growth. Simplified model

The theory behind the VLS nanowire growth has been reported in many articles with varying simplifications [68]. Here, a very simple model of the nanowire growth will be derived. This model will be applied to our experiments in order to calculate the growth characteristics of the nanowires from the measured experimental values. The most controlled experiment on VLS growth would be the one carried out on the EBL-patterned gold particles. From the nanowire growth on substrates with EBL-patterned gold particles the following dependencies could be inferred: the dependencies of the nanowire length, diameter and growth "quality" (which will be defined later) on the distance between the gold droplets.

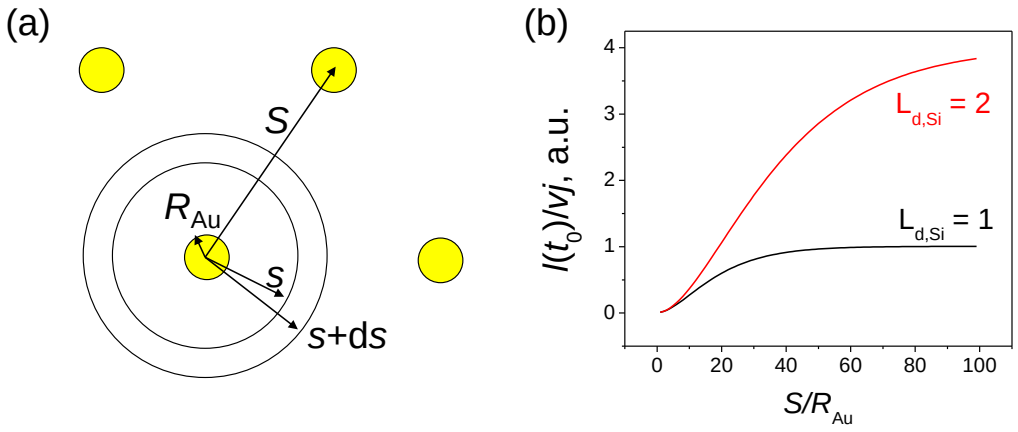

Figure 3.8: (a) Illustration of the model of the nanowire growth, yellow circles are the gold dots, S is the distance between gold dots, R_Au the radius of the gold dot, and s and ds the coordinate used for integration in equation 3.6; (b) calculated dependence of the length of the wire l at time t_0 reduced to the atomic volume ν and incoming flux j on the distance between the wires normalised to the gold dot radius, at different diffusion lengths.

Atoms arrive at the surface with a flux j. The radii of the Au dots are R_Au with area πR_Au^2, and the distance between the Au dots is S (figure 3.8.a). The

amount of particles arriving on the small surface $\mathrm{d}S$ per second is $\mathrm{d}N = j \cdot \mathrm{d}S$. Incoming atoms may arrive onto the area between the gold dots, or they may arrive directly on the dots. Assuming the sticking coefficient of the Au dot is equal to 1 [68], all the atoms arriving directly on the Au dot surface contribute to the growth of the nanowire. If the volume that each atom occupies is ν, than the increment of the length of the nanowire per second $\frac{\mathrm{d}l}{\mathrm{d}t}$ will be

$$\begin{aligned} \frac{\mathrm{d}l}{\mathrm{d}t} &= \frac{\nu \cdot \mathrm{d}N}{\pi \cdot R_{\mathrm{Au}}^2} \\ \frac{\mathrm{d}l}{\mathrm{d}t_{\mathrm{Au}}} &= \nu \cdot j, \end{aligned} \tag{3.6}$$

where $\mathrm{d}l/\mathrm{d}t_{\mathrm{Au}}$ is the contribution of the atoms arriving directly on the Au dot. The atoms that arrive on the Si substrate diffuse towards the gold dot over the substrate and the nanowire sidewalls. We assume that the sticking coefficient to the substrate and to the nanowire sidewalls is 0 (considering the growth temperature is very high). The diffusion lengths of the atoms on the Si surface and on the ZnO nanowire sidewalls are $L_{\mathrm{d,Si}}$ and $L_{\mathrm{d,ZnO}}$ respectively. The change in the length of the nanowire per second from the atoms arriving on the rim-shaped area in between distances s and $s + \mathrm{d}s$ (figure 3.8.a) from the droplet is

$$\mathrm{d}\left(\frac{\mathrm{d}l}{\mathrm{d}t_{\mathrm{Si}}}\right) = \frac{\nu j}{\pi R_{\mathrm{Au}}^2} \exp\left(-\frac{s}{L_{\mathrm{d,Si}}}\right) \exp\left(-\frac{l}{L_{\mathrm{d,ZnO}}}\right) 2\pi s \mathrm{d}s \tag{3.7}$$

If we consider equations 3.6 and 3.7 and integrate them over the distance from 0 to $S/2$ we get:

$$\frac{\mathrm{d}l}{\mathrm{d}t} = \frac{\mathrm{d}l}{\mathrm{d}t_{\mathrm{Si}}} + \frac{\mathrm{d}l}{\mathrm{d}t_{\mathrm{Au}}} = \nu j + \frac{2\nu j}{R_{\mathrm{Au}}^2} \exp\left(-\frac{l}{L_{\mathrm{d,ZnO}}}\right) \int_{R_{\mathrm{Au}}}^{S/2} \exp\left(-\frac{s}{L_{\mathrm{d,Si}}}\right) 2\pi s \mathrm{d}s \tag{3.8}$$

$$\begin{aligned} \left(\frac{\mathrm{d}l}{\mathrm{d}t} - \nu j\right) \exp\left(\frac{l(t)}{L_{\mathrm{d,ZnO}}}\right) = \frac{2\nu j}{R_{\mathrm{Au}}^2} L_{\mathrm{d,Si}} \Bigg[& \exp\left(-\frac{R_{\mathrm{Au}}}{L_{\mathrm{d,Si}}}\right) (L_{\mathrm{d,Si}} + R_{\mathrm{Au}}) - \\ & - \exp\left(-\frac{S}{2L_{\mathrm{d,Si}}}\right) (L_{\mathrm{d,Si}} + S/2) \Bigg]. \end{aligned} \tag{3.9}$$

Consider simpler case where diffusion on the ZnO sidewalls is much larger than the length of the wire $L_{\mathrm{d,ZnO}} \gg l$. Then equation 3.9 becomes easy to solve. The time dependence of the nanowire length becomes linear:

$$l(T) = \left(\nu j + \frac{2\nu j}{R_{\mathrm{Au}}^2} L_{\mathrm{d,Si}} \left[\exp\left(-\frac{R_{\mathrm{Au}}}{L_{\mathrm{d,Si}}}\right)(L_{\mathrm{d,Si}} + R_{\mathrm{Au}}) - \right.\right. \\ \left.\left. - \exp\left(-\frac{S}{2L_{\mathrm{d,Si}}}\right)(L_{\mathrm{d,Si}} + S/2)\right]\right) t. \tag{3.10}$$

Figure 3.8.b shows the dependence of the length of the wire at some time t_0, normalised by the atomic volume and incoming flux $l(t_0)/(\nu j)$, on the distance between gold dots in arbitrary units of the gold droplet radius S/R_{Au} for two different diffusion lengths ($L_{\mathrm{d,Si}} = 1, 2$. It illustrates that the length of the nanowires first increases with S and then saturates. The growth rate of the function depends on the diffusion coefficient; the saturation value depends on the diffusion coefficient and radius of the nanowire. If the radius of the Au dots is much smaller than the distance between them, then the expression becomes:

$$l(T) = \frac{2\nu j L_{\mathrm{d,Si}}^2}{R_{\mathrm{Au}}^2}\left[1 - \left(\frac{S}{2L_{\mathrm{d,Si}}} + 1\right)\exp\left(-\frac{S}{L_{\mathrm{d,Si}}}\right)\right] t. \tag{3.11}$$

Using the dependence of the length of the wires on the distance between them we can estimate the diffusion length. If we take the diffusion length of atoms and divide it by the velocity of the atoms at this substrate temperature we will get the lifetime Δt of atoms on the Si surface at this temperature (and the desorption rate $r_{\mathrm{desorption}}$):

$$L_{\mathrm{d,Si}}/\nu = \Delta t = 1/r_{\mathrm{desorption}}. \tag{3.12}$$

3.3.3 Ternary compound growth

In order to investigate ternary compounds, several different approaches can be taken. In the alloy $\mathrm{A}_{1-x}\mathrm{B}_x\mathrm{C}$, if the compounds AC and BC have the same spatial symmetries (or lattice structures), than Vegard's law (see below) can be used to study these materials [195]. If the compounds AC and BC have different lattice

structures, then no simple relationships can be inferred theoretically. Here the analysis of the extensive literature data on specific ternary compound can be taken as a reference for the new investigation. The former case is valid for InAsP material, whereas the latter case can be applied for ZnMgO material.

In the ternary compound analysis we study the dependencies of incorporation rates on the ratios between the material fluxes impinging onto the substrate. The material flux is proportional to

$$J_{\mathrm{P,Mg}} \propto P_{\mathrm{BEP}}/\eta \cdot \sqrt{T/M}, \tag{3.13}$$

where P_{BEP} is the beam equivalent pressure, T the source temperature, M the molecular mass, η the ionization coefficient relative to that of N_2. It is given by $\eta = [(0.4Z/14) + 0.6]$, where Z is the atomic number [196; 197].

3.3.3.1 InAsP

The crystal structure of two alloyed materials (*e.g.* InAs and InP) was investigated by Vegard [195]. According to Vegard's Law there is a linear relation between the crystal lattice parameter of an alloy and the concentrations of the constituent elements. Here, the constituent elements are InAs and InP, and the alloy is $InAs_{1-x}P_x$. Vegard's law states that the phosphorus content x is given by:

$$x = \frac{a_{\mathrm{InAs}} - a_{\mathrm{InAs_{1-x}P_x}}}{a_{\mathrm{InAs}} - a_{\mathrm{InP}}}, \tag{3.14}$$

where a is the lattice constant.

The alloying mechanism of ternary compounds with the example of $InAs_{1-x}P_x$ was investigated by Samuelson *et al.* [123] and used in the work by Persson *et al.* [128]. According to their model, the relationship between the chemical composition of grown nanowires and gas constituents in the chamber is as follows:

$$x = \frac{N_{\mathrm{P}}}{N_{\mathrm{As}} + N_{\mathrm{P}}} = \frac{\beta J_{\mathrm{P}}}{\alpha J_{\mathrm{As}} + \beta J_{\mathrm{P}}}, \tag{3.15}$$

where x is the percentage of P in the $InAs_{1-x}P_x$ nanowires; N_{As} and N_{P} are the fractions of As and P in the nanowires; J_{As} and J_{P} are the beam equivalent

pressures of As and P during the growth; and α and β are the incorporation rate coefficients of As and P, respectively. Experimentally the value measured during the MBE growth of crystals is the content of the phosphorus species in the vapour phase, or the phosphorus normalised flux: $J_{\mathrm{norm}}(\mathrm{P}) = J_P/(J_\mathrm{P} + J_\mathrm{As})$. The relation between phosphorus content in nanowires and phosphorus content in vapours thus may be expressed by:

$$x = \left[\frac{\alpha}{\beta} \cdot \left(J_{\mathrm{norm}}^{-1}(\mathrm{P}) - 1\right) + 1\right]^{-1}. \tag{3.16}$$

If we equate x from Vegard's law (equation 3.14) and from the simple incorporation rate model (equation 3.16) we obtain

$$a_{\mathrm{InAs}_{1-x}\mathrm{P}_x} = a_{\mathrm{InAs}} - (a_{\mathrm{InAs}} - a_{\mathrm{InP}}) \cdot \left[\frac{\alpha}{\beta} \cdot \left(J_{\mathrm{norm}}^{-1}(\mathrm{P}) - 1\right) + 1\right]^{-1}. \tag{3.17}$$

Fitting to the dependence of the lattice constant of ternary compound on the fractional flux, the ratio of the incorporation rate coefficients α/β can be obtained.

3.3.3.2 ZnMgO

The relationship between the Mg content in the vapour phase $J_{\mathrm{norm}}(\mathrm{Mg})$, the Mg content x in $\mathrm{Zn}_{1-x}\mathrm{Mg}_x\mathrm{O}$ nanowires and the Mg and Zn incorporation rate coefficients ratio is similar to equation 3.16:

$$x = \left[\frac{\alpha}{\beta} \cdot \left(J_{\mathrm{norm}}^{-1}(\mathrm{Mg}) - 1\right) + 1\right]^{-1}. \tag{3.18}$$

Measurement of the Mg incorporation into $\mathrm{Zn}_{1-x}\mathrm{Mg}_x\mathrm{O}$ nanowires is more complicated than in the case of phosphorus incorporation into $\mathrm{InAs}_{1-x}\mathrm{P}_x$. Because of the different crystal structures of MgO and ZnO (cubic rock-salt and hexagonal wurtzite respectively), Vegard's law is not applicable to these materials. One way to obtain the relationship between the lattice parameter (and band gap) of $\mathrm{Zn}_{1-x}\mathrm{Mg}_x\mathrm{O}$ and the Mg content x is by comparison with the literature data on Mg doped ZnO growth. Figures 3.9.a,b (black squares) show the lattice parame-

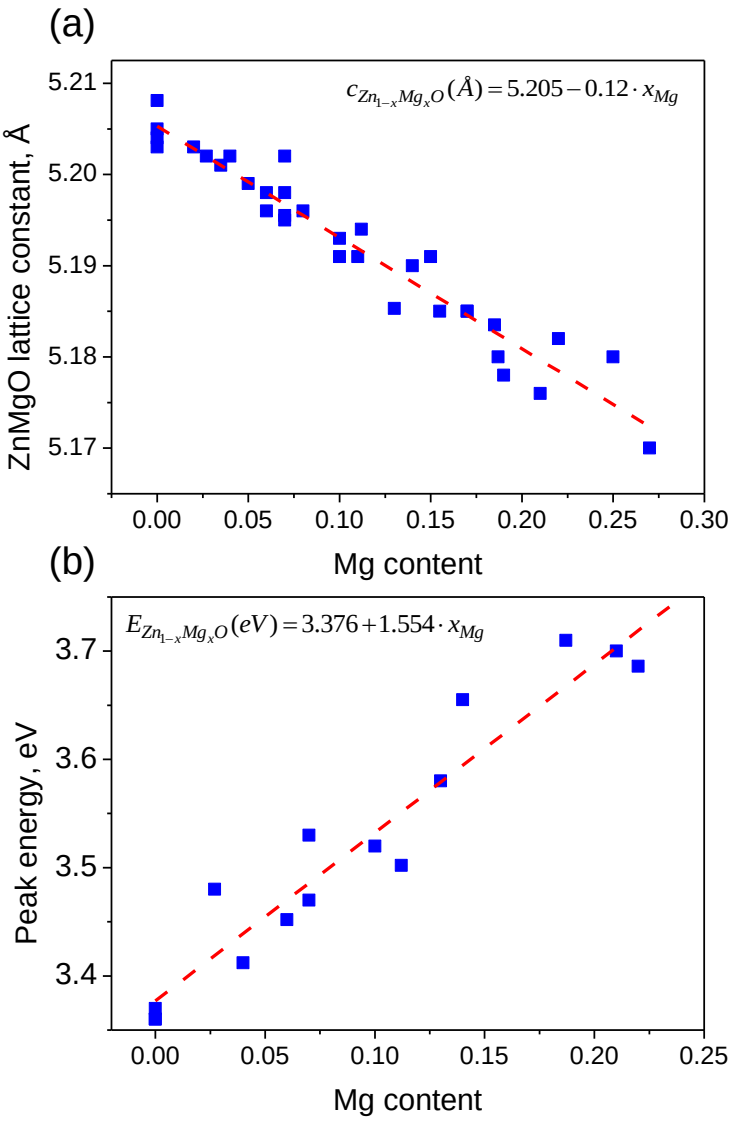

Figure 3.9: Dependences of ZnMgO lattice parameter (a) and ZnMgO band-edge PL peak position on Mg content (b) taken from literature and best linear fits.

ter and low temperature PL peak position dependence on the Mg content in solid films taken from different literature sources [115; 116; 118; 119; 150; 198; 199]. The Mg content in these papers was measured by various direct techniques such as Rutherford backscattering, ion channelling *etc.* At Mg content lower than 30 %, ZnMgO maintains the wurtzite structure without rock-salt phase inclusions [118]. Data gained from many articles shows good mutual correspondence. Therefore the fits to this data may be used as relationships between the Mg content x_{Mg} and the lattice parameter $c_{\mathrm{Zn}_{1-x}\mathrm{Mg}_x\mathrm{O}}$ and the PL peak position $E_{\mathrm{Zn}_{1-x}\mathrm{Mg}_x\mathrm{O}}$. These fits are shown as red lines in figures 3.9.a and 3.9.b and may with good accuracy be assumed to be linear:

$$\begin{aligned} E_{\mathrm{Zn}_{1-x}\mathrm{Mg}_x\mathrm{O}}(\mathrm{eV}) &= 3.376 + 1.554 \times x_{\mathrm{Mg}} \\ c_{\mathrm{Zn}_{1-x}\mathrm{Mg}_x\mathrm{O}}(\mathrm{\AA}) &= 5.205 - 0.12 \times x_{\mathrm{Mg}}. \end{aligned} \tag{3.19}$$

It should be noted, that recently Kozuka *et al.* have measured the Mg content in $\mathrm{Zn}_{1-x}\mathrm{Mg}_x\mathrm{O}$ films grown on ZnO substrates using Rutherford Back Scattering, Secondary Ion Mass Spectroscopy and XRD, and correlated it to the PL and XRD in the range of $x = 0.004$–0.4 [200]. They have found the following values for the Mg-content dependence of the lattice parameter and PL peak position: $\Delta c(\mathrm{\AA}) = -0.069 \times x$ and $\Delta E(\mathrm{eV}) = 2.2 \times x$, which are different from those shown in equation 3.19. This difference may be related to the substrate, since most of the data shown in figure 3.9 are for ZnO films grown on Al_2O_3 substrate, whereas Kozuka *et al.* have grown their films on ZnO substrates. In the present work we have grown nanowires on silicon and sapphire. For Mg content determination, we will use equations 3.19.

3.4 Structural characterisation techniques

3.4.1 Electron Microscopy

3.4.1.1 Scanning electron microscopy (SEM)

Scanning electron micrographs were obtained on two field-effect emission gun scanning electron microscopes (FEG-SEM): Leo 1540 XB cross beam and Supra 40VP Raith 150 EBL system. The microscopes are equipped with secondary

electron-, back-scattered electron- and In-Lens detectors.

3.4.1.2 High Resolution Transmission Electron Microscopy (HRTEM)

High resolution transmission electron microscopy allows imaging the atomic planes: the resolution of the microscope used in this work reaches 0.12 nm. Due to the usually higher energies of TEM than of SEM, and the smaller interaction volume between the electron beam and the material, the resolution of TEM is much better than that of SEM. The electron diffraction pattern of a crystal is used to position the specimen planes parallel to the incident electron beam to allow imaging of atomic columns.

The sample preparation procedure is as follows: first, as-grown samples were ultrasonicated for several minutes in the 2-propanol solution. This suspended the nanowires in the solution. Second, a droplet of nanowire solution was deposited onto a TEM-grid heated to 90 °C. The grid is a 3mm diameter carbon film supported by a copper grid. After the evaporation of 2-propanol, nanowires were found to stay on the TEM-grid (figure 3.10).

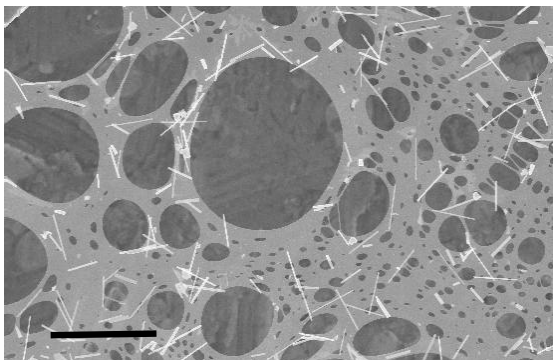

Figure 3.10: TEM copper supported carbon film with nanowires on top. Scale bar is 10 μm.

The high resolution transmission electron microscopes (HRTEM) used in this work are listed in table 3.1.

Table 3.1: Transmission electron microscopes and EDX systems used in current work, and samples investigated by these microscopes.

TEM and EDX	Operating voltage	University, operated by
Jeol JEM 2011	200 kV	University of St. Andrews, Miss Heather Greer Prof Wuzong Zhou
		InAs, InAsP and InAsSb nanowires
Jeol JEM-4000EX	400kV	University of Oxford, Dr John Hutchison
		ZnO nanowires; InAs, InAsP nanowires and clusters
FEI Titan 80/300 Oxford INCA 30 mm^2 LN_2	300kV	Imperial College London, Dr Vasiliki Tileli
		InAs, InAsP, ZnO and ZnMgO nanowires
Jeol JEM 2100 Oxford INCA 80 mm^2 X-Max^N	200 kV	University College London, myself
		InAsSb, ZnO nanowires; ZnO/ZnMgO core-shell nanowires

3.4.1.3 Energy Dispersive X-ray Spectroscopy (EDX)

Energy dispersive X-ray spectroscopy exploits the fact that an incident electron beam excites the electrons in the inner atomic shell, ejecting them from the shell while creating a hole where the electron was. An electron from the higher-energy shell then fills the hole, and the energy difference between the higher-energy shell and the lower-energy shell may be released in the form of X-ray. After measuring all the photons one can calculate the elemental composition of a sample.

EDX spectra were collected in various scanning and transmission electron microscopes with various detectors. EDX measurements on the array of nanowires were performed in Leo 1540XB FEG-SEM with EDX detector. EDX measurements on isolated nanowires were performed in transmission electron microscopes (table 3.1). Quantitative analysis of the EDX spectra was performed using a mixed standard and standard-less quantification algorithm. The cation concentrations were automatically calculated based on Kramer's law [201].

The modeling of the elemental mapping data of core-shell nanowires is shown in figure 3.11. First, the coordinate dependence of the EDX intensity $I_i(x)$ ($i =$

Zn, Mg, O) is calculated from the simple geometrical representation. Then this intensity was convoluted with the gaussian broadening of the EDX signal σ, which is comprised of the electron beam profile and the possible atomic interdiffusion. This leads to the coordinate dependence of the EDX signal $\mathrm{EDX}_i(x)$.

$$
\begin{aligned}
I_{\mathrm{Zn}}(x) &= \begin{cases} \sqrt{R^2 - x^2}, & x < R \\ 0 & x > R \end{cases} \\
I_{\mathrm{Mg}}(x) &= \begin{cases} \sqrt{(R+\Delta R)^2 - x^2} - \sqrt{R^2 - x^2}, & x < R \\ \sqrt{(R+\Delta R)^2 - x^2}, & R < x < R + \Delta R \\ 0 & x > R + \Delta R \end{cases} \\
I_{\mathrm{O}}(x) &= \begin{cases} \sqrt{(R+\Delta R)^2 - x^2}, & x < R + \Delta R \\ 0 & x > R + \Delta R \end{cases} \\
\mathrm{EDX}_i(x) &= \int_{-\infty}^{\infty} \frac{I_i(y)}{\sigma\sqrt{2\pi}} \exp\left(-\frac{(x-y)^2}{2\sigma^2}\right) \mathrm{d}y, \text{where } i = \mathrm{O},\ \mathrm{Mg},\ \mathrm{Zn}.
\end{aligned}
\tag{3.20}
$$

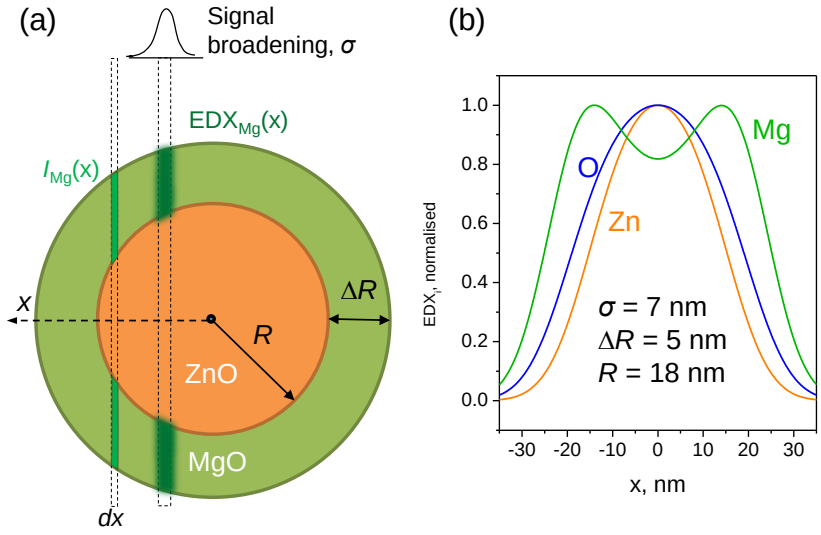

Figure 3.11: (a) Model of an EDX signal from a ZnO/MgO core-shell nanowire; (b) normalised signal from Mg, Zn and O, modelled according to equation 3.20 with $\sigma = 7$ nm, $\Delta R = 5$ nm, $R = 18$ nm.

3.4.2 X-ray Diffraction

X-ray diffraction provides information on the crystal structure of the material. It will be used in this work to measure incorporation of the foreign materials into the host lattice. X-ray diffraction allows measurement of the lattice parameter of the sample based on Bragg's law

$$2a\sin\theta = n\lambda, \tag{3.21}$$

where a is the lattice spacing, θ the reflection angle, λ the X-ray wavelength, and n the diffraction order.

Figure 3.12 schematically represents an X-ray system. The incident X-ray beam arrives at the sample at angle ω and is diffracted at angle 2θ. For a perfectly aligned sample $\omega = \theta$, but usually due to non-idealities of the substrate or a holder alignment is necessary. One or two of the angles are scanned, and the detector collects the X-ray beam diffracted from the sample, thus forming the diffractogram. The types of diffractograms that are used in this work are $\omega - 2\theta$ scans and ω scans (or "rocking curves"). The former are used to study the different crystal planes parallel to the surface of a sample and the spacings between them, the latter give information about the crystal quality of a sample, concentration of dislocations, orientation of a thin film *etc.*

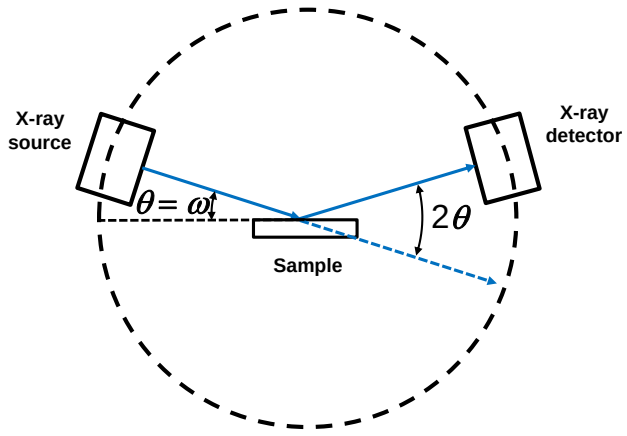

Figure 3.12: The schematic of the XRD machine.

High resolution XRD measurements were carried out on Jordan Valley Bede

D1 and on Riagku SmartLab machines, both with four bounce monochromator (with two channel cut Si crystals). Cu-K_α ($\lambda = 1.54056$ Å) radiation was used in these experiments.

The main parameters affecting the peak positions and how accurately they can be determined are: the primary X-ray beam parameters, sample alignment, accuracy of the angular movements and detector resolution. The energy of the beam is known with very high precision. The resolution ($\Delta E/E$) of the beam is 1/4000 [202]. The divergence of a beam is 0.003°. In order to eliminate the error related to the misalignment of a sample, first the sample is tilted and rotated around the most intense peak (usually the Si(111) or Si(220) peak) to find the position where the highest intensity of the reference peak is detected. After finding this position the sample is expected to be aligned. These misalignment errors arise due to a slight shift of the sample on the holder, or miscut, or bending of the sample. After this alignment procedure, for identical samples ω may vary, but 2θ should be the same due to the geometry of the machine. In order to calculate the error of the equipment alignment, ten different similar Si (111) samples were inserted in the machine and their (111) Bragg reflection was measured. The average displacement of the reflections is about 0.015°. The accuracy of angular movements is defined by a goniometer, whose error is 0.0001°. In addition, the peak fitting procedure results in a fitting error, which should be taken into account as well.

3.4.3 X-ray photoelectron spectroscopy

X-ray photoelectron spectroscopy is a surface sensitive quantitative spectroscopic technique for compositional analysis of materials. During XPS measurement the sample is irradiated by a beam of X-rays and the kinetic energy of electrons that are emitted from the material is measured. The kinetic energy of electrons will depend on their binding energy in the material. The binding energy has characteristic values for each material, thus this technique gives accurate measurement of material composition. This technique is very surface sensitive, as electrons emitted from the atom deep below the surface should travel through the material undergoing a variety of collisions, recombinations and recapture before exiting

the sample.

Due to the surface sensitivity of this technique, oxygen, hydrogen and carbon cannot be realistically measured, since the hydrocarbons adsorbed on the sample surface affect the measurement. The composition of other materials can be accurately determined by XPS if adsorption of these material is eliminated.

The XPS equipment used in this work is a Thermo Scientific K-Alpha instrument, which utilises a monochromated Al-K_α X-ray source ($E = 1486.6$ eV) and achieves ultimate spectral resolution of 0.5 eV. X-rays are focused at source to give a spot size on the sample of 30–400 microns. A dual beam (electron and Ar ion) charge compensation system is used to correct sample charging on insulating substrates. This system is very effective allowing spectra to be collected from highly insulating samples such as Al_2O_3 and MgO. The instrument is operated using Thermo Avantage software, which allows automatic execution of experimental programmes including data collection and elemental analysis [203].

3.4.4 Photoluminescence

Photoluminescence is used to study the optical properties of materials. A laser beam is used to excite carriers in semiconductors, which then quickly thermalise to the valence band top (holes) or to conduction band bottom (electrons) before recombining directly or through defect levels. Radiative recombination gives rise to an optical signal in the photodetector. Different peaks indicate different defect levels. The width of the exciton recombination peak can be used to deduce the crystal quality of a sample. The temperature dependence of photoluminescence peak position and intensity can be used to investigate the behavior of the band gap, carrier life times, recombination rates *etc.*

The band gap energy of the semiconductor material tends to decrease with increasing temperature. It happens due to the increase of the amplitude of atomic vibrations with temperature, which leads to larger interatomic spacing. The temperature dependence of the band gap may be described by the empirical Varshni formula:

$$E_g(T) = E_g(0) - \frac{\alpha T^2}{\beta + T}, \tag{3.22}$$

where α and β are the Varshni coefficients which depend on the specific material.

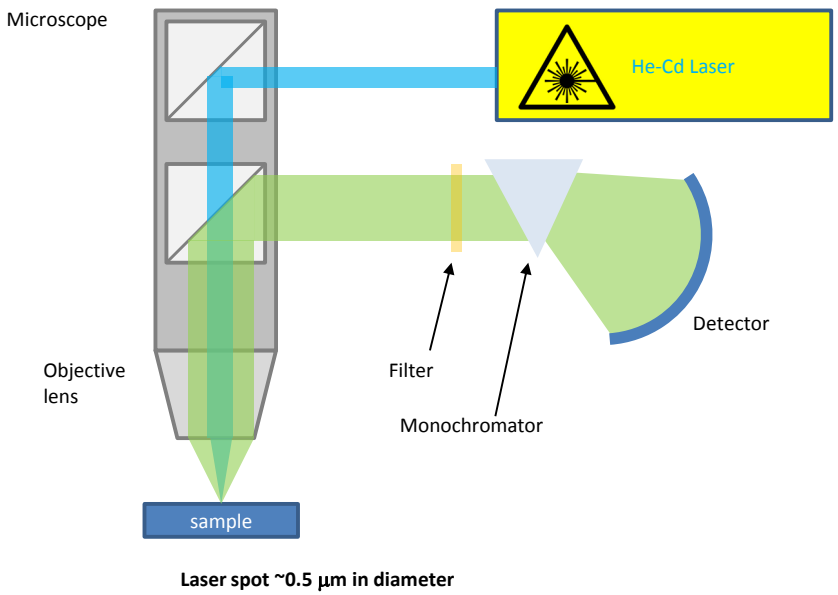

Figure 3.13: The schematic of the PL machine.

Room temperature photoluminescence was measured on the RENISHAW In-Via Raman Microscope with HeCd laser (wavelength 325 nm, excitation power 1 – 90 mW) with a 0.5 – 30 μm diameter focus (figure 3.13). The luminescent light is collected by the condenser lens and directed onto the monochromator and detector.

Low temperature photoluminescence measurements were carried out in Paderborn University by Christian Mietze and Prof Donat Joseph As. The excitation wavelength was 325 nm with power 0.8 mW. The sample was cooled in a closed cycle He cryostat with minimum temperature of 13 K.

3.5 Nanowire field effect transistors

3.5.1 Fabrication

The procedure for fabricating nanowire FETs by photo- and electron beam lithography is presented in this section.

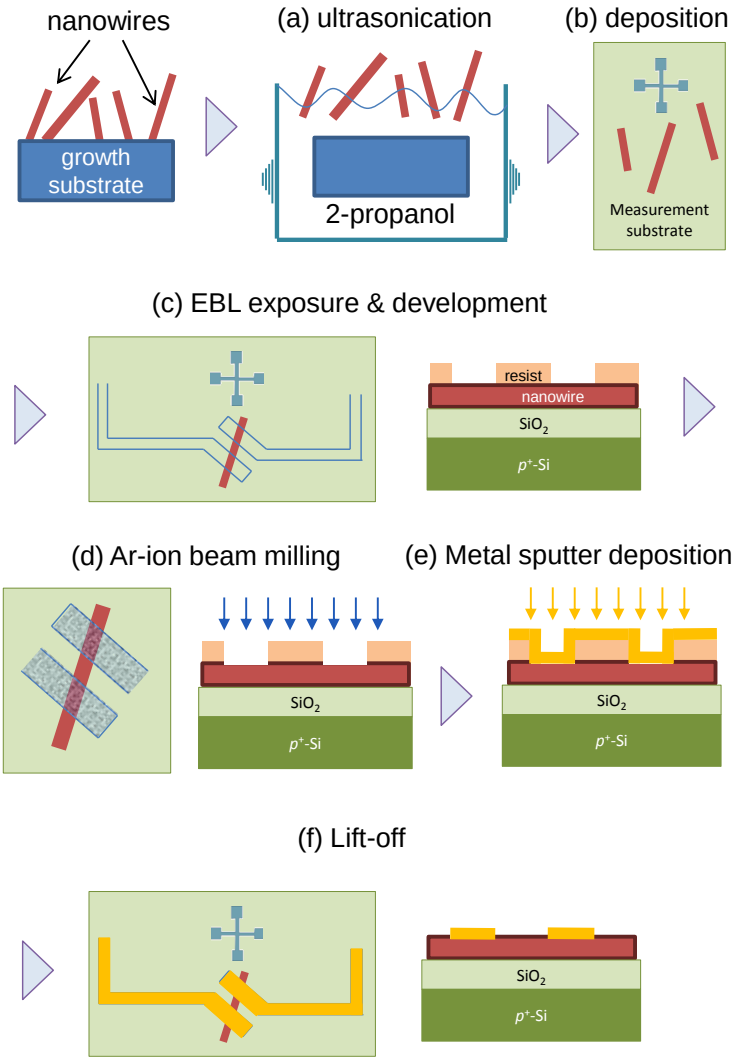

Figure 3.14: Nanowire FET fabrication procedure. (a) ultrasonication of the as-grown sample to remove nanowires from the substrate; (b) nanowire deposition onto the prepatterned thermally oxidised Si wafer; (c) EBL exposure of contact pads and development of exposed areas; (d) Ar-ion milling of EBL-exposed areas to reduce contact resistance; (e) metal deposition; (f) lift-off.

Devices were prepared in four steps. First, degenerately doped silicon wafers (resistivity 0.01 Ohm·cm) were chosen as measurement substrates for the devices. Measurement substrates were oxidised in oxygen atmosphere at a temperature of 1100 °C for one to two hours to grow a 150–400 nm SiO_2 gate insulator. Secondly, a photolithography mask was used to pattern macroscopic biasing tracks. After development of the photo-resist, a Ti/Au double-layer of 20/100 nm thickness was sputtered onto the substrate. After etching the sample in acetone, unpatterned resist with metal on top was lifted off, leaving the contact tracks attached to the substrate. As the next step, alignment-markers were patterned close to the photolithographically prepared tracks by electron-beam lithography, Ti/Au evaporation and subsequent lift-off.

Next, an as-grown nanowire sample was immersed into 2-propanol (IPA) and ultrasonicated for 1 minute (figure 3.14.a). This removed nanowires from the growth substrates and created a solution of nanowires in IPA. A droplet of this solution was deposited on the previously prepared measurement substrate with alignment-markers (figure 3.14.b) and dried. The deposited nanowires were imaged by SEM. The imaging speed was chosen to be as fast as possible to reduce nanowire damage by the electron beam. These images were used to find a suitable nanowire and to design contacts to it in the software created by my colleague Dr Marion Sourribes (figure 3.14.c). 300 nm of A4 950 PMMA resist was spin-coated onto the measurement sample with nanowires. Electron beam lithography was used to pattern nanowire contacts.

After developing the exposed PMMA in MIBK/IPA (Methyl isobutyl ketone/2-propanol) solution, samples were transferred into the vacuum chamber of the SVS ion milling/sputtering system (figure 3.14.d). First, the nanowires were ion milled to remove the surface layer (this procedure reduces the contact resistance). The Ar ion beam acceleration voltage was 390 V, the beam voltage was 200 V and the beam current was 10 mA. The effect of ion milling on the nanowires was investigated in TEM. No apparent damage of the nanowire inner structure was seen after up to 5 minutes milling.

Then, without removing nanowire from vacuum, Ti/Au or Al/Au contacts were sputtered onto the nanowires. A lift-off process in acetone was used to obtain the metal-nanowire contacts (figure 3.14.f).

3.5.2 Nanowire FET measurement

After fabricating the sample, substrates were mounted onto the copper block of a chip carrier, which, in turn, was mounted on the end of the home-built dip probe. Liquid helium was used to cool the sample down to 4.2 K. The rate of cooling depends on the rate of lowering/lifting the dip probe into/from the helium dewar. Measurements upon cooling down and warming up were carried out before the actual experiment to assess the temperature measurement error, which is approximately 0.5 K.

Stationary electrical field effect measurements were carried out using Keithley 4200 semiconductor characterisation system. Pulsed I-DLTS measurements were carried out with a home built I-DLTS system incorporating a Keithley 3390 50 MHz arbitrary waveform generator, Stanford Research SR560 low noise preamplifier and Tektronix TDS 210 digital oscilloscope.

3.5.3 Nanowire transport models

3.5.3.1 Nanowire contact resistance

Semiconductor metal contact

The metal-semiconductor interface plays a crucial role in device performance. Depending on the relative work functions and electron affinities, the contact between a metal and a semiconductor may be a rectifying Schottky contact, or a non-rectifying Ohmic contact. In field effect transistors, non-rectifying Ohmic contacts between the channel and the metal contact with low contact resistance allow fabrication of devices with the maximum performance. Understanding of metal-semiconductor interface is therefore highly important.

The band-bending diagrams of ideal Ohmic and Schottky contacts for an n-type semiconductor are shown in figure 3.15. According to the Schottky-Mott theory [204], the Schottky contact barrier ϕ_S depends on the vacuum electron affinity of the semiconductor χ_{semi} and the work function of the metal W_{metal}:

$$q\phi_S \approx W_{metal} - \chi_{semi}. \tag{3.23}$$

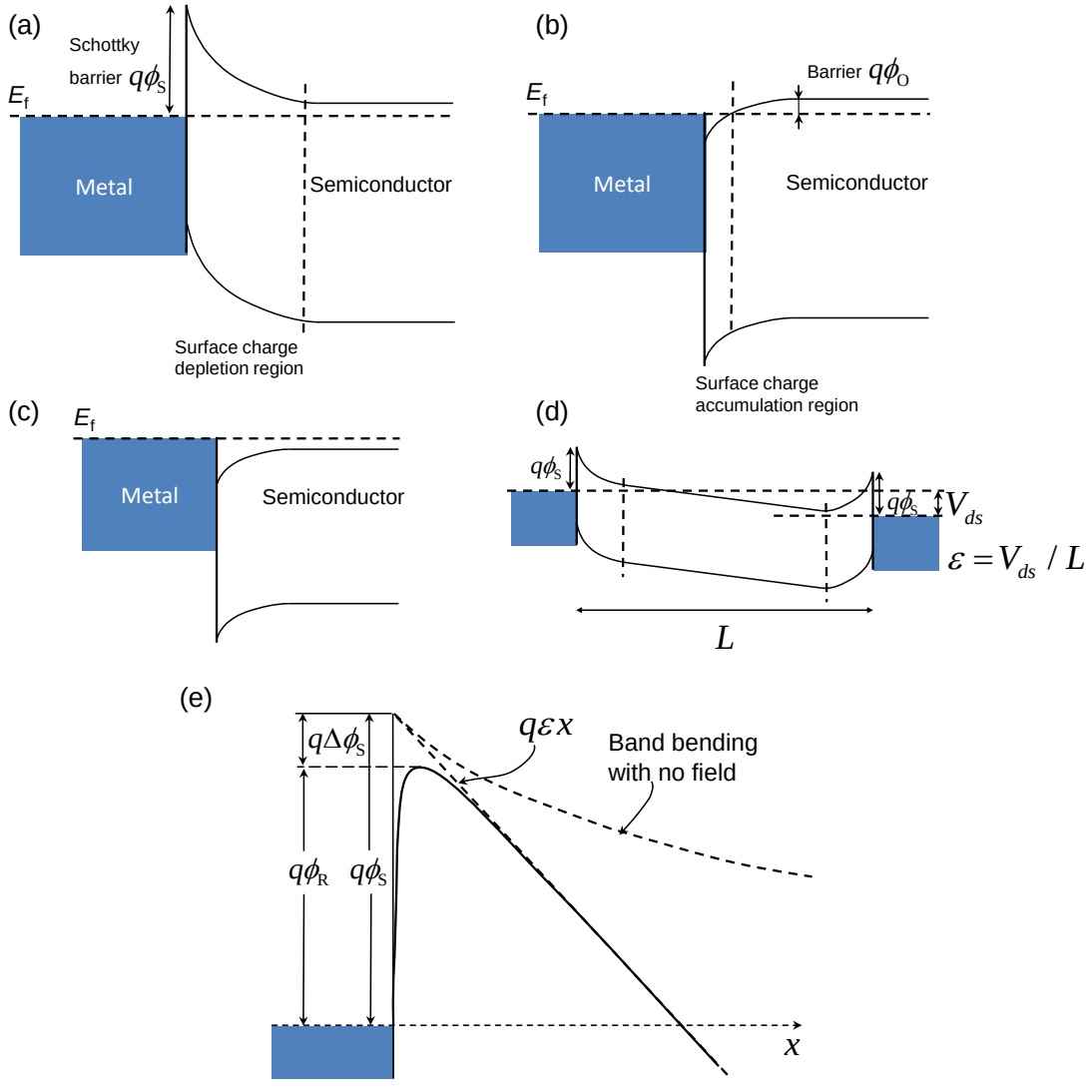

Figure 3.15: Model of a semiconductor-metal contact. (a) Schottky contact, (b) Ohmic contact for non-degenerate semiconductor, (c) Ohmic contact for degenerate semiconductor, (d) two Schottky contact with applied voltage, (e) image force barrier lowering at Schottky contact in reverse bias.

Although equation 3.23 predicts band-bending in the semiconductor and can be used for calculating the Schottky barrier height, it very often gives values not matching the experiment. This usually happens due to Fermi level pinning caused by the charged states at the metal-semiconductor interface.

The Ohmic contact barrier ϕ_{O} between a metal and a non-degenerate semiconductor is usually much smaller than the Schottky contact barrier (figure 3.15.b). Degenerate semiconductors ideally have no barrier at the contact (figure 3.15.c), with the contact resistance being zero.

Schottky barrier current and barrier lowering

The current through the Schottky contact I may be described by thermionic emission-diffusion theory [205]:

$$\begin{aligned} I &= J_S S \left(e^{qV_{\mathrm{ds}}/k_{\mathrm{B}}T} - 1\right), \\ J_S &= A^{**}T^2 \exp\left(-\frac{q\phi_{\mathrm{S}}}{k_{\mathrm{B}}T}\right), \end{aligned} \tag{3.24}$$

where S is the contact area, A^{**} is the effective Richardson constant, V the voltage applied to the Schottky barrier, and T the temperature. Equation 3.24 may allow estimation of the barrier height ϕ_{S} from the forward biased Schottky contacts, or from the temperature dependence of the current through the Schottky contact. Under negative bias, the current saturates at the value J_S.

In the work presented, the nanowire is usually connected to similar metal contacts at both ends. It will be shown that both contacts are Schottky with low barrier height (figure 3.15.d). This results in any applied voltage being a reverse voltage and the current through the nanowire saturating. However, in some conditions, the electrical field next to the Schottky barrier may lower the barrier height (figure 3.15.e). This effect is called the Schottky effect or image force barrier lowering [205]. The barrier lowering may be expressed as follows:

$$\phi_{\mathrm{R}} = \phi_{\mathrm{S}} - \Delta\phi_{\mathrm{S}} = \phi_{\mathrm{S}} - \sqrt{\frac{e\varepsilon}{4\pi\epsilon_0\epsilon_{sc}}}, \tag{3.25}$$

where ϵ_0 and ϵ_{sc} are the dielectric constants of vacuum and the semiconductor respectively, and ε the electric field which may be expressed as $\varepsilon = V_{\mathrm{ds}}/L$,

where L is the distance between drain and source contacts. Considering both equations 3.25 and 3.24, it is clear that under reverse bias, the current will increase with the voltage. At sufficiently high voltages and currents, the barrier approaches zero, and the voltage redistributes among the contact barrier resistance and the bulk resistance R_{bulk}. The voltage drop across the Schottky barrier becomes $V_{\text{ds}} - IR_{\text{bulk}}$, and the current becomes:

$$I = SA^{**}T^2 \exp\left[\frac{q\phi_{\text{S}} - \sqrt{(e(V_{\text{ds}} - IR))/(4L\pi\epsilon_0\epsilon_{sc})}}{k_{\text{B}}T}\right] \times \left[\exp\left(-\frac{q(V_{\text{ds}} - IR)}{k_{\text{B}}T}\right) - 1\right]. \tag{3.26}$$

For FET drain and source contacts, it is desirable to have Ohmic contacts for better current injection. Schottky contacts with barrier height on the order of 100 meV or lower (*i.e.* comparable to $k_{\text{B}}T$ with $T \approx 300$ K) behave as Ohmic contacts at room temperature. Equation 3.26 therefore is used only at low temperatures. At room temperature, channels in these FETs obey Ohm's law. Analysis of the current through a nanowire FET with Ohmic contacts is given in the next sections.

3.5.3.2 Nanowire surface band bending

Band bending of the semiconductor material determines the conductivity in a nanowire. For example, ZnO nanowires have a surface charge depletion layer due to a negatively charged oxygen adsorbed on the surface with the dominant conductivity happening in the core of the nanowire [177; 206]. InAs nanowires, on the other hand, have a surface electron accumulation layer which accounts for the main contribution to the conductivity [207]. A simple model for non-degenerate n-type semiconductor nanowires with a surface charge depletion region is given here. The effect of holes is omitted for clarity. First, we will show how the surface depletion region is affected by the surface states and gate voltage, then we will derive expression for current through nanowire.

We assume a nanowire to have cylindrical symmetry, uniform distribution of ionised shallow donors with concentration N_d and uniform distribution of surface states. A negative surface charge creates the surface band bending and positively

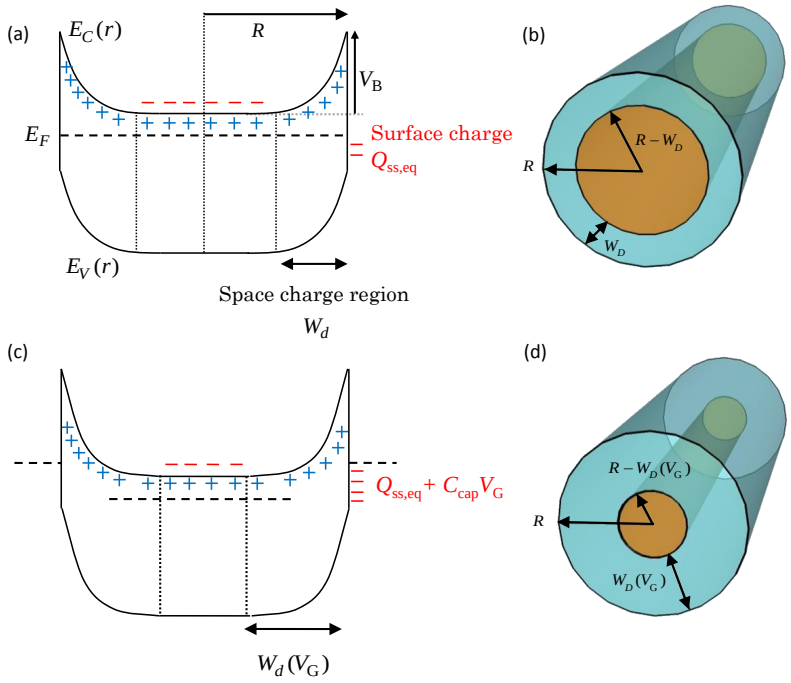

Figure 3.16: Model of nanowire band bending for an n-type nanowire with a surface depletion region. (a–b) equilibrium condition, $V_G = 0$, band diagram and graphic representation, with orange region being the conductive core and blue region being the depletion region; (c–d) band diagram of the nanowire under applied negative gate voltage, surface charge is negative

charged depletion region near the surface of the nanowire (figure 3.16). This depletion region (blue colour in figure 3.16) acts as an insulating layer surrounding the conducting core of the nanowire (orange colour, figure 3.16). The depletion region charge is composed of the charge of ionised donors:

$$Q_+ = qN_d\pi W_d(2R - W_d)L, \tag{3.27}$$

where L is the distance between contacts, R the radius of the nanowire, q the elemental charge, W_d the depletion region width which depends upon the gate voltage V_{G}. The charge of the depletion region may also be expressed as $Q_+ = C_{\mathrm{DR}}V_{\mathrm{B}}$, where V_{B} is the surface barrier height, C_{DR} the depletion region capacitance. According to a simple cylindrical capacitor model:

$$C_{\mathrm{DR}} = \frac{2\pi\epsilon_0\epsilon_{\mathrm{ZnO}}L}{\ln(R/(R - W_d))}, \tag{3.28}$$

where ϵ_{ZnO} is the dielectric constant of ZnO. The barrier height can be found from combining equations 3.27 and 3.28:

$$V_{\mathrm{B}} = \frac{qN_dW_d(2R - W_d)\ln(R/(R - W_d))}{2\epsilon_0\epsilon_{\mathrm{ZnO}}}, \tag{3.29}$$

or, equivalently,

$$V_{\mathrm{B}} = -\frac{R^2qN_d\,x(2 - x)\ln(1 - x)}{2\epsilon_0\epsilon_{\mathrm{ZnO}}}, \tag{3.30}$$

where $x = W_d/R$. Voltage barrier V_{B} dependence of the depletion width reduced to nanowire radius for different donor concentrations in ZnO nanowire with radius 25 nm is shown in figure 3.17.a. Higher charge carrier densities result in the smaller depletion region width for the same surface barrier voltages.

The charge on the nanowire surface is the sum of the negative surface state charge Q_{ss} and the charge induced by the gate voltage, $Q_- = Q_{\mathrm{ss}} + C_{\mathrm{oxide}}V_{\mathrm{G}}$ (figure 3.16.b). Here V_{G} is the gate voltage and the oxide capacitance C_{oxide} for a back-gated nanowire FET is calculated based on the model of a metallic wire above a charged plane:

$$C_{\text{oxide}} = \frac{2\pi\epsilon_0\epsilon_{\text{SiO,eff}}L}{\ln\left(d/R + \sqrt{(d/R)^2 - 1}\right)}, \tag{3.31}$$

where $\epsilon_{\text{SiO,eff}}$ is the effective relative permittivity of air and silicon oxide which can be taken to be equal 2.2 [208], and d the oxide thickness. We can define the effective negative gate voltage as $V_{\text{G,eff}} \equiv |Q_-|/C_{\text{oxide}} = |Q_{\text{ss}} + C_{\text{oxide}}V_{\text{G}}|/C_{\text{oxide}}$. Noting that $|Q_+| = |Q_-|$ due to charge equilibrium, from equation 3.27 we get the dependence of the depletion region width W_d on the effective gate voltage $V_{\text{G,eff}}$:

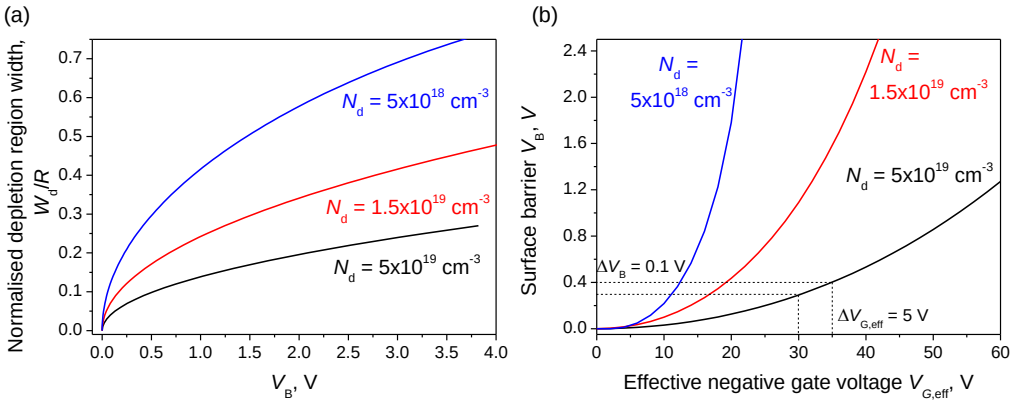

Figure 3.17: Nanowire band bending. (a) surface barrier voltage dependence of the depletion width at different donor concentrations, according to equation 3.30; (b) dependence of the surface barrier voltage on the effective negative gate voltage for ZnO nanowire with different donor concentrations, according to equations 3.30 and 3.32.

$$W_d/R = 1 - \sqrt{1 - \frac{C_{\text{oxide}}V_{\text{G,eff}}}{R^2 q N_d \pi L}}. \tag{3.32}$$

Taking into account equations 3.30 and 3.32 we can get effective gate voltage dependence of the nanowire surface barrier voltage. This dependence is shown in figure 3.17.b for ZnO nanowire with radius 25 nm and with different donor concentrations. ZnO nanowires exhibit high concentration of surface states with carrier capture onto these states depending on the surface barrier. Therefore, understanding of how gate voltage effects the surface barrier is important for

both device modelling and fabrication. Figure 3.17.b shows that for a typical ZnO nanowire with surface barrier of 0.3 eV and with donor concentration $N_d = 5 \times 10^{19}$ cm^{-3}, increase of the surface barrier by 0.1 eV, *i.e.* from 0.3 to 0.4 V, requires the gate voltage change by 5 V.

3.5.3.3 Current through the nanowire FET

Here we will not limit our consideration by discussing nanowires with depletion regions only. We shall derive the expression for charge current for any n-type nanowire. We start our derivation from reminding that the charge on the outer walls of the wire should be balanced by the nanowire charge $|Q_-| = |Q_+|$. The nanowire charge is constituted of the charge of the ionised shallow donors with concentration N_d and the charge of the free carriers $qL\int_0^R n(r)2\pi r\,\mathrm{d}r$, where $n(r)$ is the distribution of the free carrier density which depends on the conduction band profile in the nanowire. The charge in the nanowire is

$$Q_{\mathrm{NW}} = qL\int_0^R n(r)2\pi r\,\mathrm{d}r - q\pi R^2 N_d L. \tag{3.33}$$

Since $Q_- = Q_{\mathrm{ss}} + C_{\mathrm{oxide}}V_{\mathrm{G}}$, the charge of free carriers is equal to:

$$Q_{\text{free carriers}} = qL\int_0^R n(r)2\pi r\,\mathrm{d}r = Q_{\mathrm{ss}} + C_{\mathrm{oxide}}V_{\mathrm{G}} + q\pi R^2 N_d L. \tag{3.34}$$

The equation for the drain-source current I_{ds} through the nanowire may be derived from [205], assuming the drain-source voltage V_{ds} is much smaller than the gate voltage and the surface barrier voltage:

$$\begin{aligned} I_{\mathrm{ds}} &= \frac{qV_{\mathrm{ds}}}{L}\iint_A \mu n\,\mathrm{d}A = \\ &= \frac{qV_{\mathrm{ds}}}{L}\int_0^R \mu(r)n(r)2\pi r\,\mathrm{d}r, \end{aligned} \tag{3.35}$$

where $\mu(r)$ is the mobility which depends on the position (the scattering will be different at the nanowire surface and in the nanowire core), A the nanowire cross-sectional area. Next, we introduce the effective carrier mobility μ_{eff} as:

$$\mu_{\text{eff}} = \frac{\int_0^R \mu(r) n(r) 2\pi r \, \mathrm{d}r}{\int_0^R n(r) 2\pi r \, \mathrm{d}r}. \tag{3.36}$$

Now the current through the nanowire becomes:

$$I_{\text{ds}} = \frac{q V_{\text{ds}} \mu_{\text{eff}}}{L^2} Q_{\text{free carriers}} \tag{3.37}$$

Putting equations 3.34 and 3.37 together we get:

$$I_{\text{ds}} = \frac{\mu_{\text{eff}} N_d \, q}{L} \pi \left(R^2 + \frac{Q_{\text{ss}} + C_{\text{oxide}} V_{\text{G}}}{q N_d \pi L} \right) V_{\text{ds}}, \tag{3.38}$$

or, equivalently,

$$I_{\text{ds}} = \frac{\mu_{\text{eff}} \, C_{\text{oxide}}}{L^2} [V_{\text{G}} + V_{\text{T}}] V_{\text{ds}}, \tag{3.39}$$

where $V_{\text{T}} = \frac{Q_{\text{ss}}}{C_{\text{oxide}}} + \frac{N_d q \pi R^2}{C_{\text{oxide}}}$ is the threshold voltage. Equation 3.39 coincides well with the usual transistor formula in the linear regime [205]. The usual expression of the threshold voltage does not contain surface charge [166] and is used to infer the concentration of ionised shallow donors N_d, which at high temperatures coincides with carrier concentration. The term "carrier concentration" will be used interchangeably with the term "ionised shallow donor concentration" in this work. The appearance of term $Q_{\text{ss}}/C_{\text{oxide}}$ in the threshold voltage shows that the usual way of obtaining carrier concentration gives an incorrect result (either underestimating or overestimating the concentration depending on the sign of surface charges). The negative ($Q_{\text{ss}} < 0$) and positive ($Q_{\text{ss}} > 0$) surface charge will create surface depletion and accumulation layer respectively.

ZnO nanowires usually have negatively charged surface states which create surface depletion region (figure 3.16). Along with equation 3.39 the following expression is valid for current through the nanowire with surface depletion area:

$$I_{\text{ds}} = \frac{\mu_{\text{eff}} N_d q A_{\text{core}}}{L} = \frac{\mu N_d q}{L} \pi \big(R - W_d(V_{\text{G}})\big)^2 V_{\text{ds}}. \tag{3.40}$$

3.5.3.4 Corrections to nanowire FET resistance and capacitance

In this work for nanowires with Ohmic contacts we estimate the effective carrier concentration $N_{d,\text{eff}}$ by measuring the resistance of the wire $\mathbb{R}$ and using the formula:

$$\begin{aligned} \mathbb{R} &= \frac{L}{\mu_{\text{eff}} N_{d,\text{eff}} q\pi R^2}, \text{ or} \\ N_{d,\text{eff}} &= \frac{L}{\mu_{\text{eff}} \mathbb{R} q\pi R^2}. \end{aligned} \tag{3.41}$$

For nanowires with surface depletion region nanowire resistance is:

$$\mathbb{R} = \frac{L}{\mu_{\text{eff}} N_d q\pi (R - W_d)^2}. \tag{3.42}$$

The depletion region charge is equal to the charge of the surface states: $qN_{\text{ss}}2\pi RL = qN_d\pi W_d(2R - W_d)L$, where N_{ss} is the surface charge in cm^{-2}. Putting the solution of this equation into 3.42 and using 3.41 we get:

$$\begin{aligned} N_d &= \frac{L}{\mu_{\text{eff}} \mathbb{R} q\pi R^2} + \frac{2N_{\text{ss}}}{R}; \\ N_{d,\text{eff}} &= N_d - \frac{2N_{\text{ss}}}{R}. \end{aligned} \tag{3.43}$$

In the presence of surface states, the effective carrier concentration will be lower in nanowires with lower diameters.

The model of the FET capacitance C_{oxide} uses the assumption of a nanowire being an infinite metallic cylinder over a conductive plane. These approximations are not correct when nanowire has low charge carrier concentration and when the distance between the contacts is on the order of the contact dimensions. Numerical modeling shows that nanowires with diameters larger than 20 nm and the carrier concentration higher than 10^{17} cm^{-3} can be described by the usual model with high enough accuracy (error less than 1 %) [209].

Contact effects, such as imaging force, depletion region width, contact area, insulating layer, shunt resistance and effect of the minority carriers, affect the IV characteristics of the nanowire. Investigation and decoupling of these effects was carried out by Zhang *et al.* [210]. For ZnO nanowires used in this work it will be

shown that they have the carrier concentration of 10^{19} cm^{-3}, the depletion region of 2 nm, and most parameters may be determined using the equation 3.39.

3.5.4 Current-mode deep level transient spectroscopy in nanowires

3.5.4.1 I-DLTS method

In I-DLTS measurements on nanowire FETs, a fixed drain-source voltage V_{ds} is applied to the nanowire resulting in a constant current $I_{\mathrm{ds},0}$ through the nanowire. The gate voltage is kept at a quiescent value V_{GQ} and a gate voltage pulse ΔV_{G} is applied periodically with period T_{P} and width t_{P} (figure 3.18.a). In n-type nanowires (like ZnO), a positive pulse ΔV_{G} populates deep trap states with electrons, which, after the end of the pulse, get emitted from the deep traps with an emission rate e_n, contributing to the relaxation current $\Delta I(t) = I(t) - I_{\mathrm{ds},0}$ through the nanowire (figure 3.18.b). The I-DLTS signal is constructed by measuring the relaxation current at times t_1 and t_2 after the end of the pulse and subtracting them: $I_{\mathrm{DLTS}} \equiv I(t_1) - I(t_2)$.

The rate of carrier emission e_n from the deep traps can be expressed as: $e_n \propto \sigma_0 \exp(-E_{\mathrm{dl}}/k_{\mathrm{B}}T)$, where E_{dl} is the deep trap activation energy, σ_0 the trap cross-section and k_{B} Boltzmann's constant. Hence the emission rate will vary with temperature. At low temperatures the emission rate will be very low, much lower than t_2^{-1}, resulting in $I(t_1) - I(t_2)$ being close to zero. Conversely, at high temperatures the emission rate will be high, much higher than t_1^{-1}, also resulting in $I(t_1) - I(t_2) = 0$. At some intermediate temperature, T_{max}, I_{DLTS} will reach a peak value (figure 3.18.c). The value of T_{max} depends on the choice of t_1 and t_2. Assuming an exponential time dependence of the emission $\Delta I(t) \propto \exp(-e_n t)$, at temperature T_{max}, there is an unambiguous relation between the emission rate and the times t_1 and t_2: $e_n(T_{\mathrm{max}}) = \frac{\ln(t_2/t_1)}{t_2 - t_1}$ [18]. By choosing different values of t_1 and t_2 and measuring the temperature at which the maximum in $I_{\mathrm{DLTS}}(T)$ occurs, we obtain the dependence of e_n on temperature. From this dependence we can obtain the apparent cross-section of the trap σ_0 and its energy position in the band gap E_{dl}.

It will be shown later, that the electron emission from the electron traps

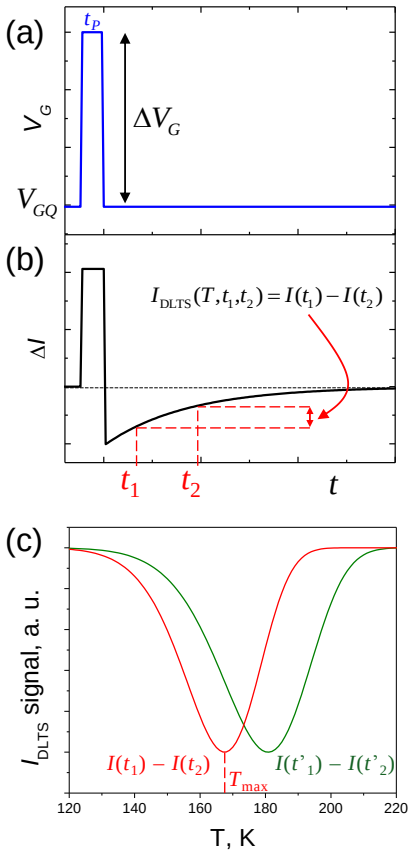

Figure 3.18: I-DLTS principle of operation. (a) Time-dependence of the gate voltage; (b) time-dependence of the current through the nanowire; (c) the I-DLTS spectra constructed using two different sets of times t_1, t_2 and t'_1, t'_2

generally results in the negative current transient signal as shown in figure 3.18.b, which gives rise to an I-DLTS minimum (figure 3.18.c). On the contrary, the hole emission will result in the opposite current transient sign, giving rise to an I-DLTS maximum. Semiconductor nanowires have different types of traps residing in the core of the nanowire, on its surface, on the semiconductor-dielectric or semiconductor-metal interface. These traps will affect current through the nanowire in different ways. The account of the physical phenomena that govern the dynamics of the carriers due to the deep trap states, surface states and charge hopping is given in the next section.

3.5.4.2 Current transient in nanowires

Bulk nanowire deep electron traps

Let us consider a deep donor level that is uniformly distributed throughout the n-type nanowire (figure 3.19.1). This donor level is neutral when empty and negatively charged when filled with electron. At quiescent gate voltage bias V_{GQ} deep traps below the Fermi energy are filled with electrons, while those traps above the Fermi energy (close to the nanowire surface) are empty (figure 3.19.a.1). When a positive gate voltage pulse ΔV_{G} is applied, the Fermi energy changes its position with deep levels below the Fermi energy promptly filling with electrons (figure 3.19.b.1). When the gate voltage returns to the quiescent bias value, the filled levels start emitting electrons into the conduction band (figure 3.19.c.1). The emission of electrons from the deep states follows an exponential decay with emission rate e_n according to Shockley-Read-Hall statistics [211; 212]. Assuming that all the deep traps are filled with electrons at time $t = 0$, the time-dependence of the number of carriers trapped on the deep levels $n_{\mathrm{dl}}(t)$ and the number of carriers emitted from the deep levels into the conduction band $n(t)$ is:

$$\begin{aligned} n_{\mathrm{dl}}(t) &= n_{\mathrm{dl},0}\exp(-e_n t); \\ n(t) &= n_{\mathrm{dl},0}(1-\exp(-e_n t)); \\ e_n &= \sigma_0 \gamma T^2 \exp(-E_{\mathrm{dl}}/k_{\mathrm{B}}T), \end{aligned} \tag{3.44}$$

where $n_{\mathrm{dl},0}$ is the number of deep traps, $n_{\mathrm{dl},0} = N_{\mathrm{dl},0} \cdot V$, $N_{\mathrm{dl},0}$ the trap concentration, V the volume of the charging-recharging traps, E_{dl} the energy difference

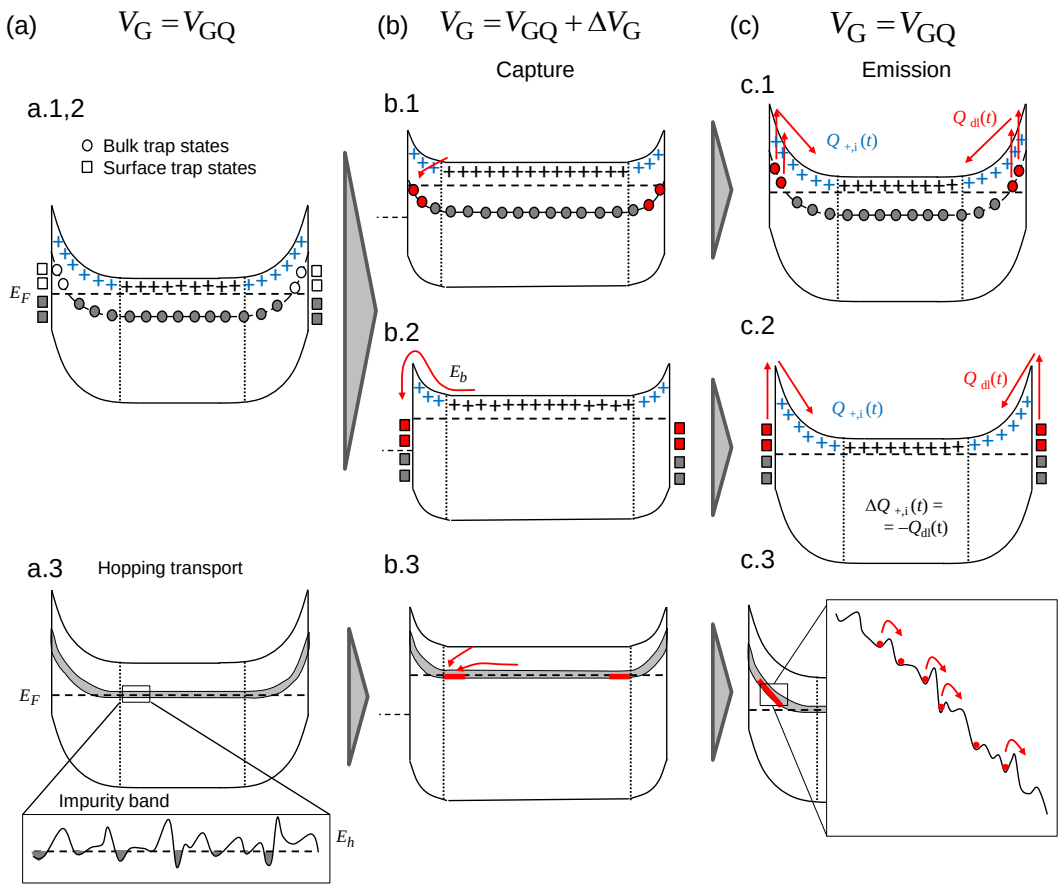

Figure 3.19: Different mechanisms of current transients: deep levels in a nanowire .1, surface states .2 and hopping mechanism .3. (a) quiescent gate voltage conditions V_{GQ}; (b) positive gate voltage pulse ΔV_G; (c) emission of electrons from the filled traps into the conduction band at the quiescent gate voltage.

between the energy level of the deep trap and the conduction band, σ_0 is an effective minority carrier capture cross section and $\gamma = 2\sqrt{3}(2\pi)^{3/2}h^{-3}k^2m^*$, with m^* the effective electron mass. Here, we will neglect the temperature dependence of the Fermi level position, the carrier concentration and, therefore, the value of $n_{\mathrm{dl},0}$.

The change in population of these levels will result in a current transient through the nanowire. There are two components of the current transient, the detrapping current, ΔI_{C}, and the depletion width modulation current, ΔI_{D}. Here we consider each of these components in turn.

The detrapping current depends on the rate of change of charge due to emission of electrons into the conduction band. Electrons emitted from the deep level are swept by the radial electric field to the nanowire core, and then by the drain-source electric field to the nanowire contacts, resulting in a drift electron current:

$$\Delta I_{\mathrm{C}} = -q\frac{\partial n_{\mathrm{dl}}(t)}{\partial t} = -q\frac{\partial[n_{\mathrm{dl},0}\exp(-e_n t)]}{\partial t} = qe_n n_{\mathrm{dl},0}\exp(-e_n t). \tag{3.45}$$

We now consider the depletion width modulation current. After the removal of the voltage pulse ΔV_{G}, the charge of the ionised donors in the depletion region is exactly balanced by the sum of the negative surface charges and the electrons on the deep trap states (this balancing is maintained by fast movement of the free electrons). When electrons are emitted from the deep traps, then this charge balance can only be maintained by a corresponding decrease in the number of ionised donors in the depletion region. Equivalently the emission of electrons from deep traps is accompanied by a decrease in the width of the depletion region. This suppression of the depletion region results in an increase in the nanowire current.

The charge of the ionised donors is $Q_{+\mathrm{i}} = qN_d\pi W_d(2R-W_d)L$, and the change in the charge of the ionised donors is equal to the change of the deep level charge: $\Delta Q_{+\mathrm{i}}(t) = Q_{\mathrm{dl}}(t) = qn_{\mathrm{dl}}(t)$. Taking into account equation 3.38, we get expression for the depletion width modulation current:

$$\begin{aligned} I_{\mathrm{ds}} =& \frac{\mu N_d q}{L}\pi\left(R^2 + \frac{Q_{\mathrm{ss}} + Q_{\mathrm{dl}}(t)}{qN_d\pi L}\right)V_{\mathrm{ds}}, \\ \Delta I_{\mathrm{D}} =& -\frac{\mu q}{L^2}V_{\mathrm{ds}} n_{\mathrm{dl},0}\exp(-e_n t). \end{aligned} \tag{3.46}$$

Summing up equations for the detrapping current and the depletion width modulation current we obtain:

$$\Delta I(t) = \left(-\frac{\mu}{L^2}V_{\mathrm{ds}} + e_n\right) q n_{\mathrm{dl}}\exp(-e_n t), \tag{3.47}$$

We will now show that these two terms can be distinguished by their temperature-dependence. Let's consider the prefactor of the transient $-\mu V_{\mathrm{ds}}/L^2 + e_n$. The weak temperature dependence of the first term lies in the carrier mobility $\mu(T)$. Division of the current transient by the static expression for the current (equation 3.39) $\Delta I(T)/I(T)$ eliminates the temperature dependence of the mobility. The temperature dependence of the static current $I(T)$ can be measured separately. Assuming no temperature dependence of carrier concentration, the value $\frac{\mu(T)V_{\mathrm{ds}}}{L^2}/I(T)$ will be nearly independent with temperature. On the other hand, the prefactor of the detrapping current component depends dramatically on temperature, as the pre-factor in equation 3.45 includes the emission rate e_n, which exponentially increases with temperature (equation 3.44).

The first term (depletion width modulation component) is usually much larger than the second term (detrapping component) in our experiment due to the parameters of our devices ($\mu \approx 20$ cm^2/(V·s), $L = 500$ nm, $V_{\mathrm{ds}} = 0.2$ V and $\mu V_{\mathrm{ds}}/L^2 \approx 10^9$ sec^{-1}, whereas $e_n \approx 2\times10^2 - 2\times10^4$ sec^{-1}). Thus, the modulation current will usually dominate the current relaxation. If, however, the Fermi level is pinned to the surface states, and the size of the depletion region W_d does not follow the recharging of the deep traps, then the detrapping component e_n will dominate the current transient and the prefactor will strongly depend on temperature.

The I-DLTS signal will be either negative or positive depending on whether the depletion width modulation component or the detrapping component dominates. Since the depletion width modulation component is usually larger than the detrapping component, we expect negative peaks in the nanowire I-DLTS

spectra.

Surface electron traps

Surface electron traps will affect current transients in a way similar to bulk deep levels (figure 3.19.2). Figure 3.19.c.2 shows that charge emission from the surface traps will express itself in the same two current components: the detrapping current and the depletion modulation current. The only difference between surface and bulk traps will be seen in the charge capture process. Whereas the bulk trap capture does not exhibit any thermally activated behaviour, figure 3.19.b.2, shows that the surface trap capture rate depends on the surface barrier E_b. The electron capture process is self-limiting, since when electrons are trapped on the surface levels, the barrier for electrons grows and repels new electrons from the surface states. This increase in surface barrier increases the depletion region width and thus reduces the current. The same behaviour was observed in un-passivated ZnO nanowire field-effect transistors in oxygen atmosphere at room temperature [190].

The charge capture process may be observed in the so-called "capture-mode" I-DLTS [193]. It exploits a negative gate-voltage pulse, during which the surface states emit trapped charge. After the negative gate voltage pulse is retracted and the higher quiescent gate voltage is restored, surface states start trapping electrons with capture rate c_n. The expression for the carrier capture rate is similar to equation 3.44:

$$c_n = \sigma_{\mathrm{ss}} \gamma T^2 \exp(-E_b / k_{\mathrm{B}} T), \tag{3.48}$$

where σ_{ss} is the surface state capture cross-section. We assume as a first approximation that E_b is constant in time. The barrier energy will however depend on the gate voltage as outlined in section 3.5.3.2, equations 3.30 and 3.32.

Hole traps

Emission from hole traps can be described by equation 3.47 with sign of q inverted. However the behaviour of holes in an n-type nanowire is very different from that of electrons. After the positive gate voltage pulse is retracted, the

electric field will attract holes towards the surface (as opposed to electrons, which are pushed away from the surface). If hole acceptor traps reside near the surface, they will start capturing these holes. The rate of change of the number of holes in the valence band and their recombination rate will be expressed as [211]:

$$\begin{aligned} \frac{\partial p(t)}{\partial t} &= -\frac{p}{\tau_p}, \text{ and} \\ p(t) &= p(0) + N_{p,0} \cdot \exp(-t/\tau_p), \end{aligned} \tag{3.49}$$

where $c_p = 1/\tau_p = N_{\mathrm{dl},0} v_{\mathrm{th}} \sigma_p$ is the hole capture rate, v_{th} the thermal carrier velocity and σ_p the trap capture cross-section, $p(0)$ the initial number of holes, $N_{p,0}$ the number of deep levels capturing the holes. The current through the nanowire is expressed as $\Delta I_p(t) = q\partial p(t)/\partial t = -qc_p N_{p,0} \exp(-c_p t)$. Some traps have thermally activated cross-section ($\sigma_c(T) = \sigma_{c,0} \times \exp(-E_a/k_{\mathrm{B}}T)$ [18]) and they may give rise to negative peaks in I-DLTS spectra. Most of the positive peaks observed in the literature on thin film FET I-DLTS are attributed to the so-called "hole-like" traps and they may both emit and capture holes [193].

Hopping transport in nanowires

It was reported that ZnO nanowires may exhibit a hopping transport mechanism [213]. In this case, the following explanation may be applied for nanowires with no deep levels (figure 3.19.3). After the end of the gate voltage pulse, the negative surface charge sweeps electrons away towards the nanowire core (figure 3.19.b.3). In the case of the hopping mechanism, the probability for an electron to move (or the "hopping rate") is $\rho = \rho_0 \exp(-E_h/k_{\mathrm{B}}T)$, where E_h is the average activation energy for charge hopping. This expression is analogous to the emission rate expression in equation 3.44. After the end of the pulse, the depletion region charge will gradually increase from $|Q_{\mathrm{ss}}| - C_{\mathrm{oxide}}\Delta V_{\mathrm{G}}$ to $|Q_{\mathrm{ss}}|$ and the current through the nanowire will decrease consequently. Thus, the expression for current in the hopping transport regime will be

$$\Delta I_H = \frac{\mu q}{L^2} V_{\mathrm{ds}} C_{\mathrm{oxide}} \Delta V_{\mathrm{G}} \exp(-\rho t). \tag{3.50}$$

The prefactor of this expression is positive. Therefore, hopping conductivity gives rise to a positive I-DLTS peak. The hopping activation energy E_h strongly

depends on the electric field at the nanowire surface according to the Poole-Frenkel law. Under very strong electric field (or large negative charge on the surface. $|Q_{\rm ss}| - C_{\rm oxide}\Delta V_{\rm G}$, the activation energy will decrease and may completely vanish.

3.5.4.3 I-DLTS. Measurement setup

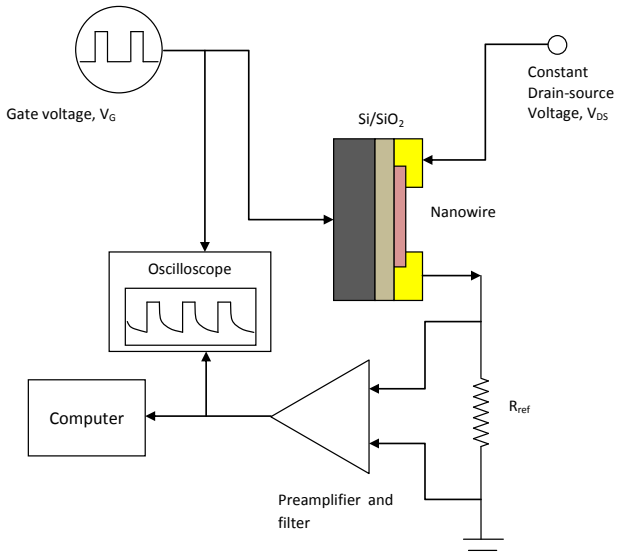

Figure 3.20: Measurement setup of I-DLTS measurement on nanowire FET.

The I-DLTS measurement setup is shown in figure 3.20. A ZnO nanowire field effect transistor with back-gate is used for the measurement. The drain-source voltage through the nanowire is kept constant at $V_{\rm ds} = 0.2$ V. A negative quiescent gate voltage bias of $V_{\rm GQ} = -10$ V keeps a large area of the n-type nanowire cross-section depleted. Gate voltage pulses $\Delta V_{\rm G}$ of 10 V amplitude and 100 μsec duration are applied to the gate of the nanowire FET with repetition rate between 0.1 and 1 kHz. The current through the nanowire is probed by the differential pre-amplifier across a reference resistor whose resistance is much smaller than the nanowire resistance. The DC component of the current is filtered out and the relaxation current is amplified. The signal is supplied to the oscilloscope, averaged and digitised. The I-DLTS signal $I_{\rm DLTS} = I(t_1) - I(t_2)$ is measured at

different temperatures.

The behaviour of the I_{DLTS} peak depends on the prefactor in equation 3.47. Considering only the depletion width modulation current component, it can be shown, that if we choose times t_1 and t_2 so that t_1 varies but the ratio t_2/t_1 is fixed, then the magnitudes of the $I_{\mathrm{DLTS}}/I(T)$ peak corresponding to a specific trap level will be independent of temperature.

For the detrapping current component, on the other hand, the I_{DLTS} peak magnitude for different t_1 and fixed t_2/t_1 will increase exponentially with temperature (second term in the prefactor equation 3.45). However the peak value of the product $t_1 \times I_{\mathrm{DLTS}}$ is independent of temperature [214]. The dependence of the I-DLTS peak magnitude on temperature may therefore be used as a feature to distinguish the detrapping and depletion width modulation processes in the nanowires.

Here for the deep level analysis the t_2/t_1 ratio is fixed to 2. The time value t_1 ranges from 50 µsec to 4 msec.

Chapter 4

InAs-based nanowires

4.1 Growth of InAs nanowires

InAs and InAsP nanowire growth and SEM-characterisation were conducted by Dr Marina Panfilova.

InAs nanowires were grown by molecular-beam epitaxy with a solid In source and As_4 and P_2 cracker cells. The as-received Si (111) substrate was annealed at 900 °C for ten minutes in the vacuum chamber to remove an oxide layer. Afterwards it was put in the fume-cupboard for 24 hours to get approximately 2 nm of a fresh natural oxide layer. The oxidised Si was annealed in an As atmosphere at 760 °C for 8 min. Nanowires were then grown on the prepared substrate at a temperature between 465 and 495 °C with As- and In- beam-equivalent pressures of 0.2–1.0$\times 10^{-5}$ and 4.3$\times 10^{-8}$ Torr respectively [95].

Table 4.1 represents the main parameters of the growth runs and resulting nanowires (density, diameter and length). The aim was to grow nanowires with the highest possible density and that they would be long enough to carry out 4-point probe electrical measurements. The aim is achieved by regulating the substrate temperature and the In:As ratio at the same time. The highest density and the longest nanowires were grown at 470–480 °C substrate temperature and In:As ratio 1:232 (sample 103R10). This sample resulted in nanowires with the most uniform density and diameter (relative fluctuations of the diameter are less than 10 %).

Table 4.1: InAs MBE grown samples. Main parameters and nanowire characteristics: Temperature of the substrate during growth, BEP readings from the ion-gauge measurement under the sample. Density, diameter and length derived from SEM investigation.

Sample	Tsub, °C	BEP (In) Torr	BEP (As) Torr	Ratio In:As
103R4	465	4.3×10^{-8}	2.2×10^{-6}	1 : 49
103R5	495	4.3×10^{-8}	8×10^{-6}	1 : 186
103R6	495	4.3×10^{-8}	1.35×10^{-5}	1 : 314
103R7	495	4.3×10^{-8}	8×10^{-6}	1 : 186
103R8	495	4.3×10^{-8}	1.35×10^{-5}	1 : 314
103R10	475	4.3×10^{-8}	1.0×10^{-5}	1 : 232

	time min	Density NW/μm^2	Diameter nm	Length μm
103R4	42			no nanowires
103R5	45	2.8–3.8	34–94	0.53–1.27
103R6	45	6.2–6.8	46–64	1.36–1.63
103R7	90	1.1–2.2	77–91	1.75–2.1
103R10	120	20–43	48–55	3

Figures 4.1.a,b show scanning electron microscope images of self-catalysed MBE-grown InAs nanowires (sample 103R7). (Other samples are similar to the one shown here.) The images show an array of mostly vertically-aligned nanowires with regular hexagonal cross-section with a diameter of 50–70 nm (figure 4.1.b, inset).

In addition to the nanowires, the substrate is covered by faceted clusters of complicated shape. Their dimensions are approximately 1 μm in width and 300 nm in height.

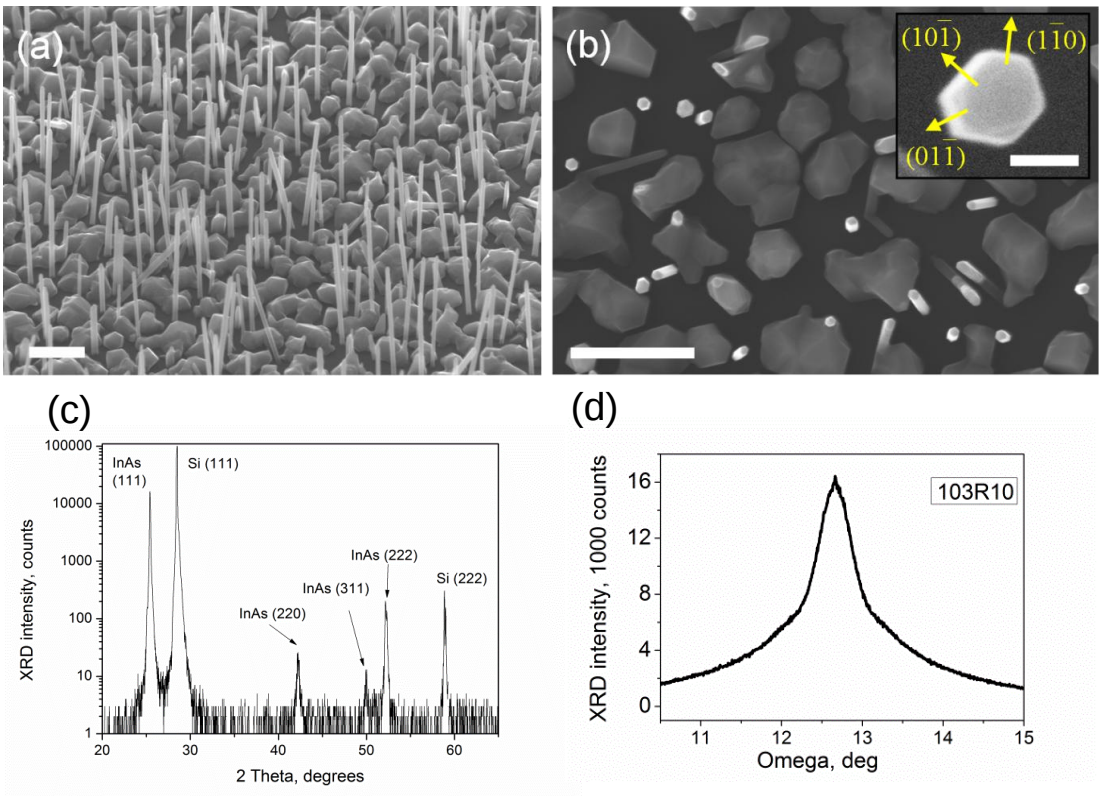

Figure 4.1: Scanning electron micrograph images of the as-grown InAs nanowires. (a) 45° view; b) top view. The scale bars are 1 μm. Inset in (b): top view of the hexagonal nanowire with indexed directions and planes, the scale bar is 50 nm; (c) X-ray diffractogram of the sample 103R10; (d) rocking curve of the sample 103R10.

Figure 4.1.c shows an XRD scan of the as-grown sample 113R10. The most intense peaks are Si(111) substrate and InAs(111) peaks confirming a strong orientation of the grown samples. In addition, the figure shows some low magnitude

cubic zinclbende phase peaks (InAs(220) and InAs(311)), which arise from polycrystalline clusters and mis-oriented nanowires. Figure 4.1.d shows the omega-scan (or "rocking" curve) of the InAs(111) reflection, showing that the full width at half-maximum (FWHM) is approximately 1 degree. FWHM of epitaxial thin films is usually in the order of 0.01–0.1 degree. The broadening of the nanowire rocking curve occurs due to mis-orientation and bending of the wires.

Figure 4.2 shows high resolution transmission electron micrographs of a representative InAs nanowire. Note that no droplet is visible at the top of the nanowire (figure 4.2.a). Although this fact might suggest vapour-solid growth mechanism of InAs nanowires, researchers have given sufficient evidence that these nanowires are grown by the VLS-growth mechanism via naturally occurring In-droplets, which then crystallise under As flux [107; 108]. The top of the wire (figure 4.2.a) shows a high density of stacking faults and phase boundaries perpendicular to the growth direction. The inset shows a fast Fourier transform (FFT) of this micrograph, the straight lines confirming the strong intermix of zincblende and wurtzite structures. The bottom of the nanowire (figure 4.2.b) shows a relatively long (about 60 nm) region with a much lower density of phase boundaries. The inset at the bottom right (figure 4.2.d) shows the FFT of this area with spots corresponding to the pure hexagonal phase. The combination of two segments, one with a lower density of phase boundaries and the other much larger one with a higher density of stacking faults is seen in many nanowires. The zincblende segment with a lower density of phase boundaries appears only at the bottom of the nanowire and is 50 to 70 nm long. The explanation for this is given in [109]: in the first moments of the growth and at low level of catalyst droplet supersaturation, wurtzite phase nucleation is favoured over zincblende phase.

Figure 4.2.c shows an HRTEM picture of a cluster. No wurtzite phase is visible in the cluster, although some twin- and grain-boundaries are present. In addition, the FFT (figure 4.2.c, inset) corresponds to a zincblende lattice. Many clusters are found to be polycrystalline.

Although both cubic zincblende and hexagonal wurtzite phases are present in the nanowires, from hereon we will use the cubic structure notations. *I.e.* the (111) and (220) zincblende lattice spacings, corresponding to the (0002) and $(11\bar{2}0)$ wurtzite lattice spacings respectively.

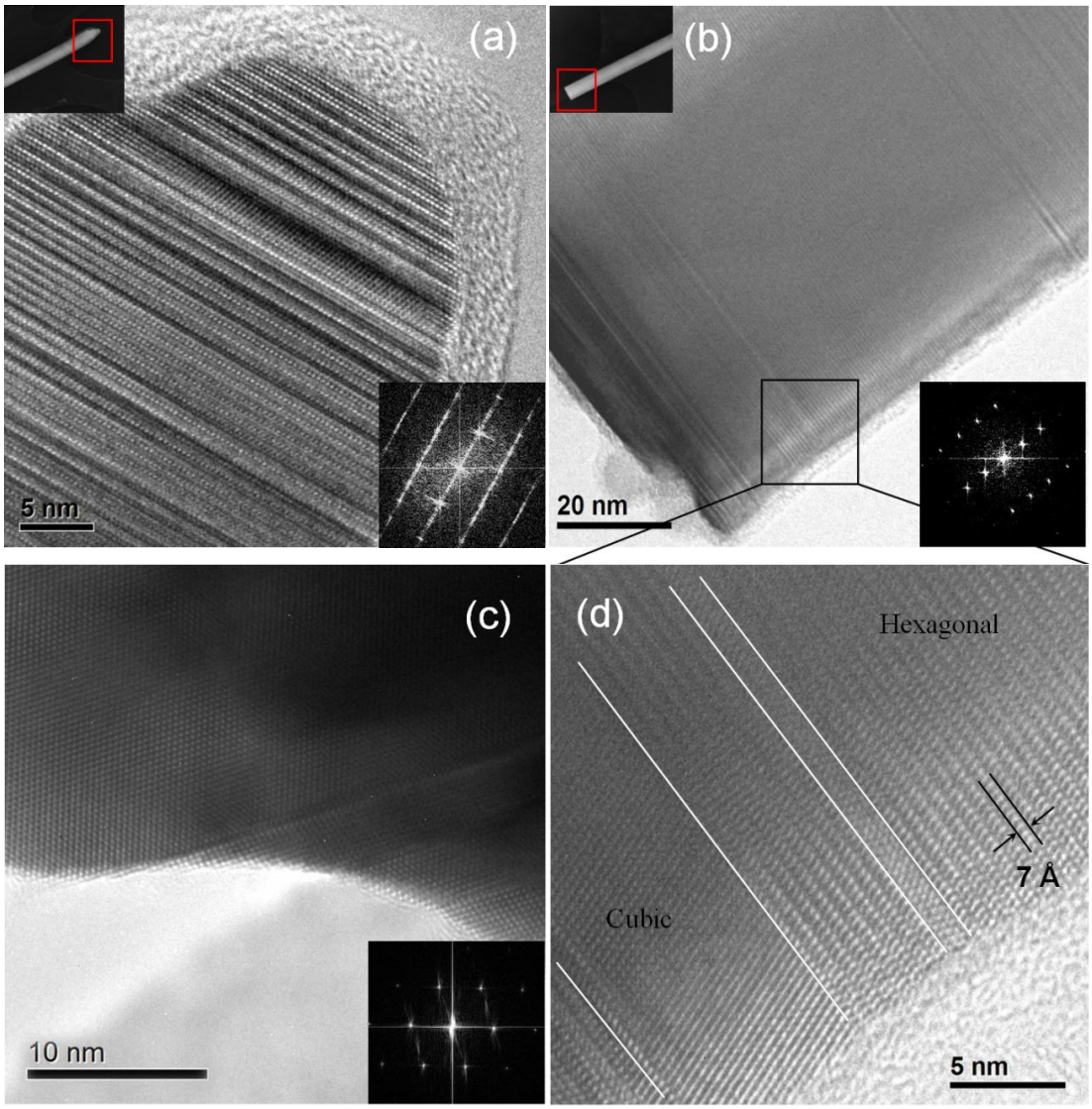

Figure 4.2: Transmission electron micrographs of a typical InAs nanowire and cluster: (a) top of the nanowire, (b) bottom of the nanowire (pure InAs) and (c) cluster. Insets at the top left corner of the nanowire images: low resolution micrographs. Insets at the bottom right corners of (a – c) images: Fast Fourier Transform (FFT) of the pictures. (d) high resolution picture of a selected part of relatively phase pure area as shown by the box in (b). The white lines denote phase boundaries.

In summary, self-catalysed growth of InAs nanowires on Si(111) substrate was achieved and optimised. InAs nanowires have diameters of approximately 50 nm and length of 3 μm. They grow in mixed wurtzite-zincblende microstructure. Phosphorus incorporation in these nanowires is studied in the next section.

4.2 InAsP nanowires

4.2.1 InAsP nanowire growth

In order to be able to fabricate InAs-based heterostructures, control of the band gap is required. The presence of phosphorus in InAs nanowires increases their band gap. Study of phosphorus incorporation is presented in the following section.

To grow $InAs_{1-x}P_x$ nanowires, In and As sources were open for 10 minutes resulting in the growth of phosphorus-free nucleation nanorods of length 150 nm (the recipe used was identical to that of sample 103R10). Phosphorus was subsequently introduced into the chamber and the nanowires were grown for a further 2 hours. To control the phosphorus content, x, the beam-equivalent pressure of phosphorus was varied from 5×10^{-7} to 4.3×10^{-6} Torr. This is equivalent to 18 to 65 per cent of the combined (As and P) group-V material flux $J_{\mathrm{norm}}(\mathrm{P}) = J_{\mathrm{P}}/(J_{\mathrm{P}} + J_{\mathrm{As}})$, where J_{P} and J_{As} are the fluxes of phosphorus and arsenic respectively calculated from the beam equivalent pressures using equation 3.13.

Figures 4.3.a–e show scanning electron microscope images of self-catalysed MBE-grown $InAs_{1-x}P_x$ nanowires with different $J_{\mathrm{norm}}(\mathrm{P})$. The images show a growth geometry similar to that of pure InAs nanowires. Figure 4.3.f shows the dependence of the density and the length of the nanowires on the phosphorus flux. The length of the wires is approximately 2–4 μm for all the samples. The density of the nanowires decreases from around 30 to 5 wires per μm^2 after introducing phosphorus into the growth chamber. The thickness of the wires is between 40 nm and 70 nm.

Figure 4.4 shows HRTEM of InAsP nanowires and clusters. The comparison between the images of InAsP and InAs nanowires (figure 4.2) does not reveal any visible difference in the crystallographic composition of nanostructures: nano-

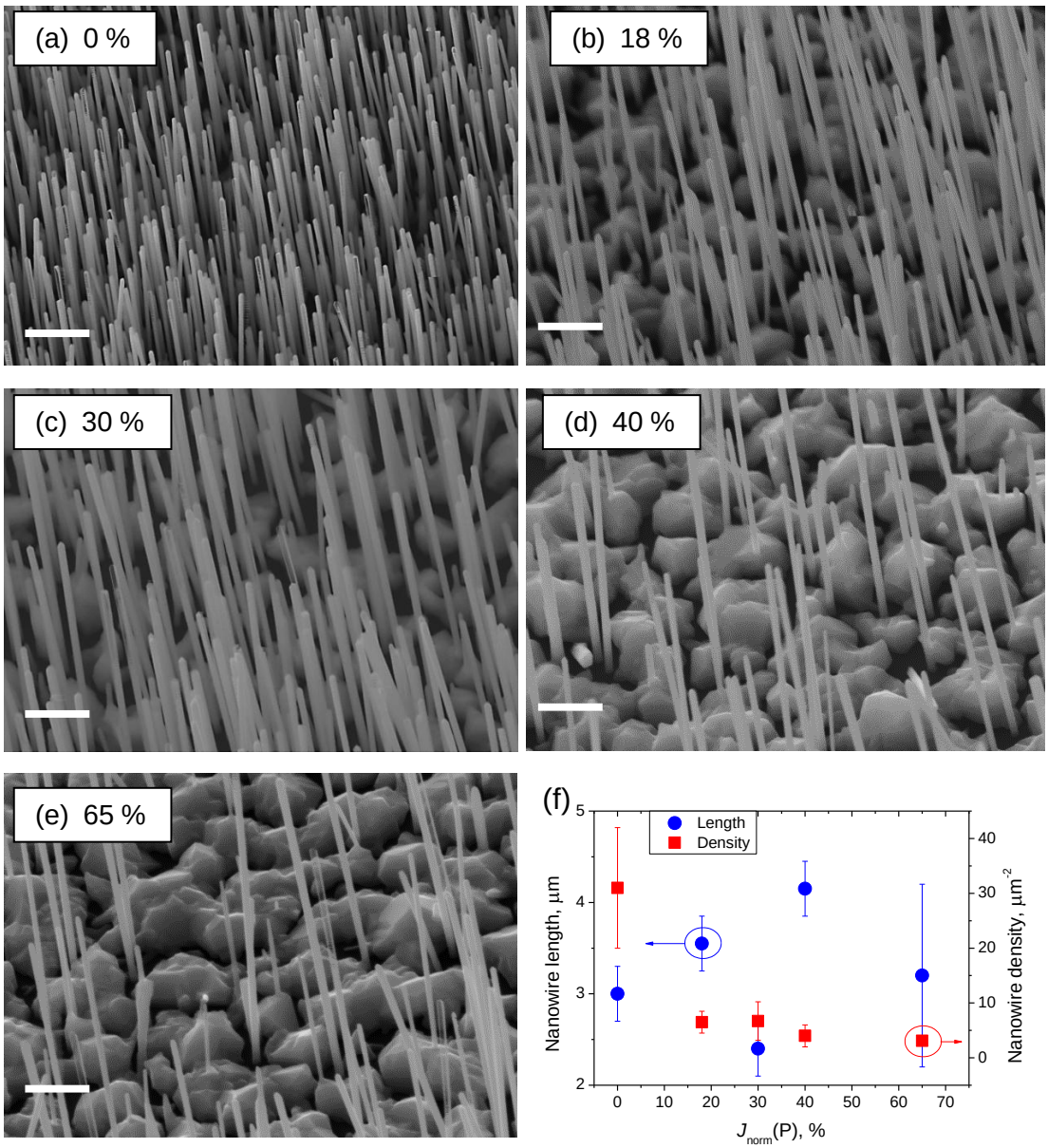

Figure 4.3: (a)–(e): Scanning electron micrograph images of the as-grown $InAs_{1-x}P_x$ nanowires with different normalised phosphorus flux, $J_{norm}(P)$, 45° view, the scale bars are 0.5 µm. (f) dependence of density and length of nanowires on normalised phosphorus flux, $J_{norm}(P)$.

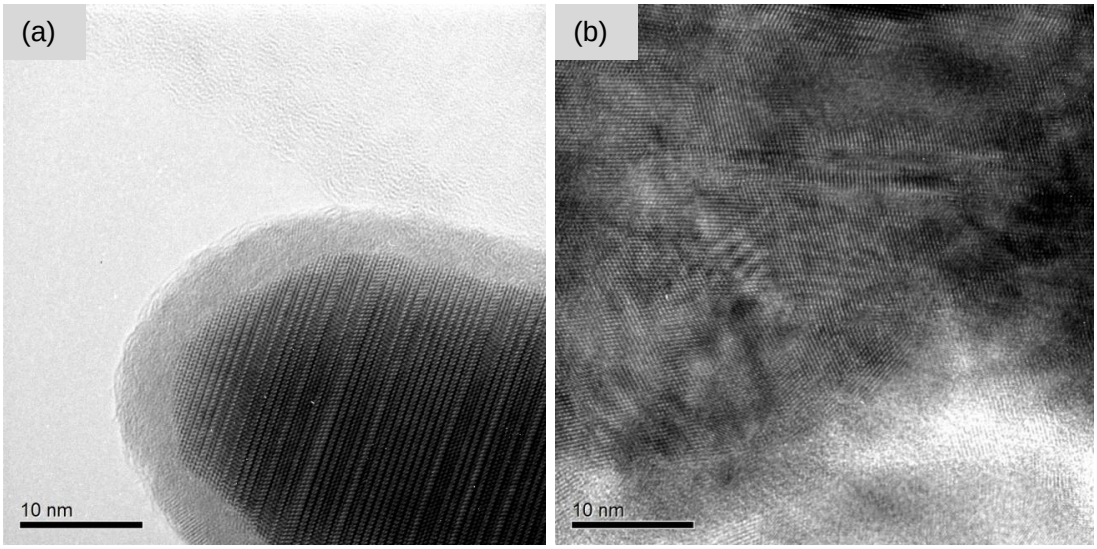

Figure 4.4: HRTEM images of (a) nanowire and (b) cluster of a $InAs_{1-x}P_x$ sample with $J_{\mathrm{norm}}(\mathrm{P}) = 30$ %.

wires consist of a wurtzite and zincblende mixture, and clusters are zincblende polycrystalline.

The relative composition of wurtzite and zincblende crystal polytypes can be counted from the HRTEM images of the nanowires. After thoroughly studying at least three nanowires from every sample, the following figures are extracted (table 4.2).

Table 4.2: InAsP samples. Relative wurtzite composition (hexagonality) extracted from HRTEM images.

$J_{\mathrm{norm}}(\mathrm{P})$, %	Relative wurtzite composition, %
0	67
30	76
40	65
65	68

4.2.2 Phosphorus incorporation

4.2.2.1 EDX on nanowires

For further analysis isolated nanowires grown under different normalised phosphorus fluxes were transferred onto a copper supported carbon film. EDX spectra measured on these samples are shown in figure 4.5. The C and Cu peaks appear because of the TEM-grid. The highest peaks are In and As, which are almost unchanged from sample to sample. The inset shows the behaviour of the P peak in more detail. The nanowires incorporate phosphorus and the phosphorus content increases with the P-flux. However the low phosphorus signal and the absence of pure InP nanowire samples for calibration hinders the possibility of quantitative analysis of the spectra.

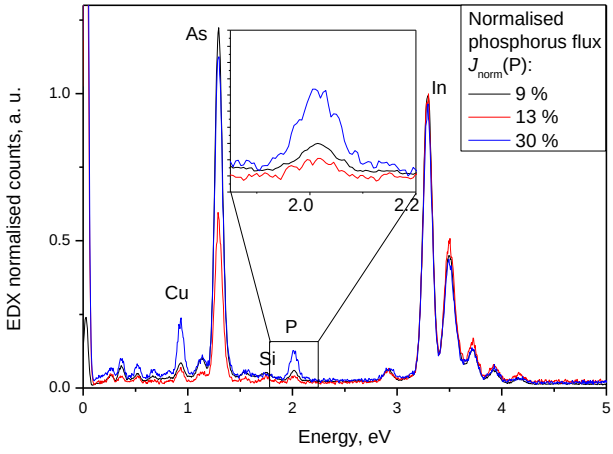

Figure 4.5: EDX-spectra of different samples. Signal from isolated $InAs_{1-x}P_x$ nanowires on a copper-supported carbon grid in the TEM chamber. Spectra were normalised to the In peak. Inset shows an enlarged view around the phosphorus peak.

4.2.2.2 XRD on as-grown samples

In order to make the analysis more quantitative X-ray diffraction was used. Nanowires grow along the $InAs_{1-x}P_x(111)$ direction, are highly parallel to the (111) direction of the Si-substrate, and are distributed on the substrate with a relatively

high density. This provides a good geometry for high accuracy XRD. The total uncertainty comprises of the instrument error, sample misalignments, detector and goniometer resolution and non-verticality of the nanowires. This allows the measurement of the change in lattice constant with an error of less than 0.01 Å. High resolution transmission electron microscopy could not reach this level of accuracy. The smallest possible error of the lattice parameter measurement achieved from FFT analysis of high magnification TEM images is 0.1 Å.

The lattice constants of bulk InAs and InP are 6.06 Å and 5.87 Å respectively. The increase of phosphorus flux should lead to a decrease in the lattice constant by an amount corresponding to the fraction of phosphorus incorporated in the sample. Phosphorus may be incorporated inhomogeneously into the nanowires due to various strain effects. However, the density of stacking faults and the diameter of the nanowires are similar for all the samples, so any nonuniformity of P incorporation would result only in a broadening of the XRD peaks. The calculated average lattice constant can therefore be used as a measure of the phosphorus content x. This is estimated using Vegard's Law (equation 3.14) $x = \left(a_{\mathrm{InAs}} - a_{\mathrm{InAs}_{1-x}\mathrm{P}_x}\right) / \left(a_{\mathrm{InAs}} - a_{\mathrm{InP}}\right)$, where a is a lattice constant of a nanostructure.

4.2.2.3 Discussion: Clusters and nanowires

The clusters present on the substrate of the as-grown samples are of a different crystal structure from the nanowires (see figures 4.2.c, 4.4.b) and may have different lattice constants; this restricts the extent to which XRD measurements of the as-grown samples can be considered to be quantitative. In order to distinguish the detected X-ray signal diffracted from the nanowires from that diffracted from the clusters, the following procedure was carried out. First, XRD measurements were taken on the as-grown sample (figure 4.6.a). Then, the nanowires were mechanically exfoliated from the as-grown sample using adhesive tape. After this procedure all the nanowires were found to be removed from the sample, leaving the clusters intact (this was confirmed by SEM – figures 4.6.b,d). This procedure was carried out with the sample attached to the XRD-stage without dismounting, in order for the X-ray beam to hit the exact same place in the following experi-

ment. Next, XRD measurements were carried out on the very same spot on the clusters-only sample with the same instrument settings (figure 4.6.b), allowing a direct comparison between the as-grown sample and clusters-only sample. Fine alignment of the XRD on the Si(111)-peak showed no tilt of the sample after exfoliation. The diffractograms with the most intense reflection at $2\theta \approx 25°$ are shown in figures 4.6.a,c. Finally, XRD measurements were carried out on the adhesive tape with nanowires only (figures 4.6.e,f). In order to differentiate between the tape XRD-peaks and nanowires XRD-peaks the comparison between the reference tape only sample with the nanowires on tape sample was carried out. The tape has many peaks, some of them overlapping with the InAsP(111) peak at $2\theta \approx 25°$. The only InAsP peak that was not present on the tape was InAsP(220) peak at $2\theta \approx 42°$. The comparison of the InAsP(220) peak for samples with different $J_{\mathrm{norm}}(\mathrm{P})$ is shown in the figure 4.6.e. Due to random orientation of the nanowires the intensity of the nanowires-only sample XRD peak is much lower and the full width at half maximum is 1.5 times higher than those of as-grown samples. This will affect the accuracy of lattice parameter determination.

The comparison of the $\mathrm{InAs}_{1-x}\mathrm{P}_x(111)$ reflection between clusters-only and as-grown samples for $J_{\mathrm{norm}}(\mathrm{P}) = 5$ % is given in figure 4.7. It shows that after the nanowire exfoliation the (111) reflection intensity of the clusters-only sample is reduced. This happens because the clusters are not perfectly oriented along the Si(111) direction; some fraction of the clusters are polycrystalline (figures 4.2.c and 4.4.b). Therefore the clusters contribute only marginally to the measurement carried out on the as-grown samples. Therefore it can be assumed that the values extracted from the as-grown samples correspond solely to the lattice parameters of the nanowires. Another important result is that the 2θ values for the (111)-reflections of as-grown and clusters-only samples do not coincide. For the sample shown, the 2θ angle for the as-grown sample equals 25.37°, whereas for the clusters-only sample it is 25.42°. This suggests that the clusters and nanowires have different lattice constants. Similar discrepancies between clusters and nanowires were obtained for all the samples.

X-ray diffractograms of the as-grown, clusters-only and nanowires-only samples grown with various $J_{\mathrm{norm}}(\mathrm{P})$ are presented in figure 4.6. The increased phosphorus flux shifts the diffracted angle of the (111) reflection to higher values in

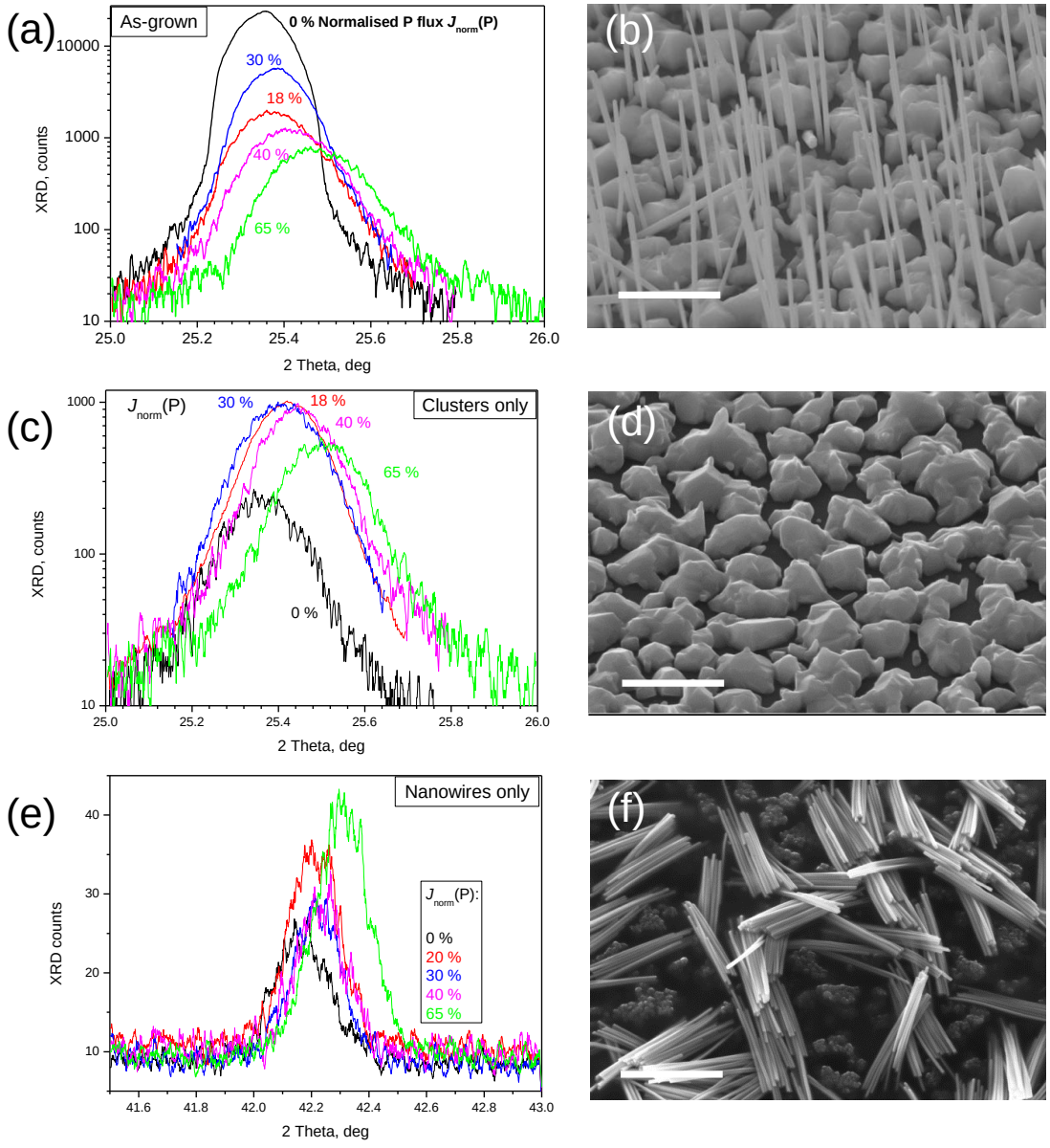

Figure 4.6: X-ray diffractograms of as-grown (a), clusters-only (c) and exfoliated nanowires on the adhesive tape (e) samples grown with different $J_{\mathrm{norm}}(\mathrm{P})$ and the corresponding SEM images. In a) and c) the $InAs_{1-x}P_x(111)$ reflection is shown; in e) the $InAs_{1-x}P_x(220)$ reflection is shown. The scale bars in SEM images are 1 μm.

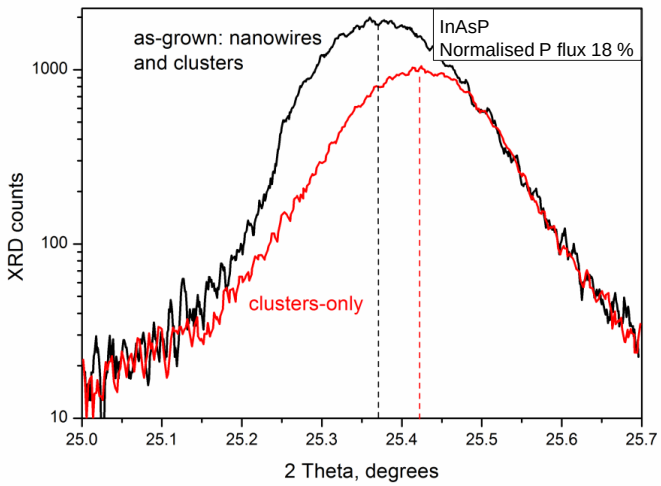

Figure 4.7: XRD data on a sample with $J_{\mathrm{norm}}(\mathrm{P}) = 18\%$ before and after nanowire exfoliation taken on the same region of a sample with the same instrument settings: black curve – as-grown nanowires + clusters, red curve – clusters-only.

all the samples. This indicates the phosphorus incorporation into nanowires and confirms the qualitative results of the EDX experiment.

The lattice spacing between (111) planes is calculated using Bragg's law (equation 3.21). In order to compare results from as-grown, clusters-only and nanowires-only samples the (111) and (220) plane spacings were recalculated into the cubic (100) lattice constant and plotted in figure 4.8.

Figure 4.8 shows that lattice constants of all the samples decrease with increasing normalised phorsphorus flux. The lattice constants of the as-grown samples are always larger than those of clusters by approximately 0.008±0.002 Å. This change in lattice constants between clusters and nanowires (clusters-only and as-grown samples respectively) is already seen for the sample with no phosphorus incorporation ($J_{\mathrm{norm}}(\mathrm{P}) = 0$ %). One of the reasons for this lattice change is the difference in crystal structures between nanowires and clusters (see figures 4.2.a–c and 4.4). The work by Kriegner *etal* [110] confirms this hypothesis by showing that wurtzite and zincblende lattice constants of the same material (InP, InAs or InSb) cannot be obtained by simple geometric recalculation. According to their

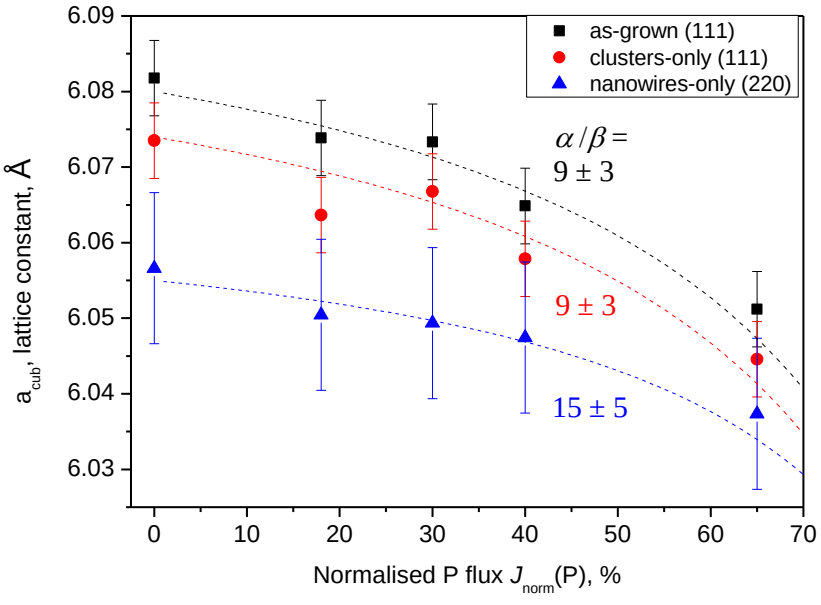

Figure 4.8: Dependence of the cubic lattice parameter of InAsP nanowires and clusters on normalised phosphorus flux. Black squares: inferred from the (111) reflection of the as-grown samples; red circles: inferred from the (111) reflection of the clusters after the nanowires had been exfoliated; blue triangles: inferred from the (220) reflection of exfoliated nanowires. Black, red and blue dotted lines are the theoretical fits according to equation 3.17 with different α/β ratios for different samples.

work, the unit cell parameters are dependent on the fraction of wurtzite phase in the crystal; the lattice expands in the (111) direction and shrinks in the (220) direction with increase of wurtzite content. Indeed, the lattice constant calculated for nanowire-only samples from the (220) reflection (figure 4.8, blue triangles) is smaller than that of the zincblende clusters.

Another argument in the favour of this hypothesis is that the change in lattice constant between clusters and nanowires is approximately the same for the samples with different $J_{\mathrm{norm}}(\mathrm{P})$. At the same time, the wurtzite content in nanowires (obtained from examination of many HRTEM images) is approximately the same for all the samples (table 4.2). Taking all these arguments into account, it can be speculated that the main reason for the difference between lattice constants of clusters and nanowires in different directions is different crystal structure, the phosphorus incorporation being similar for the clusters and nanowires.

4.2.2.4 Phosphorus content in clusters and nanowires

In order to estimate the phosphorus content in the nanowires we exploit Vegard's law (equation 3.14). However the clusters are in the zincblende phase and the nanowires are of mixed phase with different lattice parameters. Hence the values of a_{InAs} and a_{InP} will be different for clusters and nanowires. However according to Kriegner *et al.*[110; 111], the difference $a_{\mathrm{InAs}} - a_{\mathrm{InP}}$ used in Vegard's law is similar for both wurtzite and zincblende structures and equals 0.191 ± 0.002 Å(this error is smaller than the instrument error). Therefore we assume that the value $a_{\mathrm{InAs}} - a_{\mathrm{InP}}$ will be independent of the degree of hexagonality of the nanowires. We therefore can apply Vegard's law independently for the clusters and for the nanowires using the same value $a_{\mathrm{InAs}} - a_{\mathrm{InP}}$. The extracted lattice parameters are shown in table 4.3. P composition in the nanowires x is lower than the P composition in the vapour during the growth $J_{\mathrm{norm}}(\mathrm{P})$.

The P-content in nanowires x is calculated using equation 3.21. The best fit of equation 3.17 to the experimental results on as-grown, clusters-only and nanowires-only samples is plotted in figure 4.8. The ratio α/β (the ratio of As incorporation rate coefficient to P incorporation rate coefficient) is equal to 10 ± 5 for different samples. This result is of the same order of magnitude as

Table 4.3: Dependence of P-content in nanowires and clusters on the normalised phosphorus flux in the MBE-chamber during the growth..

Normalised P flux, J_{norm}(P), %	P-content as-grown samples %	P-content clusters %	P-content exfoliated nanowires %
0	0-3	0-3	0-3
18	4±3	5±3	3±3
30	4±3	4±3	4±3
40	9±3	8±3	5±3
65	16±3	15±3	10±3

reported before: see [128] and references therein, although the mentioned works used complex compounds based on P and As (PH_3, AsH_3, TBAs, TBP) whereas in this work the sources used are As_4 and P_2.

For illustrative purposes the data from the table 4.3 were re-plotted to show the P-content in the nanowires as a function of the P-content in the vapour phase (figure 4.9). The black line represents equation 3.16 with parameter α/β equal to 10.

Based on our findings and linearly interpolating between the band gap of both InAs and InP, we can estimate the difference in band gaps between the InAs and InAs/$InAs_{1-x}P_x$ sections in possible future InAs/$InAs_{1-x}P_x$ heterostructure nanowires. For our highest achieved phosphorus content of $x = 13$ % this band gap difference is approximately 130 meV. If the Fermi level in the InAs section of the nanowire lies lower than the conduction band bottom, heterostructure could in principle be operated at room temperature.

4.2.2.5 Photoluminescence on InAsP nanowires

Photoluminescence measurement at 4K were carried out on InAsP nanowire samples by Dr Peter Carrington (formerly at the University of Lancaster). InAs PL spectra consist of several peaks (figure 4.10.a) – at 0.37 eV, 0.41 eV and 0.43 eV. The 0.41 eV peak coincides with the value of bulk InAs at 4 K, which might be attributed to the clusters. The other two peaks are higher in intensity and might result from the unpassivated surface of the wire and from the wurtzite-zincblende intermixing [215]. The peak at 0.37 eV is in good agreement with the emission

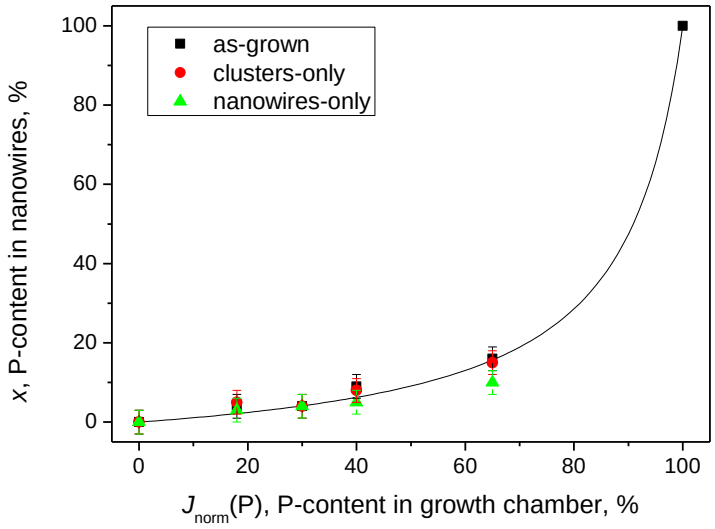

Figure 4.9: Dependence of x on normalised phosphorus flux, $J_{\mathrm{norm}}(\mathrm{P})$, for types of samples. Point (100, 100) is the theoretical value for InP nanowire. Black solid line is a theoretical curve represented by equation 3.16 with $\alpha/\beta = 10$.

peak reported in InAs nanowires by Möller *et al.* [216] where it is attributed to quantum well related recombination in the type-II band alignment between the wurtzite and zincblende sections.

PL measurements on $InAs_{1-x}P_x$ are shown in figure 4.10.c. Phosphorus introduction shifts the most intense peak to higher energies. The phosphorus flux dependence is shown in figure 4.10.b. The change in the peak energy after introducing 40 % and 65 % of phosphorus in the growth chamber is 50 meV and 115 meV, respectively. These values are in close proximity to the values derived from XRD measurements on the $InAs_{1-x}P_x$ nanowires (blue circles in figure 4.10.b).

4.2.3 Conclusion

In summary, InAs and $InAs_{1-x}P_x$ nanowires were successfully grown self-catalytically on Si (111) substrate by solid source MBE. Nanowires grow vertically together with clusters on the Si. Nanowires are 2–5 μm long and 50–100 nm thick. HRTEM was used to investigate the defect structure of the grown nanowires. The nano-

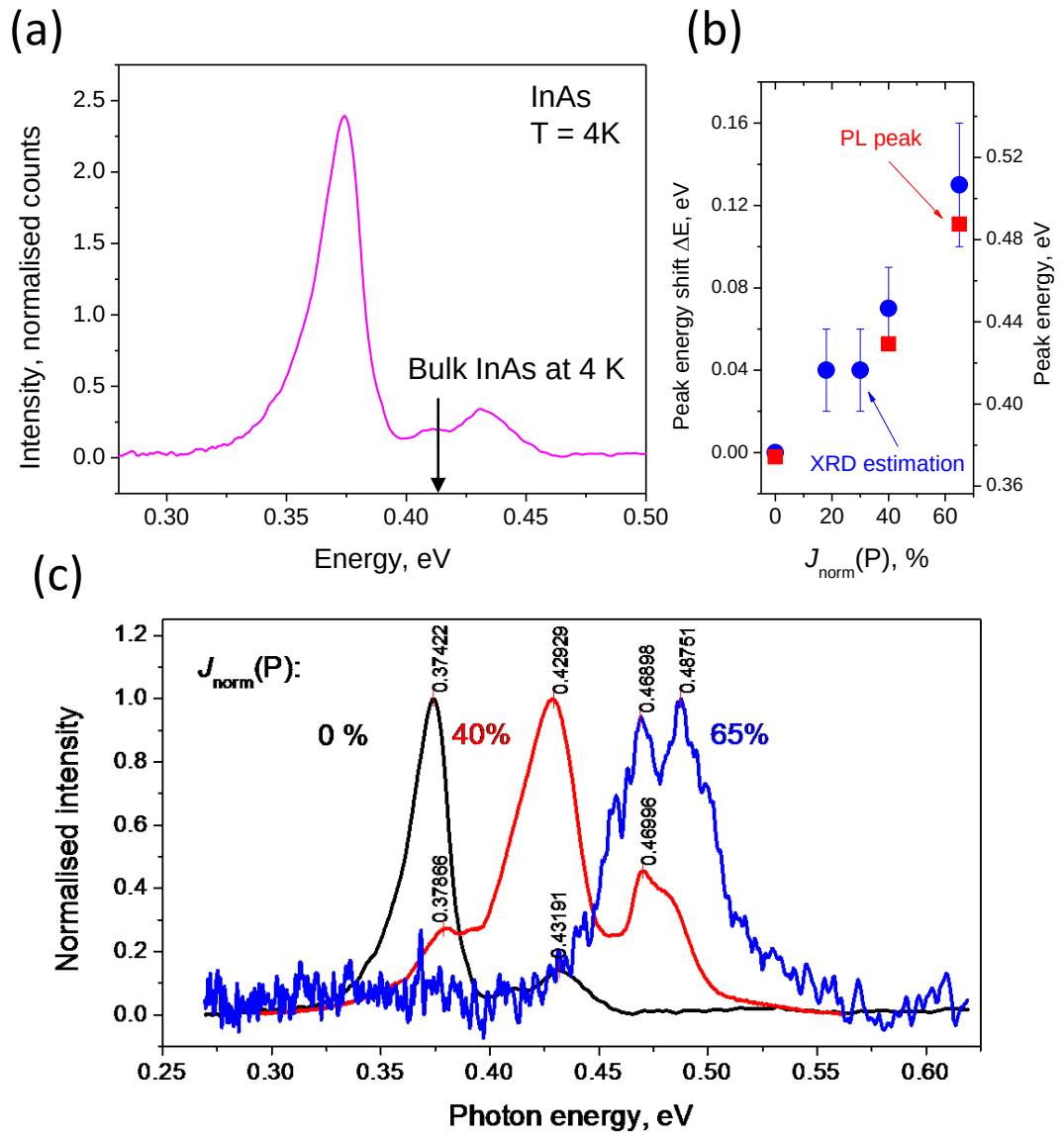

Figure 4.10: PL on InAsP nanowire samples at 4 K. (a) PL spectrum on InAs nanowire showing bulk InAs peak at this temperature; (b) red squares – normalised phosphorus flux dependence of the highest PL peak energy position, blue dots – normalised phosphorus flux dependence of the band gap energy shift based on the estimation of phosphorus content from XRD; (c) PL spectra on $InAs_{1-x}P_x$ with $J_{\mathrm{norm}}(\mathrm{P})$ =0 %, 40 %, 65 %.

wires appear to be of mixed wurtzite and zincblende structure with high density of planar defects (twin-boundaries and polytype boundaries). Clusters are polycrystalline zincblende.

XRD was used to measure the phosphorus content x in $InAs_{1-x}P_x$ nanowires. This reaches 0.10±0.03 for the sample grown with largest phosphorus fraction flux. The incorporation rate of As was found to be 10 times higher than that of P. Low temperature photoluminescence was used to measure possible band gap shift due to phosphorus incorporation in $InAs_{1-x}P_x$ nanowires. The band gap shifts towards higher energies by approximately 110 meV for nanowires with highest phosphorus content. As far as we know this is the first report of MBE self-catalysed growth of InAsP nanowires.

4.3 InAsSb nanowires

InAs can be doped by antimony in order to reduce the energy gap and to increase the carrier mobility. Moreover, InSb nanowires are known to crystallise in the zincblende phase, as opposed to the predominantly wurtzite phase in the case of InAs nanowires [102].

A study of $InAs_{1-x}Sb_x$ nanowires with varying x is shown in this section. Most of the analysis was performed by my colleague Dr Marion Sourribes and reported in [189]. I carried out TEM and PL analysis for this work.

4.3.1 Nanowire growth

The nanowires were grown and characterised by using the same method as was used for InAsP growth (page 102). Nanowires were grown by Dr Marina Panfilova and Prof Huiyun Liu. The Sb normalised flux $J_{\mathrm{norm}}(\mathrm{Sb}) = J(\mathrm{Sb})/(J(\mathrm{Sb})+J(\mathrm{As}))$ was varied from 0 to 1.5 %. Figure 4.11.a shows an SEM image of the resulting nanowires. The diameter of the wires varies from 60 to 200 nm and the length from 1.3 to 4.5 μm.

The antimony content was extracted from XRD measurements of the c-axis lattice parameter using Vegard's law (equation 3.14, measured by Dr Marina Panfilova). The dependence of the Sb content in as-grown samples on the Sb

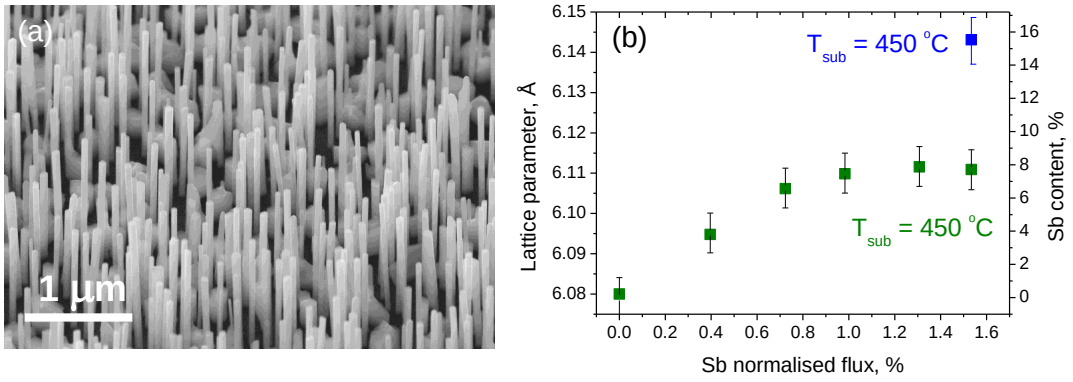

Figure 4.11: InAsSb nanowire growth. (a) SEM image of the InAsSb nanowire sample with 15 % Sb content; (b) dependence of the lattice parameter and of the inferred Sb content in as-grown samples on the Sb content in the vapour phase (or Sb normalised flux $J_{\mathrm{norm}}(\mathrm{Sb})$). Measurement and analysis performed by Dr Marina Panfilova.

normalised flux is shown in figure 4.11.b. It was possible to achieve a maximum Sb content of 15 %, with further increase in Sb normalised flux resulting in continuous film formation with no wire growth.

As was shown in figure 4.2 on page 101, InAs nanowires consist mainly of the wurtzite phase with a high density of stacking faults, twin boundaries and phase boundaries. The transmission electron microscopy of InAsSb nanowires (figure 4.12.a,b) reveals that InAsSb nanowires consist mostly of zincblende segments with stacking faults and twin boundaries. Letters "G", "I" and "T" in the image indicate grain boundaries, stacking faults and twin boundaries respectively. Figure 4.12.c shows the Sb content dependence of the fraction of the cubic zincblende phase in the nanowire (or "cubicity", as opposed to "hexagonality", the fraction of hexagonal phase in the nanowire) and the Sb content dependence of the stacking fault density. From these figures it is clear that introduction of Sb dramatically increases the cubicity and decreases the stacking fault density.

4.3.2 Photoluminescence

The photoluminescence measurements at 4 K have been carried out on InAsSb nanowire samples by Dr Peter Carrington. Figure 4.13.a shows the PL spectra

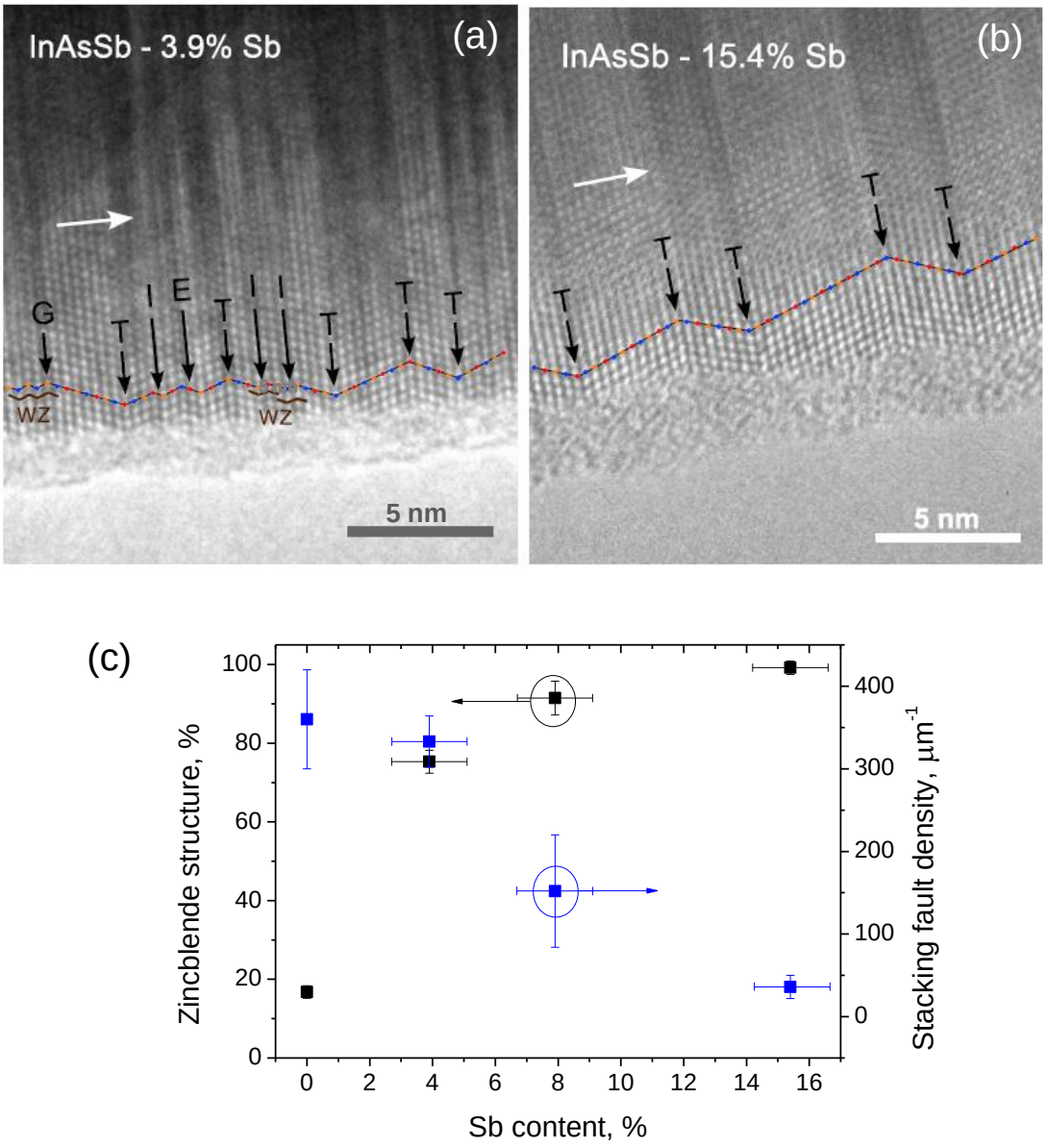

Figure 4.12: (a,b) HRTEM images of the $InAs_{1-x}Sb_x$ nanowires with $x = 3.9$ % and $x = 15.4$ % respectively; (c) Sb content dependence of the fraction of zincblende structure (or cubicity) and the stacking fault density. Defect analysis was performed by Dr Marion Sourribes.

of the as-grown InAsSb samples. The sharp drop at 0.29 eV is due to CO_2 absorption. The $InAs_{1-x}Sb_x$ sample spectra do not have any additional higher energy peaks unlike the InAs sample. This may be due to the absence of the wurtzite phase in $InAs_{1-x}Sb_x$ samples (TEM in figure 4.12.a,b).

The PL peak moves to lower energies when adding Sb into the InAs nanowires, as is expected from the smaller band gap of InSb material [217]. The band gap width of a ternary $InAs_{1-x}Sb_x$ material can be written as:

$$E_{g,\mathrm{InAsSb}} = xE_{g,\mathrm{InSb}} + (1-x)E_{g,\mathrm{InAs}} - Cx(1-x), \tag{4.1}$$

where x is the Sb content and C the bowing parameter. InAsSb nanowires have only one peak corresponding to the predominantly zincblende structure (figure 4.12.c). As was shown in the previous section (page 114), the PL spectra of the as-grown InAs sample consist of several peaks corresponding to the zincblende cluster luminescence, wurtzite-zincblende quantum well luminescence and others. Therefore, it is difficult to analyse the Sb-content dependence of the PL data considering only the highest PL peak positions. Assuming that the 0.41 eV peak in the InAs sample spectrum corresponds to the zincblende phase luminescence, and regarding the $InAs_{1-x}Sb_x$ samples with $x = 8$ % and 15 % as being entirely zincblende, we have plotted the Sb content x dependence of the zincblende $InAs_{1-x}Sb_x$ PL peak position (figure 4.13.b). The dashed red curve shows the least squares fit to the experimental data of the equation 4.1 with $C = 0.65$ eV. InAs and InSb band gap energies at 4 K were taken to be 0.4170 eV and 0.2350 eV, respectively [217]. The value of the bowing parameter coincides with the reported values [218; 219]. The large error in the fit may be related to the uncertainty due to the zincblende and wurtzite phases.

4.3.3 Electrical measurement

Electrical measurements were performed by Dr Marion Sourribes. In order to study the electrical properties of $InAs_{1-x}Sb_x$ nanowires, field effect transistors were fabricated (procedure as described in section 3.5.1, figure 4.14.a). The carrier concentration and carrier mobility were inferred from room temperature FET measurements using equation 3.39 (the sample transfer characteristic is shown

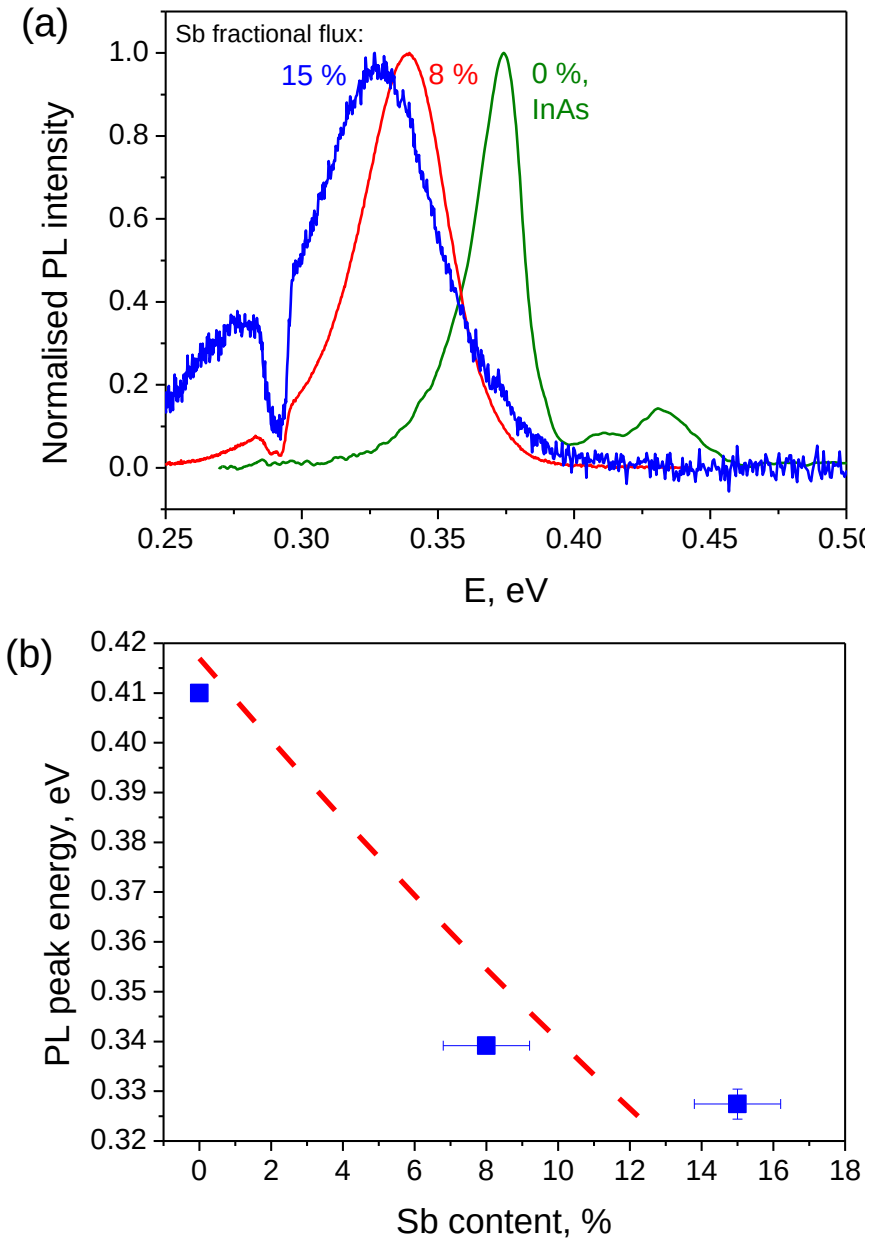

Figure 4.13: Photoluminescence of the InAsSb nanowire samples at 4 K. (a) PL spectra of the as-grown samples; (b) Sb content dependence of the cubic InAsSb peak, dashed red line shows the best fit to the equation 4.1 with a bowing parameter $C = 0.65$.

in figure 4.14.b). Mobility and carrier concentration were correlated with the Sb content, cubicity and stacking fault density. The carrier concentration did not show any systematic dependence on Sb-content or defect density. However, the carrier mobility shows a drastic improvement after Sb incorporation.

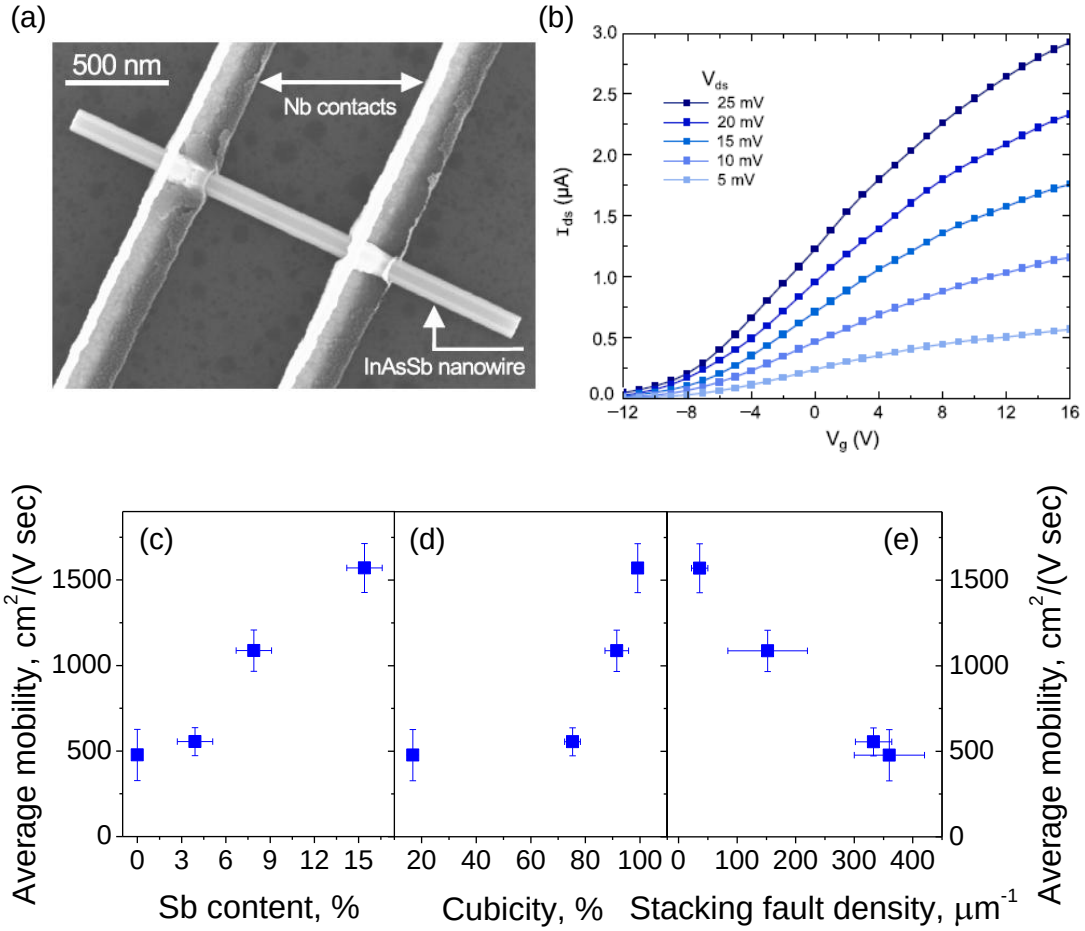

Figure 4.14: InAsSb nanowire electrical measurements. (a) SEM image of an InAsSb nanowire FET, (b) sample nanowire field effect transfer curve with different drain source voltages; the Sb-content dependence (c), cubicity dependence (d) and stacking fault density (e) dependence of the average carrier mobility in InAsSb nanowires. Courtesy of Dr Marion Sourribes.

Figures 4.14.c-e show the Sb-content dependence of the carrier mobility and concentration. The graphs show that mobility increases with increasing Sb content and cubicity, and with decreasing stacking fault density.

It may be noted that, in general, InSb material has a higher mobility than InAs. Thus Sb incorporation into InAs may increase the nanowire mobility due to the intrinsic properties of the crystalline material. However, the mobilities of bulk InAs and InSb (40,000 $cm^2/(V{\cdot}s)$ and 77,000 $cm^2/(V{\cdot}s)$ respectively [220]) are two orders of magnitude higher than those measured here (up to 1,500 $cm^2/(V{\cdot}s)$), thus making it unlikely for the Sb-dependent intrinsic properties of the materials to affect the mobility.

Figure 4.14.b shows that when cubicity increases from 20 to 60 %, mobility does not change. Therefore, cubicity cannot be the reason for mobility enhancement. Figure 4.14.c shows an almost linear dependence of the mobility on the stacking fault density. Taking into account all the outlined reasoning, we can state that the change in mobility is dominated by the stacking fault density.

4.3.4 Conclusion

In summary, $InAs_{1-x}Sb_x$ nanowires were successfully grown self-catalytically on Si (111) substrate by solid source MBE. Samples were studied by SEM, TEM, XRD, PL and electrical measurements. Up to 15 % of Sb was incorporated into the nanowires. PL measurements showed that the band gap variation of $InAs_{1-x}Sb_x$ ternary nanowires has a bowing parameter of 0.65.

Sb-incorporation affects the crystal phase of nanowires, making them cubic zincblende with a lower stacking fault density. Electrical measurements showed that the reduction of stacking faults in nanowires due to Sb incorporation increases the carrier mobility. This leads to the possibility of fully controlling polytypism and electrical transport properties in self-catalysed InAs-based nanowires.

Chapter 5

ZnO-based nanowires. Growth

This chapter describes experimental results on the catalyst assisted molecular beam epitaxy growth of ZnO nanowires. The first section gives details on the gold catalyst formation. The next section describes optimisation of ZnO nanowire growth on different substrates. In the later sections incorporation of Mg into ZnO nanowires is investigated and core-shell heterostructure nanowires are grown and studied.

5.1 Gold catalyst preparation

Three different procedures were utilised to prepare gold nanodots: gold colloids with diameter 50 nm have been deposited on the substrate, gold thin film was annealed to form gold particles, and electron beam lithography was utilised. Details on the these processes are outlined in this section.

5.1.1 Gold film on silicon annealing

In order to prepare gold catalysts a gold layer of thickness 2 to 3 nm was thermally evaporated on a silicon substrate. The substrate was transferred into an MBE chamber and annealed in vacuum at temperatures between 500 and 900 °C. This procedure made gold atoms migrate over the surface and form gold particles with sizes that depend on annealing temperature. The results of the annealing are presented in figure 5.1. The dependence of the mean radius of the Au particles

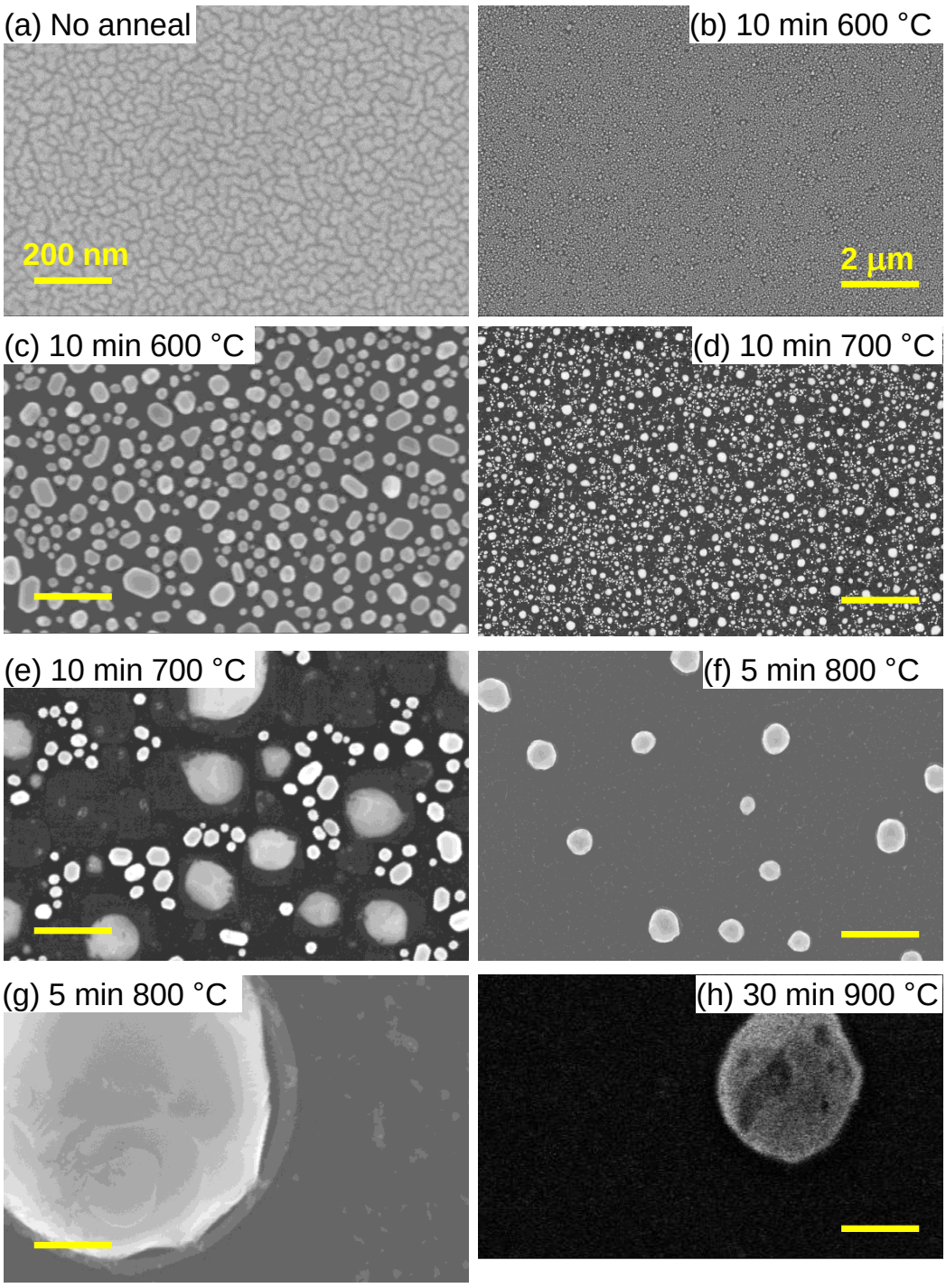

Figure 5.1: Gold on silicon. SEM images of the gold thin film annealed at different temperatures. Scale bar in the left column is 200 nm, in the right column 2 µm.

on the annealing temperature is presented in figure 5.2. The images indicate that the particles' radii grow approximately exponentially with temperature. At temperatures 700 °C and higher gold-silicon eutectics start forming (darker shaded grey particles in figure 5.1.e). It will be shown in the following sections, that the gold-silicon eutectics inhibit the nucleation of ZnO nanowires.

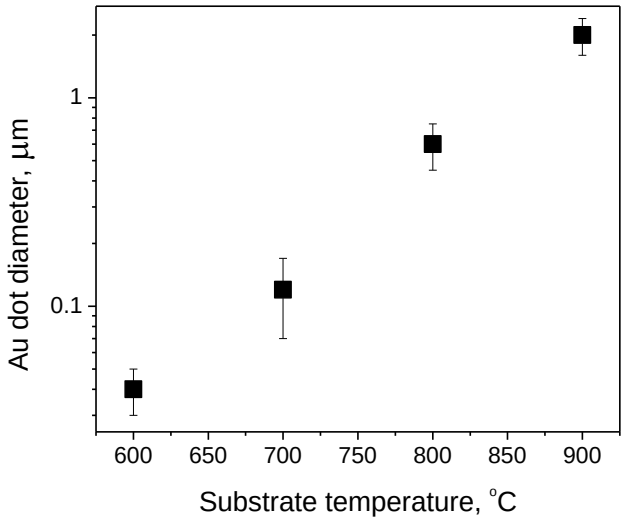

Figure 5.2: Gold on silicon. Dependence of average gold particle diameter on the annealing temperature.

5.1.2 Gold film on sapphire annealing

The same procedure was utilised to prepare gold nanoparticles on sapphire. The effect of annealing was different from that observed on gold films on silicon (figure 5.3). Gold doesn't form a eutectic with sapphire at temperatures used in this work and large gold particles are formed not as easily as those on silicon. 800 °C annealing of a 1 nm thick film for 5 minutes or for 40 minutes results in similar average sizes of particles of 14 nm. The effect of gold film thickness is depicted in figure 5.3.b. After 800 °C annealing, a gold film of 2.6 nm thickness results in an average particle size of 40 nm, which is approximately 3 times larger than the result for a 1 nm thick gold film. Films of thickness ranging from 2.6 to 3 nm were used for nanowire growth.

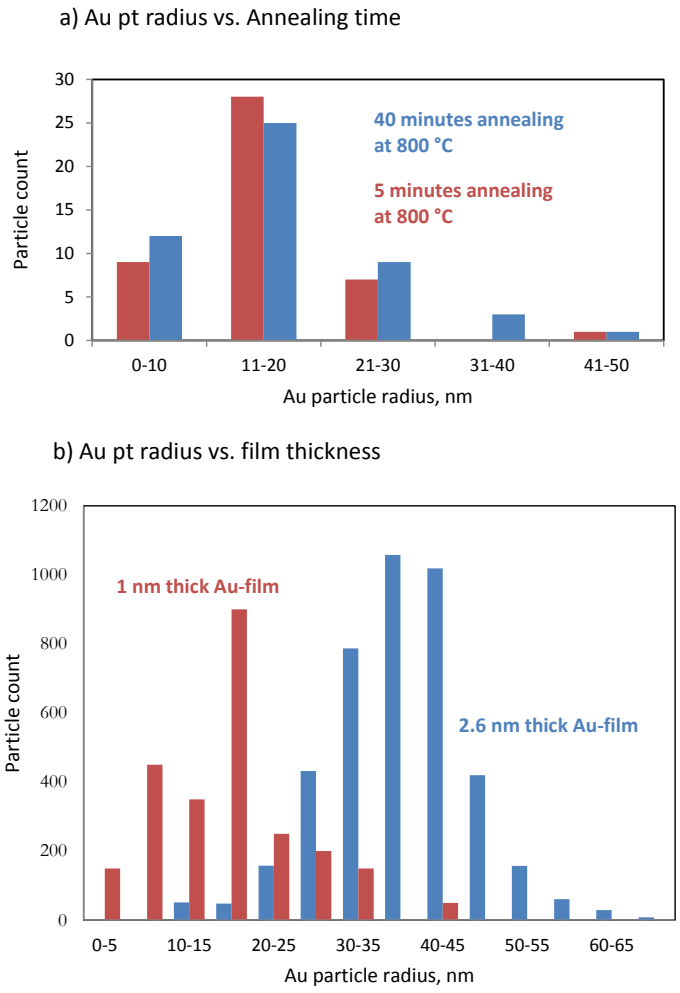

Figure 5.3: Gold on sapphire. Dependence of average gold particle radius (a) on the annealing time for 1 nm thick gold film and (b) on the gold film thickness for samples annealed at 800 °C.

5.2 ZnO nanowires grown on Si

The choice of a substrate for vacuum crystal growth should be regarded carefully due to the interaction between atoms and surface where they first move and then attach to form a crystal. Si was taken as the first substrate to study the ZnO growth, because it is cheap, very flat and high quality material with low level of defects. Whereas Si may form deep electronic levels in ZnO, it was used successfully as a ZnO growth substrate by various groups. [83; 221]

5.2.1 One-step growth

ZnO was grown on a Si substrate with an approximately 2–4 nm thick native oxide (measured by optical ellipsometry). Gold nanoparticles were deposited onto the substrate as described in the previous section. The temperature of the growth was varied from 350 to 900 °C. The oxygen flux was fixed at 2 sccm which led to a beam equivalent pressure of $(2\pm0.2)\times10^{-5}$ Torr. Temperature of the Zn cell was varied from 370 to 430 °C, which resulted in a beam equivalent pressure ranging from 7×10^{-8} to 2×10^{-6} Torr. The time of growth was fixed at 45 minutes. Scanning electron micrographs of the grown samples are presented in figures 5.4 and 5.5.

Figure 5.4 shows representative ZnO structures grown by MBE on Si substrates at temperatures from 450 to 900 °C with fixed BEP(Zn) = $2\text{–}3\times10^{-7}$ Torr. Here the gold nanoparticles are distributed on the substrate with comparatively low density (less than 5 μm^{-2}); both colloidal gold and EBL patterned gold are used. At temperatures under 600 °C (figure 5.4.a–c) ZnO grows both on the gold and the silicon, forming a grainy polycrystalline film. At temperatures of 600 °C (figure 5.4.d) no ZnO grows on Si, whereas elongated ZnO clusters grow on the gold sites. No gold dots are observed on top of the clusters. At 700 °C (figure 5.4.e) some tapered nanowires with gold droplets on top appear. At 750 °C (figure 5.4.f) more nanowires grow on gold sites with various lengths ranging from 0.2 to 1.5 μm. At temperatures higher than 800 °C (figure 5.4.h) native silicon oxide starts to evaporate bringing gold into direct contact with silicon. This results in the formation of a Si-Au eutectic alloy before the start of the ZnO growth. No ZnO growth is observed at temperatures over 800 °C. By

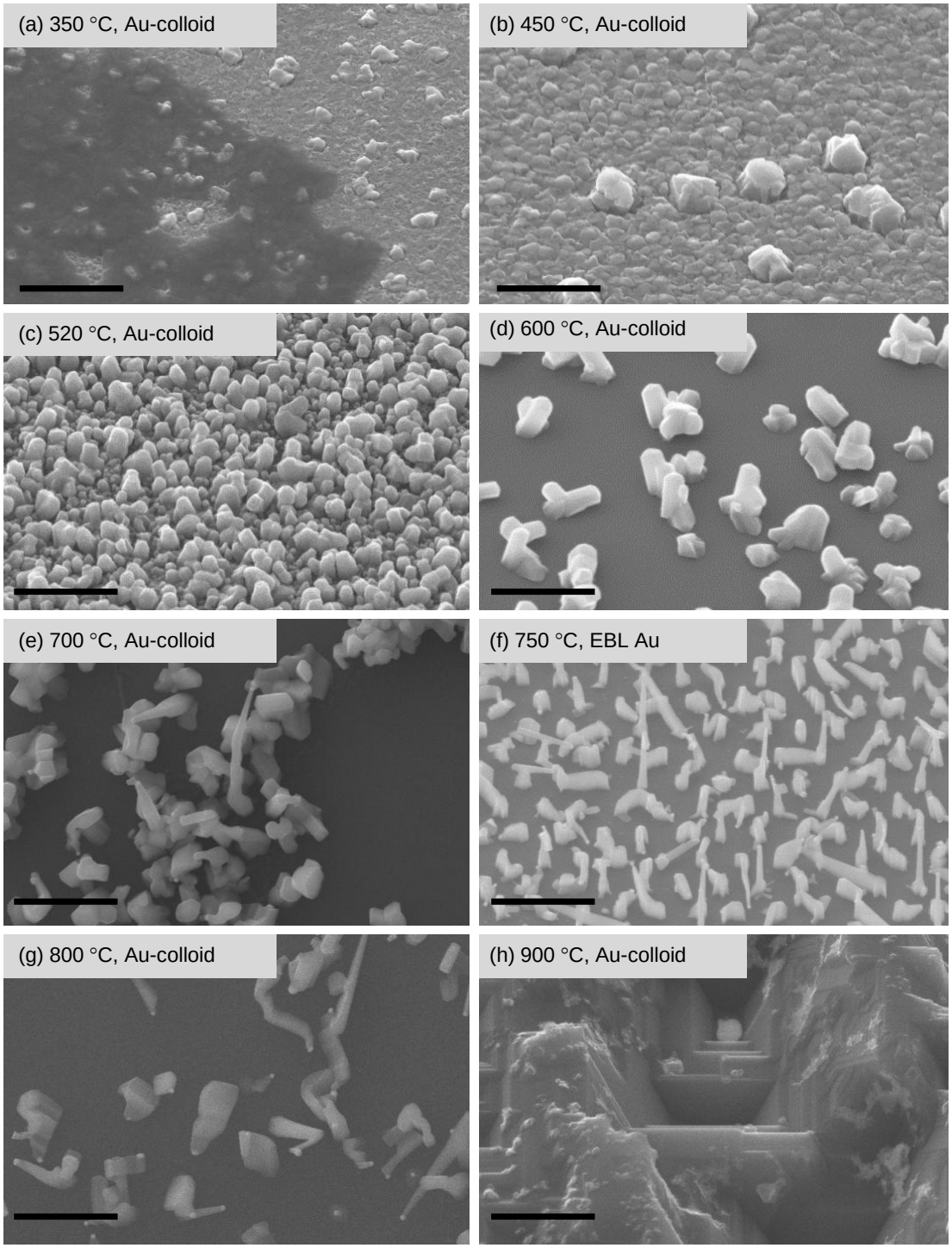

Figure 5.4: ZnO samples grown on Si substrate with low density of Au particles at different temperatures. Scale bars are 1 μm. The growth temperatures and type of catalysts are indicated.

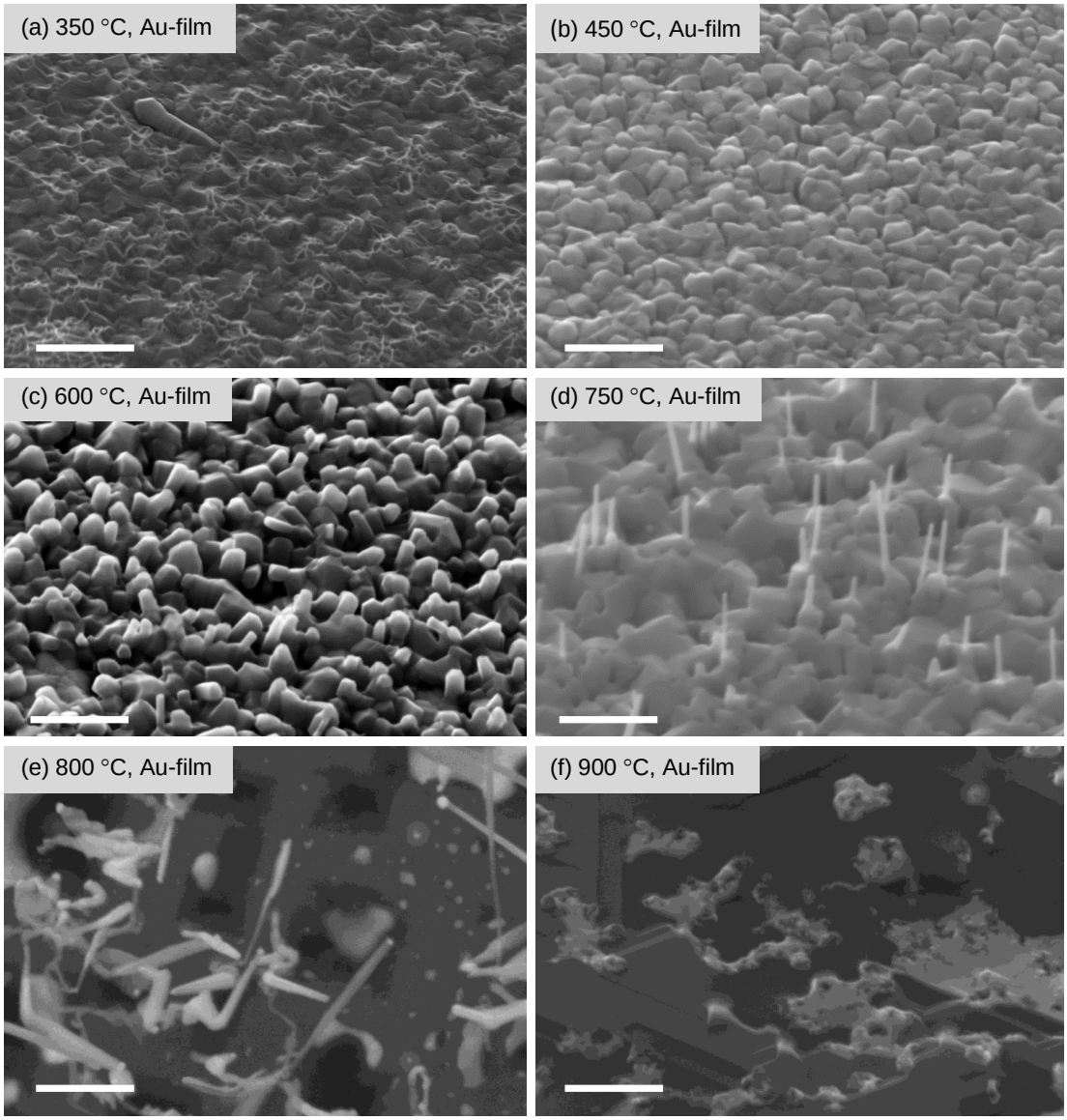

Figure 5.5: ZnO samples grown on Si with thin Au film at different temperatures. Scale bars are 0.5 μm. The growrh temperatures are indicated.

repeating these experiments with different Zn fluxes the nanowire growth window is established: the nanowires grow at temperatures from 700 to 800 °C and at Zn beam-equivalent pressures from 1×10^{-7} to 5×10^{-7} Torr (figure 5.4.f).

For ZnO growth on the thin Au-film, control over the gold particle size is needed. It was established that if sample temperature is raised fast enough (50 degrees per minute) and growth is initiated immediately after reaching the growth temperature, gold particles do not agglomerate into bigger particles than those in figure 5.1.c.

Figures 5.5 shows the images of the samples grown on Si with annealed thin Au film at different temperatures with fixed $\mathrm{BEP_{Zn}} = 2\text{–}3\times10^{-7}$ Torr. The samples grown at temperatures 350–450 °C (figures 5.5.a,b) result in similar films as samples with colloidal gold (figures 5.4 a,b). At temperatures of 600 °C and higher (figures 5.5.c–e) some of the crystallites become more elongated in one direction. Because of the small separation between gold dots, the ZnO crystallites that grow in the horizontal direction merge and form ZnO film. The growth at temperature of 750 °C and zinc pressure 3×10^{-7} Torr (figure 5.5.d) result in the film with thin vertical nanowires with density of 3–4 μm^{-2}, length up to 500 nm and diameter 30–50 nm. At higher temperatures the nanowires become longer (800 °C, figure 5.5.e). At the same time the Si oxide starts to evaporate leading to direct contact between Si and gold. At these temperatures Si-Au eutectics rapidly start forming, which changes the physical parameters of the catalyst droplet and hinders ZnO growth. At the temperatures higher than 800 °C (figure 5.5.f) no ZnO growth is observed, with silicon seeming to be etched by gold.

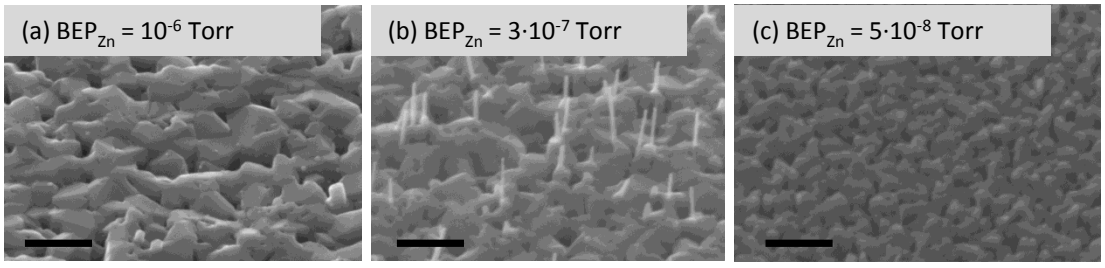

Figure 5.6: ZnO samples grown on Si with thin Au film with different Zn beam equivalent pressures at fixed temperature 750 °C. Scale bars are 0.5 μm.

Figure 5.6 shows the images of the samples grown on Si with Au film with

different BEPs of Zn at fixed temperature 750 °C. Only at $BEP_{Zn} = 3{\times}10^{-7}$ Torr is the growth of ZnO nanowires observed.

All the SEM observations are compiled into the visual growth map in figure 5.7. Growth of the best ZnO nanowires (the longest, the straightest and with the highest density) is observed at growth temperature of approximately 750 °C with BEP_{Zn} between 2 and $4{\times}10^{-7}$ Torr.

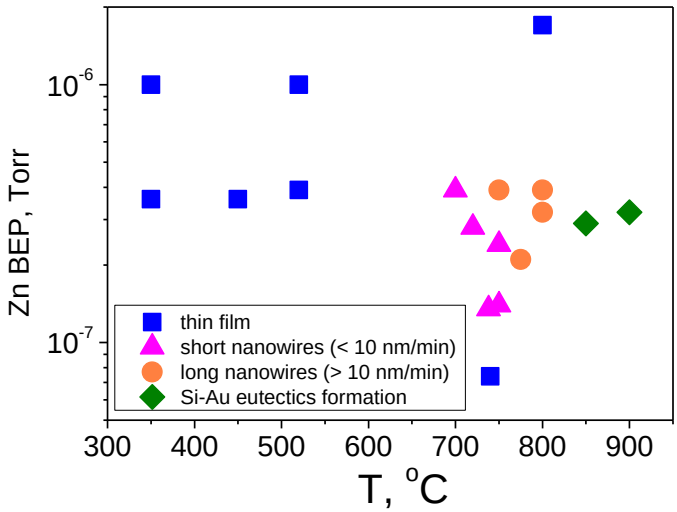

Figure 5.7: Phase map of ZnO Au-catalysed growth on silicon.

5.2.2 One-step growth. Discussion

In order to better understand the MBE growth features of ZnO on silicon with a gold catalyst, careful analysis of the SEM images in figures 5.4, 5.5 and 5.6 was carried out. Three important characteristics for the growth at these Zn pressures and temperatures were inferred: the rate of growth of ZnO film on the silicon without gold R_{Si}; the yield of the nanowires (*i.e.* the fraction of gold nanodots that would result in nanowire growth) Y_n; and the variable opposite to the degree of tapering of the nanowires – we call this function "parallelity" and it is described by the formula $P_n = d_{top}/d_{base}$, where d_{base} and d_{top} are the diameters of the nanowire at the base and the top respectively. This function is

equal to 1 when the nanowire walls are parallel. The dependences of these three parameters R_{Si} (blue squares), Y_n (red circles) and P_n (black triangles) on growth temperature are presented in figure 5.8.

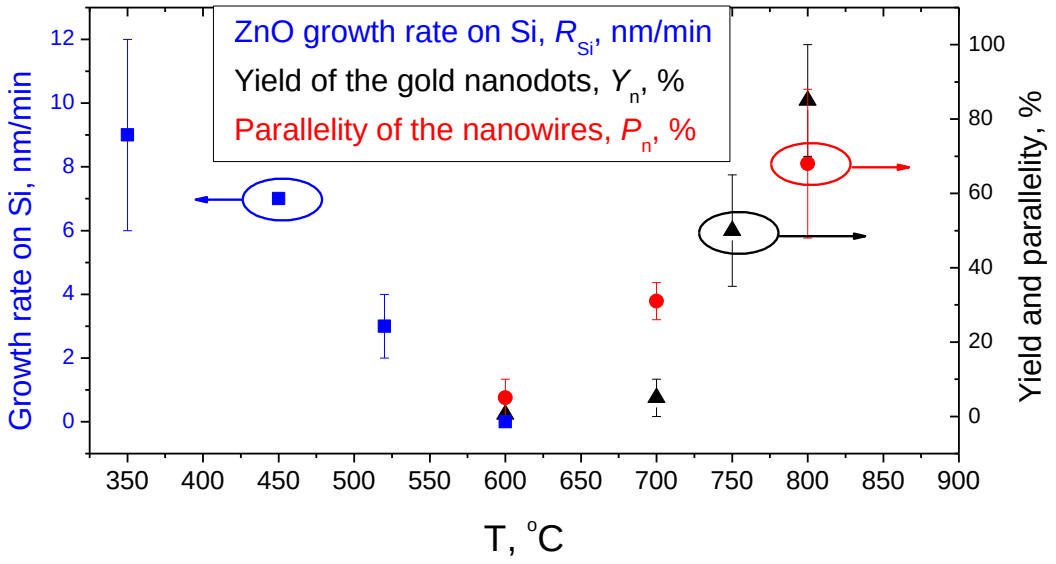

Figure 5.8: Characteristic variables for nanowire growth on silicon substrate and their dependence on temperature.

The growth rate of ZnO on silicon without gold catalyst decreases with increasing temperature (figure 5.8, blue squares). Fitting the curve of growth rate to the equation 3.5 we get the difference between desorption and adsorption activation energies $E_{\mathrm{d}} - E_{\mathrm{a}}$ which is approximately 1 eV, and the ratio of desorption and adsorption frequency factors which is approximately 10^6. At low temperatures (below 450 °C) RHEED images of the growth are similar at any angle and thus show that ZnO grows on Si textured in the (0001) direction (figure 5.9.a). At higher temperatures ZnO grows as a random polycrystalline film with no texture (figure 5.9.b).

The tapering of the wires indicates the presence of growth on both the Au-ZnO interface and the ZnO nanowire sidewalls. The tapering is a result of competing processes: diffusion and adsorption and desorption of Zn/O atoms to and from the sidewalls. The parallelity increases with temperature (figure 5.8, red squares)

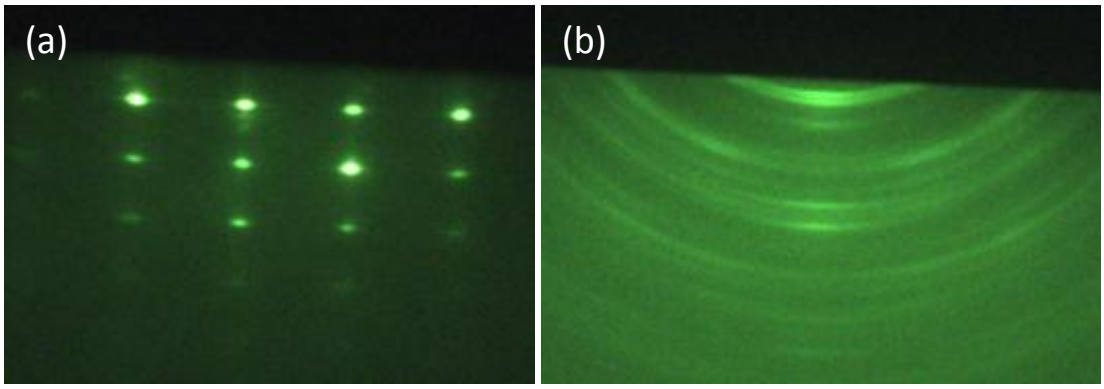

Figure 5.9: Growth of ZnO film on silicon. (a) RHEED image of the film grown at 350 °C; (b) RHEED image of the film grown at 450 °C.

indicating an increase of the desorption or/and decrease in adsorption. Although precise quantitative analysis on tapering of nanowires is not possible due to a very wide scatter of nanowire diameters and lengths, very rough estimates of the axial and radial growth rates can be made. Assuming the average length of the nanowires and clusters l to be 1 micron and the average diameter of the gold catalyst d_{Au} to be 50 nm, ratio of the growth rates in radial and in axial directions R_{radial} and R_{axial} is equal to $R_{\mathrm{radial}}/R_{\mathrm{axial}} = d_{\mathrm{Au}}(1/P_n - 1)/2l$. At temperatures 600 °C, 700 °C and 800 °C the ratio $R_{\mathrm{radial}}/R_{\mathrm{axial}}$ is equal to 0.5, 0.1 and 0.01, respectively. Taking length of the wires 1 micron, growth time 45 minutes, the radial ZnO growth rate at 600 °C is approximately 10 nm per minute. The yield of the nanowires increases with temperature (figure 5.8, black squares).

The best nanowires for electronic applications would be nanowires longer than 1 μm in order to allow multiple contacts prepared by electron beam lithography, not tapered (in order to produce perfect one-dimensional heterostructures), and the highest possible yield of gold nanodots – these features represent the growth "quality" of the nanowires. In figure 5.8 when extrapolated to higher temperatures, both yield and parallelity (red circles and black triangles) would approach unity at temperatures higher than 850 °C. However the formation of the Au-Si alloy prevents growth at temperatures higher than 800 °C. In order to overcome this obstacle a two-step procedure was devised and implemented, which is described in the next section.

5.2.3 Two-step growth

In order to improve the nanowire growth "quality", the first minutes of ZnO growth on Si with Au films were investigated. As it is shown in figure 5.10, after 5 and 10 minutes at 750 °C ZnO seeds are formed between the gold droplets and the silicon substrate, and ZnO crystals with different orientation start forming. After 20 minutes the ZnO crystals which are not perpendicular to the substrate coalesce and form a polycrystalline film.

In order to reduce gold-silicon eutectic formation, a protective layer between the gold and the silicon is required, this can be achieved by a relatively long growth time at low temperature. On the other hand, in order to increase the growth yield it is required to leave the largest possible gold droplet density on the surface of the ZnO film. It was determined that 10-minute low-temperature growth is the best compromise.

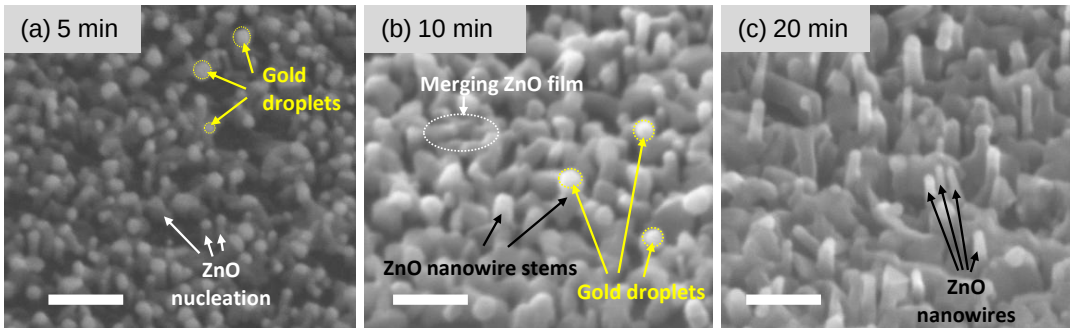

Figure 5.10: Initial stages of the growth. SEM images after (a) 5 minutes, (b) 10 minutes, (c) 20 minutes of growth. Scale bars are 200 nm.

After the first 10 minute step at 750 °C, the temperature was lifted up to 840 °C and the growth of nanowires was carried out for another 45 minutes at the same Zn and O vapour conditions. Results are presented in figures 5.11. The length of the nanowires ranges from 300 nm to 1.5 μm. The diameter ranges from 20 to 150 nm. The density of the nanowires is more than 100 per μm^2. The density of the 1 μm long nanowires is about 1 per μm^2. The nanowire walls are much more parallel than for growth runs at lower temperatures. In other words, nanowires grown by two-step technique are much more suitable for future electronic applications.

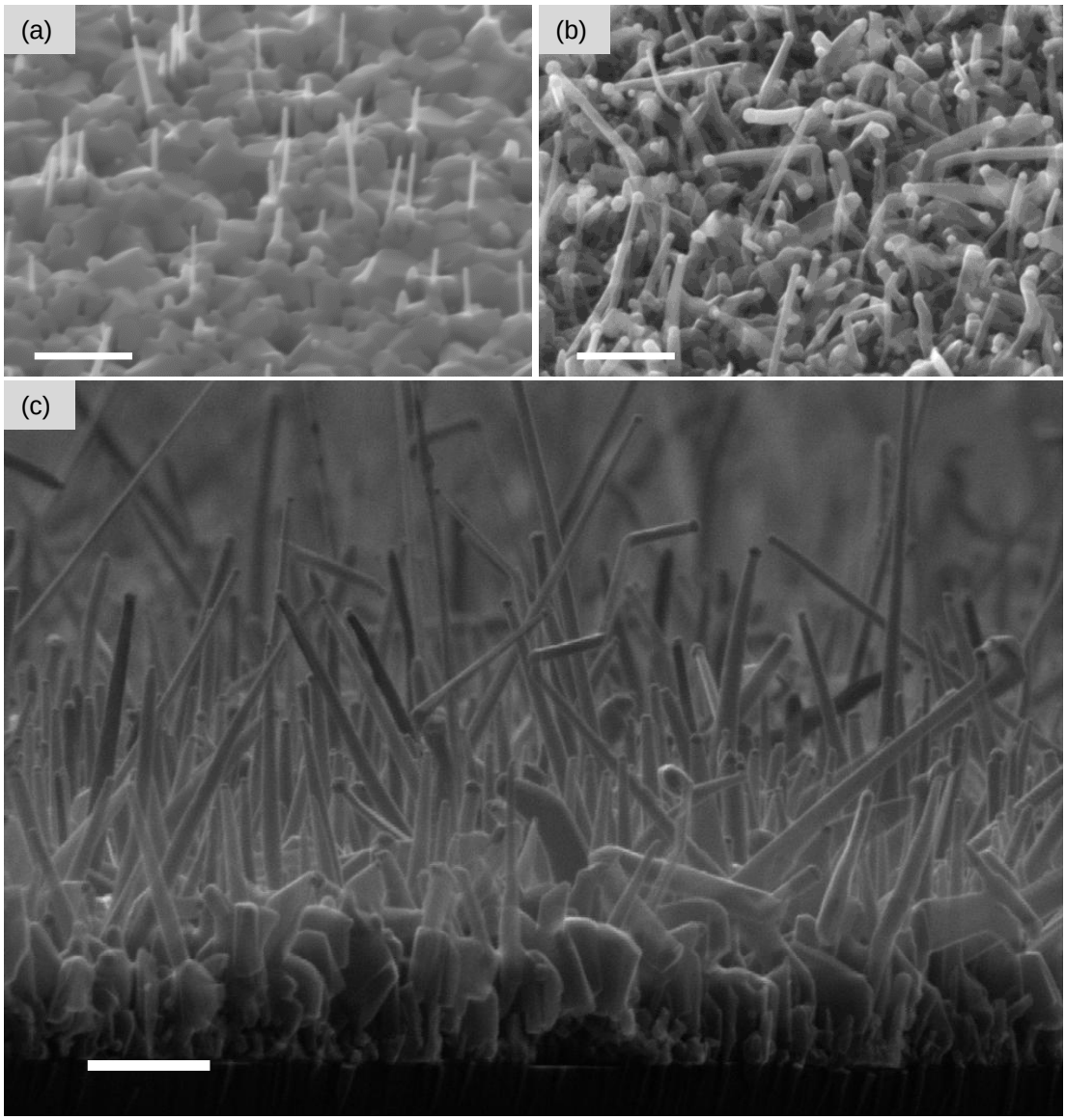

Figure 5.11: Comparison between nanowires grown via one-step (a) and two-step (b,c) procedures. Scale bars are 0.5 μm. Growth was carried out for (b) 45 minutes and (c) 120 minutes.

When continuing growth for a longer time period (120 minutes, figure 5.11.c) the mean nanowire length increases by a factor of approximately 2, with some nanowires reaching 3–5 μm. However at the same time the thickness of the wires increases and some of them become tapered. This may happen because the surface diffusion length of atoms is comparable to the length of the wire and when the wires become longer, the tapering becomes more visible; or because at the top of the wire the temperature is lower due to poor thermal conductivity of the wire, and at lower temperatures the surface diffusion length of atoms is shorter.

In order to investigate the dependence of the nanowire "quality" on the distance between the nanowires and on the dimensions of the gold droplet, the sample with EBL patterned gold droplets was fabricated.

5.2.4 Two-step growth. EBL patterning

As is seen in figures 5.12.a,b the 2-step method gives much more uniform results with higher yield and more parallel side-walls in comparison with one-step growth on an EBL-patterned substrate. Moreover, the images show that a gold dot defines the diameter of the nanowire. The detailed dependence of yield and nanowire length on the distance between the wires is presented in figure 5.13.

The dependence of the nanowire length (figure 5.13.a) on the distance between the nanowires can be fitted with equation 3.11. From this fit (red and black dashed lines in the figure 5.13.a), we obtain that the diffusion length of the Zn and O atoms on Si at 850 °C is approximately equal to 0.11 μm, and that the lifetime of atoms on Si, *i.e.* the time before atoms desorb from the Si surface, at this temperature is 2×10^{-10} sec.

Figure 5.13.b shows that Au dots with a smaller diameter produce more nanowires, but no clear dependence of the yield on the distance between the dots is observed.

ZnO nanowire growth was carried out on Si with gold catalyst by both one-step and two-step methods. Although ZnO nanowire two-step growth on Si gives better results than one-step growth, it strongly depends on small variations in native silicon oxide thickness and desorption velocity. This becomes an obstacle for repeatable growth and further development of nanowire devices. That is why

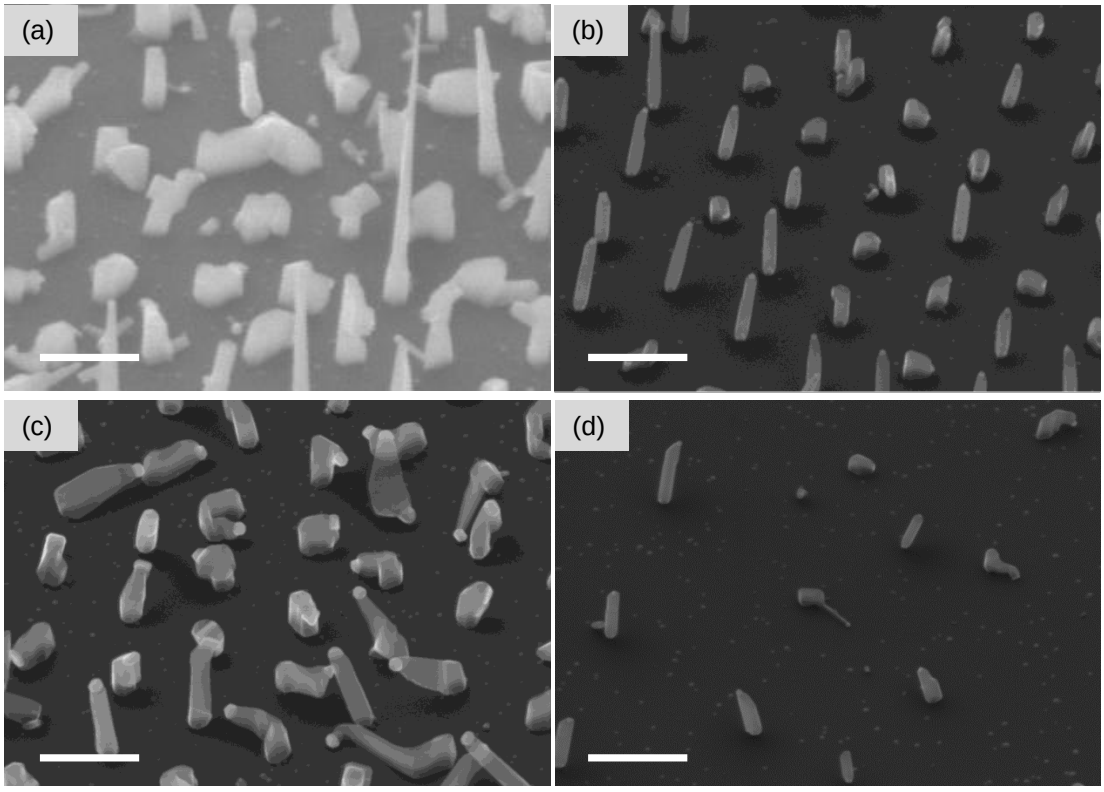

Figure 5.12: ZnO nanowires grown using EBL patterned gold catalysts. (a) one-step procedure; (b)-(d) two-step procedure; for images (b,c,d) the dot separations are 0.5, 0.5 and 1 μm, and the dot radii are 40, 90 and 40 nm respectively. Scale bars are 0.5 μm.

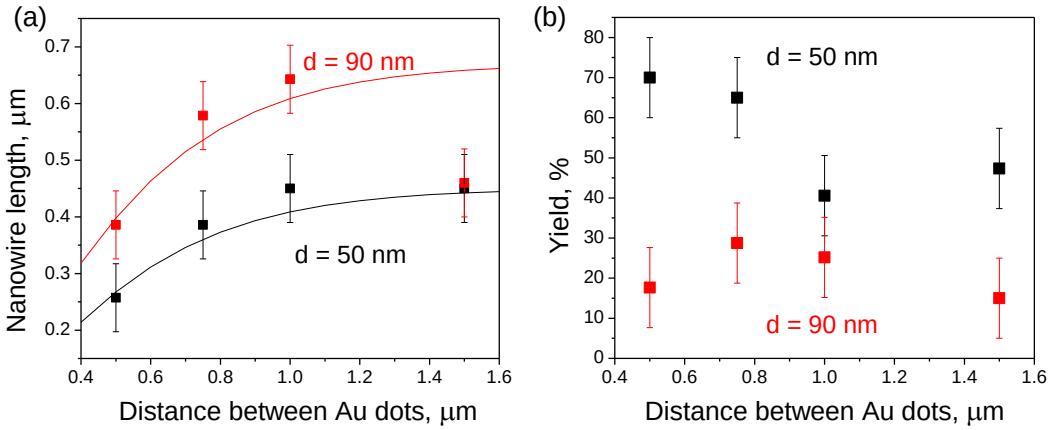

Figure 5.13: Dependence of the nanowire length (a) and nanowire yield (b) on the distance between the wires, the theoretical fit of the data from equation 3.11.

we have explored the possibility of ZnO nanowire growth on different substrates.

5.3 ZnO nanowires grown on sapphire

5.3.1 Growth phase map

As figure 5.8 shows, the desired nanowire properties ("quality" or length, parallelity and yield) get better with increasing temperature. The unstable formation of Si-Au eutectics gives poor control over nanowire morphology. Hence we have investigated nanowire growth on Al_2O_3 (0001) substrate. Sapphire has an oxide layer, which will bind with oxygen in ZnO and not form a eutectic with gold at growth temperatures. Moreover, it is known that growth on sapphire gives higher quality ZnO thin films than growth on Si [20].

During growth the oxygen BEP was kept fixed at 2 sccm, whereas the substrate temperature and the zinc BEP were changing. Figure 5.14 shows a representative SEM image of a sample grown for 1 hour at 800 °C with Zn BEP equal to 1.5×10^{-7} Torr. Both film and nanowires of various lengths and diameters are seen in the micrograph. The number of nanowires with length larger than 0.5 microns was taken as a representative measure of the growth quality. (It is worth

noting again, that "quality" in this case means the applicability for further device fabrication – *i.e.* appropriate length for multiple contact patterning, absence of tapering and density of the nanowires.) The nanowire growth map is given in figure 5.15. The color represent nanowire density measured on the sample with specific temperature and BEP_{Zn}. Only nanowires longer than 0.5 μm were taken into account. The largest nanowire density is observed at temperatures around 760 °C and a zinc BEP of 3×10^{-7} Torr. These parameters coincide with those obtained for ZnO nanowires grown on Si substrates.

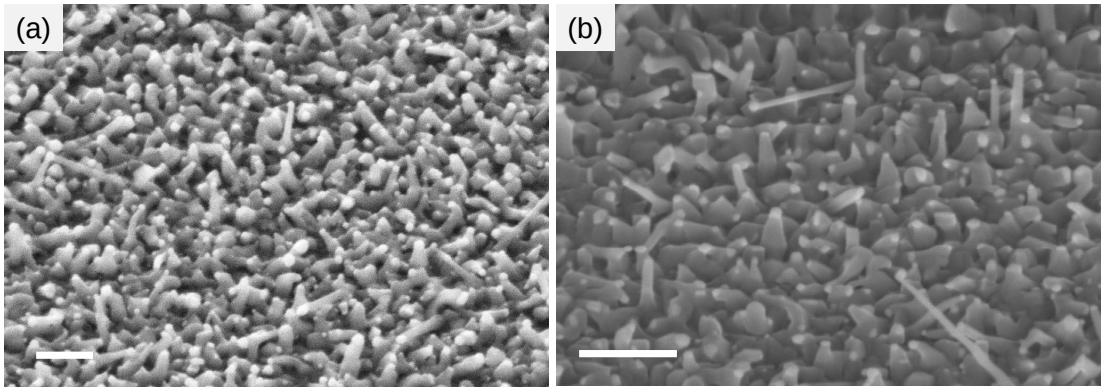

Figure 5.14: SEM images of ZnO nanowires grown on sapphire: a) Growth temperature 800 °C, $BEP_{Zn} = 1.5\times^{-7}$ Torr; b) growth tempeatures 750 °C; $BEP_{Zn} = 2.9\times^{-7}$ Torr. Scale bars are 500 nm.

The time scalability of the growth was tested on the nanowire sample grown at 750 °C. A sample grown for twice as long (2 hours) is shown in figure 5.16. The density of nanowires of length larger than 1 μm is more than 2 μm^2. The diameter of the nanowires ranges from 50 to 150 nm, with longer nanowires being thinner.

Nanowire growth has been attempted on the EBL patterned gold nanoparticles. However, due to simultaneous ZnO growth on gold and on sapphire and the low yield of gold nanoparticles, no coherent study could be made on this sample.

Nanowire growth on sapphire gives reproducible results. Although the yield of nanowire growth is very low (below 1 %), the number of gold nanodots is so high that the number of nanowires produced on one 10×10 mm sapphire substrate is high enough (∼100 millions) for further study of single nanowires and electronic devices fabrication. The attempt to improve control over the nanowire growth

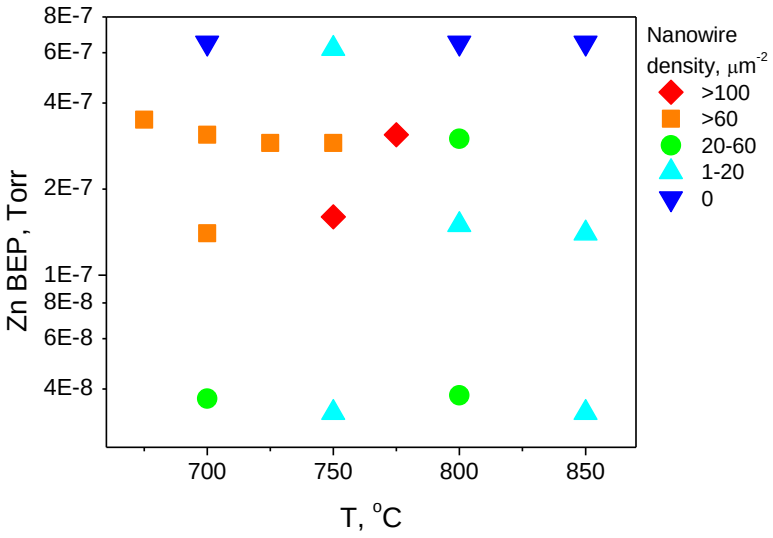

Figure 5.15: Growth phase map of ZnO nanowires grown on sapphire. Nanowires included in this plot were nanowires longer than 0.5 μm. The colours represent density of nanowires in μm^{-2}.

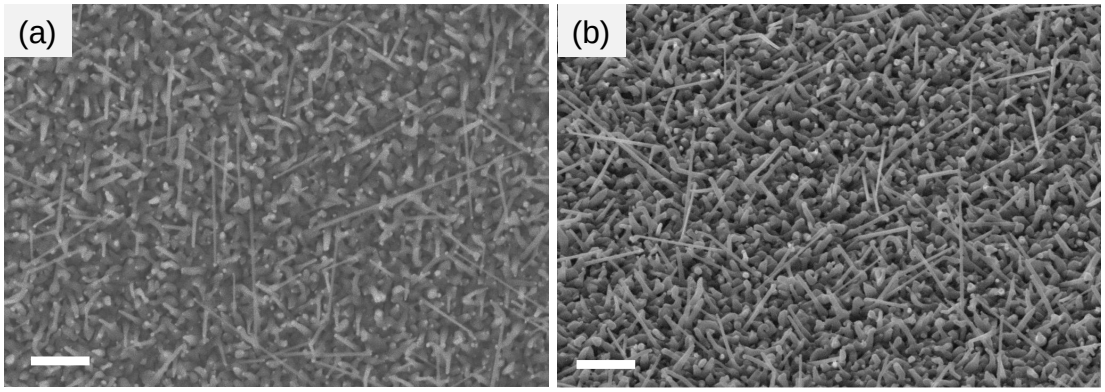

Figure 5.16: SEM images of ZnO nanowires grown on sapphire at 750 °C and $BEP_{Zn} = 2.9 \times 10^{-7}$ Torr for 2 hours. a) top view; b) 45° view. Scale bars are 1 μm.

direction was made by growing nanowires on textured ZnO substrates. It is presented in the following subsection.

5.4 ZnO nanowires grown on ZnO

In order to improve the orientation and yield of growth, ZnO nanowires were grown on polycrystalline ZnO thin-film substrates with preferred (0001) orientation. High quality bulk ZnO substrates are rare and more expensive than Al_2O_3 or Si. Thus ZnO thin film with preferential c-orientation were grown on Si at 300 °C (see section 5.2.1) and annealed at 900 °C to increase the smoothness of the film (figure 5.17).

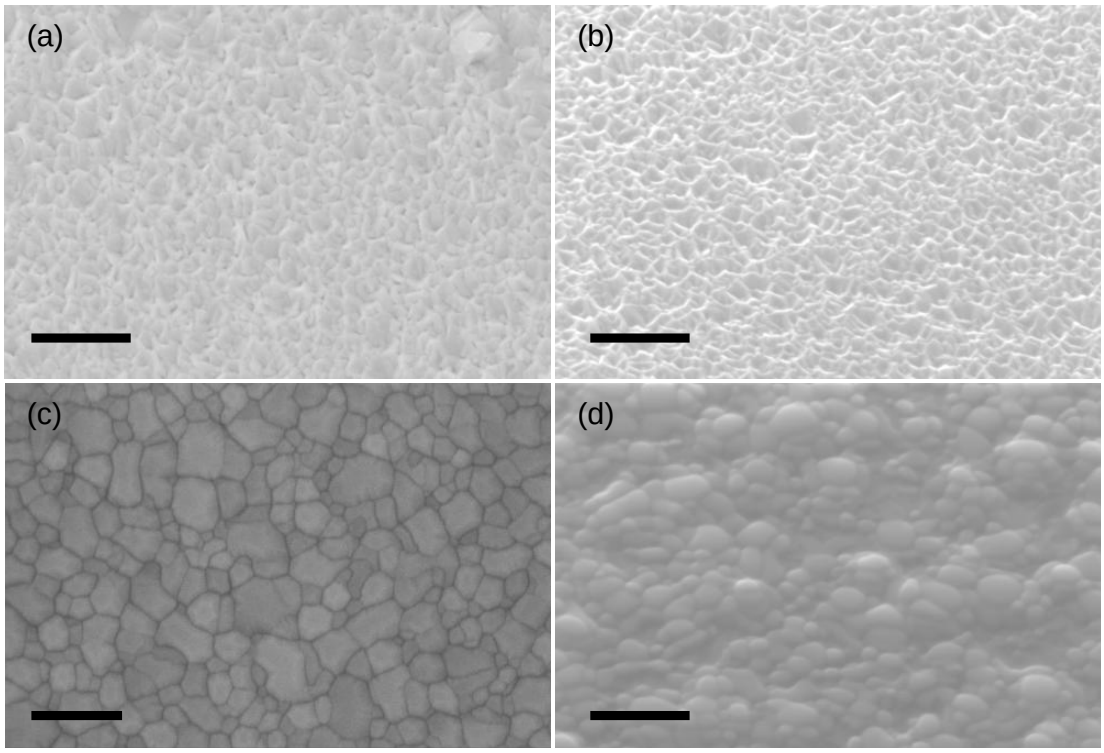

Figure 5.17: SEM images of ZnO film on silicon: (a,b) as-grown ZnO film on silicon at 350 °C (top view, and 45 degrees view, respectively), (c,d) same ZnO film annealed at 900 °C (top view and 45 degrees view, respectively). Scale bars are 500 nm.

A 3 nm gold thin film was evaporated ex-situ on this ZnO film. Samples were

grown at temperatures of 750, 850 and 875 °C. Results are shown in figure 5.18.

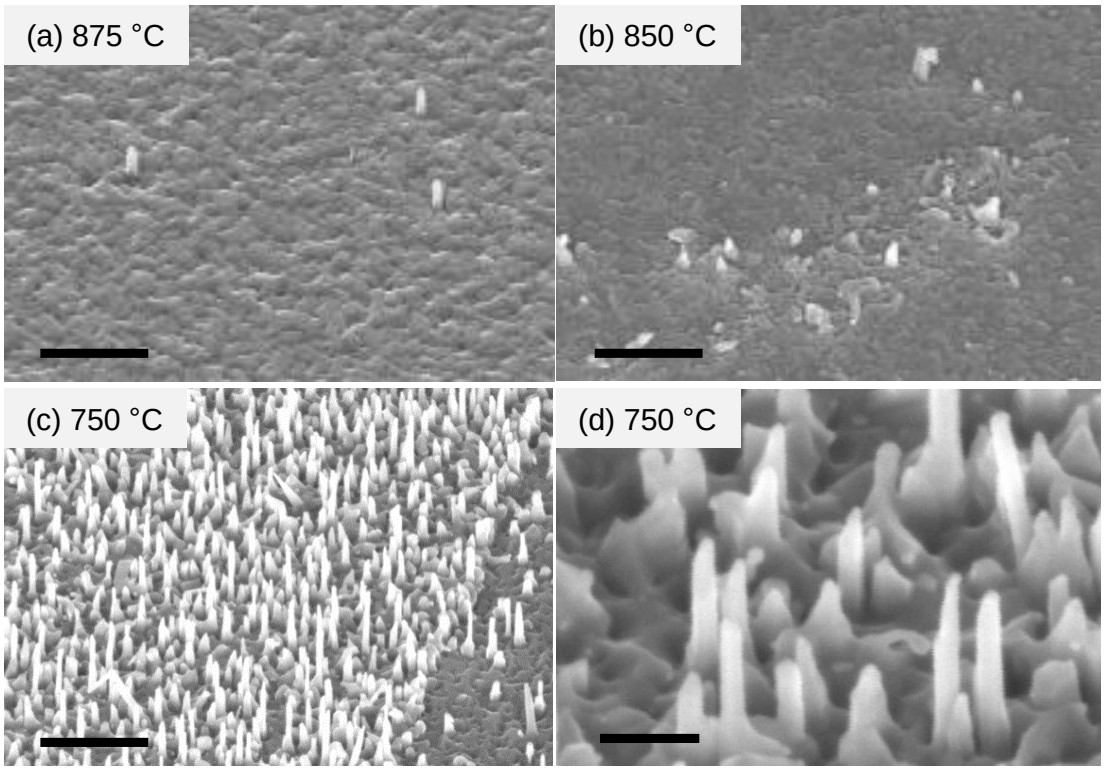

Figure 5.18: Nanowires grown on ZnO (a) at 875 °C, (b) 850C and (c) 750 °C, scale bars 1 μm and (d) at 750 °C, scale bar is 200 nm.

High density vertical nanorod growth is observed at 750 °C. They are about 50 nm in diameter and up to 500 nm in length. At this temperature a ZnO film grows at a high rate together with the nanowires, so it was impossible to grow nanowires with length much larger than those shown in the figure 5.18.d.

In summary to this section, ZnO nanowires have been grown on silicon, sapphire and ZnO substrates by plasma assisted molecular beam epitaxy. Morphology studies by scanning electron microscopy revealed nanowires of diameters 20 to 200 nm and lengths up to 5 microns. Study on structural properties of nanowires is presented in the next section.

5.5 Structural and optical properties of ZnO nanowires

The structure of ZnO nanowires was studied using high resolution transmission electron microscopy. TEM measurements were performed by Dr John Hutchison (University of Oxford), Dr Vaso Tileli (Imperial College London) and myself. No difference between one-step grown and two-step grown nanowires, between nanowires grown on Si and nanowires grown on sapphire has been observed. The HRTEM images (figure 5.19) showed that the nanowires are single phase wurtzite structures with no observable structural defects. The nanowires grow predominantly along the (0001) direction. The distance between lattice fringes is 2.6 Å, which is in good agreement with literature data on the c-lattice constant [222]. A polycrystalline gold nanoparticle is observed on top of the nanowires.

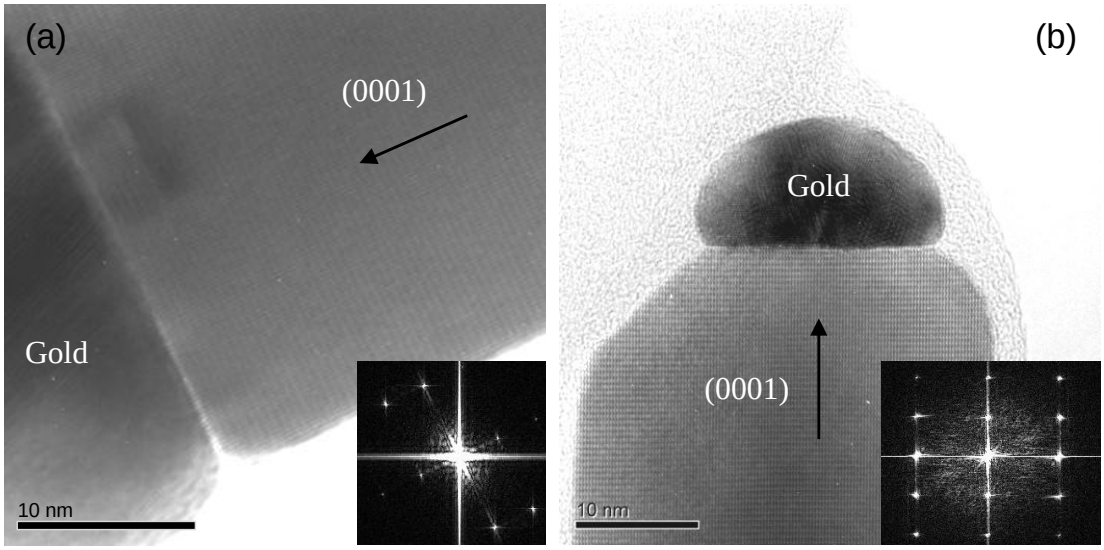

Figure 5.19: HRTEM images of typical ZnO nanowires, insets show FFTs of the images.

The PL spectra of the nanowires were measured by Cristian Mietze and Prof Donat As (University of Paderborn). Spectra were collected at different temperatures and are presented in figure 5.20. Two regions can be distinguished in the spectra: one at ∼3.3 eV which consists of narrow peaks related to band-to-band recombination and recombination between shallow donors, shallow acceptors and

conduction and valence bands; and another broad peak at 2–2.5 eV which is usually called the "green band" and is related to levels located deep in the band gap and is attributed to oxygen vacancies and copper impurities [182; 223]. The room temperature PL spectra show that the deep level green band is more than 2 orders of magnitude lower in intensity than the band edge emission peak. The prevalence of the band edge emission demonstrates that the density of deep levels is low, which indicates the good quality of the ZnO samples.

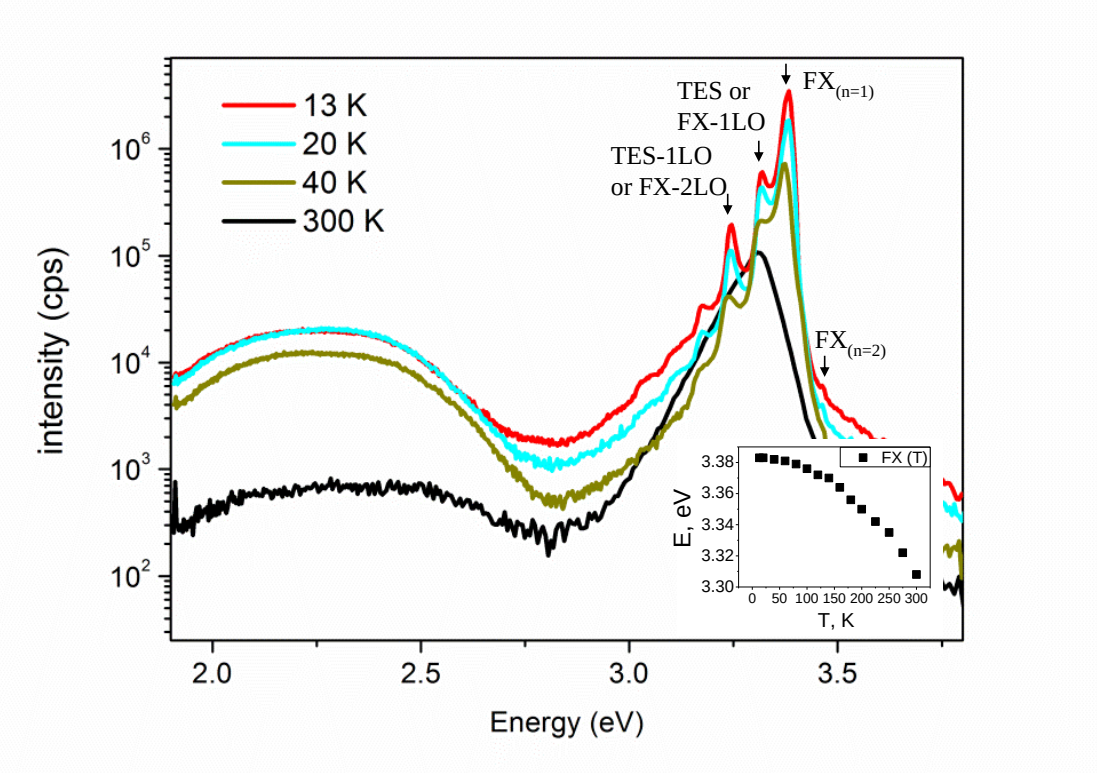

Figure 5.20: PL spectra of the as-grown ZnO nanowire samples. full spectra at different temperatures, origins of the band-edge emission fine-structure at different temperatures, inset: temperature dependence of the free exciton peak energy position.

The low temperature PL spectra in figure 5.20 show the fine structure of band edge emission. Origin of these peaks is evaluated from comparison with literature data on ZnO films and nanowires [21; 224; 225]. The observed peaks are the ground state free exciton at 3.383 eV ($FX_{n=1}$), free exciton in the first excited state at 3.46 eV ($FX_{n=2}$), two-electron satellite (TES) transition or LO-

phonon replica of FX at 3.32 eV and other LO-phonon replicas at 3.25 eV and 3.18 eV. The FWHM of the free exciton peak is as small as 22 meV at temperature 13 K. Other reports revealed donor-bound excitons [224; 226], although they are not visible in the present spectra due to the resolution of the detector which is 0.5 nm (or approximately 4–6 meV at these energies).

Inset in the figure 5.20 shows temperature dependence of the free exciton (FX) PL energy peak position. The FX curve follows the Varshni law (equation 3.22). The best fit of the Varshni formula gives Varshni coefficients $\alpha = (6.4 \pm 0.5) \times 10^{-4}$ eV/K and $\beta = -1050 \pm 30$ K, which are close to the reported values [224]. The zero temperature energy of the free exciton peak, 3.383 eV is by 4−6 meV higher than those observed in the literature [224; 226]. This may be due to the resolution of the detector used or due to the quantum size effect of the nanowires or nanocrystalline thin film.

Table 5.1: MBE grown ZnMgO samples, Mg beam equivalent pressure and fractional Mg flux.

P_{Mg}(Torr)	normalised Mg flux, J_{norm}(Mg), %
0	0
4.5×10^{-9}	3
7×10^{-9}	7
1.8×10^{-8}	15
4×10^{-8}	29
7.6×10^{-8}	43
1×10^{-7}	54

In conclusion, highly crystalline nanowires have been grown on silicon, sapphire and ZnO.

5.6 Ternary compound ZnO-based nanowires. ZnMgO nanowires

One of the main aims of using molecular beam epitaxy equipment for growing ZnO nanowires is the manufacturing of abrupt heterostructures. In order to

prepare heterostructures, the incorporation of foreign elements into ZnO should be studied first. Mg can enlarge the band gap of ZnO. This helps fabricating barriers for electrons in semiconductors, which can lead to the formation of a high mobility channel, or a 2DEG, to the manufacturing of quantum cascade diodes, single electron transistors, lasers *etc.* Therefore we have carried out a study of Mg incorporation into ZnO, which is presented in this section.

ZnMgO nanowires were grown at 750 °C and zinc BEP of 3×10^{-7} Torr both on silicon and on sapphire. The details on the magnesium BEP and normalised flux $J_{\mathrm{norm}}(\mathrm{Mg})$ calculated using equation 3.13 are presented in table 5.1.

5.6.1 Morphology and microstructure

SEM images of ZnMgO nanowires grown on sapphire are shown in figure 5.21. The morphology of the samples is similar at all the Mg fluxes except at the highest Mg flux of 54 %, where only short very thin nanowires and a thick film are seen. The density of nanowires of length below and above 0.5 micron is plotted as a function of Mg flux in figure 5.21.d. The density of nanowires decreases with increasing Mg flux. Dynamics of Mg atoms, which are different from that of Zn, alter the growth behaviour and reduce the number of nanowires at these temperatures and BEP conditions.

HRTEM investigation of the samples with normalised Mg flux below 20 % shows that they are single crystal hexagonal phase nanowires indistinguishable from those with no Mg (figure 5.22).

5.6.2 Mg incorporation

Mg incorporation was studied by EDX, PL, XRD and XPS. EDX spectra obtained on isolated $Zn_{1-x}Mg_xO$ nanowires are shown in figure 5.23. The inset shows the larger area EDX spectrum with Zn, O, Mg and Au signals. The presence of a Mg signal proves the incorporation of Mg into nanowires. Moreover the Mg signal increases with higher Mg flux. A more quantitative description is hindered by the non-trivial nanowire geometry and the absence of pure MgO nanowires for calibration.

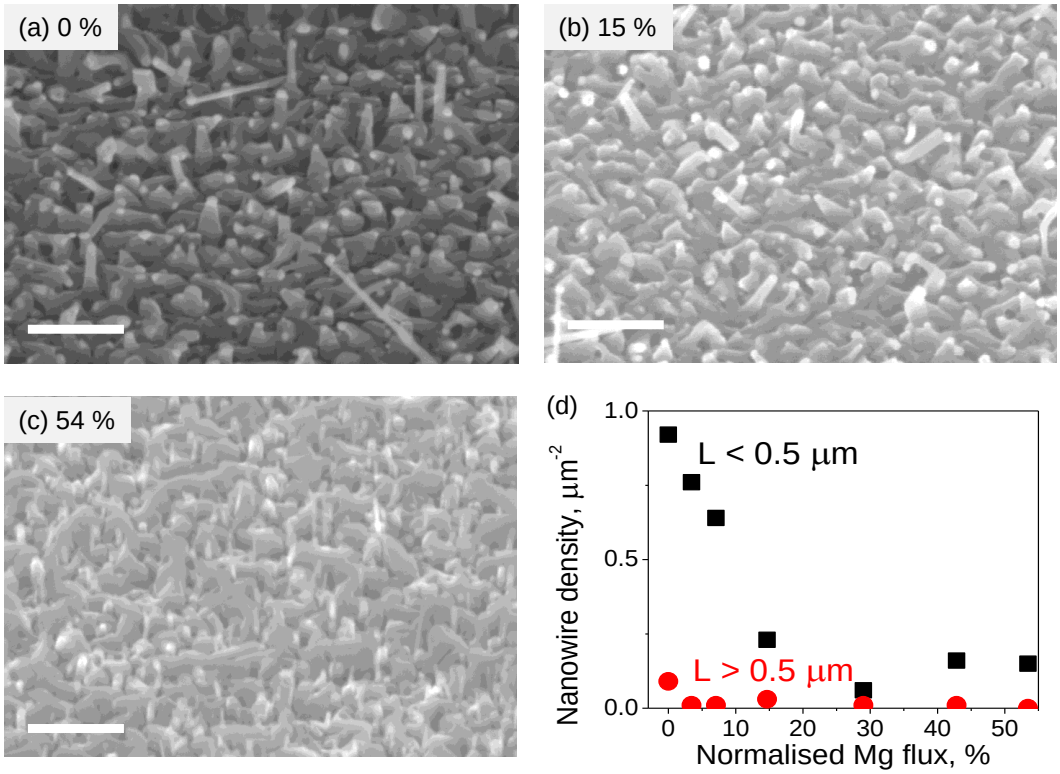

Figure 5.21: SEM images of ZnMgO grown at different Mg fluxes: (a) 0 %, (b) 15 %, (c) 54 %, scale bars are 500 nm; (d) Mg flux dependence on the density of nanowires with length below 0.5 μm (black) and over 0.5 μm (red).

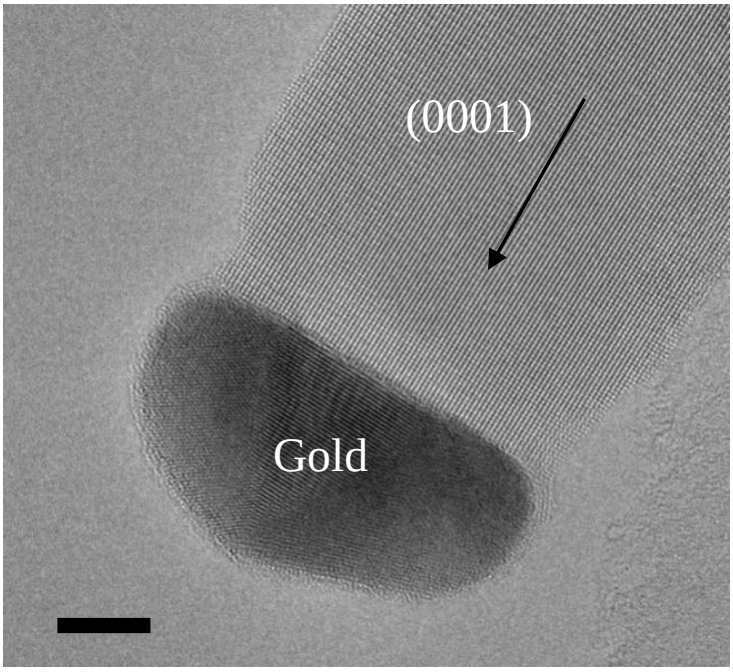

Figure 5.22: HRTEM image of ZnMgO nanowire, scale bar is 5 nm. Mg normalised flux is 28 %.

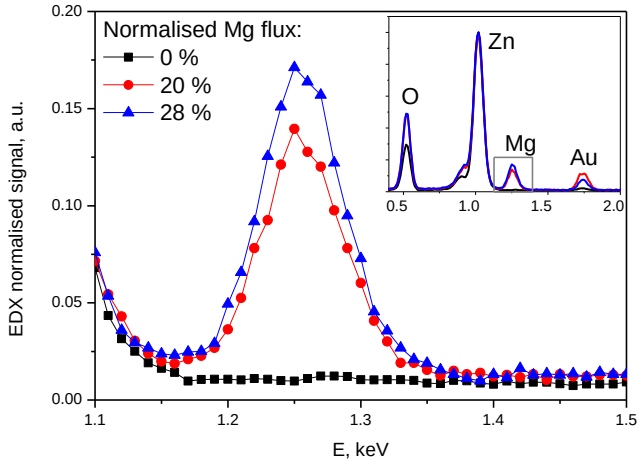

Figure 5.23: EDX spectra (normalised to the oxygen peak) of isolated ZnMgO nanowires with different Mg fluxes. Inset: lower resolution EDX spectra normalised to the Zn peak, showing peaks of other elements.

Figure 5.24 shows XRD measurements on samples grown on sapphire. Figure 5.24.a shows ZnMgO (0002) peaks, the Au (111) peak and the substrate peak (in this case the Al_2O_3 (0006) peak). At Mg flux higher than 40 % a new peak at $\sim 37^\circ$ appears. This peak is attributed to MgZnO rock-salt phase inclusions in the wurtzite ZnMgO matrix. The cubic phase usually has higher Mg content than the wurtzite structure [121]. This introduces phase boundaries in the nanowires and an alteration of the band gap, thus reducing their crystalline quality and increasing scattering centres for electrons. Figure 5.24.b shows that the $Zn_{1-x}Mg_xO$ (002) peak shifts to higher angles for samples with higher Mg content, indicating the decrease of the c-lattice parameter. The lattice constants of $Zn_{1-x}Mg_xO$ nanowire samples were extracted from $Zn_{1-x}Mg_xO$ (0002) XRD reflections using Bragg's law.

Figure 5.24.c shows the dependence of the lattice parameter on the Mg normalised flux for samples grown on silicon and on sapphire. The lattice constant changes by approximately 0.04 Å when the normalised Mg flux is increased up to 50 %. As noted in section 3.3.3.2, the Mg content cannot be inferred from Vegard's law, as no pure wurtzite MgO exists. Analysis of literature data on the c-lattice parameter in ZnMgO and the Mg-content measured using independent techniques is used as a method to infer the Mg content in nanowires (explained in more detail in 3.3.3.2, equation 3.19). The Mg content inferred from XRD data is given in table 5.2.

Figure 5.24.d shows XPS data for nanowires grown on sapphire. The Mg 1s peak at 1305 eV increases with increasing Mg fractional flux, which is consistent with the XRD data. The Mg content measured by XPS is given in table 5.2.

Pure MgO has a band gap of 7.7 eV, whereas pure ZnO has a band gap of 3.37 eV. Thus, the band gap of ZnMgO is expected to increase with increasing Mg content. Figure 5.25 shows PL data on the $Zn_{1-x}Mg_xO$ nanowire samples. No significant difference between the as-grown samples grown on silicon and sapphire was observed in the room temperature PL measurements. The band-edge emission peak shifts to higher energies as expected, as shown in figure 5.25.a,b at room temperature and at 13 K, respectively. The Mg flux dependence of the emission peak position is shown in figure 5.25.c.

The full width at half maximum of the band-edge peak increases with increas-

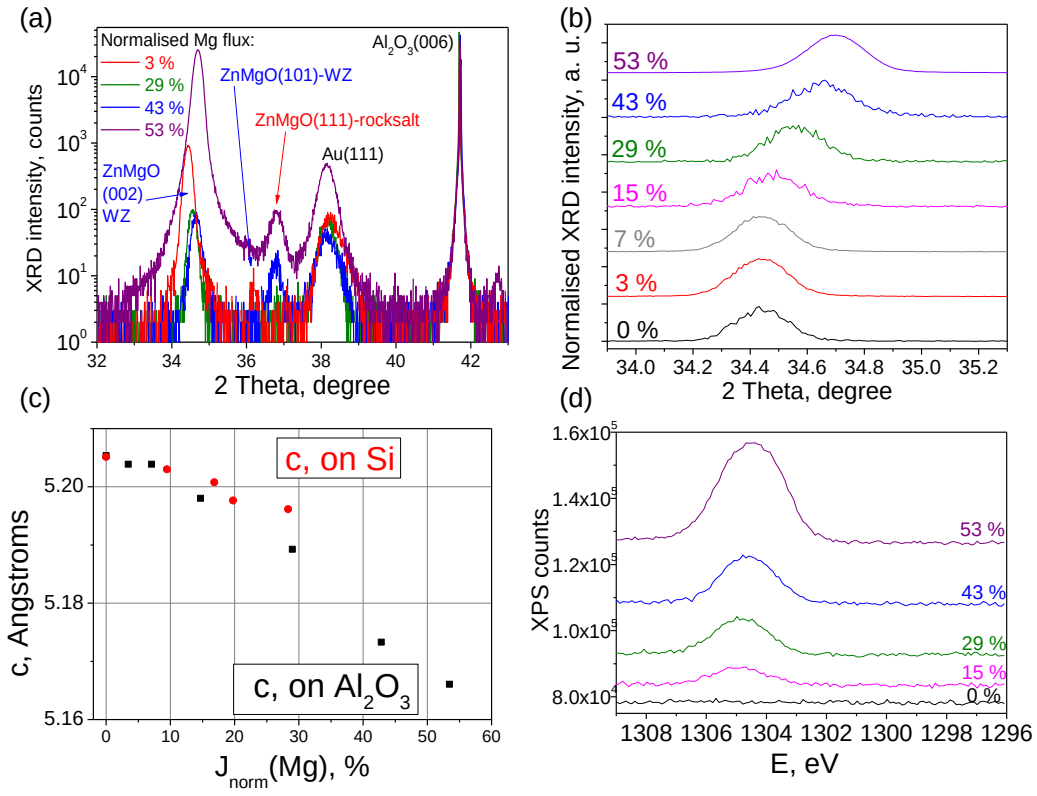

Figure 5.24: XRD diffractograms and XPS spectra of $Zn_{1-x}Mg_xO$ samples with different $J_{\text{norm}}(\text{Mg})$. (a) low resolution XRD diffractogram, showing various $Zn_{1-x}Mg_xO$ wurtzite and rocksalt, Au and sapphire peaks; (b) $Zn_{1-x}Mg_xO(002)$ peak for samples grown at different normalised Mg flux, showing shift towards higher angles; (c) c-lattice constants inferred from the XRD data and Bragg's law for ZnMgO samples grown on Si and on sapphire; (d) XPS Mg1s peak on $Zn_{1-x}Mg_xO$ samples.

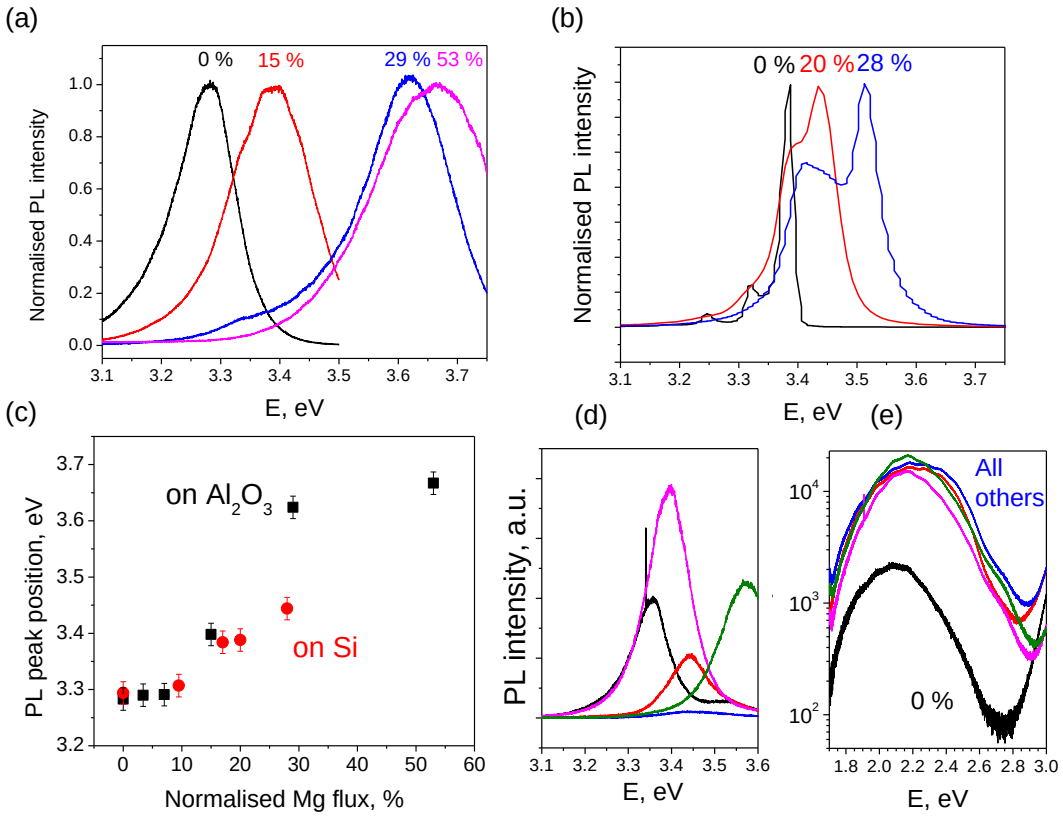

Figure 5.25: PL measurements on $Zn_{1-x}Mg_xO$ samples. (a) PL band-edge spectra at room temperature for as-grown samples grown on sapphire with different normalised Mg fluxes; (b) 13 K PL band-edge spectra of the samples grown on silicon; (c) band-edge peak position as a function of normalised Mg fluxes for samples grown on Si and on sapphire; d) PL band-edge spectra of individual nanowires grown with normalised Mg flux of 15 %; (e) green band PL emission normalised to the band-edge peak for as-grown samples with different Mg fluxes.

ing Mg flux. At room temperature it increases from 100 meV to almost 200 meV. At low temperatures this effect is much more pronounced: the FWHM increases from 28 meV to 160 meV and the peak splits into two closely located peaks. This effect might be caused by the presence of $Zn_{1-x}Mg_xO$ phases with different Mg concentration x, and hence with different band gap. The suggestion of varying incorporation of Mg in nanowires was tested by measuring the PL response on single nanowires, deposited on SiO_2. Figure 5.25.d shows spectra taken from 5 single nanowires grown at fractional Mg flux of 15 %. The peak energies range from 3.35 to 3.57 eV. This indicates very irregular Mg incorporation in nanowires during growth. As a result, the measurement on as-grown sample gives only an average value of the nanowire Mg content. This discrepancy between nanowire properties should be taken into account when preparing ZnMgO nanowire devices. The presence of various $Zn_{1-x}Mg_xO$ phases with different x affects the density of deep levels: the deep level luminescence increases by one order of magnitude after incorporation of Mg into ZnO (figure 5.25.e).

The dependence of the PL band edge peak position of ZnMgO nanowire samples grown on sapphire and silicon on the Mg normalised flux is depicted in figure 5.25.c. Analysis of literature data on the PL peak position in ZnMgO nanowires and thin films and Mg-content measured using independent techniques is used as a method to infer Mg content in nanowires (equation 3.19) as it was done for XRD measurements. The Mg content inferred from PL data is given in table 5.2.

Table 5.2 gives information on all the values of Mg concentration inferred from various techniques. The last column provides an estimation of energy band gap differences between ZnO and ZnMgO samples, which may be used for band engineering.

Figure 5.26 compares PL, XRD and XPS data. It depicts the dependence of the Mg content in the samples x on the Mg content in the growth vapours. Fitting experimental results of the dependence of x on (J_{norm}(Mg)) to the formula 3.18 for samples with no phase separation we get the ratio between the incorporation rate coefficients for Zn and Mg. The fitting gives the value of 3.5±1 (black curve in figure 5.26), *i.e.* the Zn incorporation rate into wurtzite ZnMgO is 3.5 times higher than the incorporation rate of Mg.

Table 5.2: Incorporation of Mg into ZnMgO nanowire samples grown on sapphire.

normalised Mg flux, %, J_{norm}(Mg)	% of Mg in wires, measured from XRD	XPS	PL	Estimated band gap offset in ZnMgO/ZnO heterojunction
0	0	0	0	0
3.4	1	0		0.02
7	1	0		0.02
15	6	10±2	8±2	0.10±0.02
29	13±3	15±3	23±4	0.22±0.03
43	27±3	28±3		0.40±0.05
53	33±3	40±4	26±5	0.55±0.08

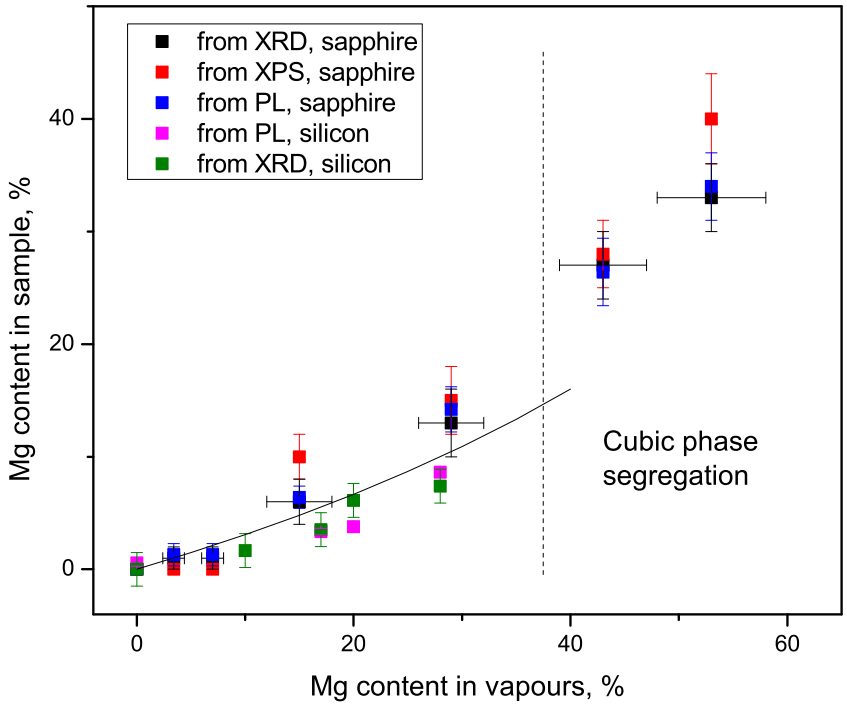

Figure 5.26: Dependence of Mg content x on the normalised Mg flux for different types of analysis. The black solid line is a fit with $\alpha/\beta = 3.5$.

In conclusion, Mg incorporation in ZnO nanowires was studied. The Mg atom incorporation rate is 3.5 times lower than that of Zn atoms. At Mg content larger than 20 % cubic phases segregate in ZnMgO wurtzite samples. At Mg content of 20 % the band gap difference between ZnO and $Zn_{0.8}Mg_{0.2}O$ is approximately 0.2 eV. This value is enough for fabricating barriers that are operational at room temperature. Studies of axial and radial heterostructures are presented in the next section.

5.7 Heterostructures

5.7.1 Radial heterosctructures

Compositional and band gap modulation can be performed axially and radially. At usual nanowire growth temperatures of 750 °C Mg diffuses along the nanowire [152; 153] severely complicating the fabrication of ZnO/ZnMgO/ZnO axial heterostructures or quantum wells. On the other hand, growth of the nanowire shell at lower temperatures will slow down diffusion of Mg, allowing the epitaxial growth in the radial direction and thus achieving radial compositional modulation. In order to prepare radial heterostructures (or "core-shell" heterostructures) the following growth procedure was carried out:

First, normal growth of ZnO nanowires was conducted at 750 °C for two hours. The temperature was then reduced to 500 °C and different material growth (MgO, ZnMgO, or ZnMgO/ZnO/ZnMgO) was carried out for 5–15 minutes. The reduction of temperature reduced the growth rate along the c-axis and increased the growth rate along the m- and a- axes. Five different radial heterostructure samples with different normalised Mg content ($J_{\mathrm{norm}}(\mathrm{Mg}) = J(\mathrm{Mg})/(J(\mathrm{Mg})+J(\mathrm{Zn}))$) have been grown:

1. ZnO for 2 hours at 750 °C + MgO for 15 minutes at 500 °C;
2. ZnO for 2 hours at 750 °C + ZnO for 5 minutes at 500 °C;
3. ZnO for 2 hours at 750 °C + ZnMgO for 5 minutes at 500 °C; $J_{\mathrm{norm}}(\mathrm{Mg})$ = 30 %;
4. ZnO for 2 hours at 750 °C + ZnMgO for 15 minutes at 500 °C; $J_{\mathrm{norm}}(\mathrm{Mg})$ = 40 %;

5. ZnO for 2 hours at 750 °C + [ZnMgO/ZnO]×4 superlattice at 500 °C; each half-layer growth was 2 minutes long; $J_{\mathrm{norm}}(\mathrm{Mg}) = 40$ %.

SEM images of these samples are shown in figure 5.27. No radical change is found in nanowire morphology. No overgrowth of the film over nanowires is observed, and no big change in diameter is observed (inset in figure 5.27).

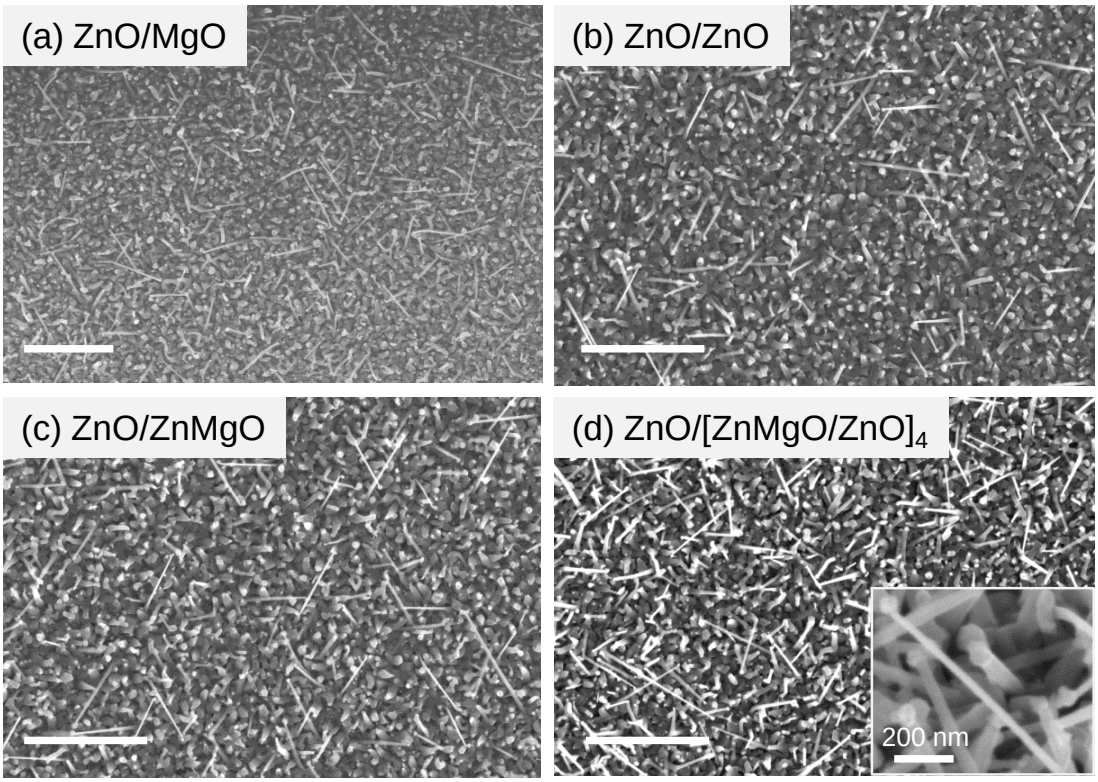

Figure 5.27: SEM images of the core-shell nanowires: (a) ZnO/MgO; (b) ZnO/ZnO; (c) ZnO/ZnMgO; (d) ZnO/$[\mathrm{ZnMgO/ZnO}]_4$. Scale bars are 2 μm. Inset: higher magnification SEM image of ZnO/$[\mathrm{ZnMgO/ZnO}]_4$ as-grown nanowires.

5.7.2 TEM on heterostructure nanowires.

TEM images of ZnO/MgO core-shell nanowires are shown in figure 5.28. The MgO layer does not grow in a single crystal arrangement, but forms a polycrystalline cubic shell around the wurtzite core. A polycrystalline shell can result in an irregular band structure which may be detrimental to the device performance.

In order to confirm no significant intermixing between the core and the shell, EDX line scans were performed across a ZnO/MgO nanowire cross-section in TEM (figure 5.28.c). The EDX signal can be fitted by equation 3.20. Three fits to different line scans on oxygen, zinc and magnesium signals gives similar results: the radius of the core is 26±0.5 nm (d_{core} = 52 nm), the thickness of the shell is 4±0.3 nm (*i.e.* the diameter of the whole wire is 60 nm), and the signal broadening is 9±0.7 nm. Note that a signal broadening represents the combination of the effective interaction area between the beam and the nanowire and the Mg and Zn interdiffusion. In the current geometry it is possible only to estimate the upper limit of the interdiffusion between the core and shell at a temperature of 500 °C, which is 9 nm.

$Zn_{1-x}Mg_xO$ material with $x < 0.2$ grows epitaxially without any rock-salt phase inclusions and thus can be exploited for defect free heterostructure formation with ZnO nanowires.

TEM images of a core-shell heterostructure with ZnMgO shells are shown in figure 5.29. The shell growth is confirmed by the overgrowth of the ZnMgO shell over the gold droplet as observed in the nanowire in figure 5.29.c. TEM contrast between core and shell is not clearly visible due to the low concentration of Mg. EDX data collected from the whole core-shell heterostructure nanowire did show a small amount of Mg in the wire. However, cross-sectional scans of the wires by scanning TEM techniques such as HAADF, EDX and EELS didn't show any visible contrast at the sides of the wire. Simulation of the EDX data (equation 3.20) indicates that the Mg signal in $Zn_{1-x}Mg_xO$ with x below 20 % will be of the same order of magnitude as the noise. Attempting to increase the signal-to-noise ratio by keeping the electron beam on the wire for a longer time to collect more data points results in destruction of the wire.

Multiple core-shell nanowires with four double layers have been grown and investigated by TEM (figure 5.30). The nanowire shown in figure 5.30.a was grown without gold droplet overgrowth. Side areas of the wire in figure 5.30.b show four brighter contrast regions. The same periodical TEM contrast stripes were observed in approximately half of the investigated nanowires grown. The number of brightness change regions correlates with the number of intended quantum well structures. The width of these regions is approximately 1–2 nm, suggesting

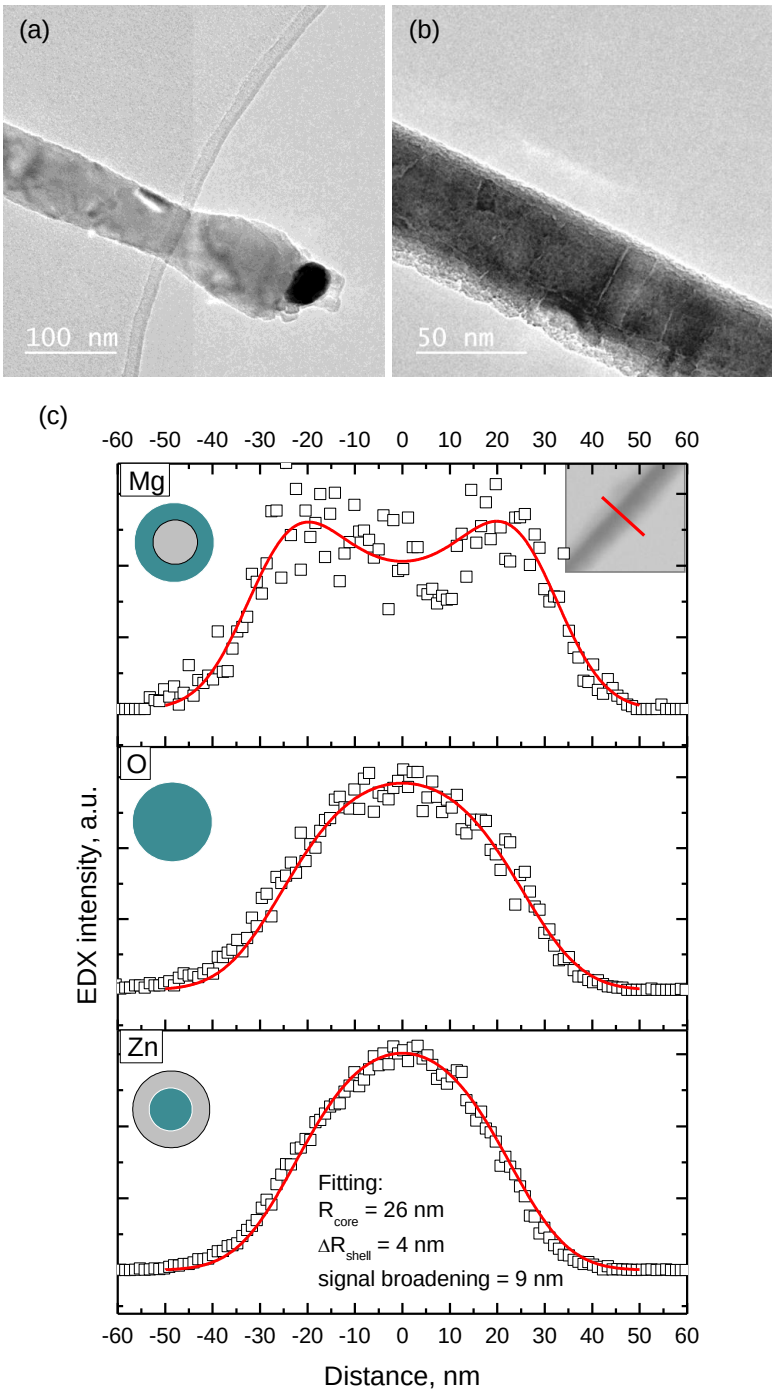

Figure 5.28: ZnO/MgO core-shell nanowires: (a–b) TEM images; (c) EDX lines-cans on the ZnO/MgO core-shell nanowire cross-section, Zn, O and Mg signals, with the solid red line showing the theoretical fit as calculated using equation 3.20

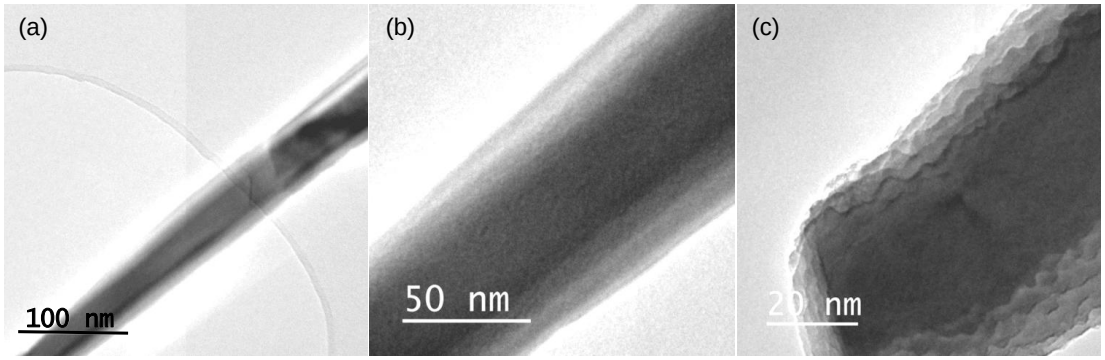

Figure 5.29: TEM images of ZnO/ZnMgO core-shell nanowires at different magnifications. (c) shows the Au particle overgrown by ZnMgO shell.

a radial growth rate of approximately 0.5–1 nm per minute. Since not all the nanowires exhibit the same TEM contrast, we can conclude that the radial growth rate is unevenly distributed from wire to wire on the same growth sample.

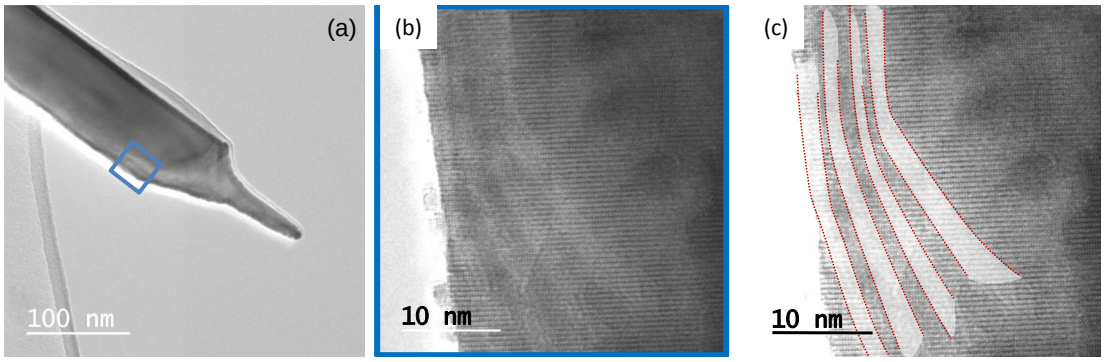

Figure 5.30: TEM images of ZnO/$[ZnMgO/ZnO]_4$ multiple core-shell nanowires at different magnifications. (a) top of the nanowire; (b-c) higher resolution TEM image of the same nanowire showing striped contrast due to different layers of ZnO and ZnMgO materials, white lines in (c) are guides to the eye.

5.7.3 Photoluminescence of heterostructure nanowires.

In order to carry out a PL study on the as-grown heterostructure samples, it should be noted that the nanowire coverage of the as-grown samples varies over the sample surface. Figure 5.31.a shows the nanowire density on the as-grown sample as a function of the position on the sample. At the edge of the as-grown

sample, the nanowires cover almost 100 % of the sample surface, whereas in its centre they cover 10 % or less. This fact is of high importance for the PL investigation, due to the excitation beam being only on the order of 1 micrometer in diameter. The PL investigation is therefore much more localised than XPS or XRD. This difference in the nanowire density was not important in the PL measurement on the as-grown ZnO or ZnMgO samples, as the PL spectra were very similar in the middle and at the edge of the sample. However, the heterostructure samples have very different PL behaviour at these two positions (figure 5.31.b). This spatial variation in PL spectra and in the nanowire density together allows us to assume that the PL spectra taken at the centre and edge of the as-grown sample may be attributed to the film and to the nanowires, respectively. In summary, we will use measurements taken at the sample centre to investigate the thin film, measurements taken at the sample edge to investigate the nanowire ensemble, and measurements taken on individual nanowires to corroborate the nanowire ensemble data. All the measurements were taken at room temperature.

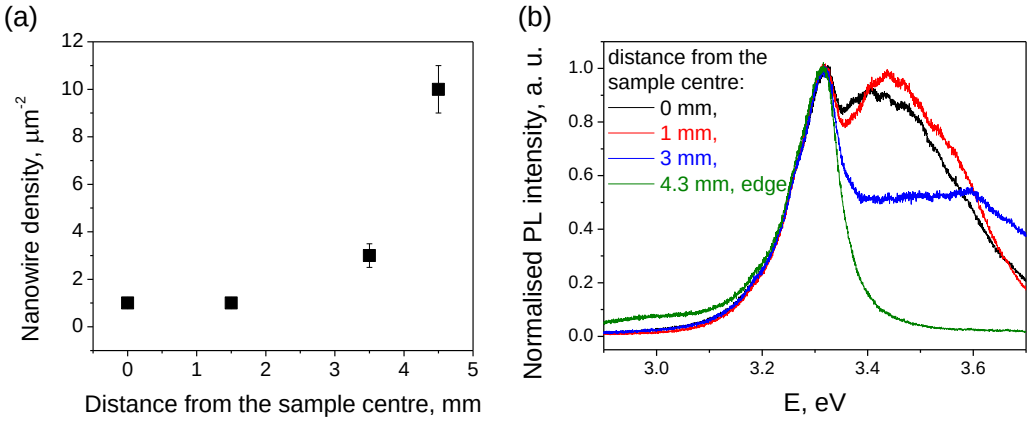

Figure 5.31: (a) Nanowire density variation on the as-grown sample, (b) room temperature PL signal variation taken at different places on the as-grown multiple quantum well heterostructure nanowire sample.

5.7.3.1 Thin film PL

First we will examine the thin film spectra (figures 5.32.a,b). Thin films with no Mg and a short period (5 minutes) of ZnMgO layer growth (blue and green curves

respectively) show similar PL band-edge emission peak positions at approximately 3.28 eV (inset in figure 5.32.a). We speculate that no PL signal of the ZnMgO thin layer can be observed due to a very small volume of material. The sample with a longer period of ZnMgO layer growth (15 minutes) has its peak shifted to 3.3 eV, which may be attributed to the low Mg content ZnMgO layer luminescence with Mg composition of 1–2 % (inferred from the peak position and equation 3.19), or to strain effects near the ZnO/ZnMgO interface. The same sample has another low intensity peak at 3.59 eV (figure 5.32.b, red curve). This peak is attributed to a high Mg content ZnMgO layer, with an Mg content of approximately 20 %, as inferred from the peak position. This value coincides well with what we would expect if we add 40 % of Mg into the vapour phase (figure 5.26).

The thin film grown with a pure MgO layer has the same peak at 3.3 eV, indicating minor intermixing between ZnO and MgO or strain (figure 5.32.a, grey curve). The MgO luminescence peak cannot be observed because of its position at 7.7 eV, which is out of the range of the PL instrument used.

The black curve in figures 5.32.a,b shows the PL measurement on the ZnO/ZnMgO multiple heterostructures. The band-edge peak is observed at 3.32 eV, which is higher than that of ZnO or ZnO/ZnMgO samples and may indicate that the peak is constituted of many peaks, some of them with energies higher than usual ZnO emission. Moreover, the graph shows a pronounced large tail at higher energies. Automatic Gaussian deconvolution of the spectrum in the Origin software package shows the presence of various peaks with energies spaced from the ZnO peak by 50 to 300 meV. We attribute peaks with energies between 3.35 eV and 3.6 eV to emission from multiple quantum wells (MQW) with varying well thicknesses. These energies correspond to quantum wells of thickness ranging from 1 to 5 nm [139; 156].

5.7.3.2 Nanowire PL

Figure 5.32.c shows nanowire PL spectra. The highest band-edge peak shows trend similar to that of thin films, with pure ZnO nanowire peak at 3.28 eV, ZnO/ZnMgO single heterostructure PL peak at 3.295 eV and ZnO/ZnMgO MQW at 3.315 eV. No distinct $Zn_{0.8}Mg_{0.2}O$ or MQW peaks are observed in nanowire

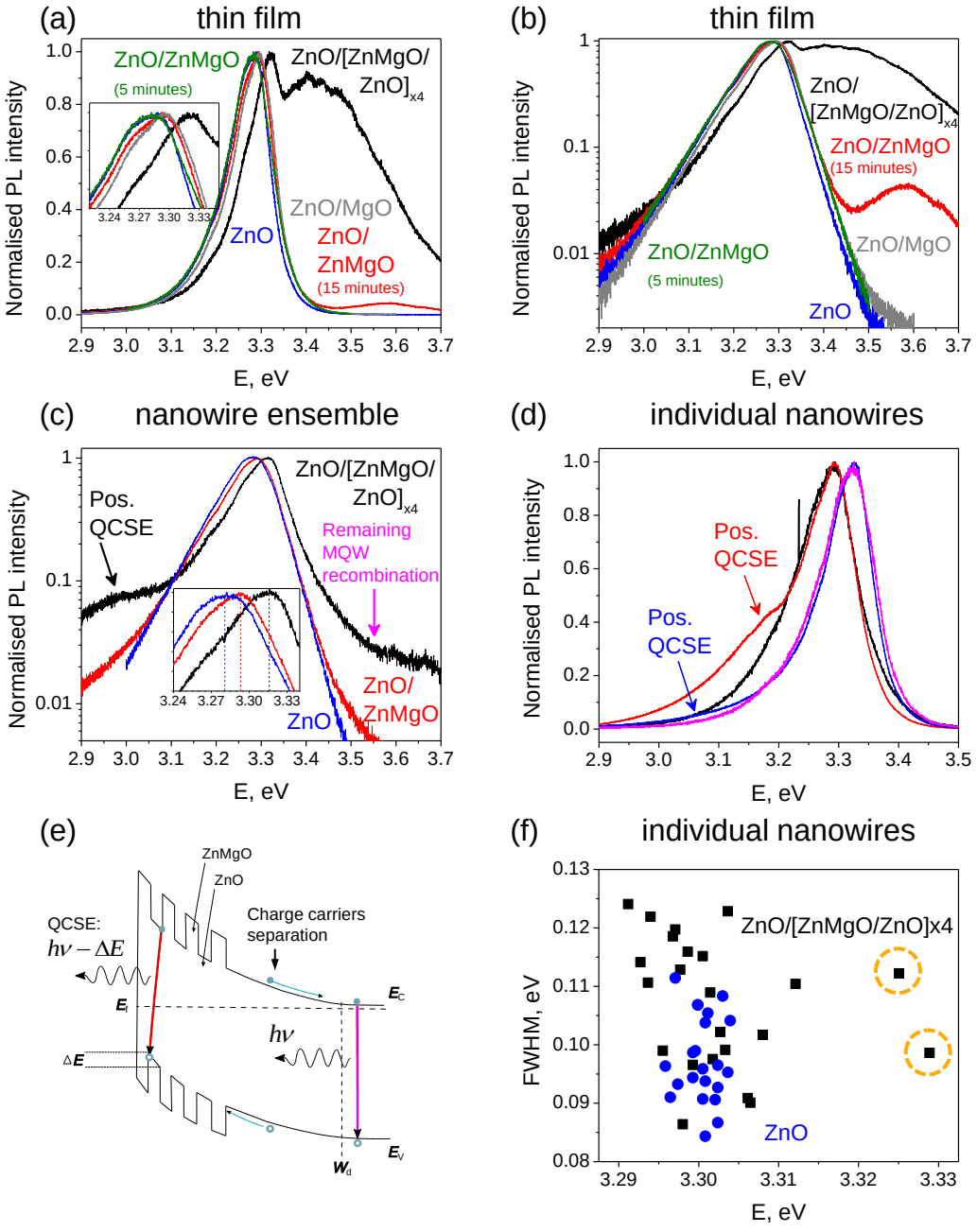

Figure 5.32: Photoluminescence of heterostructure samples. (a) thin films, all the band-edge PL spectra, inset shows shift in the band-edge peak position; (b) thin films, semi-logarithmic plot of the band-edge PL spectra; (c) nanowire ensembles, semi-logarithmic plot of the band-edge PL spectra, inset shows shift in the band-edge peak position; (d) PL on four individual nanowires from the MQW sample, possible quantum confined Stark effect (QCSE) indicated by arrows; (e) nanowire surface band diagram explaining the charge carrier separation and possible QCSE; (f) PL peak energy position dependence of the FWHM measured on individual MQW ZnO/ZnMgO nanowires and ZnO nanowires, yellow circles indicating nanowires with potential MQW emission.

samples as opposed to thin films. The PL spectrum of ZnO/MgO core-shell nanowires are not shown on this graph because it is similar to that of the thin film (figure 5.32.a, grey curve).

Absence of high energy peak in the nanowire PL

Usually the fine features of the MQW are observed in low temperature PL [139; 156]. We performed our measurements at room temperature, with high temperature smearing out any additional peaks. Although no clear additional peaks are visible, the shift of the peak position in the single and multiple quantum well nanowire samples by 15 and 35 meV, respectively, may give a hint to the heterostructure formation (figure 5.32.c inset).

On the other hand, by the same logic, room temperature smearing should apply to the thin film PL as well. However, we have clearly observed the MQW and $Zn_{0.8}Mg_{0.2}O$ layer emission peaks in the thin film PL. The absence of the MQW luminescence in the nanowire PL cannot be explained by the absence of the MQW core-shell geometry in nanowires, because it was observed by TEM (figure 5.30). One possible explanation of this effect may be found by considering the band bending diagram near the nanowire surface (figure 5.32.e). ZnO nanowires are known to have large band bending due to adsorbed species (mainly oxygen) and the electric field directed towards the centre of the nanowire. The electric field at the nanowire surface separates electrons and holes and reduces their recombination in the surface depletion region. Therefore, most of recombination is happening in the core of the nanowire, where the bands are parallel. Since ZnMgO layers are on the surface of the wire, only a very small fraction of electron-hole pairs recombine in the ZnMgO layers or in the ZnMgO/ZnO quantum wells. The remaining MQW recombination is seen by the slight increase of the high-energy tail of the MQW sample PL (pink arrow in figure 5.32.c).

Quantum Confined Stark Effect

Surface band-bending may potentially induce another effect, called Quantum-Confined Stark Effect (QCSE) [227; 228]. It is illustrated in figure 5.32.e. The surface barrier creates a large radial electric field. In turn, the electric field shifts

the electron states in the quantum well to lower energies and the hole states to higher energies. This reduces the recombination energy to $h\nu - \Delta E$ and may cause light emission with energy below the material's band gap. Using a simple one-dimensional potential model for the ZnO nanowire surface and assuming a reasonable surface barrier of 0.5 eV [177], carrier concentration of 2×10^{18} cm^{-3} and quantum well thickness of 2 nm, this emission energy lowering may reach 0.2 eV. Although this is a significant value which at these distances results in an electric field close to the material breakdown field, similar magnitude quantum-confined Stark effect was observed in the tips of ZnO heterostructure nanowires [146].

The MQW nanowire sample has a peak below the ZnO band gap at approximately 3.0 eV (black arrow in figure 5.32.c). Similar peaks with energies 3.05 eV and 3.15 eV are observed in the PL spectra measured on some individual nanowires (arrows in figure 5.32.d). This observation gives evidence for the possible QCSE on some of the nanowire core-shell heterostructures. No QCSE peaks are observed in thin films. This indicates a nearly flat band arrangement of the ZnO thin films.

Individual nanowires

It should be noted that not all individual nanowires show the QCSE peak or high energy peak (*e.g.* black and purple curves in figure 5.32.d). It is, however, possible to analyze nanowires statistically by performing PL measurements on multiple MQW ZnO/ZnMgO nanowires and pure ZnO nanowires. Figure 5.32.f shows the dependence of the full width at half maximum (FWHM) on the PL peak energy position for twenty MQW nanowires and twenty ZnO nanowires, with each data point representing one nanowire (samples were grown on the same day to minimise any MBE instrumental error, although in a different month from the samples shown previously in figures 5.32.a-c). The MQW nanowires have a higher scatter of the PL peak position and an increased FWHM value. The increased FWHM indicates the presence of extra peaks, the fine features of which may become visible at low temperatures. Encircled data points in figure 5.32.f show nanowires with their peak energies much higher than the average value of ZnO nanowires. This may be indicative of the existence of the emission from the

quantum wells in these nanowires. Low temperature PL measurement on these samples would allow the unambiguous determination of the existence of quantum well emission.

In conclusion, ZnO/MgO, ZnO/ZnMgO and ZnO/$[ZnMgO/ZnO]_4$ core-shell nanowires have been grown by gold-catalysed MBE with the core grown at 750 °C and the shell grown at 500 °C. TEM and EDX measurements confirmed shell-formation with low core-shell intermixing. PL measurements were carried out to separate the effects of the nanowires and the parasitic thin film. The multiple heterostructure thin film shows quantum well luminescence with emission energy in the range 3.35–3.6 eV. Nanowire multiple heterostructures showed a PL peak luminescence energy higher on average than that of ZnO nanowires, a low intensity high energy tail and low energy peak, which we tentatively attribute to quantum confined Stark effect. All these effects indicate the presence of quantum well luminescent emission in multiple core-shell ZnO/ZnMgO heterostructure nanowires. In order to unambiguously prove that, low temperature PL measurement will be carried out on these nanowires in the future. Poor repeatability of the growth complicates the further study of the multiple-quantum well nanowire devices.

5.8 Drawbacks

There are several indications of the poor control over the nanowire growth conditions which may hamper application of as-grown samples to electronics.

(i) As it was shown in the previous section on page 159, figure 5.31.a, the ZnO nanowire density distribution for ZnO grown on 10×10 mm sapphire substrate is very uneven. It increases from 1 to 10 μm^2 from the centre to the sides of the growth substrate. The middle of the sample is mostly covered with a polycrystalline film.

(ii) The level of Mg incorporation can not be controlled precisely in nanowires. This was shown by the varying PL peak positions measured on individual ZnMgO nanowires (figure 5.25.d), by different PL peak positions measured in the multiple quantum well ZnO/ZnMgO heterostructure and ZnO nanowires (figures 5.32.d,f). Not all the TEM images of the nanowires from the mulitple heterostructure sample have shown multiple heterostructure contrast.

Poor growth control may arise due to several reasons, both instrumental and fundamental.

(i) Possible instrumental reasons:

Rotation of the sample and geometry of the sample holder, which forms a wedge at the side of the sample, results in different fluxes of the gas species in the immediate proximity to the sample surface. Accumulation of species at the side of the sample may improve nanowire growth as it is known that ZnO nanowires can be grown at high pressures [27]. At the same time this accumulation may be the reason of fluctuations of Zn and Mg fluxes and thus different growth rates in different spots on the sample surface. Additionally, the point of contact between the metallic sample holder and the sample will change the temperature distribution of the sample surface.

(ii) Fundamental reasons:

Nanowires of different diameters, clusters and thin film may all have different Mg incorporation rates. The same exfoliation technique used for InAs samples to distinguish between nanowires and clusters cannot be used for ZnO nanowires, because the ZnO film has poor adhesion to substrate and after exfoliation both ZnO nanowires and thin film are removed from it.

Another reason for the poor repeatability may be our lack of full control over the gold catalyst. The chemical composition of a gold particle at the start of the nanowire growth plays a crucial role. Full control over the chemical potential in a gold catalyst is needed to achieve the global uniformity of nanowire parameters.

In conclusion, nanowire growth is governed not only by the average growth parameters (substrate temperature, beam fluxes), but as well by the local growth parameters (local nanowire temperature and local fluxes, gold particle sizes, separation and composition). The variation of the local growth parameters along a single nanowire is potentially much smaller than the variation of the local growth parameters over the whole sample, and thus properties of one single nanowire may be studied independently by different techniques and correlated among each other, providing useful information on various nanowire properties. For this reason, correlation studies on electrical and optical properties of individual ZnO nanowires have been performed and are presented in the next chapter.

5.9 Conclusion

ZnO nanowires were grown on various substrates (silicon, sapphire and ZnO). Gold catalyst nanoparticles were prepared by gold thin-film high-temperature annealing, by electron beam lithography and by gold colloidal deposition. Growth of ZnO nanowires is governed by the competing processes of the oriented growth along the (0001) direction, growth on the nanowire walls, desorption of Zn and O atoms from the surface of the substrate and of ZnO, and, in the case of silicon substrates, gold-eutectic formation at higher temperatures. The main parameters of ZnO MBE growth, such as axial and radial growth rates, ZnO film growth on Si, the efficiency of nanowire formation and others, were measured. A two-step procedure for ZnO nanowire growth on silicon was implemented, which showed improved "quality" of the grown nanowires. Nanowires are 0.5 to 4 μm long, 20 to 200 nm in diameter, with wurtzite structure and no apparent crystallographic defects, such as dislocations or stacking faults.

$Zn_{1-x}Mg_xO$ nanowires with varying Mg content x were grown on silicon and sapphire. A variety of techniques were used to study Mg incorporation into $Zn_{1-x}Mg_xO$ nanowires (SEM, HRTEM, EDX, PL, XPS and XRD). x was shown to be in the range 0–40 %. The Mg incorporation rate coefficient was measured to be 3.5 times smaller than that of Zn. It was shown that with Mg content in as-grown samples higher than 20 % some rock-salt/wurtzite phase separation occurs.

ZnO core-shell heterostructure nanowires with shells of MgO, ZnMgO of various Mg contents and thicknesses, and multiple quantum well core-shell heterostructure were grown on sapphire by growing the core at 750 °C and then reducing the temperature to 500 °C to grow the shell. HRTEM, EDX and PL have confirmed formation of the shell with little intermixing between core and shell.

The uniform growth of the wires can still be optimised to achieve complete control over the nanowire growth on the whole area of the substrate and to fabricate macroscopic arrays of core-shell heterostructure nanowires with fully reliable and reproducible properties.

Chapter 6

ZnO-based nanowires. Electronic devices

ZnO nanowires can be potentially used for a variety of electronic devices: sensors, LEDs, photodiodes, lasers, processing and memory devices *etc.* [33; 39; 47; 56]. Investigation of their electrical properties allows us to better understand their potential for use in these applications. One of the nanowire-devices that is sufficiently universal and allows the study of a wide variety of properties is the nanowire-based field effect transistor (FET). This chapter addresses the electrical and optical studies of ZnO nanowire transistors. Investigation of the spectral distribution of the defect states in ZnO nanowire transistors by current mode deep level transient spectroscopy is discussed.

6.1 Field effect transistor optimisation

The procedure of fabricating nanowire FETs is presented in section 3.5.1 (figure 6.1). Details of the FET optimisation are given below.

Any effect of the processing steps on the electronic properties of nanowire FET should be minimised in order to study nanowire properties with better accuracy. The dependence of the nanowire resistance on the processing parameters, such as Ar ion milling time, electron irradiation and contact metal choice are investigated in this subsection.

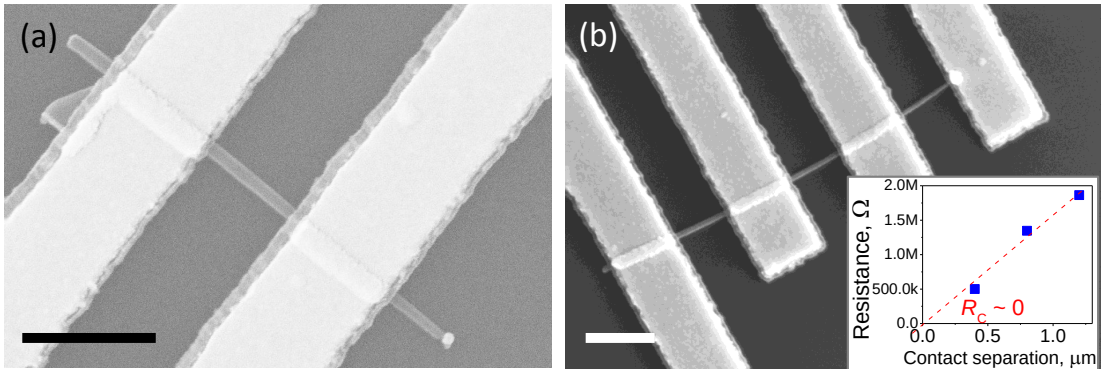

Figure 6.1: SEM images of the nanowire FETs: (a) two point probe configuration; (b) 4 point probe configuration. Scale bars are 500 nm. Inset in (b): contact resistance measurement on the 4-point-probe nanowire sample.

The procedure of Ar ion milling InAs nanowires prior to contact sputtering was reported by our group in [189]. The same procedure was used to improve contact resistance of ZnO nanowires. The dependence of the average nanowire resistance on milling time is shown in figure 6.2. Nanowire devices prepared with no milling did not show any measurable current through the nanowire. If milled longer than 2 minutes, the nanowire dimensions are reduced and the resistance of the nanowire increases. A resistance minimum is observed after about 1 minute milling time. All nanowire devices were therefore milled for 1 minute prior to contact sputtering.

The effect of the subsequent choice of contact material on nanowire resistance was investigated. Ti, Al and Nb metals were compared. No dramatic difference in resistance could be observed for Ti and Al contacts (figure 6.3). However, Ti and Al contacts have average resistance approximately 3 times lower than that of Nb contacts. The work functions of Al, Ti and Nb are 4.19–4.28 eV, 4.10–4.33 eV and 4.30 eV respectively [229; 230]. This is lower than the work function of ZnO – 4.5 eV [a]. This difference in work functions between ZnO and all three metals (Al, Ti and Nb) result in Ohmic contacts to ZnO (figure 3.15.b,c). The small difference between contact resistances may be also caused by the nanowire

[a]It should be noted, that values of ZnO work function ranging from 3 to 5 eV have been reported. Moreover, these values may be altered by oxygenation, annealing, doping and other methods. We take the value averaged over a number of publications [231–233].

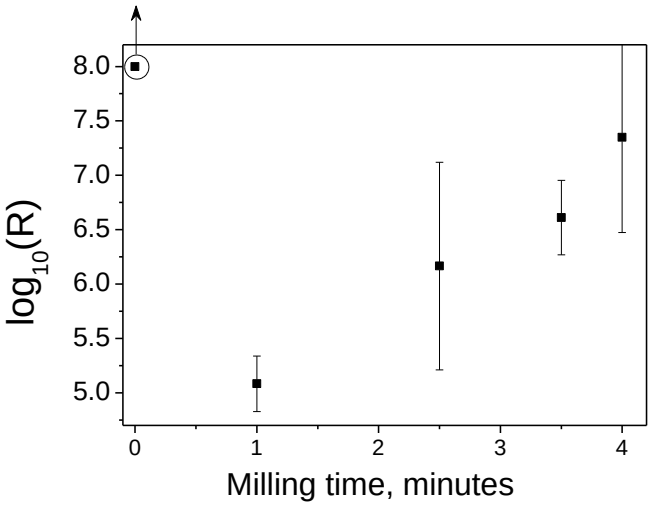

Figure 6.2: Dependence of the average nanowire resistance on Ar ion milling time before contact metallisation.

surface. It may have a high density of surface states that pin the Fermi level and thus eliminates the effect of different contact materials for Al and Ti, or it can indicate that sputtered metals are highly energetic and thus diffuse into the nanowire, doping it and reducing the contact resistance.

The contact resistance was investigated at room temperature on several 4-point-probe contacted nanowires with Al-contacts (figure 6.1.b and the inset). For this particular nanowire shown in the figure, the contact resistance may be regarded as 0. However, the contact resistance varies from nanowire to nanowire and may reach up to 5 % of the nanowire bulk resistance. Overall, even in the case of the highest contact resistance, it can be neglected in room temperature transport measurements.

SEM was used to image nanowires in order to design contact patterns. This procedure has a certain drawback, as the electron beam may damage the nanowires and change their electrical properties. A comparison between SEM and optical imaging for design patterning was carried out and is shown in figure 6.3.b. No considerable difference in resistances is observed between these two processes. On the other hand, use of SEM results in much higher yield of nanowire devices per chip – up to 90 % as opposed to 25 % for optical microscope imaging. Hereafter,

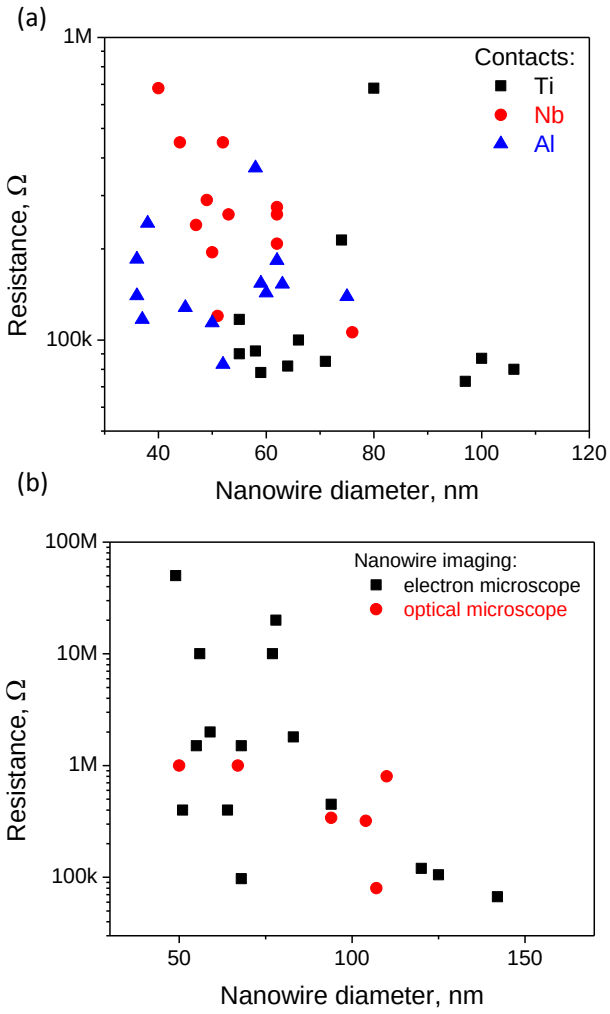

Figure 6.3: Diameter dependence of the room temperature nanowire resistance: (a) for nanowires with contacts of different metals; (b) for nanowires imaged by optical and electron microscopy prior to the EBL contact patterning process.

only SEM imaging is used in this work in order to improve efficiency of FET fabrication.

6.2 Electrical measurements on ZnO nanowires

Electrical transport measurements of a nanowire FET allow evaluation of various important nanowire parameters, such as carrier type, the value of electrical conductivity, carrier mobility, carrier concentration, the electrical transport mechanism, thermal activation energy *etc.* Along with providing information on material properties, these values give insight into the possibilities for device fabrication. This chapter presents experimental details of transport properties of ZnO nanowires at room and cryogenic temperatures, discusses possible transport mechanisms and compares two different ZnO nanowire types: those grown on a silicon substrate and those grown on a sapphire substrate.

6.2.1 Room temperature transport measurement

Room temperature FET measurements have been carried out on approximately 300 conductive nanowires. All the wires show linear behaviour in their 2-point IV characteristics which indicates Ohmic contacts (figure 6.4.a). Dependence of the 2-point resistance on nanowire diameter is shown in figure 6.5, where the vast majority of the wires have resistances ranging between 50 kΩ and 60 MΩ.

FET characteristics were measured on these wires. IV characteristics at different gate voltages are shown in figure 6.4.a. The resistance decreases at positive gate voltages which indicates the n-type conductivity of the wires. This unintentional ZnO n-type doping is universally observed and is variously attributed to H atoms, Zn interstitials and Zn_i-N_O complexes [182–184]. FET transfer characteristics (*i.e.* the dependence of the drain-source current on the gate voltage at a fixed drain-source voltage of 0.2 V) are shown in figures 6.4.b and c. Depending on the wire and on the measurement conditions, the threshold voltage varies from –30 to –5 V. As was mentioned earlier in section 3.5.3.3 equation 3.39 on page 85, the threshold voltage depends on the density of surface states and on the carrier concentration. Thus this large scatter of threshold voltages may indicate both

varying density of surface states and varying carrier concentration in the nanowires. Some of the nanowires exhibit hystereses in their transfer characteristics (figure 6.4.c, inset). They are attributed to the surface states that charge and discharge at positive and negative voltages respectively, and thus affect the transport behaviour. From the difference in the threshold voltages V_T for the forward and backward curves we can estimate the density of the recharging surface states $N_{ss} \sim 10^{11}$ cm^{-2} (equation 3.39).

The carrier mobility and the effective carrier concentration in nanowires were calculated from the linear sections of transfer curves and from IV-curves according to equations 3.39 and 3.41.

The field effect mobility ranges from 1 to 60 cm^2/(V·s) (figure 6.6.a) with an average mobility of approximately 15 cm^2/(V·s). These numbers are in a good agreement with the literature [166; 171–174]. The highest mobilities of 40 to 60 cm^2/(V·s) are observed in nanowires with diameters 50 to 100 nm. These nanowires also experience the largest scatter of mobility. The mobility of the nanowires with higher diameters is less scattered and approaches values of 10 cm^2/(V·s). A large variation in the mobility values may be caused by non-uniformity of the growth conditions for nanowires with low diameters which affects the concentration of scattering centres both in the core and on the surface of the nanowire.

The dependence of the effective carrier concentration on the nanowire diameter is shown in figure 6.6.b. The average effective carrier concentration is approximately 10^{19} cm^{-3}. From this value of the carrier concentration and the effective density of states in ZnO conduction band ($N_c \sim 4\times10^{18}$ cm^{-3}, [205]) we estimate that the Fermi level is located 0.02 eV above the conduction band minimum (figure 3.15). The carrier concentration varies much more in nanowires with lower diameters. At higher diameters, the carrier concentration stabilizes and decreases a little, approaching values of 3×10^{18} cm^{-3} in 200 nm diameter nanowires. This large scatter of the carrier concentration values for nanowire diameters below 100 nm may be related to the varying surface state spectra (section 3.5.3.3). Large variation in the density of the surface and bulk defects may be caused by the unstable growth dynamics in nanowires with small diameters.

After observing non-uniformities in the electrical properties of ZnO nanowires

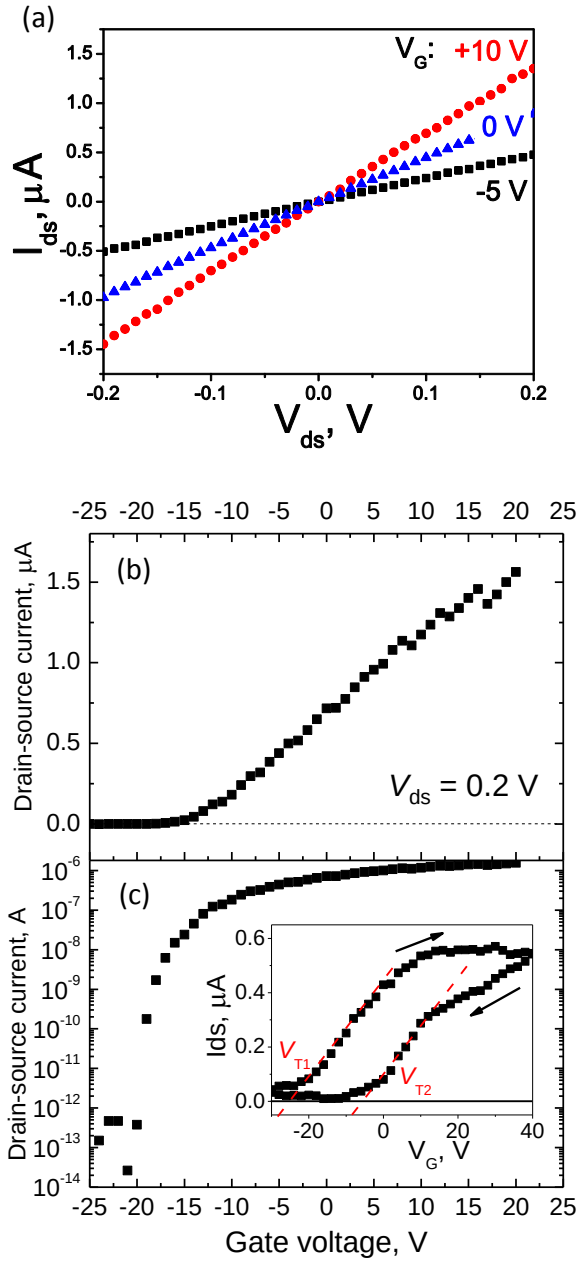

Figure 6.4: Nanowire FET characterisation: (a) IV characteristics at different gate voltages; (b-c) transfer characteristic in linear (b) and semi-logarithmic (c) plots. Inset in (c): transfer characteristic of a different nanowire showing hysteresis in the forward and backward scan directions.

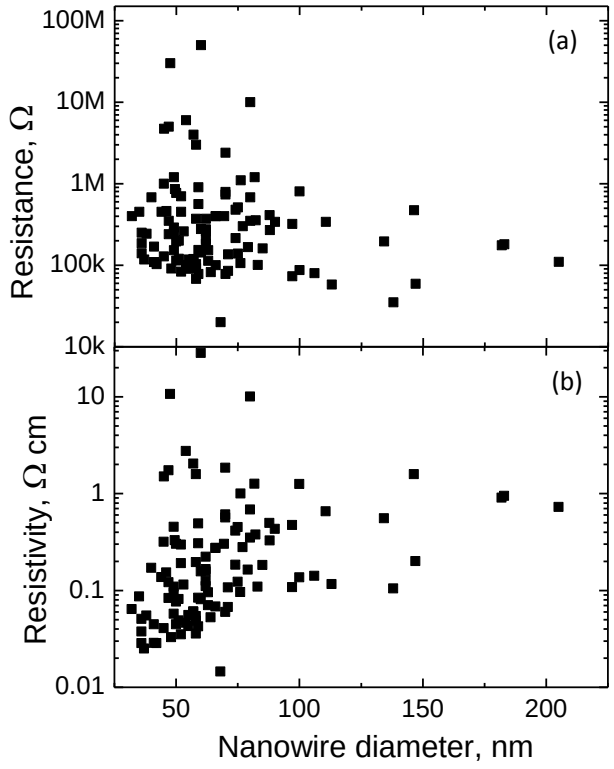

Figure 6.5: Resistance (a) and resistivity (b) of all the ZnO nanowires measured.

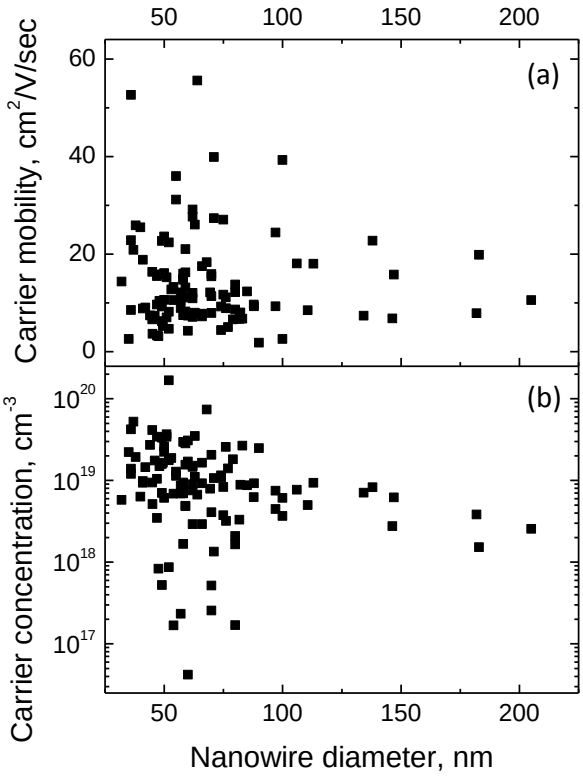

Figure 6.6: Nanowire diameter dependence of carrier mobility (a) and carrier concentration (b) inferred from transfer and IV characteristic measurements.

due to inhomogeneous growth dynamics, we may pose the following question: is this inhomogeneity inherent to the ZnO nanowire growth or does it depend on the macroscopic growth conditions such as substrate rotation, tilt and temperature variations? If inherent, then the transport properties such as mobility and carrier concentration in one nanowire will fluctuate over the length of one nanowire. If it is not inherent, however, the mobility and the carrier concentration in one nanowire will be similar throughout its length, because the macroscopic growth conditions may be regarded as constant in such a small volume. In order to answer this question, multiple contacts (*i.e.* more than two) were made to nanowires longer than 2 microns (figure 6.1.b). Multiple contacts allow measurements of transport characteristics at different places in one nanowire. Multiple measurements of the mobilities and carrier concentrations were done on each of the three different nanowires and are shown in table 6.1. Close accordance between the measured values in each nanowire confirms homogeneity of the main properties in each single nanowire. This result suggests different macroscopic growth dynamics for each nanowire.

Table 6.1: Multiple mobilities and carrier concentrations measurements done on each nanowire in different places.

Nanowire No.	Mobilities, $cm^2/(V{\cdot}s)$	Carrier concentration, $1{\times}10^{18}$ cm^{-3}
No. 1	14.7 and 13.2	7.7 and 6.8
No. 2	11.3 and 10.5	6.9 and 6.9
No. 3	9.2 and 8.8	7 and 9

In conclusion, electron mobility and carrier concentration were measured in ZnO nanowire FETs. These values ranged over 2–3 orders of magnitude for different nanowires. In nanowires with small diameters (below 100 nm), the variation of the carrier mobility and of the carrier concentration is large, whereas in nanowires with diameters larger than 100 nm, mobility and carrier concentration saturate to values of 10 $cm^2/(V{\cdot}s)$ and $3{\times}10^{18}$ cm^{-3}, respectively. The scatter of transport characteristics is attributed to the different growth dynamics over the growth substrate, which affects mainly small diameter nanowires (less than 100 nm) by randomly introducing impurities and point-defects in the nanowire

bulk and on the surface.

6.2.2 Temperature dependence

Temperature dependent measurement of the transport properties give information on transport mechanisms, the main scattering mechanisms, contact barrier values, energy positions of shallow donors and other nanowire characteristics. Figure 6.7.a shows ZnO nanowire IV-curves at different temperatures. The resistance of the nanowires (calculated in this case as $R = V_{\mathrm{ds}}/I_{\mathrm{ds}}$) decreases with increasing temperature (figure 6.7.b). This can be explained by multiple mechanisms: the activation mechanism of the Schottky contacts (figure 3.15.a), the activation mechanism of Ohmic contacts (figure 3.15.b), a reduction in carrier concentration, or a decrease of the carrier mobility. Thermal activation process can be described by the simple exponential term $\sim \exp(-E_a/k_{\mathrm{B}}T)$. Activation energies calculated from Arrhenius plots (dependence of the logarithm of resistance on the inverse temperature) at temperatures higher than 50 K range from 20 to 60 meV and seem not correlate with any other characteristics of the nanowire.

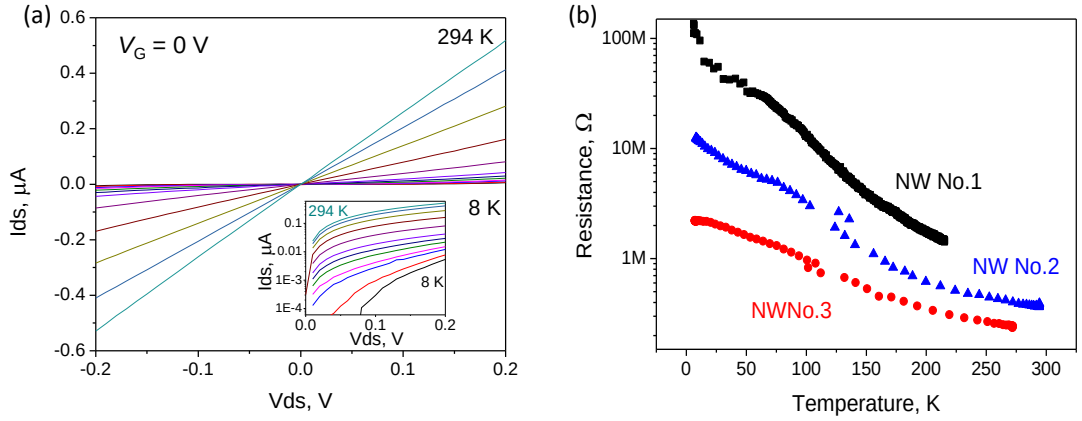

Figure 6.7: Temperature dependent measurements: (a) IV characteristics at temperatures ranging from 294 to 8 K, inset: semi-logarithmic plot of the positive branch of IV characteristics at different temperatures; (b) temperature dependence of resistance of various nanowires.

Whereas at high temperatures nanowires exhibit Ohmic behaviour, at temperatures below 60 K nanowires start showing non-linear behaviour. The nanowire

IV curves at low temperatures (figure 6.8.a) have different slopes at zero-voltage bias and at 0.2 V voltage, which indicate a higher resistance at lower voltage and a lower resistance at higher voltages (figure 6.8.b). This behaviour can be explained by the band bending diagram in figure 3.15.b section 3.5.3.1, where the nanowire-metal contact is the Ohmic contact with a small barrier, which can be overcome by the application of positive voltage. This behaviour might occur only if the Fermi level in the nanowire bulk lies below the conduction band. This is valid if the carrier concentration is smaller than 3×10^{18} cm^{-3}, which is not true for the ZnO nanowires in this work [a]. If the Fermi level in the bulk of the wire lies above the conduction band minimum, then the increase of resistance at low temperatures can be ascribed to a Schottky barrier with small activation energy (figure 3.15.a). The IV curve shape at low temperatures may be explained by the lowering of a barrier by image forces (chapter 3.5.3.1). Some researchers argue [213] that this behaviour can be explained by Efros-Shklovsii variable-range hopping conduction with strong electron-electron interaction. Here we will not consider this case since it was not confirmed by the temperature dependence of the nanowire resistivity.

These potential descriptions (*i.e.* Ohmic contact with a small barrier and Schottky contact with image force barrier lowering) indicate that there are two components of resistance: zero-bias resistance and high bias resistance. At zero voltage bias the IV-curve gives information on the barrier properties and are exponentially dependent on the drain-source voltage. At high bias, when the contact potential barrier flattens, the IV-curve, and the differential resistance in particular, shows behaviour corresponding to the bulk of the wire. The bulk resistance R_{bulk} depends on the intrinsic nanowire properties, the carrier mobility and the carrier concentration: $R_{\text{bulk}} = l/(S\sigma) = l/(Sn\mu q)$, where l is the distance between the contacts, S is the nanowire cross-sectional area, σ is the nanowire conductivity, n is the carrier concentration, μ is the carrier mobility and q is the elementary charge. The net resistance of the nanowire R_{net} is the sum of the contact resistance R_C and the bulk resistance R_{bulk}: $R_{\text{net}} = R_C + R_{\text{bulk}}$. Therefore the more accurate contact resistance value can be found by subtracting R_{bulk} from

[a] Although this explanation was used in the paper [170] for nanowires with the same carrier concentration of 10^{19} cm^{-3}.

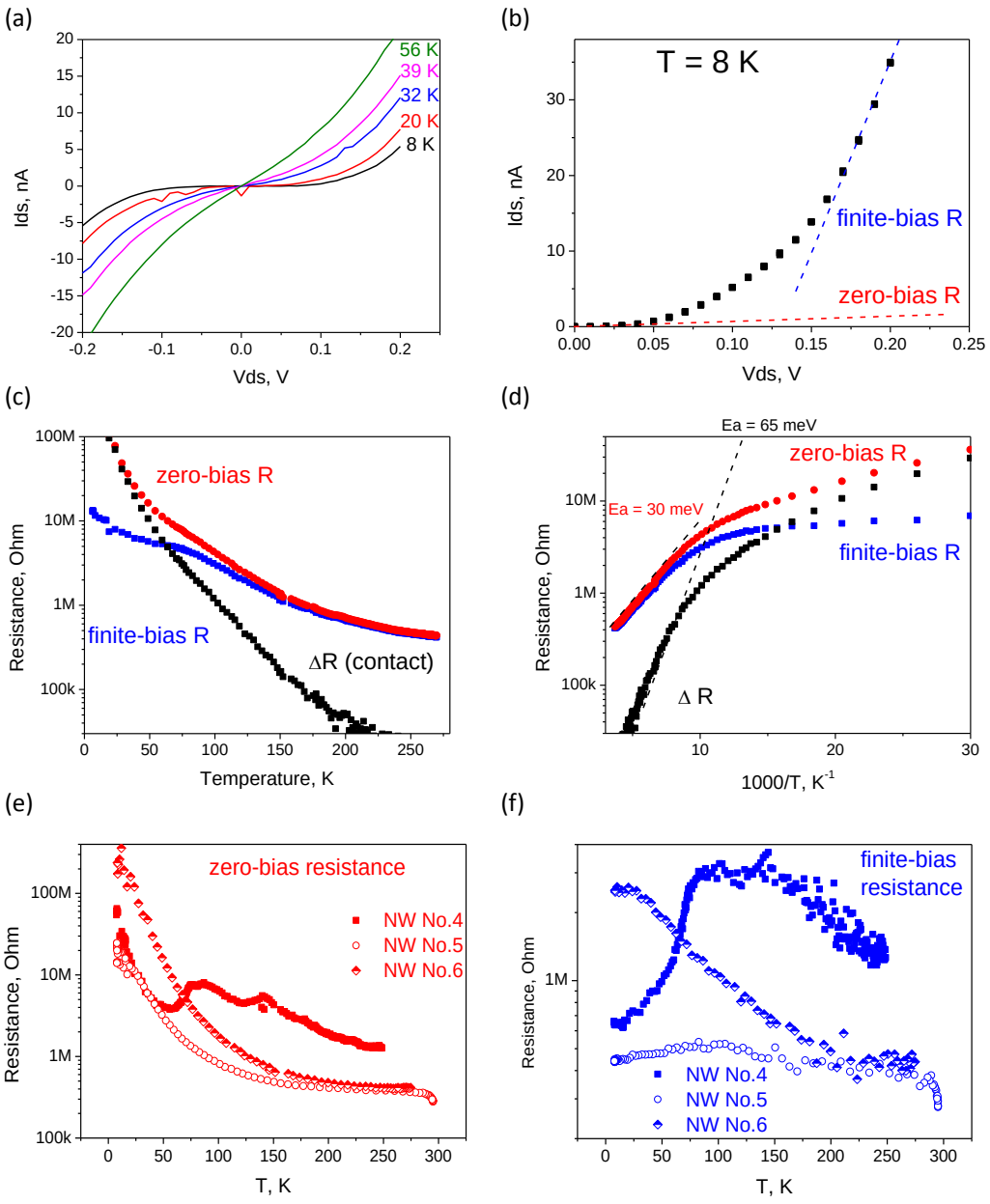

Figure 6.8: Temperature dependent measurements: (a) low temperature IV curves showing non-linear behaviour; (b) illustration of zero-bias and finite-bias resistances; (c-d) dependence of nanowire resistance on temperature (c) and inverse temperature (d) showing activation energies for two resistance types; (e-f) temperature dependence of zero-bias (e) and 0.2 V-bias (f) nanowire resistances for 3 different ZnO nanowires.

R_{net}.

We have investigated resistances calculated from the slope at zero bias (zero-bias resistance), at 0.2 V bias (finite-bias resistance) and the difference between these values ΔR. Figures 6.8.c–f show the temperature dependences of zero-bias and the finite-bias resistances and ΔR. The finite-bias resistance has either a kink (nanowire No.2,6), or saturation (nanowire No.5, a "metallic-like" behaviour [234; 235]) or even a reduction in magnitude (nanowire No.4) at low temperatures and unlike the zero-bias resistance does not usually have an activation behaviour. For the wire No.5 (figure 6.8.f, open circles) these values are nearly constant at different temperatures. Some nanowire resistances increase at lower temperatures and they exhibit activation behaviour. The activation energies range between 20 to 60 meV (figure 6.8.d, red curve). As the finite-bias resistance accounts for the bulk properties of the nanowire, these values may indicate the shallow donor energy. It should be noted that ideally, in order to measure the bulk resistance, the linear part of the IV curve at high voltages should be reached. For some nanowires, it may be that a 0.2 V bias voltage is not large enough to reach the situation of the full barrier flattening. Higher drain-source bias voltages were not applied to the nanowires, as they are often destroyed by the higher voltage bias.

We assume that the difference resistance ΔR gives information on the nanowire-metal contact (figure 6.8.c,d, black curve). It is complicated to measure zero-bias resistance at low temperatures with high accuracy, as the IV-curves should be differentiated with very high precision around 0 V. Therefore, measurements performed at temperatures below 50 K show underestimated resistance values. The activation energies calculated from the high temperature part of the $\Delta R(T)$ dependence give values for the contact barrier between 60 and 100 meV (figure 6.8.d). These values indicate the Schottky barrier height for ZnO nanowires with Al/Ti metal contacts.

The carrier mobility and carrier concentration are bulk characteristics of the ZnO nanowires, therefore only the bulk (or finite-bias) resistance can be used for their estimation. The mobility and carrier concentration were extracted from the gate voltage dependence of the finite-bias resistance at different temperatures. Data measured on two nanowire FETs is shown in figure 6.9. Both nanowires have similar temperature dependences of the carrier mobility with mobility increasing

at lower temperatures. Double logarithmic plots of the temperature dependences of the carrier mobility (insets in figures 6.9) show that the mobility varies as T^{-1}. This indicates the complex scattering mechanism involving acoustic and optical phonons, and was observed in other polar materials, such as n-type GaAs [205]. The carrier concentration behaves differently for these nanowires. Nanowire No.5 has weak decrease in concentration from 5×10^{18} to 3×10^{18} cm^{-3} at 100 K and then increase at lower temperatures. Carrier concentration of the nanowire No.6 decreases dramatically from 3.5×10^{19} cm^{-3} down to 2×10^{18} cm^{-3}, fitting of the Arrhenius plot gives energy 40 meV – the position of the shallow donor relative to the conduction band minimum.

In summary, low temperature transport characteristics of ZnO nanowires have been investigated and allowed the study of different conductivity mechanisms, defined by the contact properties and the bulk nanowire properties. The dependence of the nanowire FET drain-source current on voltage, temperature and gate voltage is a valuable tool to study nanowire FET properties and compare different types of the nanowire FETs. The next subsection describes application of these methods to ZnO nanowires grown on different substrates: silicon and sapphire.

6.2.3 Comparison between nanowires grown on silicon and sapphire.

The electrical properties of nanowires grown on (a) silicon and (b) sapphire were measured and compared. Nanowires were grown on sapphire at 750 °C and on silicon by the two-step-method at 750 °C for 10 minutes and at 850 °C for 2 hours. The diameter distribution of measured nanowires is shown in figure 6.10.a. Nanowires grown on sapphire have much smaller diameter range than those grown on silicon (table 6.2). This might be caused by the more uniform distribution of gold particles on sapphire than on silicon. The diameter dependences of the mobility (figure 6.10.b) show that nanowires grown on silicon and sapphire have similarly scattered mobility, with average values of mobility of 15 and 12 cm^2/(V·s), respectively.

The diameter dependence of the carrier concentration (figure 6.10.b) shows that some nanowires grown on silicon have very low apparent carrier concentra-

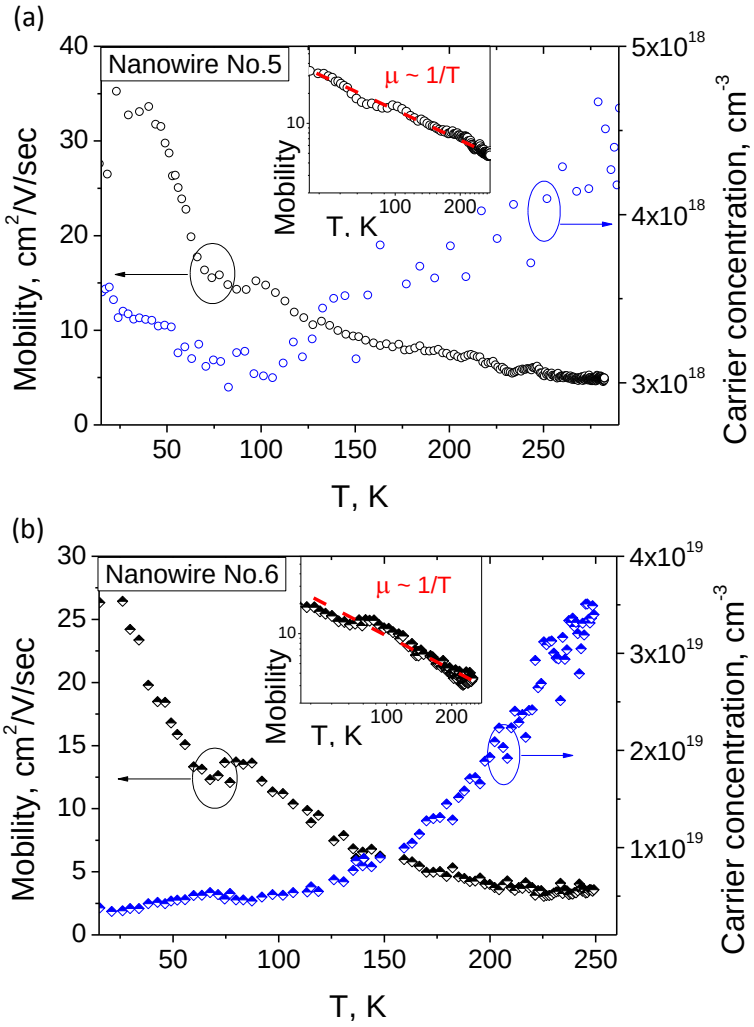

Figure 6.9: Temperature dependence of the field effect carrier mobility and the carrier concentration extracted from the finite-bias resistance on two nanowires: (a) No.5 and (b) No.6. Insets show logarithmic plots of the temperature dependence of the mobility.

tion ($< 10^{18}$ cm^{-3}) as opposed to the nanowires grown on sapphire. This may indicate the presence of the surface states in the nanowires grown on silicon. The measurement on the wires with diameters below 100 nm and with the actual carrier concentration below 1×10^{19} cm^{-3} are dramatically affected by the presence of surface states. The blue and green curves in figure 6.6.b show the theoretical diameter dependence of the apparent carrier concentration for nanowires with the same actual carrier concentration of $N_d = 7 \times 10^{18}$ cm^{-3} and fixed negatively charged surface level density $N_{ss} = 1.3 \times 10^{13}$ cm^{-2} for blue curve and $N_{ss} = 7 \times 10^{12}$ cm^{-2} for green curve, equation 3.43. Considering low diameter nanowires, on average nanowire grown on silicon have higher surface state density than nanowires grown on sapphire.

Table 6.2: Diameter, mobility and carrier concentration measured on nanowires grown on different substrates.

Grown on	Diameter nm	Mobility at RT cm^2/(V·s)	Carrier concentration cm^{-3}
Si	100 ± 40	15 ± 11	8×10^{18}
Al_2O_3	55 ± 10	12± 7	1.4×10^{19}

Although there are some minor differences in the statistical study on these nanowires, there exist nanowires of the same diameters, mobilities and carrier concentrations grown on different substrates that are indistinguishable in their room temperature transport characteristics.

The temperature dependences of the resistance and the mobility of two nanowires (one grown on Si and one on sapphire) are shown in figure 6.11. The nanowires were chosen to have similar resistances, diameters and carrier concentrations (300 kΩ and 1 MΩ, 55 nm and 49 nm, 2.5×10^{18} cm^{-3} and 1.3×10^{18} cm^{-3} – for those grown on sapphire and silicon, respectively).

Figure 6.11.a shows that the nanowire grown on silicon becomes insulating below 50 K, whereas the nanowire grown on sapphire conducts at much lower temperatures, some still conducting at liquid helium temperatures. Figure 6.11.a shows that at high temperatures, when Ohmic behaviour dominates the transport properties, activation energies of the bulk resistances in both types of nanowire are

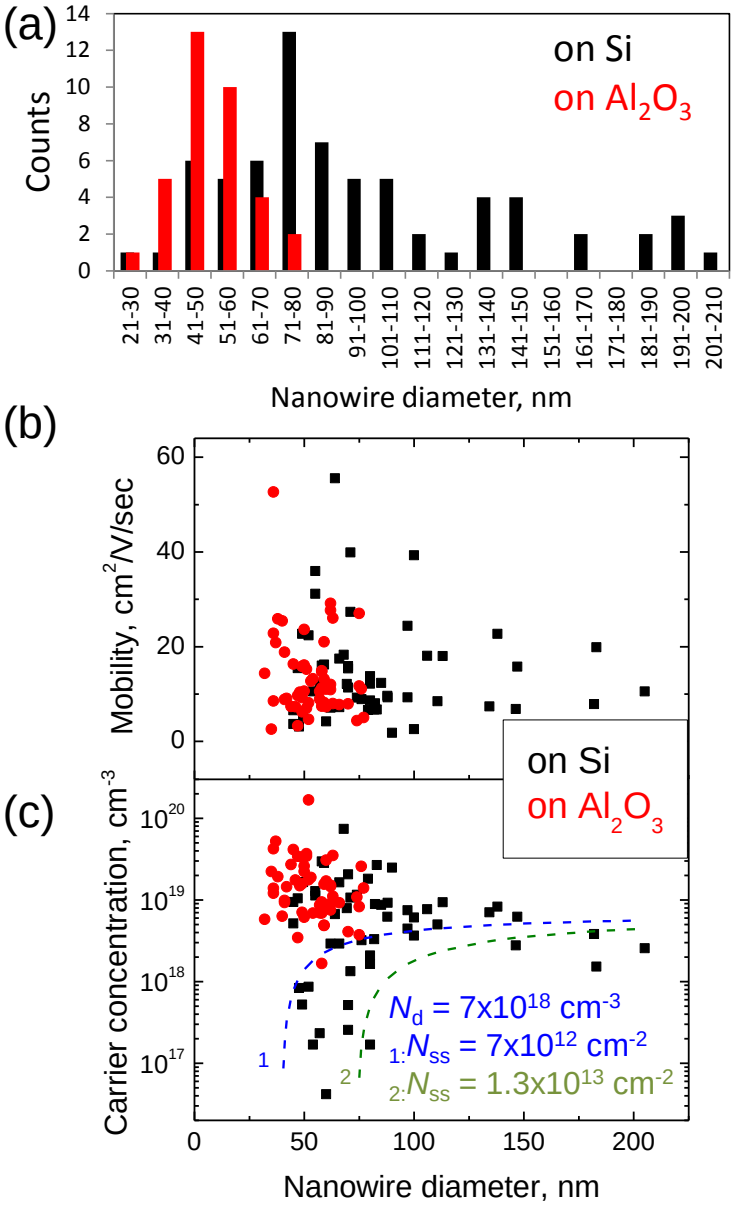

Figure 6.10: Comparison between nanowires grown on silicon and on sapphire: (a) diameter distribution; (b) nanowire diameter dependence of carrier mobility and (c) carrier concentration.

similar (30 meV and 32 meV in figure 6.11.a, or 20–60 meV in all the nanowires), and activation energies of the contact resistances are similar as well (80 meV and 100 meV).

However, at lower temperatures the behaviour is drastically different: ZnO nanowires grown on silicon become insulating, but the resistivity of the nanowire grown on sapphire saturates, showing "metallic-like" conductance. These two distinct behaviours of the nanowires grown on silicon and on sapphire at low temperatures hold true for all the measured samples. This dramatic change in resistance may be caused by the change in both bulk nanowire conductivity and in the contact resistance. The Schottky contact resistance cannot account for the change in conductivity, since the Schottky barriers heights extracted from the temperature dependences of the contact resistance are similar for both types of nanowires (100 meV and 80 meV). Thus only the difference in the bulk properties of the nanowires account for different transport behaviour at low temperatures.

The bulk resistance of the nanowires may vary due to the different types of dopants. It is known that Al is a shallow donor in ZnO with the energy level position at 50–120 meV [182; 236], *i.e.* the migration of Al from the Al_2O_3 substrate during the growth may cause it. In addition to a different growth substrate, different growth temperatures may have an effect on shallow donor concentration. Growth at higher temperatures (for samples grown on silicon) may reduce the number of Zn_i-N_O complexes and H atoms, which act as shallow donors in ZnO with activation energies ∼30 meV [182–184; 236]. Since the room temperature and low temperature behaviours differ so much, at least two types of donors determine nanowire transport properties. The first donors, with activation energy of ∼20–60 meV, determine the room temperature conductivity in the nanowires grown both on silicon and sapphire. At low temperatures the first donors freeze out, and only donors left in the nanowires grown on sapphire (like Al, or H, or Zn_i-N_O complexes) determine the position of Fermi level and thus the nanowire conductivity. For nanowires with metallic temperature dependences of bulk resistance, donors form an an impurity band that controls the transport behaviour at low temperatures.

Figure 6.11.b shows temperature dependences of the carrier mobility. Mobility of the nanowires grown on sapphire behaves as the usual semiconductor – it in-

creases with decreasing temperature. Nanowires grown on Si cannot be analysed in a similar fashion since at low temperatures the contact resistance becomes the main current limiting factor and the usual method of obtaining mobility (equation 3.39) is not valid anymore. The decrease of mobility at lower temperatures depicted in figure 6.11.b, black squares, does not represent a physical decrease in mobility but is an artefact of the measurement.

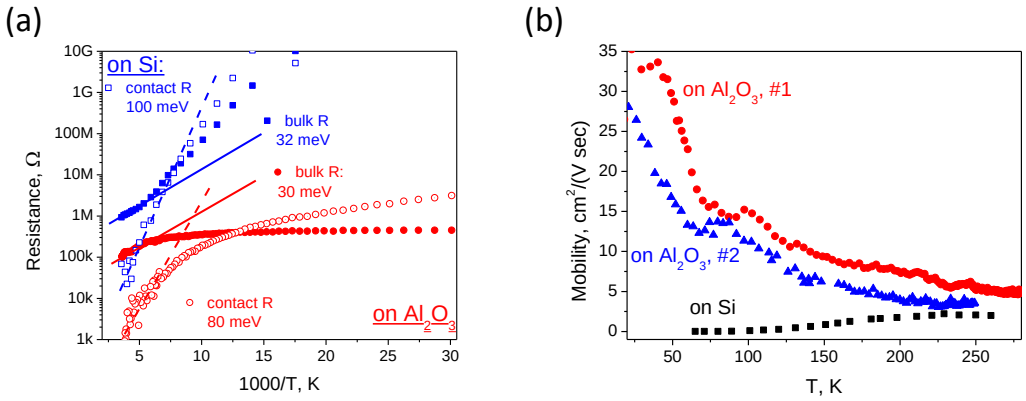

Figure 6.11: Comparison between nanowires grown on silicon and on sapphire at low temperatures: (a) dependence of resistance on inverse temperature; (b) temperature dependence of nanowire carrier mobility, inset: transfer characteristics of these nanowires at room temperature.

In conclusion, transport measurements on nanowires grown on different substrates have shown different charge dynamics in those nanowires. The low temperature conductivity of the nanowires grown on sapphire is likely to be caused by the higher density of shallow donors (H, Zn_i-N_O complexes or Al). Al diffuses from the sapphire substrate into the nanowire during the high-temperature growth. H and Zn_i-N_O complexes diffuse out of the nanowire at higher temperatures of the nanowire growth on silicon.

6.3 Optical measurement on ZnO nanowires

Optical measurements on individual nanowires may supply useful information on the materials properties of nanowires, such as the band gap size, the presence

of shallow and deep defects and the spectral properties of the centres for the radiative and non-radiative recombination.

Measuring optical properties on a single nanowire is a challenging task due to the small dimensions of nanowire (*i.e.* the width of the nanowire is smaller than the diffraction limit of optical microscopes). Micro-photoluminescence and cathodoluminescence are two of the available techniques to do so.

6.3.1 Cathodoluminescence

Room temperature cathodoluminescence (CL) measurements were carried out with Dr Paul Edwards at the University of Strathclyde. CL mapping resulting in hyper-spectral images, *i.e.* having the full CL spectrum at each pixel, was used to investigate luminescent features in nanowires and clusters. Figure 6.12.a shows an SEM image of the part of the ZnO nanowire sample grown on sapphire next to a scratch in the catalyst gold layer. Two isolated nanowires are seen in this image. The hyper-spectral image of this area was processed using principal component analysis [237]. CL maps of the same area are shown in figures 6.12.b and c. Figure 6.12.b shows the intensity map. Both ZnO thin films and nanowires give strong CL signal as expected. The intensity slightly varies over ZnO due to different adsorbents, structure thickness fluctuations and impurities. Figure 6.12.c shows the band-edge peak position map. The band-edge peak varies from 3.25 to 3.35 eV. The film and clusters have, in general, a lower peak position (3.25 to 3.3 eV) than the nanowires ($\sim$3.3 eV). In order to study the band-edge recombination in one nanowire, a line-scan was recorded from the bottom right nanowire (figure 6.12.e,f). This figure shows that the band-edge and defect band peak positions (3.3 eV and 1.8 eV respectively) are constant over the length of the nanowire. On the other hand, the intensity of the band-edge peak decreases in intensity at the top of the wire, while the defect band (at $\sim$1.8 eV) is constant in intensity over the length of the nanowire. This might indicate different growth dynamics at the beginning and at the end of the growth, and thus different incorporation of defects which increase non-radiative recombination. Although CL is a powerful tool to investigate the optical properties of the nanowires, the electron beam damages them. It reduces the luminescent intensity of a nanowire, bending

it due to heating, evaporates atoms from it *etc.* Using optical excitation may be more useful way to investigate nanowire optical properties.

6.3.2 Photoluminescence

6.3.2.1 Nanowires grown on Si and on Al2O3

The optical properties of ZnO nanowire field-effect transistors were measured by micro-PL at room temperature. The majority of the nanowires have high luminescent intensity and thus can provide useful information. Figure 6.13.a shows the band-edge region of PL spectra of one representative chip with twenty four nanowire FETs. The band-edge emission peak consists of several overlapping narrower peaks, free, donor-bound and acceptor-bound excitons, two-electron satellites *etc.* (figure 5.20). Depending on the density of shallow donors, the band-edge emission will shift to lower or to higher energies. The PL intensity of the devices ranges over wide limits (figure 6.13.b). This might be a function of the position of the laser beam, the gold contact position, the luminescent intensity of the wire itself, the polarisation of the laser beam *etc.* No correlation of the PL intensity with any other measurable parameter of the device has been observed.

The dependence of the PL band-edge peak position on the diameter of the nanowires on silicon and sapphire is shown in figure 6.13.c. A clear difference in the optical properties is observed. Nanowires grown on silicon have a higher average PL band-edge emission peak energy and a narrower distribution of peak positions. The scatter in the PL peak position might occur due to several reasons: differences in the nanowire band gap, the carrier concentration [238], the concentration of impurities that correspond to donor-bound-exciton or acceptor-bound-exciton emission, strain *etc.*

Figure 6.13.d shows the diameter dependence of the band-edge peak FWHM of the nanowires grown on sapphire and silicon. Nanowires grown on sapphire have larger average value of PL peak FWHM (140 meV) and a larger range of FWHM, whereas nanowires grown on silicon have average value of FWHM of 100 meV becoming less scattered for nanowires with diameters larger than 100 nm. The decrease of FWHM and tendency toward one value at high diameters is similar to the diameter dependences of the nanowire carrier concentration and

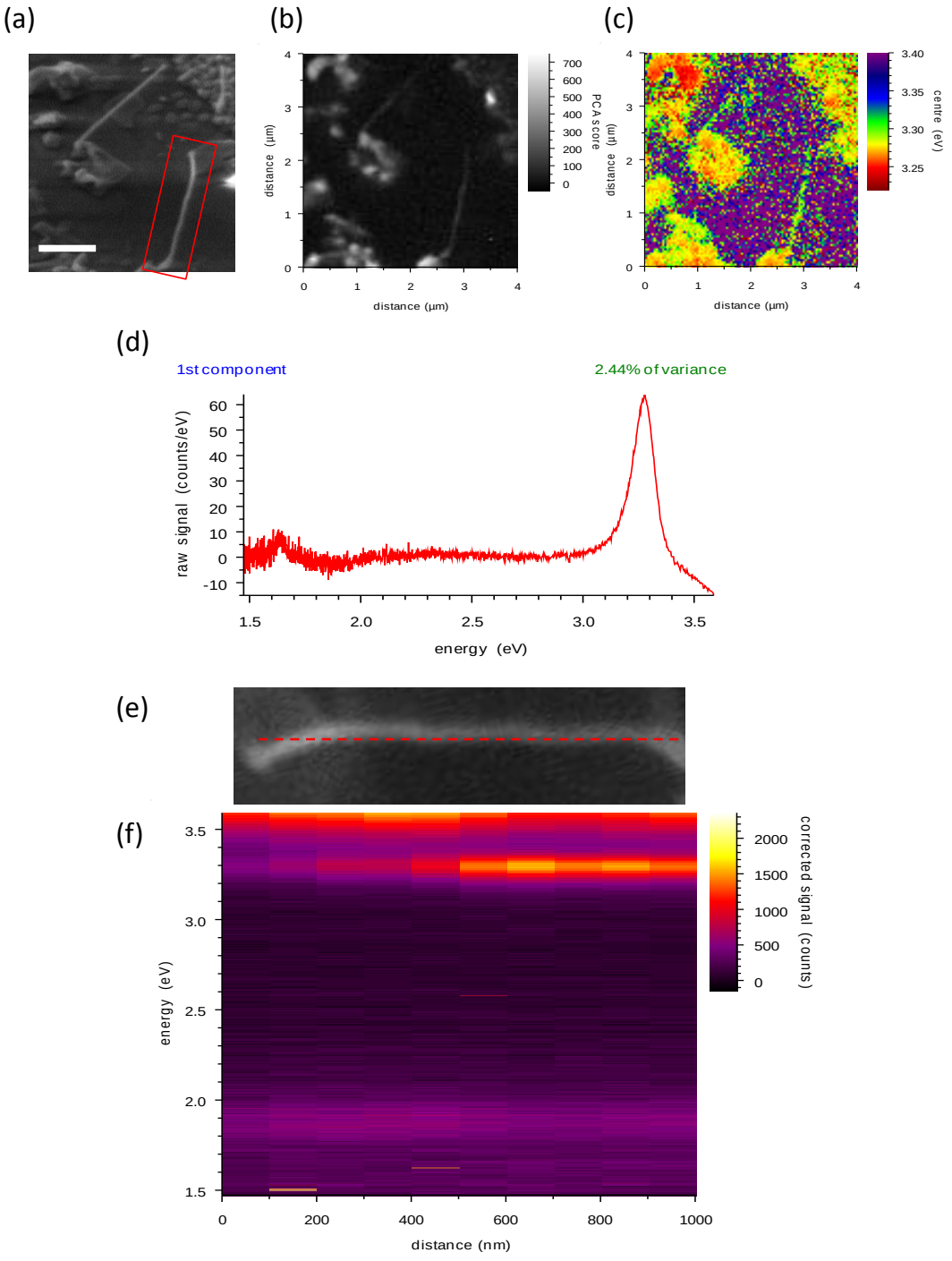

Figure 6.12: Cathodoluminescence of ZnO nanowires: (a) SEM image of representative as-grown sample with two nanowires over the scratch, (b) same area map of the integrated intensity, (c) same area map of the highest peak energy position, (d) spectrum of 1st component of the principal component analysis of the nanowire, (e-f) PL spectral line scan along the ZnO nanowire.

the carrier mobility described in the section 6.2.1.

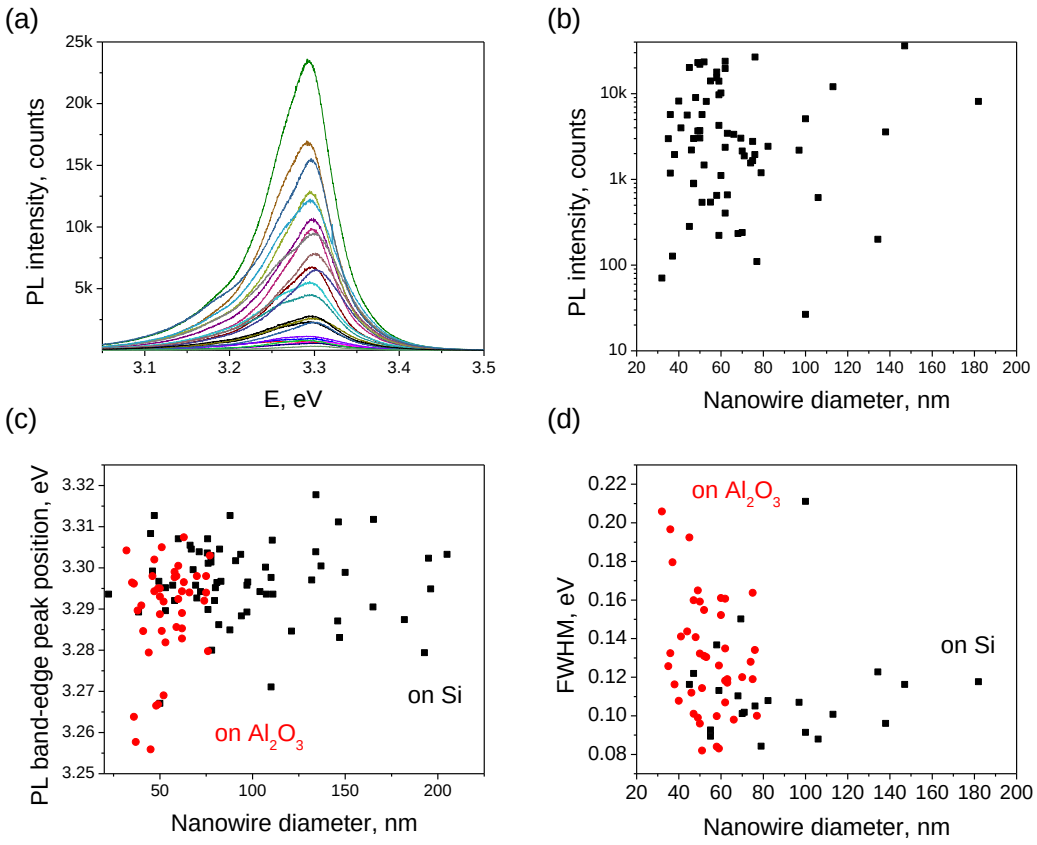

Figure 6.13: Photoluminescence of ZnO nanowire FETs: (a) Band-edge PL spectra of the 20 nanowires taken from one chip, (b) diameter dependence of the intensity of nanowire band-edge peak taken from several chips, (c) diameter dependence of the PL band-edge peak position (a) and of this peak's full width at half maximum (b) for nanowires grown on silicon (black) and on sapphire (red).

The dependence of FWHM on the PL peak energy position depicted in figure 6.14.a shows an approximately linear trend for nanowires grown on sapphire. This linear trend may be explained by the following model. The band-edge emission consists of several closely located unresolved peaks (free exciton, donor-bound exciton emission, two electron satellites *etc.* (figure 6.14.b). If, for example, the intensity of the lower energy peak increases, the net peak will shift to the lower energies and at the same time the FWHM will expand. The behaviour of the two closely located Gaussian peaks have been modelled to confirm this hy-

pothesis. Model example for two levels, one with the peak position at 3.29 eV and FWHM of 0.1 eV and another with the peak at 3.24 eV and FWHM of 0.18 eV is shown in figure 6.14.a, open circles. The model repeats the general trend of increase of the FWHM with the decreasing PL peak position. However, the fit is not perfect possibly due to non-Gaussian peak shape and due to the presence of more than two peaks.

The model suggests that ZnO nanowires grown on sapphire have several distinct levels that participate in radiative recombination. On the other hand, nanowires grown on silicon do not exhibit this behaviour. This can be explained either by the absence of the distinct peaks in the luminescence spectra, or by the presence of a single dominant peak. The distinct peaks in the PL of the nanowires grown on sapphire may be attributed to the exciton bound to some distinct donor which is not present in the nanowires grown on silicon. This explanation is confirmed by the low-temperature transport behaviour of ZnO nanowires grown on different substrates (6.2.3, table 6.14). Conductivity at low temperatures observed in ZnO nanowires grown on sapphire may be defined by the extra shallow donor which is absent in the nanowires grown on silicon. As was suggested before, this donor may be Al dopant from the substrate, Zn_i-N_O complex or H atom.

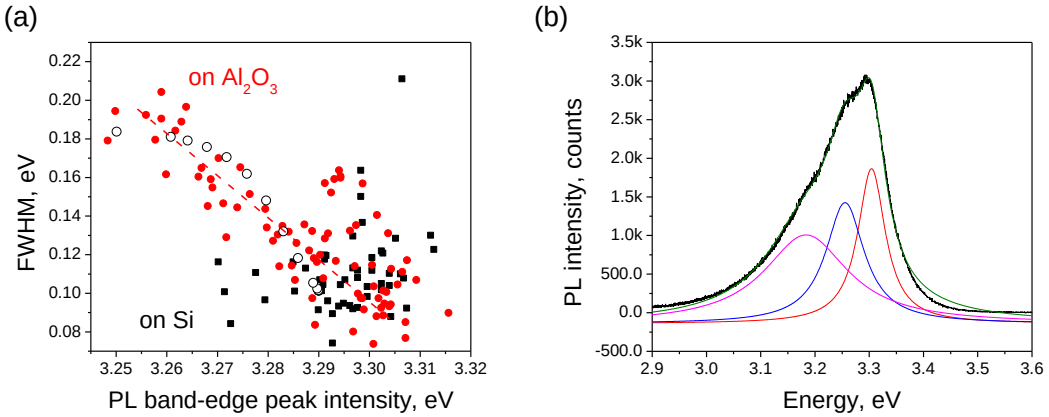

Figure 6.14: (a) Dependence of the FWHM of the nanowire band-edge PL peak on the PL peak position for nanowires grown on silicon and on sapphire, open circles are the model behaviour of two Gaussian peak system with peak positions at 3.29 eV and 3.24 eV and FWHM of 0.1 and 0.18 eV; (b) PL spectrum of the nanowire grown on sapphire with deconvolution into three peaks.

Table 6.3: Main parameters of nanowires grown on silicon and on sapphire measured by optical and electrical methods.

Parameter	silicon	sapphire
Average diameter	100±40 nm	55±10 nm
PL peak position	3.30 eV	3.28 eV
PL FWHM	100 meV	140 meV
RT mobility	15±11 $cm^2/(V{\cdot}s)$	12±7 $cm^2/(V{\cdot}s)$
LT mobiliy	0	15 $cm^2/(V{\cdot}s)$
Contact barrier height	∼70 meV	80±20 meV
Bulk resistance activation energy	∼30 meV	40±20 meV

6.4 PL and electrical measurement summary.

In summary, PL and electrical measurements have been applied to study ZnO nanowire FETs and to correlate electrical and optical properties with the growth conditions.

ZnO nanowires are n-type with a carrier mobility of 1 to 60 $cm^2/(V{\cdot}s)$ and carrier concentration of 10^{18} to 10^{20} cm^{-3}. The nanowires with small diameters (below 100 nm) have large sample-to-sample variation of the carrier mobility, carrier concentration and PL band-edge peak FWHM. At high diameters the nanowire carrier concentration tends toward a value of $3{\times}10^{18}$ cm^{-3}, the mobility toward 10 $cm^2/(V{\cdot}s)$ and FWHM toward 100 meV. This diameter dependence is determined by surface states which change optical and electrical properties, or by variable growth dynamics in the nanowires with small diameters.

The low temperature measurements allowed independent investigation of the metal-nanowire contact resistance and the bulk nanowire resistance. The contact resistance has thermally activated behaviour at high temperatures with activation energies ranging from 60 to 100 meV. Bulk resistance (dependent on the mobility and the carrier concentration) has a complex behaviour with many different mechanisms taking part in the nanowire conductivity.

ZnO nanowires grown on different substrates (silicon and sapphire) were compared. The main parameters obtained are listed in table 6.3. Nanowires grown

on silicon have smaller average FWHM, larger average PL band-edge peak energy position and much higher resistance at low temperatures. According to this analysis, our main hypothesis is that nanowires grown on sapphire have higher number of shallow donors which might arise due to Al diffusion from the sapphire substrate, or higher density of H atoms and Zn_i-N_O complexes in the nanowires grown at lower temperatures.

6.4.1 ZnMgO and heterostructure nanowires.

Field effect transistors have been fabricated using ZnO/ZnMgO single and multiple quantum well heterostructures nanowires. Optical and electrical measurements have been carried out on these heterostructure nanowires. No apparent difference was observed in photoluminescence and electrical measurements between pure ZnO nanowires and core-shell ZnO/ZnMgO heterostructure nanowires. Resistance, mobility, carrier concentration, photoluminescence peak and FWHM values measured on heterostructure nanowires are scattered over the same range as values measured on pure ZnO nanowires.

Room temperature photoluminescence measurements on ZnO/ZnMgO core-shell nanowires (both single and multiple quantum well structures) did not show any extra peaks. The absence of ZnMgO and quantum well peaks may occur due to the small volume of luminescent material, due to non-radiative recombination at the nanowire surface or due to the surface band bending.

The fact that the electrical transport properties of the nanowires do not change after adding a ZnMgO shell indicates that the main electrical properties depend on the ZnO core of the wires and are not affected by a thin ZnMgO shell.

6.5 I-DLTS

6.5.1 I-DLTS. Temperature dependence

I-DLTS measurements were performed on four ZnO nanowires. Table 6.4 shows their main parameters such as diameter and room temperature resistance, mobility and carrier concentration. Current transients at different temperatures

for one nanowire are presented in figure 6.15.a. The relaxation curves show the temperature-evolution of the current behaviour due to the deep trap. As outlined in section 3.5.4.2, the emission rate follows an exponential law (equation 3.44).

Table 6.4: Nanowires used for I-DLTS measurements.

Nanowire No.	Diameter nm	Resistance kΩ	Mobility $cm^2/(V \cdot s)$	Carrier concentration cm^{-3}
No.1	60	330	16	8.5×10^{18}
No.2	50	400	15	6.5×10^{18}
No.3	53	260	13	1.9×10^{19}
No.4	64	300	19	2.7×10^{19}

I-DLTS spectra for ZnO nanowire No.1 are shown in figure 6.15.b. Peaks in this particular I-DLTS dependence may be attributed to two electron trap levels E1 and E2 and one hole-like trap level H1. The activation energies and apparent capture cross sections of these traps can be determined from the Arrhenius plots (figure 6.15.c, inset). Parameters of the deep levels measured on four different nanowires are listed in table 6.5. The nanowires exhibit similar hole-like trap H1 but different electron traps. Levels E2 and E3 are present in I-DLTS spectra of nanowires No.1 and No.2, whereas levels E1 and E4 were observed only in the nanowires No.1 and No.3, respectively.

For a first approximation, we will consider all the traps to be traps in the core of the nanowire. The characteristic values of these traps (cross-section and energy) can be compared with the values of traps observed in the literature. The E1 trap energy coincides with the E1 level energy in [185–187] and was related to oxygen vacancies in [186]. The E2 trap level coincides with E2 trap level in [239] where it is also attributed to oxygen vacancies. The origin of the E3 trap is not clear, with different groups giving evidence for its native origin [186], its relation to oxygen vacancies [187] and the effect of hydrogen [188]. The E4 trap level is similar to the E4 level in [187], [185] and [240], where it is attributed to oxygen vacancies.

This crude comparison with literature data on deep levels in ZnO should be regarded with caution, since the levels observed in this work have several pronounced traits that are not expected from simple bulk deep traps. First,

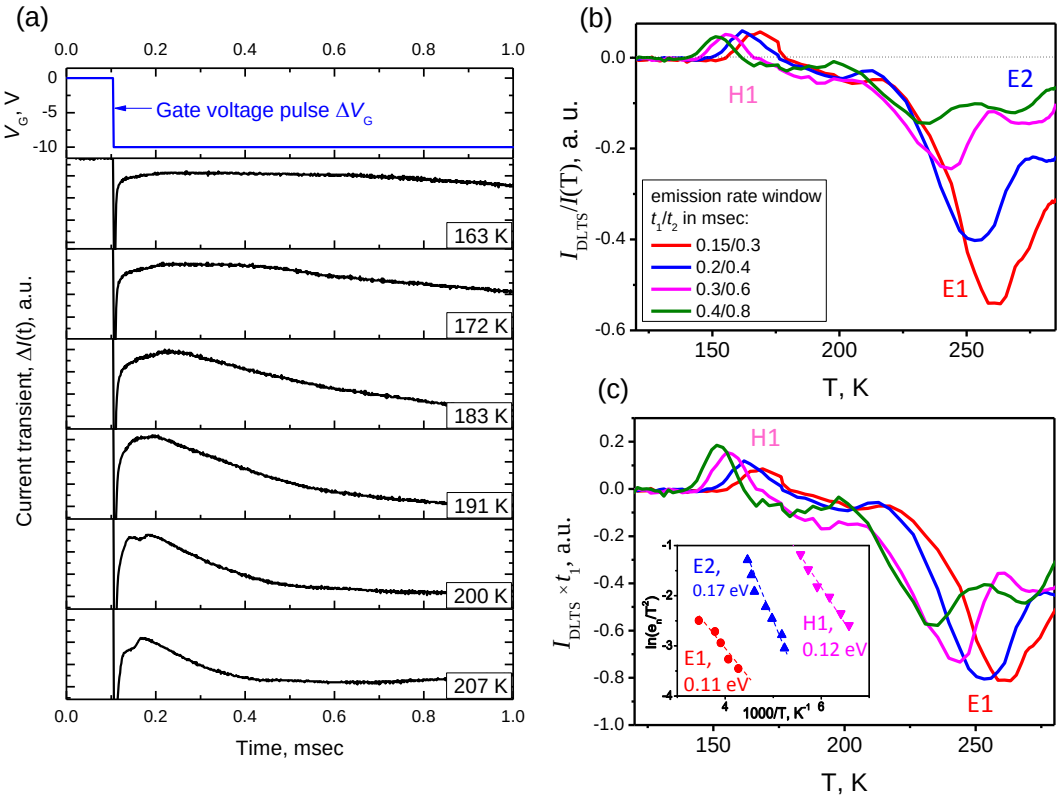

Figure 6.15: (a) Current transients of the nanowire No.1 at different temperatures for $\Delta V_G = 10$ V, the negative current peak at 0.1 msec is due to equipment response; (b) I-DLTS signal of the same nanowire normalised to a static current measured on ZnO nanowire with deep levels indicated; (c) I-DLTS signal normalised to rate window, the color-coding is the same as in the figure (b); inset: Arrhenius plots of levels E1, E2 and H1 taken from the I-DLTS graphs in figure (b).

Table 6.5: Activation energies and apparent cross-section of trap levels derived from Arrhenius plots for four ZnO nanowires.

Levels	Nanowire No.	Energy, eV	Cross-section cm^2
E1	1	0.11	7×10^{-21}
E2	1, 2	0.15-0.2	4×10^{-19}–2×10^{-18}
E3	1, 2	0.25-0.3	$(1–5)\times10^{-18}$
E4	3	0.45	3×10^{-12}
H1	1, 2, 3, 4	0.1–0.2	2×10^{-19}–2×10^{-18}

whereas the I-DLTS H1 maximum value at different rate-windows stays constant at different temperatures, absolute values of the peak maxima attributed to the electron traps, E1, rapidly increase with temperature (figure 6.15.b). If we plot the same graphs with different normalisation, multiplying the I-DLTS signal by its time constant ($t_1 \times I_{\mathrm{DLTS}}$), the magnitude of the E1 peak becomes almost constant with temperature (figure 6.15.c). This behaviour means that the de-trapping current component dominates the carrier dynamics and the depletion region width does not change substantially during carrier emission from the level E1. Conversely, emission from the level H1 is dominated by the depletion width modulation current component.

Hole-like levels, like H1, have been observed in some n-type FETs and they are usually ascribed to the hole-traps on the un-passivated surface of the FET ([193] and references therein). In the case of n-type ZnO nanowires, it is very unlikely for the level H1 to be a real hole trap due to the following reasons. For some ZnO nanowires, the amplitude of the current transient corresponding to the level H1 is comparable to the static current through the nanowire ($I_{\text{I-DLTS}}(T_{\max})/I(T_{\max}) \approx 0.1 - 0.5$), which, assuming the level H1 being a real hole trap, would indicate concentration of holes comparable to that of electrons. No inversion current was observed however in the FET transfer characteristics at large negative gate biases down to –60 V and lower, indicating negligible concentration of holes. Therefore, the level H1 cannot be a real hole trap.

Here, we cannot unambiguously determine the exact origin of the observed levels. Therefore we will restrict our discussion to the phenomenological description of the trap recharging characteristics.

6.5.2 I-DLTS. Quiescent gate voltage dependence

Additional information from the I-DLTS measurement can be obtained by varying the quiescent gate voltage bias V_{GQ}:

A. In the case of bulk traps, according to the simple model shown in figures 3.16 and 3.19, a varying quiescent gate voltage changes the radial position of the edge of the depletion region $W_d(V_{\mathrm{GQ}})$. Consequently, a positive gate voltage pulse ΔV_{G} will populate and depopulate deep levels located between the positions

$W_d(V_{GQ})$ and $W_d(V_{GQ} + \Delta V_G)$. Thus, the quiescent gate voltage dependence of the I-DLTS signal with fixed ΔV_G may give information on the radial distribution of the deep traps in nanowire.

B. In the case of surface traps, a higher positive quiescent voltage will lower the barrier E_b for electrons between the nanowire core and the surface traps (figure 3.19.b.2, equations 3.30 and 3.32). Thus we would expect faster electron capture at higher V_{GQ}. Capture-mode I-DLTS is needed to study electron capture, during which the gate voltage pulse is kept negative and the current transient is measured after the negative gate voltage pulse.

Figure 6.16.a shows I-DLTS measurements taken on nanowire No.3 at two different quiescent gate voltages (the blue curve shows $V_{GQ} = -10$ V and the red one $V_{GQ} = 0$ V, with $\Delta V_G = 10$ V in both cases). The blue curve shows one electron level E4 with a broad peak at a temperature around 220 K (the level E4 in table 6.5 with activation energy 0.45 eV) and the red curve shows one hole level H1 with a peak at 242 K (the level H1 in table 6.5 with activation energy 0.20 eV). The H1 peak magnitude is 50 times larger than that of the E4 peak.

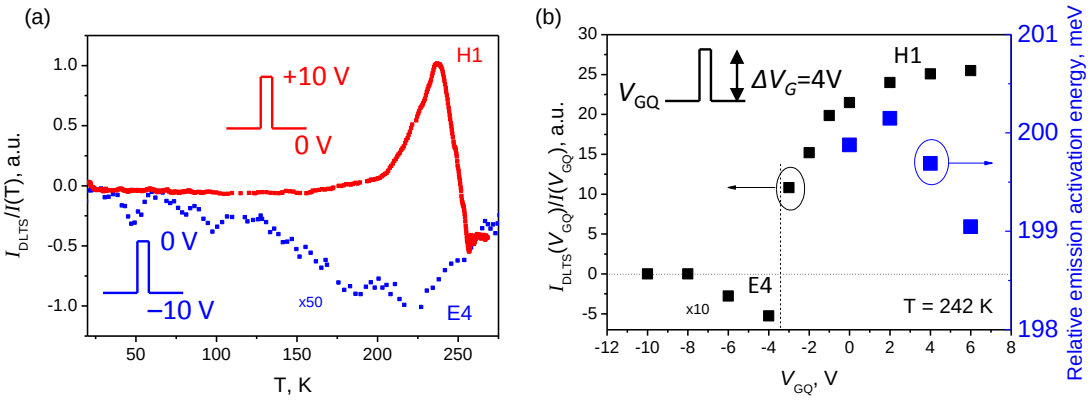

Figure 6.16: (a) Emission-mode I-DLTS measurement on a ZnO nanowire with different quiescent gate voltage: $V_{GQ} = 0$ V (red), $V_{GQ} = -10$ V (black), the hole-like peak in red curve is observed at 242 K, emission rate constants t_1/t_2 was 1.6/3.2 msec; (b) quiescent gate voltage V_{GQ} dependence of the I-DLTS signal magnitude and the relative emission activation energy for the same nanowire, gate voltage pulse is 4 V, $T = 242$ K.

Figure 6.16.b shows the evolution of the I-DLTS peaks from figure 6.16.a at 242 K in more detail. The I-DLTS signal is measured with the gate voltage pulse

ΔV_G fixed at 4 V, and the quiescent gate voltage varied from –10 to +6 V. No I-DLTS signal is observed at large negative quiescent voltage < -6 V. At these gate voltages the barrier for electrons E_b to travel from the nanowire core onto the surface trap levels is very high, making it virtually impossible for electrons to get trapped. Thus no I-DLTS peak is observed at large negative quiescent voltages. At higher quiescent voltages (-6 V $< V_{GQ} <$ –4 V) the negative I-DLTS signal E4 appears. This corresponds to normal electron emission from the surface trap E4 over the surface barrier into the nanowire conduction band, which causes the surface barrier to decrease, the depletion region to shrink and the current through nanowire to increase. At quiescent voltages higher than –3 V, the large positive I-DLTS signal (H1) dominates the current transient. The next paragraph addresses the level H1 in more detail.

The positive sign of the peak H1 may be explained by hopping transport behaviour. However, with decreasing quiescent gate voltages, the electric field that sweeps electrons from the surface becomes larger. This will reduce the hopping activation energy according to the Poole-Frenkel effect [241], and hence reduce the emission rate. However inspection of the decay curves showed that the emission time constant does not vary with the quiescent voltage – it stays at 1.4±0.05 msec for quiescent voltages from 0 to 6 V. The emission activation energy, calculated using equation 3.44, is plotted in figure 6.16.b (blue squares). The level H1 activation energy changes non-monotonically by only 1 meV when the gate voltage is varied from 0 to 6 V, which rules out the simple thermally activated hopping mechanism. In addition, the level H1 cannot be attributed to a simple gate voltage leak at positive gate voltages, since in nanowire No.4 the I-DLTS magnitude of the same level H1 was nearly constant at quiescent voltages ranging from –10 V to +6 V. All these facts suggest a more complex picture of the electron re-charging dynamics than the simple picture presented in section 3.5.3.2.

Capture-mode I-DLTS was carried out on the same nanowire sample (figure 6.17). Figure 6.17.a shows capture-mode I-DLTS spectra with the most prominent peaks at 220 K and 230 K. We assume that these two peaks correspond to the process of carrier capture by the same surface trap level which we denote by C1. According to the model in figure 3.19.b.2, the level C1 exhibits

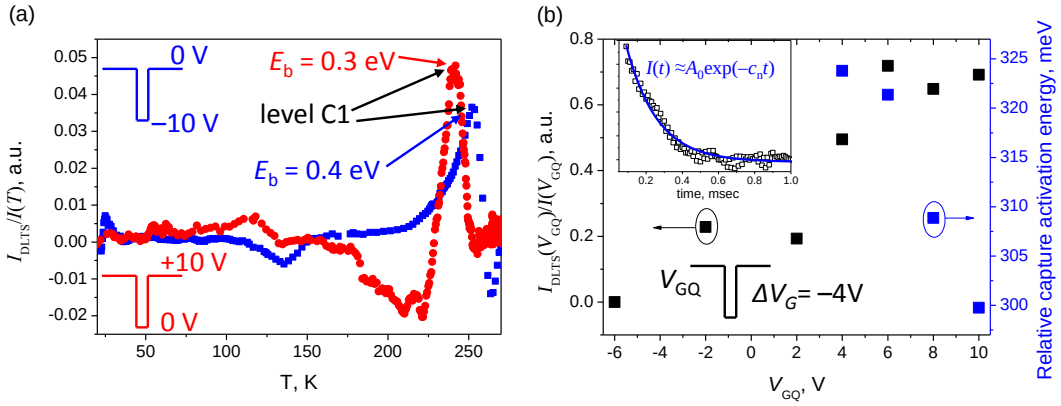

Figure 6.17: (a) Capture-mode I-DLTS measurement on a ZnO nanowire with different quiescent gate voltage: $V_{\mathrm{GQ}} = +10$ V (red), $V_{\mathrm{GQ}} = 0$ V (blue), emission rate constant t_1/t_2 was 0.4/0.8 msec. Hole-like peaks are observed at 220–240 K; (b) quiescent voltage dependence of the capture-mode I-DLTS signal and capture activation energy, gate voltage pulse is –4 V; inset: current transient at $V_{\mathrm{GQ}} = 10$ V, $\Delta V_{\mathrm{G}} = -4$ V, blue line shows the exponential fit to the experimental data.

varying capture activation energy (or barrier energy) depending on the quiescent voltage. The barrier energy E_b decreases from 0.4 eV to 0.3 eV when the quiescent voltage increases from 0 to +10 V (figure 6.17.a). This value is similar to that obtained from the model described in section 3.5.3.2, figure 3.17.

Figure 6.17.b shows more detailed quiescent voltage dependence of the I-DLTS signal magnitude, with fixed gate voltage bias of –4 V. The peak increases with quiescent voltage. Since the capture follows an exponential time-dependence (figure 6.17.b, inset), the capture time-constant can be inferred from the fit. The capture time constant changes from 0.5 to 0.17 msec when the quiescent voltage increases from +4 to +10 V. The capture activation energy (or barrier energy E_b) is calculated using equation 3.48 for $V_{\mathrm{GQ}} > 4$ V and plotted in figure 6.17.b, blue squares. The barrier energy monotonically decreases as expected from the depletion region model.

Although level H1 and level C1 are observed at similar temperatures, they cannot represent the same trap level due to the different dynamics. The level H1 may correspond to SiO_x-ZnO interface states or to states on the ZnO-contact interface.

6.5.3 Conclusion

In conclusion, we have proposed and successfully implemented the I-DLTS method with gate-voltage pulsing to probe deep electronic states in individual ZnO nanowires. A variety of deep levels (E1, E2, E3, E4 and H1) were observed, with both electron-like and hole-like character. A comparison with the literature was made to understand the origin of the deep levels. A model of the nanowire current transient was applied to the results. Levels exhibiting dominant detrapping and depletion width modulation current components were distinguished from the I-DLTS temperature dependences.

Quiescent voltage dependences were used in order to study electron emission and capture on surface states. The surface barrier was found to be 0.3–0.4 eV at 240 K.

Although the levels observed originate from the features of the ZnO nanowire FET and are most likely surface related defects, it is not clear yet whether these levels are intrinsic to ZnO nanowires, or whether they are ZnO-SiO_2 or ZnO-contact interface levels.

6.6 Generic ZnO nanowire

Figure 6.18 shows a room temperature band diagram of a generic ZnO nanowire grown by MBE. According to the PL measurements in section 5.5, the band gap is 3.30 eV. The average nanowire is 54 nm in diameter, with the carrier concentration of 1.4×10^{19} cm^{-3} measured by field effect in section 6.2.1. The Fermi level lies 0.02 eV above the conduction band minimum calculated based on the average carrier concentration and the effective density of states in ZnO (section 6.2.1). According to the capture-mode I-DLTS measurements, figure 6.10 and depletion region model (section 3.5.3.2), the surface barrier energy and surface state density are 0.4 eV and 8×10^{12} cm^{-2} respectively. The surface states spectrum consists of localised states. Some of them may be free of electrons at ambient conditions and some have captured electrons (open and closed squares in the figure respectively). An example localised state (the level E4, according to I-DLTS measurement) lies 0.45 eV deep in the band gap.

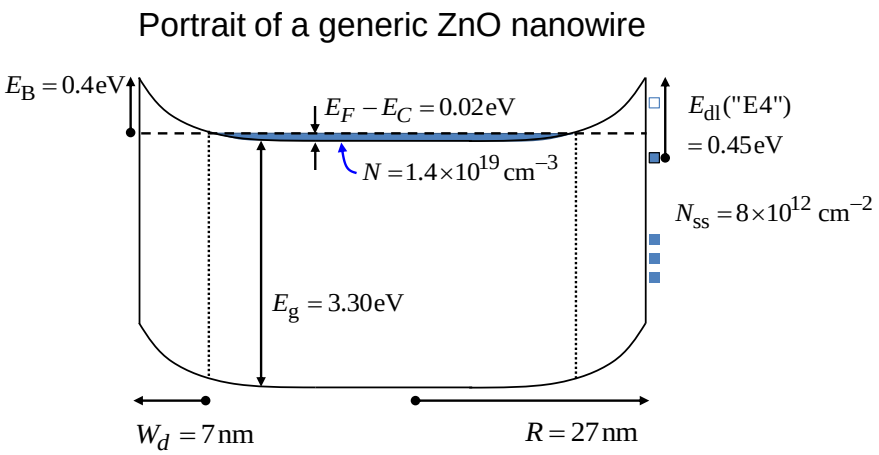

Figure 6.18: Generic ZnO nanowire with parameters inferred from electrical measurements.

Chapter 7

Conclusions and future work

7.1 Conclusions

In this work I have studied semiconductor nanowires grown by molecular beam epitaxy for electronics applications. Nanowires were studied by SEM, HRTEM, XRD, XPS, EDX, PL and electrical transport.

InAs, InAsP and InAsSb nanowires were grown by solid-source MBE self-catalytically on silicon substrates. Study of phosphorus incorporation revealed that the phosphorus incorporation rate coefficient is 10 times smaller than that of arsenic. A mechanical exfoliation technique was used to discriminate the effects of the zincblende InAsP clusters and the mostly wurtzite InAsP nanowires. Study of antimony incorporation showed that antimony affects the nanowire crystal structure, changing it from wurtzite with a high density of various defects to zincblende with a low density of stacking faults. The decrease in the stacking fault density also improved the nanowire transport properties – the carrier mobility tripled upon addition of 15 % of Sb. The band gap of resulting zincblende InAsSb nanowires was shown to vary from 0.32 to 0.41 eV at low temperature. The band gap of wurtzite InAsP nanowires was shown to vary from 0.37 to 0.5 eV.

ZnO and ZnMgO nanowires and ZnO/ZnMgO core-shell nanowires were grown by plasma source MBE with use of a gold catalyst on various substrates. The conditions for ZnO nanowire growth were optimised to achieve high yield growth. ZnO nanowires grow in the wurtzite structure without any crystallographic defects. A study of magnesium incorporation showed that at Mg content higher than

20 %, the rocksalt phase segregates in the as-grown samples. The magnesium incorporation rate is four times lower than that of zinc. ZnO/MgO, ZnO/ZnMgO and multiple ZnO/[ZnMgO/ZnO]$_4$ core-shell nanowires have been grown by growing the core and the shell at 750 °C and 500 °C respectively. HRTEM and PL confirmed the shell formation.

ZnO nanowire FETs with Ohmic drain-source contacts were fabricated and optimised and their electrical and optical properties were studied. The nanowire carrier concentration and carrier mobility vary from 10^{18} to 5×10^{20} cm^{-3} and from 1 to 60 cm^2/(V sec) respectively. Low temperature transport characteristics of ZnO nanowires have been investigated and allowed the study of different conductivity mechanisms, defined by the contact properties and the bulk nanowire properties. Transport properties and PL measurement of nanowires grown on silicon and sapphire indicated the presence of an extra shallow donor in nanowires grown on sapphire, which is likely to be H, Zn_i-N_O complex or Al. A novel method to study trap levels (I-DLTS) in semiconductor nanowires was applied to ZnO nanowire FETs. Several defects with different temperature dependences were observed. Different mechanisms were proposed and analysed.

7.2 Future work

7.2.1 Optimisation of the growth conditions

Control over nucleation of nanowires will potentially result in repeatable growth parameters of both InAs- and ZnO-based nanowires. In the case of InAs nanowires, self-catalysed nucleation depends on the precise oxide thickness and the properties of the oxide openings. The accurate choice of substrate temperature and component BEPs may result in better crystallinity of the nanowires. In the case of ZnO nanowires, improvement of the yield of gold particles can be achieved by controlling the chemical potential of the droplets by starting the nanowire growth at different temperatures or by saturating the gold droplets with zinc metal atoms before introducing oxygen. The chemical treatment of growth substrates may improve growth control by removing residual oxides or organic

components. The choice of different substrates such as monocrystalline GaN or ZnO may improve the growth characteristics.

7.2.2 Nanowire devices

Improvements to ZnO nanowire FET performance will be made next. First, the nanowire surface can be passivated by in-situ MgO shell deposition or by ex-situ SiN/SiO insulator deposition. Nanowire FET annealing may be used in order to improve low temperature Ohmicity of the nanowire-metal contact.

Further efforts will be made into the research of correlated transport phenomena, in particular Majorana particle study, in defect free InAsSb nanowires.

7.2.3 Nanowire heterostructures

The next natural step in the functionalisation of InAs-based nanowires is to grow InAs/InAsP and InAs/InAsSb heterostructure nanowires and study their electrical and optical properties.

The further study of ZnO/ZnMgO nanowire heterostructure devices requires the optimisation of heterostructure nanowire growth. The control over radial growth rates and over the heterostructure interface is needed to fabricate working devices.

In order to confirm the presence of multiple quantum well heterostructures and the quantum confined Stark effect proposed in section 5.7.3.2, low temperature PL and CL should be carried out on nanowire ensembles and on individual nanowires.

Since ZnO/ZnMgO thin films exhibit a two-dimensional electron gas at the heterointerface, the possibility of a cylindrical 2DEG at the interface between ZnMgO and ZnO in ZnO/ZnMgO core-shell nanowires may promise many applications ranging from high mobility nanowire transistors experiments in fundamental physical phenomena. Hence the low temperature study of ZnO/ZnMgO core-shell nanowire transport and magnetotransport is the next step in oxide core-shell nanowire heterostructures.

7.2.4 I-DLTS

Improved I-DLTS theory and semiconductor device modeling are needed for a complete understanding of the nanowire current transient behaviour.

In addition, a variety of material systems can be studied by the I-DLTS method. I-DLTS may give information on the defect states that account for sensing properties in nanowires; and more sophisticated analyses of defect depth-profiling may give information on the spatial location of defect states in nanowires with non-uniform composition (such as axial and core-shell nanowires).

List of publications

The first two publications are included in the text.

- "InAsP nanowires grown by catalyst-free molecular-beam epitaxy"

  I. Isakov, M. Panfilova, M. J. L. Sourribes, V. Tileli, A. E. Porter and P. A. Warburton, *Nanotechnology*, **24**, 8, 085707, 2013.

- "Growth of ZnO and ZnMgO nanowires by Au-catalysed molecular-beam epitaxy"

  I. Isakov, M. Panfilova, M. J. L. Sourribes and P. A.Warburton, *Physica Status Solidi (C)*, **10**, 10, 1308–1313, 2013.

- "Mobility enhancement by Sb-mediated minimisation of stacking fault density in InAs nanowires grown on silicon"

  M. J. L. Sourribes, **I. Isakov**, M. Panfilova, H. Liu and P. A. Warburton, *Nano Letters*, **14**, 3, 1643–1650, 2014.

- "Minimization of the contact resistance between InAs nanowires and metallic contacts"

  M. J. L. Sourribes, **I. Isakov**, M. Panfilova and P. A. Warburton, *Nanotechnology*, **24**, 4, 045703, 2013.

- "Voltage controlled modification of flux closure domains in planar magnetic structures for microwave applications"

  D.E. Parkes, R. Beardsley, S. Bowe, **I. Isakov**, P.A. Warburton, K.W. Edmonds, R.P. Campion, B.L. Gallagher, A.W. Rushforth, and S.A. Cavill, *Applied Physics Letters*, **105**, 062405, 2014

References

[1] W. Haensch, E. J. Nowak, R. H. Dennard, P. M. Solomon, A. Bryant, O. H. Dokumaci, A. Kumar, X. Wang, J. B. Johnson, and M. V. Fischetti, "Silicon CMOS devices beyond scaling," *IBM journal of research and development*, vol. 50, no. 4/5, 2006. 19

[2] C. Liu, M. Östlinga, and J. Hannon, "New materials for post-Si computing," *MRS Bulletin*, vol. 39, pp. 658–662, 2014. 20

[3] "New materials for post-Si computing," *MRS Bulletin*, vol. 39, 2014. Journal issue. 20

[4] M. W. Larsson, J. B. Wagner, M. Wallin, P. Hakansson, L. E. Froberg, L. Samuelson, and L. R. Wallenberg, "Strain mapping in free-standing heterostructured wurtzite InAs/InP nanowires," *Nanotechnology*, vol. 18, 2007. 20

[5] C. P. T. Svensson, T. Mårtensson, J. Trägårdh, C. Larsson, M. Rask, D. Hessman, L. Samuelson, and J. Ohlsson, "Monolithic GaAs/InGaP nanowire light emitting diodes on silicon," *Nanotechnology*, vol. 19, no. 30, p. 305201, 2008. 20, 26

[6] H.-J. Choi, J. C. Johnson, R. He, S.-K. Lee, F. Kim, P. Pauzauskie, J. Goldberger, R. J. Saykally, and P. Yang, "Self-organized gan quantum wire UV lasers," *The Journal of Physical Chemistry B*, vol. 107, no. 34, pp. 8721–8725, 2003. 20, 41

[7] S. voltaics, "Sol voltaics," 2014. 20

[8] Z. L. Wang, "Piezopotential gated nanowire devices: Piezotronics and piezophototronics," *Nano Today*, vol. 5, no. 6, pp. 540 – 552, 2010. 20, 27

[9] Y. S. Park, C. M. Park, C. J. Park, H. Y. Cho, S. J. Lee, T. W. Kang, S. H. Lee, J.-E. Oh, K.-H. Yoo, and M.-S. Son, "Electron trap level in a GaN nanorod p-n junction grown by molecular-beam epitaxy," *Applied Physics Letters*, vol. 88, no. 19, pp. –, 2006. 21, 49

[10] X.-Y. Liu, C.-X. Shan, S.-P. Wang, Z.-Z. Zhang, and D.-Z. Shen, "Electrically pumped random lasers fabricated from ZnO nanowire arrays," *Nanoscale*, vol. 4, pp. 2843–2846, 2012. 21, 25

[11] H. Huang, B. Liang, Z. Liu, X. Wang, D. Chen, and G. Shen, "Metal oxide nanowire transistors," *J. Mater. Chem.*, vol. 22, pp. 13428–13445, 2012. 21, 25, 26, 44

[12] M. T. Björk, B. J. Ohlsson, C. Thelander, A. I. Persson, K. Deppert, L. R. Wallenberg, and L. Samuelson, "Nanowire resonant tunneling diodes," *Applied Physics Letters*, vol. 81, no. 23, 2002. 21, 26, 37

[13] C. Thelander, T. Mårtensson, M. T. Björk, B. J. Ohlsson, M. W. Larsson, L. R. Wallenberg, and L. Samuelson, "Single-electron transistors in heterostructure nanowires," *Applied Physics Letters*, vol. 83, no. 10, 2003. 21, 26

[14] M. Heiss, A. Gustafsson, S. Conesa-Boj, F. Peiro, J. R. Morante, G. Abstreiter, J. Arbiol, L. Samuelson, and A. Fontcuberta i Morral, "Catalyst-free nanowires with axial $In_xGa_{1-x}As$/GaAs heterostructures," *Nanotechnology*, vol. 20, 2009. 21, 22, 36

[15] J. Faist, F. Capasso, D. L. Sivco, C. Sirtori, A. L. Hutchison, and A. Y. Cho, "Quantum cascade laser," *Science*, vol. 264, pp. 553–556. 21

[16] A. Tsukazaki, S. Akasaka, K. Nakahara, Y. Ohno, H. Ohno, D. Maryenko, A. Ohtomo, and M. Kawasaki, "Observation of the fractional quantum hall effect in an oxide," *Nature Materials*, vol. 9, pp. 889–893, 2010. 21, 43

[17] I. T. R. for Semiconductors, "2013 ITRS edition," 2013. 22

[18] D. V. Lang, "Deep-level transient spectroscopy: A new method to characterize traps in semiconductors," *Journal of Applied Physics*, vol. 45, no. 7, 1974. 22, 49, 87, 94

[19] T. Xu, K. A. Dick, S. Plissard, T. H. Nguyen, Y. Makoudi, M. Berthe, J.-P. Nys, X. Wallart, B. Grandidier, and P. Caroff, "Faceting, composition and crystal phase evolution in III-V antimonide nanowire heterostructures revealed by combining microscopy techniques," *Nanotechnology*, vol. 23, no. 9, p. 095702, 2012. 23

[20] Ü. Özgür, Y. I. Alivov, C. Liu, A. Teke, M. A. Reshchikov, S. Doğan, V. Avrutin, S.-J. Cho, and H. Morkoç, "A comprehensive review of ZnO materials and devices," *Journal of Applied Physics*, vol. 98, no. 4, pp. –, 2005. 23, 45, 138

[21] Z. H. S. J. T. C. M.-F. F. S. D. K. H. Klingshirn C, Fallert J, "65 years of ZnO research – old and very recent results," *Physica Status Solidi B*, vol. 247, pp. 1424–1447, 2010. 23, 144

[22] M. C. Newton and P. A. Warburton, "ZnO tetrapod nanocrystals," *Materials Today*, vol. 10, 2007. 23

[23] N. P. Dasgupta, J. Sun, C. Liu, S. Brittman, S. C. Andrews, J. Lim, H. Gao, R. Yan, and P. Yang, "25th anniversary article: Semiconductor nanowires âĂŞ synthesis, characterization, and applications," *Advanced Materials*, vol. 26, no. 14, pp. 2137–2184, 2014. 25

[24] C. Thelander, P. Agarwal, S. Brongersma, J. Eymery, L. Feiner, A. Forchel, M. Scheffler, W. Riess, B. Ohlsson, U. Gösele, and L. Samuelson, "Nanowire-based one-dimensional electronics," *Materials Today*, vol. 9, no. 10, pp. 28 – 35, 2006.

[25] Y. Li, F. Qian, J. Xiang, and C. M. Lieber, "Nanowire electronic and optoelectronic devices," *Materials Today*, vol. 9, no. 10, pp. 18 – 27, 2006. 25

[26] S. A. Dayeh, "Electron transport in indium arsenide nanowires," *Semiconductor Science and Technology*, vol. 25, 2010. 25, 26

[27] M. Willander, O. Nur, Q. X. Zhao, L. L. Yang, M. Lorenz, B. Q. Cao, J. Zuniga-Perez, C. Czekalla, G. Zimmermann, M. Grundmann, A. Bakin, A. Behrends, M. Al-Suleiman, A. El-Shaer, A. Che Mofor, B. Postels, A. Waag, N. Boukos, A. Travlos, H. S. Kwack, J. Guinard, and D. Le Si Dang, "Zinc oxide nanorod based photonic devices: recent progress in growth, light emitting diodes and lasers," *Nanotechnology*, vol. 20, 2009. 25, 30, 165

[28] H. J. Fan, P. Werner, and M. Zacharias, "Semiconductor nanowires: from self-organization to patterned growth," *Small*, vol. 6, pp. 700–717, 2006. 25, 30

[29] B. R. Nag, ed., *Physics of quantum well devices*. Springer, 2000. 25

[30] E. W. S. Wagner R S, "The vapor-liquid-solid mechanism of crystal growth and its application to silicon," *Transactions of the Metallurgical Society of the American Institute of Mechanical Engineers*, vol. 233, 1965. 25, 27

[31] "A special issue on carbon nanotubes," *Account of chemical research*, vol. 36, 2002. 25

[32] M. H. Huang, S. Mao, H. Feick, H. Yan, Y. Wu, H. Kind, E. Weber, R. Russo, and P. Yang, "Room-temperature ultraviolet nanowire nanolasers," *Science*, vol. 292, no. 5523, pp. 1897–1899, 2001. 25, 30

[33] S. Chu, G. Wang, W. Zhou, Y. Lin, L. Chernyak, J. Zhao, J. Kong, L. Li, J. Ren, and J. Liu, "Electrically pumped waveguide lasing from ZnO nanowires," *Nature Nanotechnology*, no. 8, pp. 506 – 510, 2011. 25, 167

[34] X. F. Duan, Y. Huang, R. Agarwal, and C. M. Lieber, "Single-nanowire electrically driven lasers," *Nature Nanotechnology*, vol. 421, pp. 241–245, 2003. 25

[35] D. Saxena, S. Mokkapati, P. Parkinson, N. Jiang, Q. Gao, H. H. Tan, and C. Jagadish, "Optically pumped room-temperature GaAs nanowire lasers," *Nature Photonics*, vol. 7, pp. 963–969, 2013. 25

[36] X. Liu, Q. Zhang, J. N. Yip, Q. Xiong, and T. C. Sum, "Wavelength tunable single nanowire lasers based on surface plasmon polariton enhanced burstein-moss effect," *Nano Letters*, vol. 13, no. 11, pp. 5336–5343, 2013. PMID: 24134588. 26

[37] C. J. Novotny, E. T. Yu, and P. K. L. Yu, "InP nanowire/polymer hybrid photodiode," *Nano Letters*, vol. 8, no. 3, pp. 775–779, 2008. PMID: 18266333. 26

[38] W. Wei, X.-Y. Bao, C. Soci, Y. Ding, Z.-L. Wang, and D. Wang, "Direct Heteroepitaxy of Vertical InAs Nanowires on Si Substrates for Broad Band Photovoltaics and Photodetection," *Nano Letters*, vol. 9, no. 8, pp. 2926–2934, 2009. PMID: 19624100.

[39] H. Zhou, G. Fang, L. Yuan, C. Wang, X. Yang, H. Huang, C. Zhou, and X. Zhao, "Deep ultraviolet and near infrared photodiode based on n-ZnO/p-silicon nanowire heterojunction fabricated at low temperature," *Applied Physics Letters*, vol. 94, no. 1, pp. –, 2009. 26, 167

[40] C. Soci, A. Zhang, B. Xiang, S. A. Dayeh, D. P. R. Aplin, J. Park, X. Y. Bao, Y. H. Lo, and D. Wang, "ZnO nanowire UV photodetectors with high internal gain," *Nano Letters*, vol. 7, no. 4, pp. 1003 – 1009, 2007. 26, 45

[41] D. C. Kim, B. O. Jung, J. H. Lee, H. K. Cho, J. Y. Lee, and J. H. Lee, "Dramatically enhanced ultraviolet photosensing mechanism in a n-ZnO nanowires/i-MgO/n-Si structure with highly dense nanowires and ultrathin MgO layers," *Nanotechnology*, vol. 22, 2011. 26

[42] M. Law, L. E. Green, J. C. Johnson, R. Saykally, and P. Yang, "Nanowire dye-sensitized solar cells," *Nature Materials*, vol. 4, pp. 455–459, 2005. 26

[43] B. Tian, X. Zheng, T. J. Kempa, Y. Fang, N. Yu, G. Yu, J. Huang, and C. M. Lieber, "Coaxial silicon nanowires as solar cells and nanoelectronic power sources," *Nature*, vol. 449, pp. 885–U8, 2007. 26

[44] X. Tang, G. Li, and S. Zhou, "Ultraviolet electroluminescence of light-emitting diodes based on single n-ZnO/p-AlGaN heterojunction nanowires," *Nano Letters*, vol. 13, no. 11, pp. 5046–5050, 2013. PMID: 24073683. 26

[45] F. Qian, S. Gradečak, Y. Li, C.-Y. Wen, and C. M. Lieber, "Core/multishell nanowire heterostructures as multicolor, high-efficiency light-emitting diodes," *Nano Letters*, vol. 5, no. 11, pp. 2287–2291, 2005. PMID: 16277469.

[46] F. Qian, S. Gradečak, H.-G. Park, Y. Dong, Y. Ding, Z. L. Wang, and C. M. Lieber, "Multi-quantum-well nanowire heterostructures for wavelength-controlled lasers," *Nature Materials*, vol. 7, pp. 701–706, 2008. 26, 41

[47] KnowMade, "LED : Nanowire led patent investigation," 2014. 26, 167

[48] Aledia, "Aledia - pioneering next generation products to lead the led revolution," 2014. 26, 38

[49] M. J. L. Sourribes, I. Isakov, M. Panfilova, H. Liu, and P. A. Warburton, "Mobility enhancement by Sb-mediated minimisation of stacking fault density in InAs nanowires grown on silicon," *Nano Letters*, vol. 14, no. 3, pp. 1643–1650, 2014. 26, 34, 43

[50] S. A. Dayeh, D. P. R. Aplin, X. Zhou, P. K. L. Yu, E. T. Yu, and D. Wang, "High electron mobility InAs nanowire field-effect transistors," *Small*, vol. 3, pp. 326–332, 2007. 26, 43

[51] C. Thelander, L. E. Froberg, C. Rehnstedt, L. Samuelson, and L.-E. Wernersson, "Vertical enhancement-mode InAs nanowire field-effect transistor with 50-nm wrap gate," *IEEE Electron Device Letters*, vol. 29, 2008. 30, 43

[52] S. Dhara, S. Sengupta, H. S. Solanki, A. Maurya, A. A. Pavan, M. R. Gokhale, A. Bhattacharya, and M. M. Deshmukh, "Facile fabrication of

lateral nanowire wrap-gate devices with improved performace," *Applied Physics Letterse*, vol. 99, 2011. 26, 43

[53] M. T. Björk, B. J. Ohlsson, T. Sass, A. I. Persson, C. Thelander, M. H. Magnusson, K. Deppert, L. R. Wallenberg, and L. Samuelson, "One-dimensional steeplechase for electrons realized," *Nano Letters*, vol. 2, no. 2, pp. 87 – 89, 2002. 26, 37, 38

[54] C. Thelander, M. Björk, M. Larsson, A. Hansen, L. Wallenberg, and L. Samuelson, "Electron transport in inas nanowires and heterostructure nanowire devices," *Solid State Communications*, vol. 131, no. 9âĂŞ10, pp. 573 – 579, 2004. New advances on collective phenomena in one-dimensional systems. 26, 37

[55] Y. Cui, Q. Wei, H. Park, and C. M. Lieber, "Nanowire nanosensors for highly sensitive and selective detection of biological and chemical species," *Science*, vol. 293, no. 5533, pp. 1289 – 1292, 2001. 26, 38

[56] Q. Wan, Q. Li, Y. Chen, T. Wang, X. He, J. Li, and C. Lin, "Fabrication and ethanol sensing characteristics of ZnO nanowire gas sensors," *Applied physics letters*, vol. 84, pp. 3654–3656, MAY 3 2004. 26, 167

[57] C. Chan, H. Peng, G. Liu, K. McIlwrath, X. Zhang, R. Huggins, and Y. Cui, "High-performance lithium battery anodes using silicon nanowires," *Nature Nanotechnology*, vol. 3, pp. 31–35, 2008. 26

[58] H. Wong, S. Tan, N. Wang, and C. Durkan, "Hydrothermally-grown ZnO nanowire tips for scanning tunnelling microscopy," *Journal of Nanoscience and Nanotechnology*, vol. 12, no. 3, pp. 2394–2398(5), 2012. 26

[59] K. Flöhr, K. Sladek, H. Yusuf Günel, M. Ion Lepsa, H. Hardtdegen, M. Liebmann, T. Schäpers, and M. Morgenstern, "Scanning tunneling microscopy with InAs nanowire tips," *Applied Physics Letters*, vol. 101, no. 24, pp. –, 2012. 26

[60] A. Hochbaum, R. Chen, R. Delgado, W. Liang, E. Garnett, M. Najarian, A. Majumdar, and P. Yang, "Enhanced thermoelectric performance of rough silicon nanowires," *Nature Nanotechnology*, vol. 451, pp. 163–U5, 2008. 26

[61] S. Roddaro, D. Ercolani, M. A. Safeen, S. Suomalainen, F. Rossella, F. Giazotto, L. Sorba, and F. Beltram, "Giant thermovoltage in single InAs nanowire field-effect transistors," *Nano Letters*, vol. 13, no. 8, pp. 3638–3642, 2013. PMID: 23869467. 27

[62] V. Mourik, K. Zuo, S. M. Frolov, R. Plissard, E. P. A. M. Bakkers, and L. P. Kouwenhoven, "Signatures of Majorana fermions in hybrid superconductor-semiconductor nanowire devices," *Science*, vol. 336, pp. 1003–1007, 2012. 27

[63] A. Das, Y. Ronen, Y. Most, Y. Oreg, M. Heiblum, and H. Shtrikman, "Zero-bias peaks and splitting in an Al-InAs nanowire topological superconductor as a signature of Majorana fermions," *Nature Physics*, vol. 8, pp. 887–895, 2012. 27

[64] H. J. He, C. L. Hsin, J. Liu, L. J. Chen, and Z. L. Wang, "Piezoelectric gated diode of a single ZnO nanowire," *Advanced Materials*, vol. 19, pp. 781–784, 2007. 27

[65] X. Wang, J. Zhou, J. Song, J. Liu, N. Xu, and Z. L. Wang, "Piezoelectric field effect transistor and nanoforce sensor based on a single ZnO nanowire," *Nano Letters*, vol. 6, pp. 2768–2772, 2006. 27

[66] M. Hansen and K. Anderko, *Constitution of binary alloys*. New-York: McGraw-Hill, 1958. 27

[67] F. Glas, "The statistics of sub-poissonian nucleation in nanowire growth," in *Nanowire Growth Workshop Nanowires - 2014*, 2014. Eindhoven. 29

[68] V. G. Dubrovskii, N. V. Sibirev, G. E. Cirlin, J. C. Harmand, and V. M. Ustinov, "Theoretical analysis of the vapor-liquid solid mechanism of nanowire growth during molecular beam epitaxy," *Physical Review E*, vol. 73, 2006. 29, 61, 62

[69] V. G. Dubrovskii, N. V. Sibirev, G. E. Cirlin, I. P. Soshnikov, W. H. Chen, R. Larde, E. Cadel, P. Pareige, T. Xu, B. Grandidier, J.-P. Nys, D. Stievenard, M. Moewe, L. C. Chuang, and C. Chang-Hasnain, "Gibbs-thomson and diffusion-induced contributions to the growth rate of Si, InP, and GaAs nanowires," *Phys. Rev. B*, vol. 79, p. 205316, May 2009. 29

[70] M. Tchernycheva, G. E. Cirlin, G. Patriarche, L. Travers, V. Zwiller, U. Perinetti, and J.-C. Harmand, "Growth and characterization of InP nanowires with InAsP insertions," *Nano Letters*, vol. 7, pp. 1500–1504, 2007. 36

[71] S. N. Mohammad, "General hypothesis governing the growth of single-crystal nanowires," *Journal of Applied Physics*, vol. 107, 2010. 31

[72] J. C. Harmand, G. Patriarche, N. Péré-Laperne, M.-N. Mérat-Combes, L. Travers, and F. Glas, "Analysis of vapor-liquid-solid mechanism in Au-assisted GaAs nanowire growth," *Applied Physics Letters*, vol. 87, no. 20, pp. –, 2005. 29

[73] J. Johansson, B. A. Wacaser, K. A. Dick, and W. Seifert, "Growth related aspects of epitaxial nanowires," *Nanotechnology*, vol. 17, no. 11, p. S355, 2006. 29

[74] G. Shen, B. Liang, X. Wang, H. Huang, D. Chen, and Z. L. Wang, "Ultrathin In_2O_3 nanowires with diameters below 4 nm: Synthesis, reversible wettability switching behavior, and transparent thin-film transistor applications," *ACS Nano*, vol. 5, no. 8, pp. 6148–6155, 2011. PMID: 21749098. 30

[75] P. Caroff, K. A. Dick, J. Johansson, M. E. Messing, K. Deppert, and L. Samuelson, "Controlled polytypic and twin-plane superlattices in III-V nanowires," *Nature Nanotechnology*, vol. 4, pp. 50–55, 2009. 30

[76] K. A. Dick, C. Thelander, L. Samuelson, and P. Caroff, "Crystal phase engineering in single InAs nanowires," *Nano Letters*, vol. 10, pp. 3494–3499, 2010. 30

[77] W. I. Park, D. H. Kim, S.-W. Jung, and G.-C. Yi, "Metalorganic vapor-phase epitaxial growth of vertically well-aligned ZnO nanorods," *Applied Physics Letters*, vol. 80, 2002. 30, 31

[78] S. C. Lyu, Y. Zhang, H. Ruh, H.-J. Lee, H.-W. Shim, E.-K. Suh, and C. J. Lee, "Low temperature growth and photoluminescence of well-aligned zinc oxide nanowires," *Chemical Physics Letters*, vol. 363, pp. 134–138, 2002.

[79] I. Levin, A. Davydov, B. Nikoobakht, N. Sanford, and P. Mogilevsky, "Growth habits and defects in ZnO nanowires grown on GaN/sapphire substrates," *Applied Physics Letters*, vol. 87, 2005.

[80] M. Heurlin, M. H. Magnusson, D. Lindgren, M. Ek, L. R. Wallenberg, K. Deppert, and L. Samuelson, "Continuous gas-phase synthesis of nanowires with tunable properties," *Nature*, vol. 492, pp. 90–94, 2012. 30

[81] K. Takahashi and T. Moriizumi, "Growth of InAs whiskers in wurtzite structure," *Japanese Journal of Applied Physics*, vol. 5, 1966. 30

[82] C. Thelander, P. Caroff, S. Plissard, A. W. Dey, and K. A. Dick, "Effects of crystal phase mixing on the electrical properties of InAs nanowires," *Nano Letters*, vol. 11, no. 6, pp. 2424–2429, 2011. PMID: 21528899. 30, 34, 48

[83] Y. W. Heo, V. Varadarajan, M. Kaufman, K. Kim, D. P. Norton, F. Ren, and P. H. Fleming, "Site-specific growth of ZnO nanorods using catalysis-driven molecular beam epitaxy," *Applied Physics Letters*, vol. 81, 2002. 30, 31, 127

[84] A. P. Levitt, *Whisker Technology*. New York - London - Sydney - Toronto: Wiley Interscience, 1970. 30

[85] T. Mårtensson, P. Carlberg, M. Borgström, L. Montelius, W. Seifert, and L. Samuelson, "Nanowire arrays defined by nanoimprint lithography," *Nano Letters*, vol. 4, no. 4, pp. 699–702, 2004. 30

[86] M. G. Jenke, D. Lerose, C. Niederberger, J. Michler, S. Christiansen, and I. Utke, "Toward local growth of individual nanowires on three-dimensional

microstructures by using a minimally invasive catalyst templating method," *Nano Letters*, vol. 11, no. 10, pp. 4213–4217, 2011. PMID: 21899320. 30

[87] M. H. Magnusson, K. Deppert, J.-O. Malm, J.-O. Bovin, and L. Samuelson, "Gold nanoparticles: Production, reshaping, and thermal charging," *Journal of Nanoparticle Research*, vol. 1, pp. 243–251, 1999. 30

[88] Y. Wang, V. Schmidt, S. Senz, and U. Gösele, "Epitaxial growth of silicon nanowires using an aluminium catalyst," *Nature Nanotechnology*, vol. 1, pp. 186–189, 2006. 31

[89] A. Fortcuberta i Morral, C. Colombo, G. Abstreiter, J. Arbiol, and J. R. Morante, "Nucleation mechanism of gallium-assisted molecular beam epitaxy growth of gallium arsenide nanowires," *Applied Physics Letters*, vol. 92, 2008. 31, 32

[90] K. Sato, A. Castaldini, N. Fukata, and A. Cavallini, "Electronic level scheme in boron- and phosphorus-doped silicon nanowires," *Nano Letters*, vol. 12, no. 6, pp. 3012–3017, 2012. 31, 49

[91] D. E. Perea, J. E. Allen, S. J. Ma, B. W. Wessels, D. N. Seidman, and L. J. Lauhon, "Three-dimensional nanoscale composition mapping of semiconductor nanowires," *Nano Letters*, vol. 6, pp. 181–185, 2006. 31

[92] Y. Wang, V. Schmidt, S. Senz, and U. Gösele, "Epitaxial growth of silicon nanowires using an aluminium catalyst," *Nature Nanotechnology*, vol. 1, pp. 186–189, 2006. 31

[93] J. Johansson, B. A. Wacaser, K. A. Dick, and W. Seifert, "Growth related aspects of epitaxial nanowires," *Nanotechnology*, vol. 17, pp. S355–S361, 2006. 31

[94] Y. Xia, P. Yang, Y. Sun, Y. Wu, B. Mayers, B. Gates, Y. Yin, F. Kim, and H. Yan, "One-dimensional nanostructures: Synthesis, characterization, and applications," *Advanced Materials*, vol. 15, no. 5, pp. 353–389, 2003. 31

[95] G. Koblmüller, S. Hertenberger, K. Vizbaras, M. Bichler, F. Bao, J.-P. Zhang, and G. Abstreiter, "Self-induced growth of vertical free-standing InAs nanowires on Si(111) by molecular beam epitaxy," *Nanotechnology*, vol. 21, 2010. 31, 32, 97

[96] C. Thiandoume, J. Barjon, O. Ka, A. Lusson, P. Galtier, and V. Sallet, "Morphology transition of one-dimensional ZnO grown by metal organic vapour phase epitaxy on (0001)-ZnO substrate," *Journal of Crystal Growth*, vol. 311, no. 18, pp. 4311 – 4316, 2009. 31

[97] C.-H. Kwak, B.-H. Kim, S.-H. Park, S.-Y. Seo, C.-I. Park, S.-H. Kim, and S.-W. Han, "In-situ and ex-situ ZnO nanorod growth on ZnO homo-buffer layers," *Journal of Crystal Growth*, vol. 311, no. 20, pp. 4491 – 4494, 2009. 31

[98] D. J. Lee, J. Y. Park, Y. S. Yun, Y. S. Hong, J. H. Moon, B.-T. Lee, and S. S. Kim, "Comparative studies on the growth behavior of ZnO nanorods by metalorganic chemical vapor deposition depending on the type of substrates," *Journal of Crystal Growth*, vol. 276, no. 3-4, pp. 458 – 464, 2005. 31

[99] S.-S. Park, J.-M. Lee, S.-J. Kim, S.-W. Kim, H. H. Lee, S.-H. Kim, and S. Fujita, "Catalyst-free synthesis of ZnO nanorods on metal substrates by using thermal chemical vapor deposition," *Journal of Korean Physical Society*, vol. 53, no. 1, pp. 183–187, 2008. 31

[100] Y.-J. Kim, J.-H. Lee, and G.-C. Yi, "Vertically aligned ZnO nanostructures grown on graphene layers," *Applied Physics Letters*, vol. 95, no. 21, pp. –, 2009. 31, 44

[101] E. Dimakis, J. Lahnemann, U. Jahn, S. Breuer, M. Hilse, L. Geelhaar, and H. Riechert, "Self-assisted nucleation and vapor-solid growth of InAs nanowires on bare Si(111)," *Crystal Growth and Design*, vol. 11, pp. 4001–4008, 2011. 32

[102] D. Ercolani, F. Rossi, A. Li, S. Roddaro, V. Grillo, G. Salviati, F. Beltram, and L. Sorba, "InAs/InSb nanowire heterostructures grown by chemical beam epitaxy," *Nanotechnology*, vol. 20, 2009. 36, 38, 115

[103] S. Hertenberger, D. Rudolph, S. Bolte, M. Doblinger, M. Bichler, D. Sprikoska, J. J. Finley, G. Abstreiter, and K. G, "Absence of vapor-liquid solid growth during molecular beam epitaxy of self-induced InAs nanowires on Si," *Appllied Physics Letters*, vol. 98, 2011. 32

[104] B. Mandl, J. Stangl, T. Mårtensson, A. Mikkelsen, J. Eriksson, L. Karlsson, G. Bauer, L. Samuelston, and W. Seifert, "Au-free epitaxial growth of InAs nanowires," *Nano Letters*, vol. 6, pp. 1817–1821, 2006. 32

[105] B. Mandl, A. W. Dey, J. Stangl, M. Cantoro, L.-E. Wernersson, G. Bauer, L. Samuelson, K. Deppert, and C. Thelander, "Self-seeded, position-controlled inas nanowire growth on Si: A growth parameter study," *Journal of Crystal Growth*, vol. 334, no. 1, pp. 51 – 56, 2011. 32

[106] L. C. Chuang, M. Moewe, C. Chase, N. P. Kobayashi, C. Chang-Hasnain, and S. Crankshaw, "Critical diameter for III-V nanowires grown on lattice-mismatched substrates," *Applied Physics Letters*, vol. 90, 2007. 32

[107] B. Mandl, J. Stangl, E. Hilner, A. A. Zakharov, K. Hillerich, A. W. Dey, L. Samuelson, G. Bauer, K. Deppert, and A. Mikkelsen, "Growth mechanism of self-catalyzed group III-V nanowires," *Nano Letters*, vol. 10, no. 11, pp. 4443 – 4449, 2010. PMID: 20939507. 32, 33, 100

[108] T. Grap, T. Rieger, C. Blömers, T. Schäpers, D. Grützmacher, and M. I. Lepsa, "Self-catalyzed VLS grown InAs nanowires with twinning superlattices," *Nanotechnology*, vol. 24, no. 33, p. 335601, 2013. 32, 100

[109] F. Glas, J.-C. Harmand, and G. Patriarche, "Why does wurtzite form in nanowires of III-V zinc blende semiconductors?," *Phys. Rev. Lett.*, vol. 99, p. 146101, Oct 2007. 32, 100

[110] D. Kriegner, C. Panse, B. Mandl, K. Dick, M. Keplinger, J. M. Persson, P. Caroff, D. Ercolani, L. Sorba, F. Bechstedt, J. Stangl, and G. Bauer,

"Unit cell structure of crystal polytypes in InAs and InSb nanowires," *Nano Letters*, vol. 11, pp. 1483 – 1489, 2011. 33, 34, 109, 111

[111] D. Kriegner, E. Wintersberger, K. Kawaguchi, J. Wallentin, M. T. Borgstrom, and J. Stangl, "Unit cell parameters of wurtzite InP nanowires determined by X-ray diffraction," *Nanotechnology*, vol. 22, 2011. 33, 111

[112] L. Li, Z. Yang, J. Y. Kong, and J. L. Liu, "Blue electroluminescence from ZnO based heterojunction diodes with CdZnO active layers," *Applied Physics Letters*, vol. 95, 2009. 35

[113] S. Sadofev, S. Blumstengel, J. Cui, J. Puls, S. Rogaschewski, P. Schäfer, and F. Henneberger, "Visible band-gap ZnCdO heterostructures grown by molecular beam epitaxy," *Applied Physics Letters*, vol. 89, no. 20, pp. –, 2006. 35

[114] M. Lopez-Ponce, A. Hierro, J. M. Ulloa, P. Lefebvre, E. Muñoz, S. Agouram, V. Muñoz-Sanjosé, K. Yamamoto, A. Nakamura, and J. Temmyo, "Optical properties and microstructure of 2.02–3.30 eV ZnCdO nanowires: Effect of thermal annealing," *Applied Physics Letters*, vol. 102, no. 14, pp. –, 2013. 35

[115] K. Koike, K. Hama, I. Nakashima, G. Takada, K. Ogata, S. Sasa, M. Inoue, and M. Yano, "Molecular beam epitaxial growth of wide bandgap ZnMgO alloy films on (111)-oriented Si substrate towards UV-detector applications," *Journal of Crystal Growth*, vol. 278, pp. 288–292, 2005. 35, 67

[116] Z. Liu, Z. Mei, T. Zhang, Y. Liu, Y. Guo, X. Du, A. Hallen, J. Zhu, and A. Kuznetsov, "Solar-blind 4.55 eV band gap $Mg_{0.55}Zn_{0.45}O$ components fabricated using quasi-homo buffers," *Journal of Crystal Growth*, vol. 311, no. 18, pp. 4356 – 4359, 2009. 35, 67

[117] Y. Heo, M. Kaufman, K. Pruessner, D. Norton, F. Ren, M. Chisholm, and P. Fleming, "Optical properties of $Zn_{1-x}Mg_xO$ nanorods using catalysis-driven molecular beam epitaxy," *Solid-State Electronics*, vol. 47, no. 12, pp. 2269 – 2273, 2003. Proceedings of the 9th International Workshop on Oxide Electronics. 35, 36, 40

[118] A. Ohtomo, M. Kawasaki, T. Koida, K. Masubuchi, H. Koinuma, Y. Sakurai, Y. Yoshida, T. Yasuda, and Y. Segawa, "$Mg_xZn_{1-x}O$ as a II-VI widegap semiconductor alloy," *Applied Physics Letters*, vol. 72, pp. 2466–2468, May 1998. 35, 67

[119] Y. Matsumoto, M. Murakami, J. Zhengwu, A. Ohtomo, M. Lippmaa, M. Kawasaki, and H. Koinuma, "Combinatorial laser molecular beam epitaxy growth of Mg-Zn-O alloy for band gap engineering," *Japanese Journal of Applied Physics*, vol. 38, pp. L603–L605, 1999. 35, 67

[120] Y. W. Heo, C. Abernathy, K. Pruessner, W. Sigmund, D. P. Norton, M. Overberg, F. Ren, and M. F. Chisholm, "Structure and optical properties of cored wurtzite (Zn,Mg)O heteroepitaxial nanowires," *Journal of Applied Physics*, vol. 96, 2004. 35

[121] Y. Heo, M. Kaufman, K. Pruessner, K. Siebein, D. Norton, and F. Ren, "ZnO/cubic (Mg,Zn)O radial nanowire heterostructures," *Applied Physics A*, vol. 80, no. 2, pp. 263–266, 2005. 38, 39, 149

[122] Y. W. Heo, L.-C. Tien, and D. P. Norton, "Cubic (MgZn)O nanowire growth using catalyst-driven molecular beam epitaxy," *Journal of Material Research*, vol. 20, pp. 3028 – 3033, 2005. 35, 40

[123] L. Samuelson, P. Omling, and H. G. Grimmeiss, "Alloying mechanisms in MOVPE $GaAs_{1-x}P_x$," *Journal of Crystal Growth*, vol. 61, pp. 425 – 426, 1983. 36, 64

[124] H. Seki and A. Koukitu, "Thermodynamic analysis of molecular beam epitaxy of III-V semiconductors," *Journal of Crystal Growth*, vol. 78, pp. 342–352, 1986. 36

[125] B. G. Stringfellow, "Calculation of ternary and quaternary III-V phase diagrams," *Journal of Crystal Growth*, pp. 21–34, 1974.

[126] Z.-B. Hao, Z.-Y. Ren, W.-P. Guo, and Y. Luo, "Studies on incorporation of As_2 and As_4 in III-V compound semiconductors with two group V elements

grown by molecular beam epitaxy," *Journal of Crystal Growth*, vol. 224, pp. 224–229, 2001.

[127] H. Seki and A. Koukitu, "Solid composition of alloy semiconductors grown by MOVPE, MBE, VPE and ALE," *Journal of Crystal Growth*, vol. 98, pp. 118–126, 1989. 36

[128] A. I. Persson, M. T. Björk, S. Jeppesen, J. B. Wagner, L. R. Wallengerg, and L. Samuelson, "$InAs_{1-x}P_x$ nanowires for device engineering," *Nano Letters*, vol. 6, pp. 403–407, 2006. 36, 64, 112

[129] M. Mattila, T. Hakkarainen, H. Lipsanen, H. Jiang, and E. I. Kauppinen, "Catalyst-free growth of In(As)P nanowires on silicon," *Applied Physics Letters*, vol. 89, 2006. 36

[130] J. Trägårdh, A. I. Persson, J. B. Wagner, D. Hessman, and L. Samuelson, "Measurements of the band gap of wurtzite $InAs_{1-x}P_x$ nanowires using photocurrent spectroscopy," *Journal of applied physics*, vol. 101, 2007. 36

[131] J. C. Shin, K. H. Kim, K. J. Yu, H. Hu, L. Yin, C.-Z. Ning, J. A. Rogers, J.-M. Zuo, and X. Li, "$In_xGa_{1-x}As$ nanowires on silicon: one-dimensional heterogeneous epitaxy, bandgap engineering, and photovoltaics," *Nano Letters*, vol. 11, pp. 4831 – 4838, 2011. 36

[132] Y. Hu, H. O. H. Churchill, D. J. Reilly, J. Xiang, and C. M. Lieber, "A Ge//Si heterostructure nanowire-based double quantum dot with integrated charge sensor," *Nature Nanotechnology*. 37

[133] C. Fasth, A. Fuhrer, M. T. Björk, and L. Samuelson, "Tunable double quantum dots in InAs nanowires defined by local gate electrodes," *Nano Letters*, vol. 5, no. 7, pp. 1487–1490, 2005. PMID: 16178262.

[134] Y. Huang, X. Duan, Y. Cui, and C. M. Lieber, "Gallium nitride nanowire nanodevices," *Nano Letters*, vol. 2, no. 2, pp. 101–104, 2002.

[135] R. Songmuang, G. Katsaros, E. Monroy, P. Spathis, C. Bougerol, M. Mongillo, and S. De Franceschi, "Quantum Transport in GaN/AlN

Double-Barrier Heterostructure Nanowires," *Nano Letters*, vol. 10, no. 9, pp. 3545–3550, 2010. PMID: 20731363. 37

[136] M. T. Björk, B. J. Ohlsson, T. Sass, A. I. Persson, C. Thelander, M. H. Magnusson, K. Depeprt, L. R. Wallenberg, and L. Samuelson, "One-dimensional heterostructures in semiconductor nanowhiskers," *Aplpied Physics Letters*, vol. 80, 2002. 38

[137] C. M. Haapamaki and R. R. LaPierre, "Mechanisms of molecular beam epitaxy growth in InAs/InP nanowire heterostructrues," *Nanotechnology*, vol. 22, 2011. 38

[138] B. J. Ohlsson, M. T. Björk, A. I. Persson, C. Thelander, L. R. Wallenberg, M. H. Magnusson, K. Deppert, and L. Samuelson, "Growth and characterization of GaAs and InAs nanowhiskers and InAs/GaAs heterostructures," *Physica E*, pp. 1126–1130, 2002. 38

[139] W. I. Park, G.-C. Yi, M. Kim, and S. J. Pennycook, "Quantum confinement observed in ZnO/ZnMgO nanorod heterostrucutres," *Advanced Materials*, vol. 15, 2003. 38, 40, 41, 160, 162

[140] A. Bakin, A. El-Shaer, A. C. Mofor, M. Al-Suleiman, E. Schlenker, and A. Waag, "ZnMgO-ZnO quantum wells embedded in ZnO nanopillars: Towards realisation of nano-LEDs," *Physica Status Solidi C*, vol. 4, pp. 158–161, 2007. 38

[141] J. Falson, D. Maryenko, Y. Kozuka, A. Tsukazaki, and M. Kawasaki, "Magnesium doping controlled density and mobility of two-dimensional electron gas in $Mg_xZn_{1-x}O$/ZnO heterostructures," *Applied Physics Express*, vol. 4, no. 9, p. 091101, 2011. 38

[142] D. Maryenko, J. Falson, Y. Kozuka, A. Tsukazaki, M. Onoda, H. Aoki, and M. Kawasaki, "Temperature-Dependent Magnetotransport around $\nu = 1/2$ in ZnO Heterostructures," *Phys. Rev. Lett.*, vol. 108, p. 186803, May 2012. 38

[143] A. Tsukazaki, A. Ohtomo, T. Kita, Y. Ohno, H. Ohno, and M. Kawasaki, "Quantum hall effect in polar oxide heterostructures," *Science*, vol. 315, 2007. 38

[144] W. Lu, J. Xiang, B. P. Timko, Y. Wu, and C. M. Lieber, "One-dimensional hole gas in germanium/silicon nanowire heterostructures," *Proceedings of the National Academy of Sciences of the United States of America*, vol. 102, no. 29, pp. 10046–10051, 2005. 38, 41

[145] J. Xiang, W. Lu, Y. Hu, Y. Wu, H. Yan, and C. M. Lieber, "Ge/Si nanowire heterostructures as highperformance field-effect transistors," *Nature*, vol. 441, pp. 489–493, 2006. 38, 41

[146] R. Thierry, G. Perillat-Merceroz, P. H. Jouneau, P. Ferret, and G. Feuillet, "Core-shell multi-quantum wells in ZnO/ZnMgO nanowires with high optical efficiency at room temperature," *Nanotechnology*, vol. 23, 2012. 38, 39, 40, 41, 42, 163

[147] X. Jiang, Q. Xiong, S. Nam, F. Qian, Y. Li, and C. M. Lieber, "InAs/InP radial nanowire heterostructures as high-electron mobility devices," *Nano Letters*, vol. 7, pp. 3214–3218, 2007. 38, 39, 40, 41, 44, 48

[148] J. W. W. v. Tilburg, R. E. Algra, W. G. G. Immink, M. Verheijen, E. P. A. M. Bakkers, and L. P. Kowenhoven, "Surface passivated InAs/InP core/shell nanowires," *Semiconductor Science and Technology*, vol. 25, 2010. 38, 39, 41

[149] T. Haggren, H. Jiang, J.-P. Kakko, T. Huhtio, V. Dhaka, E. Kauppinen, and H. Lipsanen, "Strong surface passivation of GaAs nanowires with ultrathin InP and GaP capping layers," *Applied Physics Letters*, vol. 105, no. 3, pp. –, 2014. 39, 48

[150] K. Matsumura, A. Ohnishi, M. Sasaki, T. Kakuta, M. Kurihara, and M. Sakamoto, "Fabrication of $Zn_{1-x}Mg_xO$ fine bulk crystals and nanocrystals by complex decomposition method and their characterization," *Japanese Journal of Applied Physics*, vol. 46, pp. 1432–1436, 2007. 39, 67

[151] J. Yoo, C. Bonghwan, W. Tang, T. Joo, L. S. Dang, and G.-C. Yi, "Excitonic origin of enhanced luminescence quantum efficiency in MgZnO/ZnO coaxial nanowire heterostructures," *Applied Physics Letters*, vol. 100, 2012. 40

[152] M. Lange, C. P. Dietrich, J. Zúñiga-Pérez, H. von Wenckstern, M. Lorenz, and M. Grundmann, "MgZnO/ZnO quantum well nanowire heterostructures with large confinement energies," *Journal of Vacuum Science Technology A*, vol. 29, no. 3, 2011. 154

[153] W. I. Park, J. Yoo, D.-W. Kim, G.-C. Yi, and M. Kim, "Fabrication and photoluminescent properties of heteroepitaxial ZnO/$Zn_{0.8}Mg_{0.2}O$ coaxial nanorod heterostructures," *The Journal of Physical Chemistry B*, vol. 110, no. 4, pp. 1516–1519, 2006. PMID: 16471707. 40, 154

[154] B. Q. Cao, J. Zuniga-Perez, N. Boukos, C. Czekalla, H. Hilmer, J. Lenzner, A. Travlos, M. Lorenz, and M. Grudnmann, "Homogeneous core/shell ZnO/ZnMgO quantum well heterostructures on vertical zno nanowires," *Nanotechnology*, vol. 20, 2009. 40

[155] G. Perillat-Merceroz, R. Thierry, P.-H. Jouneau, P. Ferret, and G. Feuillet, "Strain relaxation by dislocation glide in ZnO/ZnMgO core-shell nanowires," *Applied Physics Letters*, vol. 100, no. 17, pp. –, 2012. 40

[156] E.-S. Jang, J. Y. Bae, J. Yoo, W. I. Park, D.-W. Kim, G.-C. Yi, T. Yatsui, and M. Ohtsu, "Quantum confinement effect in ZnO/$Mg_{0.2}Zn_{0.8}O$ multishell nanorod heterostructures," *Applied Physics Letters*, vol. 88, no. 2, pp. –, 2006. 40, 41, 42, 160, 162

[157] C.-H. Lee, J. Yoo, Y.-J. Doh, and G.-C. Yi, "ZnO/$Mg_{0.2}Zn_{0.8}O$ coaxial nanorod heterostructures for high-performance electronic nanodevice applications," *Applied Physics Letters*, vol. 94, no. 4, pp. –, 2009. 41

[158] Y. Li, J. Xiang, F. Qian, S. Gradečak, Y. Wu, H. Yan, D. A. Blom, and C. M. Lieber, "Dopant-free GaN/AlN/AlGaN radial nanowire heterostructures as high electron mobility transistors," *Nano Letters*, vol. 6, no. 7, pp. 1468–1473, 2006. PMID: 16834431. 41

[159] B. L. Altshuler, A. G. Aronov, and B. Z. Spivak, "The Aharonov-Bohm effect in disordered conductors," *Pis'ma Zh. Eksp. Teor. Fiz.*, vol. 33, pp. 101–103, 1981. 43

[160] O. Gül, N. Demarina, C. Blömers, T. Rieger, H. Lüth, M. I. Lepsa, D. Grützmacher, and T. Schäpers, "Flux periodic magnetoconductance oscillations in GaAs/InAs core/shell nanowires," *Phys. Rev. B*, vol. 89, p. 045417, Jan 2014. 43

[161] M. Jung, J. S. Lee, W. Song, Y. H. Kim, S. D. Lee, N. Kim, J. Park, M.-S. Choi, S. Katsumoto, H. Lee, and J. Kim, "Quantum interference in radial heterostructure nanowires," *Nano Letters*, vol. 8, no. 10, pp. 3189–3193, 2008. PMID: 18767885. 43

[162] A. Tsukazaki, Y. Hiroyuki, A. Shunsuke, T. Kentaro, N. Ken, T. Tetsuhiro, T. Hidemi, A. Ohtomo, and M. Kasawaki, "High Electron Mobility Exceeding 10^4 $cm^2/(V\ s)$ in $Mg_xZn_{1-x}O/ZnO$ Single Heterostructures Grown by Molecular Beam Epitaxy," *Applied Physics Express*, vol. 1, 2008. 43

[163] D. M. Kim and Y.-H. Jeong, *Nanowire Field Effect Transistors: Principles and Applications*. Springer, 2014. 43

[164] S. N. Cha, J. E. Jang, Y. Choi, G. A. J. Amaratunga, G. W. Ho, M. E. Welland, D. G. Hasko, D.-J. Kang, and J. M. Kim, "High performance ZnO nanowire field effect transistor using self-aligned nanogap gate electrodes," *Applied Physics Letters*, vol. 89, 2006. 43, 44, 45

[165] V. Schmidt, H. Riel, S. Senz, S. Karg, W. Riess, and U. Gösele, "Realization of a silicon nanowire vertical surround-gate field-effect transistor," *Small*, vol. 2, no. 1, pp. 85–88, 2006. 43

[166] J. Goldberger, A. I. Hochbaum, R. Fan, and P. Yang, "Silicon vertically integrated nanowire field effect transistors," *Nano Letters*, vol. 6, no. 5, pp. 973–977, 2006. 43, 44, 85, 172

[167] C. Blömers, T. Rieger, T. Grap, M. Raux, M. I. Lepsa, H. Lüth, D. Grützmacher, and T. Schäpers, "Gate-induced transition between metal-type and

thermally activated transport in self-catalyzed MBE-grown InAs nanowires," *Nanotechnology*, vol. 24, no. 32, p. 325201, 2013. 44

[168] D. Wang, Y.-L. Chang, Q. Wang, J. Cao, D. B. Farmer, R. G. Gordon, and H. Dai, "Surface chemistry and electrical properties of germanium nanowires," *Journal of the American Chemical Society*, vol. 126, no. 37, pp. 11602–11611, 2004. PMID: 15366907. 44, 48

[169] W. I. Park, J. S. Kim, G.-C. Yi, M. H. Bae, and H.-J. Lee, "Fabrication and electrical characteristics of high-performance ZnO nanorod field-effect transistors," *Applied Physics Letters*, vol. 85, no. 21, 2004. 44

[170] L.-T. Chang, C.-Y. Wang, J. Tang, T. Nie, W. Jiang, C.-P. Chu, S. Arafin, L. He, M. Afsal, L.-J. Chen, and K. L. Wang, "Electric-field control of ferromagnetism in Mn-doped ZnO nanowires," *Nano Letters*, vol. 14, no. 4, pp. 1823–1829, 2014. PMID: 24564741. 44, 45, 178

[171] Y. W. Heo, L. C. Tien, D. P. Norton, B. S. Kang, F. Ren, B. P. Gila, and S. J. Pearton, "Electrical transport properties of single ZnO nanorods," *Applied Physics Letters*, vol. 85, 2004. 44, 45, 172

[172] Q. H. Li, Y. X. Liang, Q. Wan, and T. H. Wang, "Oxygen sensing characteristics of individual ZnO nanowire transistors," *Applied Physics Letters*, vol. 85, no. 26, 2004.

[173] W.-K. Hong, D.-K. Hwang, I.-K. Park, G. Jo, S. Song, S.-J. Park, T. Lee, B.-J. Kim, and E. A. Stach, "Realization of highly reproducible ZnO nanowire field effect transistors with n-channel depletion and enhancement modes," *Applied Physics Letters*, vol. 90, no. 24, pp. –, 2007. 44

[174] Z. Fan, D. Wang, P.-C. Chang, W.-Y. Tseng, and J. G. Lu, "ZnO nanowire field-effect transistor and oxygen sensing property," *Applied Physics Letters*, vol. 85, no. 24, 2004. 44, 172

[175] P.-C. Chang, Z. Fan, C.-J. Chien, D. Stichtenoth, C. Ronning, and J. G. Lu, "High-performance ZnO nanowire field effect transistors," *Applied Physics Letters*, vol. 89, no. 13, pp. –, 2006. 45

[176] J. Goldberger, D. J. Sirbuly, M. Law, and P. Yang, "ZnO nanowire transistors," *The Journal of Physical Chemistry B*, vol. 109, no. 1, pp. 9–14, 2005. 45

[177] C.-Y. Chen, J. R. D. Retamal, I.-W. Wu, D.-H. Lien, M.-W. Chen, Y. Ding, Y.-L. Chueh, C.-I. Wu, and J.-H. He, "Probing surface band bending of surface-engineered metal oxide nanowires," *ACS Nano*, vol. 6, no. 11, pp. 9366–9372, 2012. 45, 80, 163

[178] L. J. Brillson and Y. Lu, "ZnO schottky barriers and ohmic contacts," *Journal of Applied Physics*, vol. 109, no. 12, pp. –, 2011. 45

[179] H. F. Matare, *Defect Electronics in Semiconductors*. John Wilet Sons Inc, 1971. 46

[180] A. Bondarenko, O. Vyvenko, I. Isakov, and O. Kononchuk, "Correlation between cathodoluminescent and electrical properties of dislocation network in the space charge region of schottky-diode," *physica status solidi (c)*, vol. 8, no. 4, pp. 1273–1277, 2011. 46

[181] M. Kittler and M. Reiche, "Dislocations as active components in novel silicon devices," *Advanced Engineering Materials*, vol. 11, no. 4, pp. 249–258, 2009. 46

[182] A. Janotti and C. G. V. de Walle, "Fundamentals of zinc oxide as a semiconductor," *Reports on Progress in Physics*, vol. 72, no. 12, p. 126501, 2009. 47, 144, 171, 185

[183] D. M. Hofmann, A. Hofstaetter, F. Leiter, H. Zhou, F. Henecker, B. K. Meyer, S. B. Orlinskii, J. Schmidt, and P. G. Baranov, "Hydrogen: A relevant shallow donor in zinc oxide," *Phys. Rev. Lett.*, vol. 88, p. 045504, Jan 2002. 47

[184] D. C. Look, G. C. Farlow, P. Reunchan, S. Limpijumnong, S. B. Zhang, and K. Nordlund, "Evidence for Native-Defect Donors in n-Type ZnO," *Phys. Rev. Lett.*, vol. 95, p. 225502, Nov 2005. 47, 171, 185

[185] V. Quemener, L. Vines, E. V. Monakhov, and B. G. Svensson, "Evolution of deep electronic states in ZnO during heat treatment in oxygen- and zinc-rich ambients," *Applied Physics Letters*, vol. 100, no. 11, pp. –, 2012. 47, 48, 194

[186] F. Schmidt, S. Müller, H. von Wenckstern, C. P. Dietrich, R. Heinhold, H.-S. Kim, M. W. Allen, and M. Grundmann, "Comparative study of deep defects in ZnO microwires, thin films and bulk single crystals," *Applied Physics Letters*, vol. 103, no. 6, pp. –, 2013. 48, 194

[187] F. D. Auret, S. A. Goodman, M. J. Legodi, W. E. Meyer, and D. C. Look, "Electrical characterization of vapor-phase-grown single-crystal ZnO," *Applied Physics Letters*, vol. 80, no. 8, 2002. 48, 194

[188] A. Hupfer, C. Bhoodoo, L. Vines, and B. G. Svensson, "The E3 center in zinc oxide: Evidence for involvement of hydrogen," *Applied Physics Letters*, vol. 104, no. 9, pp. –, 2014. 47, 48, 194

[189] M. J. Sourribes, I. Isakov, M. Panfilova, and P. A. Warburton, "Minimization of the contact resistance between InAs nanowires and metallic contacts," *Nanotechnology*, vol. 24, no. 4, p. 045703, 2013. 48, 115, 168

[190] J. Maeng, W. Park, M. Choe, G. Jo, Y. H. Kahng, and T. Lee, "Transient drain current characteristics of zno nanowire field effect transistors," *Applied Physics Letters*, vol. 95, no. 12, pp. –, 2009. 48, 93

[191] A. Motayed, S. Krylyuk, and A. V. Davydov, "Characterization of deep-levels in silicon nanowires by low-frequency noise spectroscopy," *Applied Physics Letters*, vol. 99, pp. 113107–113107–3, Sep 2011. 49

[192] D. Sharma, A. Motayed, S. Krylyuk, Q. Li, and A. Davydov, "Detection of deep-levels in doped silicon nanowires using low-frequency noise spectroscopy," *Electron Devices, IEEE Transactions on*, vol. 60, pp. 4206–4212, Dec 2013. 49

[193] A. Cavallini, G. Verzellesi, A. F. Basile, C. Canali, A. Castaldini, and E. Zanoni, "Origin of hole-like peaks in current deep level transient spec-

troscopy of n-channel AlGaAs/GaAs heterostructure field-effect transistors," *Journal of Applied Physics*, vol. 94, no. 8, 2003. 49, 93, 94, 196

[194] G. A. Somorjai and Y. Li, *Introduction to Surface Chemistry and Catalysis*. John Wiley and Sons, 2010. 60

[195] L. Vegard, "Die Konstitution der Mischkristalle und die Raumfüllung der Atome," *Zeitschrift fur Physik*, vol. 5, pp. 17–26, 1921. 63, 64

[196] T. B. Joyce and T. J. Bullough, "Beam equivalent pressure measurements in chemical beam epitaxy," *Journal of Crystal Growth*, vol. 127, pp. 265–269, 1993. 64

[197] C. E. C. Wood, D. Desimone, K. Singer, and G. W. Wicks, "Magnesium- and calcium-doping behavior in molecular-beam epitaxial III-V compounds," *Journal of Applied Physics*, vol. 1982, 1982. 64

[198] K. Ogata, K. Koike, T. Tanite, T. Komuro, F. Yan, S. San, M. Inoue, and M. Yano, "ZnO and ZnMgO growth on a-plane sapphire by molecular beam epitaxy," *Journal of Crystal Growth*, vol. 251, pp. 623–627, 2003. 67

[199] A. El-Shaer, A. Bakin, M. Al-Suleiman, S. Ivanov, A. Che Mofor, and A. Waag, "Growth of wide band gap wurtzite znmgo layers on (0001) Al_2O_3 by radical-source molecular beam epitaxy," *Superlattices and Microstructures*, vol. 42, pp. 129–133, 2007. 67

[200] Y. Kozuka, J. Falson, Y. Segawa, T. Makino, A. Tsukazaki, and M. Kawasaki, "Precise calibration of mg concentration in $Mg_xZn_{1x}O$ thin films grown on ZnO substrates," *Journal of Applied Physics*, vol. 112, no. 4, pp. –, 2012. 67

[201] H. A. Kramers, "XCIII. On the theory of X-ray absorption and of the continuous X-ray spectrum," *Philosophical Magazine Series 6*, vol. 46, no. 275, pp. 836–871, 1923. 69

[202] M. Haungs, *A brief table of X-ray line energies and widths*. 1986. 72

[203] R. Palgrave, "UCL X-ray photoelectron spectrometer," 2014. 73

[204] W. Schottky, "Zur Halbleitertheorie der Sperrschicht- und Spitzengleichrichter," *Zeitschrift fÃijr Physik*, vol. 113, no. 5-6, pp. 367–414, 1939. 77

[205] S. M. Sze, *Physics of semiconductor devices*. New York, London, Sydney, Toronto: Wiley Intescience, 1969. 79, 84, 85, 172, 181

[206] A. Soudi, C.-H. Hsu, and Y. Gu, "Diameter-dependent surface photovoltage and surface state density in single semiconductor nanowires," *Nano Letters*, vol. 12, no. 10, pp. 5111–5116, 2012. 80

[207] C. Blömers, T. Grap, M. I. Lepsa, J. Moers, S. Trellenkamp, D. Grützmacher, H. Lüth, and T. Schäpers, "Hall effect measurements on InAs nanowires," *Applied Physics Letters*, vol. 101, no. 15, pp. –, 2012. 80

[208] O. Wunnicke, "Gate capacitance of back-gated nanowire field-effect transistors," *Applied Physics Letters*, vol. 89, no. 8, pp. –, 2006. 83

[209] D. Vashaee, A. Shakouri, J. Goldberger, T. Kuykendall, P. Pauzauskie, and P. Yang, "Electrostatics of nanowire transistors with triangular cross sections," *Journal of Applied Physics*, vol. 99, no. 5, pp. –, 2006. 86

[210] Z. Zhang, K. Yao, Y. Liu, C. Jin, X. Liang, Q. Chen, and L.-M. Peng, "Quantitative analysis of current-voltage characteristics of semiconducting nanowires: Decoupling of contact effects," *Advanced Functional Materials*, vol. 17, no. 14, pp. 2478–2489, 2007. 86

[211] W. Shockley and W. T. Read, "Statistics of the recombinations of holes and electrons," *Phys. Rev.*, vol. 87, pp. 835–842, Sep 1952. 89, 94

[212] R. N. Hall, "Electron-hole recombination in germanium," *Phys. Rev.*, vol. 87, pp. 387–387, Jul 1952. 89

[213] M. Yong-Jun, Z. Ze, Z. Feng, L. Li, J. Aizi, and G. Changzhi, "Hopping conduction in single ZnO nanowires," *Nanotechnology*, vol. 16, no. 6, p. 746, 2005. 94, 178

[214] Z. Li, "Systematic modelling and comparisons of capacitance and current-based microscopic defect analysis techniques for measurements of high-resistivity silicon detectors after irradiation," *Nuclear Instruments and Methods in Physics Research Section A: Accelerators, Spectrometers, Detectors and Associated Equipment*, vol. 403, no. 2 - 3, pp. 399 – 416, 1998. 96

[215] M. H. Sun, H. J. Joyce, Q. Gao, H. H. Tan, C. Jagadish, and C. Z. Ning, "Removal of Surface States and Recovery of Band-Edge Emission in InAs Nanowires through Surface Passivation," *Nano Letters*, vol. 12, no. 7, pp. 3378–3384, 2012. PMID: 22663381. 112

[216] M. Möller, M. M. de Lima Jr, A. Cantarero, T. Chiaramonte, M. A. Cotta, and F. Iikawa, "Optical emission of InAs nanowires," *Nanotechnology*, vol. 23, no. 37, p. 375704, 2012. 113

[217] I. Vurgaftman, J. R. Meyer, and L. R. Ram-Mohan, "Band parameters for III-V compound semiconductors and their alloys," *Journal of Applied Physics*, vol. 89, no. 11, 2001. 118

[218] M. Y. Yen, R. People, K. W. Wecht, and A. Y. Cho, "Long-wavelength photoluminescence of $InAs_{1-x}Sb_x$ ($0 < x < 1$) grown by molecular beam epitaxy on (100) InAs," *Applied Physics Letters*, vol. 52, no. 6, 1988. 118

[219] Z. M. Fang, K. Y. Ma, D. H. Jaw, R. M. Cohen, and G. B. Stringfellow, "Photoluminescence of InSb, InAs, and InAsSb grown by organometallic vapor phase epitaxy," *Journal of Applied Physics*, vol. 67, no. 11, 1990. 118

[220] R. Weast, *CRC handbook of chemistry and physics: a ready-reference book of chemical and physical data*. Boca Raton, Fla: CRC Press, 1985. 121

[221] K. Haga, T. Suzuki, Y. Kashiwaba, H. Watanabe, B. Zhang, and Y. Segawa, "High-quality ZnO films prepared on Si wafers by low-pressure MO-CVD," *Thin Solid Films*, vol. 433, no. 1 - 2, pp. 131 – 134, 2003. Proceedings from the 12th International Conference on Thin Films. 127

[222] C. W. Bunn, "The lattice-dimensions of zinc oxide," *Proceedings of the Physical Society*, vol. 47, no. 5, p. 835, 1935. 143

[223] N. Y. Garces, L. Wang, L. Bai, N. C. Giles, L. E. Halliburton, and G. Cantwell, "Role of copper in the green luminescence from ZnO crystals," *Applied Physics Letters*, vol. 81, no. 4, 2002. 144

[224] H. J. Ko, Y. F. Chen, Z. Zhu, T. Yao, I. Kobayashi, and H. Uchiki, "Photoluminescence properties of ZnO epilayers grown on CaF_2(111) by plasma assisted molecular beam epitaxy," *Applied Physics Letters*, vol. 76, no. 14, 2000. 144, 145

[225] D. W. Hamby, D. A. Lucca, M. J. Klopfstein, and G. Cantwell, "Temperature dependent exciton photoluminescence of bulk ZnO," *Journal of Applied Physics*, vol. 93, no. 6, 2003. 144

[226] K. Sakai, K. Noguchi, A. Fukuyama, T. Ikari, and T. Okada, "Low-temperature photoluminescence of nanostructured ZnO crystal synthesized by pulsed-laser ablation," *Japanese Journal of Applied Physics*, vol. 48, 2009. 145

[227] L. F. Zagonel, S. Mazzucco, M. Tencé, K. March, R. Bernard, B. Laslier, G. Jacopin, M. Tchernycheva, L. Rigutti, F. H. Julien, R. Songmuang, and M. Kociak, "Nanometer scale spectral imaging of quantum emitters in nanowires and its correlation to their atomically resolved structure," *Nano Letters*, vol. 11, no. 2, pp. 568–573, 2011. PMID: 21182283. 162

[228] D. A. B. Miller, D. S. Chemla, T. C. Damen, A. C. Gossard, W. Wiegmann, T. H. Wood, and C. A. Burrus, "Band-edge electroabsorption in quantum well structures: The quantum-confined Stark Effect," *Phys. Rev. Lett.*, vol. 53, pp. 2173–2176, Nov 1984. 162

[229] J. C. Rivière, *Solid State Surface Science*, vol. 1. Marcel Dekker, New York, 1969. 168

[230] J. Hölzl and F. K. Schulte, *Solid Surface Physics*, vol. 85. Springer, 1979. 168

[231] K. Jacobi, G. Zwicker, and A. Gutmann, "Work function, electron affinity and band bending of zinc oxide surfaces," *Surface Science*, vol. 141, no. 1, pp. 109 – 125, 1984. 168

[232] H. Moormann, D. Kohl, and G. Heiland, "Work function and band bending on clean cleaved zinc oxide surfaces," *Surface Science*, vol. 80, no. 0, pp. 261 – 264, 1979. The solid-vacuum interface V.

[233] T. Minami, T. Miyata, and T. Yamamoto, "Work function of transparent conducting multicomponent oxide thin films prepared by magnetron sputtering," *Surface and Coatings Technology*, vol. 108-109, no. 0, pp. 583 – 587, 1998. 168

[234] S.-P. Chiu, Y.-H. Lin, and J.-J. Lin, "Electrical conduction mechanisms in natively doped ZnO nanowires," *Nanotechnology*, vol. 20, no. 1, p. 015203, 2009. 180

[235] W. T. N.F. Mott, "The theory of impurity conduction," *Advances in Physics*, 1961. 180

[236] B. K. Meyer, J. Sann, D. M. Hofmann, C. Neumann, and A. Zeuner, "Shallow donors and acceptors in ZnO," *Semiconductor Science and Technology*, vol. 20, no. 4, p. S62, 2005. 185

[237] I. Jolliffe, *Principal Component Analysis*. 2002, Springer. 187

[238] M. Bugajski and W. Lewandowski, "Concentration-dependent absorption and photoluminescence of n-type InP," *Journal of Applied Physics*, vol. 57, no. 2, 1985. 188

[239] V. Quemener, L. Vines, E. V. Monakhov, and B. G. Svensson, "Electrical Characterization of Hydrothermally Grown ZnO Annealed in Different Atmospheres," *International Journal of Applied Ceramic Technology*, vol. 8, no. 5, pp. 1017–1022, 2011. 194

[240] D. Seghier and H. P. Gislason, "On intrinsic defects in Co-doped ZnO thin films," *Physica Scripta*, vol. 2010, no. T141, p. 014007, 2010. 194

[241] J. G. Simmons, "Poole-frenkel effect and schottky effect in metal-insulator-metal systems," *Phys. Rev.*, vol. 155, pp. 657–660, Mar 1967. 198